Measurement of the diffractive contribution to the DIS cross section using the ZEUS Forward Plug Calorimeter

by

Florian Goebel

Measurement of the diffractive contribution to the DIS cross section using the ZEUS Forward Plug Calorimeter

DISSERTATION

zur Erlangung des Doktorgrades
des Fachbereichs Physik
der Universität Hamburg

vorgelegt von

Florian Goebel
aus Köln

Hamburg
April 2001

Gutachter der Dissertation:	Prof. Dr. V. Blobel Prof. Dr. K. Meier Prof. Dr. G. Wolf
Gutachter der Disputation:	Prof. Dr. R.-D. Heuer Prof. Dr. G. Wolf
Datum der Disputation:	12.09.2001
Dekan des Fachbereichs Physik und Vorsitzender des Promotionsausschusses:	Prof. Dr. F.-W. Büßer

Abstract

The aim of this thesis has been the measurement of the diffractive process $ep \to eXp$ in deep inelastic scattering over a much larger kinematic range than attained in previous measurements. The extension to high masses M_X has been made possible by the construction and installation of a Forward Plug Calorimeter (FPC) in the 20×20 cm^2 forward beam hole of the ZEUS calorimeter. With an inner hole diameter of only 6.3 cm the FPC extends the calorimetric coverage in pseudorapidity η from $\eta \approx 4.0$ to $\eta \approx 5.0$. Before installation in ZEUS the FPC has been tested and calibrated with test beams of 10-100 GeV. The diffractive cross section $d\sigma^{diff}_{\gamma^* p}/dM_X$ has been measured in deep inelastic scattering of 27.6 GeV electrons and 920 GeV protons at HERA. The analyzed data sample was collected with the ZEUS detector during the 1998/99 data taking period and corresponds to an integrated luminosity of 4.2 pb^{-1}. The measurement covers the mass range $M_X \leq 25$ GeV of the photon dissociation system X for photon virtualities $Q^2 = 3$ to 160 GeV^2 and $\gamma^* p$ center of mass energies $W = 40$ to 245 GeV which extends substantially the range covered by previous ZEUS analyses. The diffractive cross section $d\sigma^{diff}_{\gamma^* p}/dM_X(Q^2, W, M_X)$ has been compared to the total $\gamma^* p$ cross section $\sigma^{tot}_{\gamma^* p}(Q^2, W)$ which was determined in the course of this analysis. The ratio of the two has been found to be W independent. From the diffractive cross section the diffractive structure function $F_2^{D(3)}(Q^2, \beta, x_{I\!P})$ has been determined. The data is compatible with the assumption that $F_2^{D(3)}$ factorizes according to $x_{I\!P} F_2^{D(3)}(Q^2, \beta, x_{I\!P}) = (x_0/x_{I\!P})^n F_2^{D(2)}(Q^2, \beta)$. The dependence of $F_2^{D(2)}$ on Q^2 and β has been found to be weak in the measured range. However, a tendency of increasing $F_2^{D(2)}$ towards small β values has been observed which might be taken as an indication for parton evolution.

Zusammenfassung

Das Ziel dieser Arbeit war die Messung diffraktiver Prozesse $ep \to eXp$ in tiefunelastischer Streuung in einem wesentlich größeren kinematischen Bereich als dies in bisherigen Messungen erreicht worden war. Die Erweiterung zu großen Massen M_X wurde durch die Konstruktion und den Einbau eines Vorwärts-Stopfen-Kalorimeters (FPC) in das 20×20 cm^2 große Strahlrohrloch des ZEUS Kalorimeters ermöglicht. Der Durchmesser des inneren Strahlrohrlochs des FPC beträgt nur 6.3 cm. Die kalorimetrischen Akzeptanz in Pseudorapidität η wurde dadurch von $\eta \approx 4.0$ auf $\eta \approx 5.0$ erweitert. Vor dem Einbau in ZEUS ist das FPC mit Teststrahlen von 10-100 GeV getestet und geeicht worden. Der diffraktive Wirkungsquerschnitt $d\sigma^{diff}_{\gamma^* p}/dM_X$ wurde in der tiefunelastischen Streuung von 27.6 GeV Elektronen und 920 GeV Protonen bei HERA gemessen. Der analysierte Datensatz wurde mit dem ZEUS Detektor während der Datennahmeperiode 1998/99 aufgenommen und entspricht einer integrierten Luminosität von 4.2 pb^{-1}. Die Messung wurde im Massenbereich $M_X \leq 25$ GeV bei einer Virtualität des ausgetauschten Photons im Bereich von $Q^2 = 3$ bis 160 GeV^2 und bei $\gamma^* p$ Schwerpunktsenergien im Bereich von $W = 40$ bis 245 GeV durchgeführt, wodurch der kinematische Bereich erheblich gegenüber vorhergehenden ZEUS Arbeiten erweitert wurde. Der diffraktive Wirkungsquerschnitt $d\sigma^{diff}_{\gamma^* p}/dM_X(Q^2, W, M_X)$ wurde mit dem in dieser Arbeit bestimmten totalen $\gamma^* p$ Wirkungsquerschnitt $\sigma^{tot}_{\gamma^* p}(Q^2, W)$ verglichen. Ein W unabhängiges Verhältnis der Wirkungsquerschnitte wurde beobachtet. Aus dem diffraktiven Wirkungsquerschnitt wurde die diffraktive Strukturfunktion $F_2^{D(3)}(Q^2, \beta, x_{I\!P})$ bestimmt. Die Daten sind verträglich mit der Annahme, daß $F_2^{D(3)}$ in $x_{I\!P} F_2^{D(3)}(Q^2, \beta, x_{I\!P}) = (x_0/x_{I\!P})^n F_2^{D(2)}(Q^2, \beta)$ faktorisiert. Im gemessenen Bereich hängt $F_2^{D(2)}$ nur schwach von Q^2 und β ab. Die beobachtete Tendenz, daß $F_2^{D(2)}$ zu kleinen Werten von β ansteigt, kann jedoch als ein Hinweis auf Parton Evolution angesehen werden.

Contents

List of Figures

List of Tables

Introduction

Quantum Chromodynamics (QCD), the fundamental theory of strong interactions, is one of the integral components of the Standard Model of elementary particle physics. It describes strong interactions as the exchange of massless gauge bosons (gluons) between quarks and gluons, the fundamental constituents of hadrons. Developed in the 1970's QCD predictions have been confirmed in many experimental tests [1]. However, QCD can only be directly confronted with experiment in hard interactions occurring at short distances, where the coupling constant α_s becomes small and perturbative methods can be applied.

An important property of strong forces is that colored quarks and gluons are confined within hadrons and are unobservable as free particles. This is believed to be a feature of QCD but has never been proven rigorously, as perturbative QCD (pQCD) is not applicable in the region of long range forces which are responsible for confinement.

Peripheral scattering of hadrons is another important aspect of non-perturbative strong interactions. Several global features of these interactions are successfully described by the Regge formalism [34]. In the Regge approach these peripheral interactions are mediated by the exchange of Regge trajectories in the t-channel which are characterized by the quantum numbers - such as charge, isospin etc. - which they carry. Examples are the π and the ρ trajectories. These trajectories lead to a fast decrease of the cross section with the center of mass energy $\sqrt{s}$. There is however a special class of peripheral processes: diffractive scattering, where no quantum numbers are exchanged and which has (almost) energy independent cross sections. These processes are described by the Regge trajectory of a hypothetical particle called the pomeron [38].

Diffraction has been studied extensively in hadron-hadron scattering. Despite the wealth of data the nature of the pomeron has remained elusive. First evidence for a pomeron structure came from the observation of high transverse momentum jets in diffractively produced high mass systems in $p\bar{p}$ scattering [52] which was predicted by Ingelman and Schlein [51]. The observation that a substantial amount ($\sim$ 10%) of deep inelastic electron-proton scattering (DIS) events is of diffractive origin, reported by the HERA experiments ZEUS [48] and H1 [49], opened a new chapter in the study of the diffractive production mechanism. Previously, diffractive scattering was mostly studied in soft processes. In DIS the photon virtuality Q^2 provides a hard scale which, together with the $\gamma^* p$ center of mass energy W, can be varied over a wide range in a well defined manner. DIS therefore promises an ideal testing ground for QCD models of diffractive scattering.

Diffractive events in DIS are of the type $ep \to eXN$, where the system X (N) results from diffractive dissociation of the virtual photon (proton). The experimental signature is a rapidity gap in the hadronic final state between the systems X and N. This is in contrast to the dominant production mechanism in DIS where the color transfer between the struck quark and the proton remnant leads to a rather uniform distribution of emitted particles along the $\gamma^* p$ rapidity axis.

Based on the observation of high transverse momentum jets in diffractively produced high mass systems in pp and $p\bar{p}$ scattering, Ingelman and Schlein [51] suggested that the pomeron may have a partonic structure. The concept of the pomeron structure function was studied in terms of pQCD by many authors [54, 55, 56, 57, 58, 59, 60]. The simplest realization of a pomeron in QCD is the exchange of two gluons with no net color transfer. Diffractive scattering in DIS can be understood in the framework of QCD as follows: in the rest frame of the proton the virtual photon fluctuates into a $q\bar{q}$ pair or, at higher masses M_X, into a $q\bar{q}g$ state which interact with the proton via the exchange of two gluons. The observation of two and three jet diffractive events [139] might be taken as an experimental signature of these $q\bar{q}$ and $q\bar{q}g$ states, respectively.

The measurement of the diffractive DIS cross section $d\sigma^{\gamma^* p}/dM_X(Q^2, W, M_X)$ over a wide range in Q^2, W and M_X is essential for understanding the production mechanism of diffraction. The maximum mass of the system X up to which diffractive events can be separated from the non-diffractive background is determined by the coverage of the detector in the forward direction which is defined as the direction of the incoming proton. In 1998 a Forward Plug Calorimeter (FPC) was installed in ZEUS which extended the calorimetric coverage in the forward direction by one unit in pseudorapidity η from $\eta \approx 4.0$ to $\eta \approx 5.0$. This extension of the detector has substantially increased the potential for the measurement of the diffractive cross section at high M_X and low W as well as for the study of jet production in diffractive events with high mass M_X.

In this thesis a measurement of $d\sigma^{\gamma^* p}/dM_X(Q^2, W, M_X)$ is presented. Exploiting the extended calorimetric coverage due to the installation of the FPC the analysis covers a kinematic range which is substantially extended in W, M_X and Q^2 compared to previously published ZEUS results [140, 142].

A review of the basic theoretical concepts for the description of deep inelastic lepton-proton scattering as well as diffractive phenomena is presented in the first chapter following this introduction. In chapter two the HERA collider and the ZEUS detector are briefly described. The design and construction of the FPC is the main focus of chapter three. It includes a short review of the basic concepts in calorimetry. The simulation of the FPC and the ZEUS detector are introduced in chapter four. In chapter five the calibration and performance of the FPC are discussed in some detail mainly focusing on the analysis of test beam data taken with 10-100 GeV electrons, pions and muons. The simulation of diffractive and non-diffractive ep scattering is summarized in chapter six. The reconstruction and selection of DIS events with the ZEUS detector is discussed in chapter seven and eight, followed by a measurement of the inclusive proton structure function $F_2(Q^2, W)$ in chapter nine. The extraction of the diffractive sample is discussed in chapter ten. The measurement of the diffractive cross section $d\sigma^{\gamma^* p}/dM_X(Q^2, W, M_X)$ and the corresponding structure function F_2^D is presented in chapter eleven followed by a discussion of the results and a conclusion.

Chapter 1

Theoretical background

1.1 Deep inelastic scattering

1.1.1 Brief historical review

The experimental investigation of the structure of matter by scattering small projectiles off a target goes back to the famous experiments performed by Rutherford and coworkers in 1909-1911. They scattered α-particles off a thin gold foil. The distribution of the scattering angles suggested that the mass of the atom is concentrated in a tiny positively charged nucleus surrounded by a cloud of electrons [2].

The formula developed by Rutherford to describe the observed scattering distributions was based on the Coulomb interaction of a spinless pointlike projectile on a heavy spinless pointlike target. Corrections to the Rutherford formula for relativistic spin-$\frac{1}{2}$ particles scattering off spinless pointlike targets were calculated by Mott in 1929 [3]. Cross section calculations that allowed for an extended structure of a spin-$\frac{1}{2}$ proton target were first performed by Rosenbluth in 1950 [4].

The first experimental evidence for a substructure of the proton was found in 1953. When scattering electrons with energies up to 188 MeV off protons Hofstadter et al. observed a sharper drop of the cross section with increasing momentum transfer than expected for a pointlike particle [5]. The proton radius was estimated to be $(0.7 \pm 0.2)\ 10^{-13}$ cm.

In the late 1960s a series of electron proton (ep) scattering experiments was performed at the Stanford Linear Accelerator Center (SLAC) with electron beam energies up to 17 GeV. The deep inelastic structure functions were found to have little dependence on the momentum transfer [6], and depended only on the fraction x of the proton momentum carried by the struck constituent. This behavior, known as scaling, agrees with the expectation for electrons scattering off free point-like objects within the nucleus as pointed out by Bjorken [7]. Feynman in 1969 was able to explain the results with his parton model [8], which assumes that the electron scatters incoherently off free pointlike partons inside the proton.

In 1961, Gell-Mann and Ne'eman proposed the 'Eightfold Way', which classifies the observed baryons and mesons with the same spin [9]. A deeper understanding of the Eightfold Way is provided by the Quark Model which was developed by Gell-Mann and Zweig in 1964 [10]. It suggests that the proton consists of elementary constituents carrying spin $\frac{1}{2}$ and a fractional charge of -$\frac{1}{3}$e or +$\frac{2}{3}$e where e is the charge of the proton. In order to resolve the contradiction

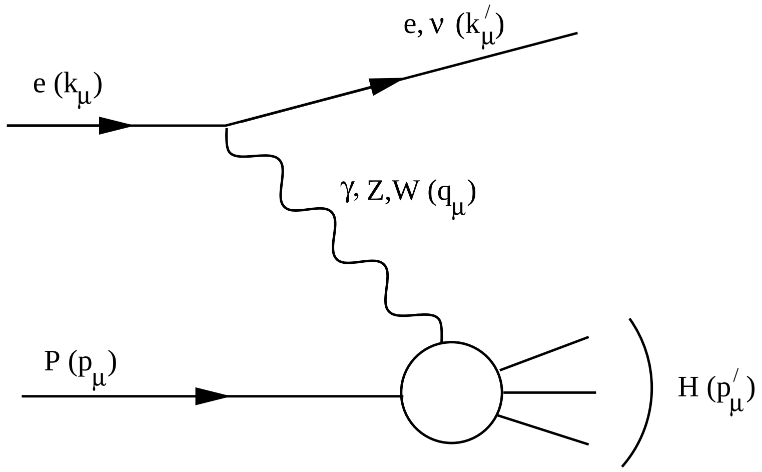

Figure 1.1: Schematic diagram for deep inelastic lepton nucleon scattering.

to Pauli's exclusion principle found e.g. in the case of the Δ^{++} particle an additional quantum number named color was introduced. The quark composition in hadrons is such that all hadrons observed in nature appear colorless. In 1969 Bjorken and Paschos suggested that quarks can be identified with Feynman's partons [11]. Up to now free quarks have not been observed in nature which is known as quark confinement.

In the 1970's and 80's a series of deep inelastic fixed target experiments were carried out at CERN, FNAL and SLAC using beams of electrons, muons and neutrinos with energies up to 300 GeV. An important result of these experiments was the observation of $\ln Q^2$-type breaking of scale invariance which lead to the development of Quantum Chromodynamics (QCD), the theory of strong interactions [12, 13, 14].

With the advent of the electron-proton collider HERA in 1992 a factor of 100 higher equivalent beam energies and therefore an order of magnitude finer spatial resolution became available and opened a new chapter in the study of deep inelastic scattering of electrons on protons.

1.1.2 Kinematics in DIS

When scattering electrons off protons at large transverse momenta in general a substantial number of particles are produced with high total invariant mass. This process is called 'deep inelastic scattering' (DIS). It is of the general form (see Fig. 1.1):

$$e(k) + P(p) \rightarrow l(k') + H(p') \; , \tag{1.1}$$

where the four-momenta of the incoming and outgoing lepton are $k = (E_e; \vec{k})$ and $k' = (E'_e; \vec{k}')$, and $p = (E_p; \vec{p})$ and $p' = (E'_p; \vec{p}')$ those of the incoming proton and the hadronic final state. Depending on the charge of the exchanged vector boson DIS events are characterized either as neutral current (NC) or charge current (CC) events. In NC processes a virtual photon γ^* or a Z^0 boson is exchanged and the flavor of the incoming lepton is conserved. In CC events the outgoing lepton is a (anti-) neutrino as a result of the exchange of a $W^\pm$ boson.

The kinematics of inclusive DIS events for a given center of mass energy $\sqrt{s}$ are described by two independent relativistic invariant variables. The following are frequently used variables to describe DIS events[1]:

$$\begin{aligned}
s &= (k+p)^2 \simeq 4E_eE_p \;, && (1.2)\\
Q^2 &= -q^2 = -(k-k')^2 \;, && (1.3)\\
x &= \frac{Q^2}{2\,p\cdot q} \;, && (1.4)\\
y &= \frac{p\cdot q}{p\cdot k} \;, && (1.5)\\
W^2 &= (p+q)^2 = m_p^2 + \frac{Q^2}{x}(1-x) \;, && (1.6)\\
\nu &= \frac{p\cdot q}{m_p} \;. && (1.7)
\end{aligned}$$

With beam energies of $E_e = 27.6$ GeV and $E_p = 920$ GeV HERA reached a center-of-mass energy $\sqrt{s} = 319$ GeV in the 1998/99 running period. The negative of the four-momentum transfer square Q^2 determines the transverse object size Δ that can be resolved in the scattering process. From the uncertainty relation it follows that[2] $\Delta = 1/Q$. In the parton model the Bjorken scaling variable x is interpreted as the proton momentum fraction carried by the struck quark. In the proton rest frame $\nu = (E_e - E_e')$ is the energy transfered from the lepton to the proton and y is the fractional energy transfer (ν/ν_{max}). W is the center of mass energy of the vectorboson-proton system. Neglecting the mass of the beam particles Q^2, x, y and s are related by:

$$Q^2 = x \cdot y \cdot s \;. \qquad (1.8)$$

1.1.3 Cross section and structure functions

The cross section for the exchange of the massive $W^{\pm}$ and Z bosons is suppressed with respect to photon exchange by the ratio of the propagators squared, $Q^4/(Q^2 + M_{Z,W}^2)^2$, and the $\gamma - Z$ interference by a factor $Q^2/(Q^2 + M_Z^2)$. In the kinematic range $Q^2 \ll 1000$ GeV^2 relevant for this thesis photon exchange is by far the dominant process and contributions from W,Z exchange can be neglected.

The single photon exchange cross section for electron proton scattering can be factorized into a leptonic tensor $L_{\mu\nu}$ and a hadronic tensor $W^{\mu\nu}$

$$d\sigma \propto L_{\mu\nu}W^{\mu\nu} \;. \qquad (1.9)$$

The leptonic tensor is calculable in Quantum Electrodynamics (QED). The ignorance about the proton structure and hence the details of the interaction are parameterized in the hadronic tensor $W^{\mu\nu}$. Taking into account the symmetries of $L_{\mu\nu}$ and current conservation $W^{\mu\nu}$ can be written in the general form:

$$W^{\mu\nu} = \left(-g^{\mu\nu} + \frac{q^\mu q^\nu}{q^2}\right) W_1 + \left(p^\mu - q^\mu \frac{p\cdot q}{q^2}\right)\left(p^\nu - q^\nu \frac{p\cdot q}{q^2}\right)\frac{W_2}{m_p^2} \;, \qquad (1.10)$$

[1] Throughout this thesis the natural system of units is used, where $\hbar = c = 1$.

[2] $\Delta = 1/Q$ is strictly valid in the Breit frame where the virtual boson transfers only momentum but no energy and q = (0;0,0,$\sqrt{Q^2}$)

where the W_i are functions of the two independent scalars q^2 and $p \cdot q$. The proton structure functions F_i are related to the W_i via:

$$F_1(x, Q^2) = m_p W_1 \quad \text{and} \quad F_2(x, Q^2) = \nu W_2 \; . \tag{1.11}$$

The cross section can now be written as[3]

$$\frac{d^2\sigma^{NC}}{dxdQ^2} = \frac{2\pi\alpha^2}{xQ^4} \left[(1 + (1-y)^2) F_2(x, Q^2) - y^2 F_L(x, Q^2) \right] \; , \tag{1.12}$$

where $F_L = F_2 - 2xF_1$.

The ep cross section can be interpreted as the product of a virtual photon flux and the total cross section $\sigma_{tot}^{\gamma^* p}$ for scattering of virtual photons on protons provided the lifetime of the virtual photon is large compared to the interaction time, a requirement which is satisfied when

$$x \ll \frac{\sqrt{1 + 4m_p^2 x^2/Q^2}}{2r_p m_p} \; , \tag{1.13}$$

where $r_p \sim 4$ GeV^{-1} is the radius of the proton. The total virtual photon-proton cross section is defined as

$$\sigma_{tot}^{\gamma^* p} = \sigma_T^{\gamma^* p} + \sigma_L^{\gamma^* p} \; , \tag{1.14}$$

where $\sigma_T^{\gamma^* p}$ and $\sigma_L^{\gamma^* p}$ are the cross sections for scattering of transverse and longitudinally polarized photons off a proton. Using the Hand convention [16] for the definition of the virtual photon flux, the relation between the structure functions and the virtual photon-proton cross sections can be expressed as

$$F_2(x, Q^2) = \frac{Q^2(1-x)}{4\pi^2\alpha} \frac{Q^2}{Q^2 + 4m_p^2 x^2} \cdot \sigma_{tot}^{\gamma^* p} \approx \frac{Q^2}{4\pi^2\alpha} \cdot (\sigma_T^{\gamma^* p} + \sigma_L^{\gamma^* p}) \; , \tag{1.15}$$

$$F_L(x, Q^2) = \frac{Q^2(1-x)}{4\pi^2\alpha} \cdot \sigma_L^{\gamma^* p} \approx \frac{Q^2}{4\pi^2\alpha} \cdot \sigma_L^{\gamma^* p} \; , \tag{1.16}$$

where the approximations are valid for small values of x.

1.1.4 Quark parton model

According to Feynman's parton model [8] the proton is composed of free point-like objects called partons. In the infinite momentum frame of the proton where all transverse momenta are negligibly small compared to the longitudinal momenta the Bjorken scaling variable x corresponds to the fraction ξ of the proton momentum p carried by the struck parton. Due to time dilatation in this frame the parton distribution is in effect frozen during the ep interaction. Deep inelastic scattering can therefore be described as the incoherent sum of quasi elastic electron parton scatterings.

A consequence of the proton being composed of point-like constituents is that the structure functions are independent of Q^2, $F_i(x, Q^2) = F_i(x)$, and $Q^2\sigma_{tot}^{\gamma^* p}(W, Q^2)$ is independent of Q^2. This behavior originally proposed by Bjorken [7] in the limit $Q^2 \to \infty$ and finite x is known

[3]The structure function F_3 which measures parity violating contributions resulting from Z exchange contributes only at $Q^2 \gg 10^3$ GeV^2 and has been omitted.

as 'scale invariance' and has first been observed by SLAC-MIT [6] for $Q^2 < 7\,\text{GeV}^2$ and $0.2 < x < 0.02$.

The structure function F_2 can be expressed in terms of the parton density functions f_i

$$F_2(x) = x \sum_i e_i^2 f_i(x) \; , \tag{1.17}$$

where e_i is the charge of parton i and $f_i(x)dx$ is the probability to find a parton of type i in the momentum range between x and $x + dx$.

For spin-$\frac{1}{2}$ partons the Callan-Gross relation [17]

$$F_1(x) = \frac{1}{2x} F_2(x) \quad \Rightarrow \quad F_L = 0 \tag{1.18}$$

holds since in head on collisions longitudinally polarized photons only couple to spin-0 particles while transverse photons only couple to spin-$\frac{1}{2}$ particles. Since the Callan-Gross relation was found to hold by the SLAC-MIT measurements Feynman's partons were identified with Gell-Mann's quarks. The fractional charge of the partons and the postulated number of three valence quarks in the nucleons was confirmed by neutrino-nucleon scattering [18].

Experimentally it was found that [19]

$$\sum_i \int_0^1 x f_i(x) dx \approx 0.5 \; , \tag{1.19}$$

which implies that only half of the proton momentum is carried by charged quarks. The other half is carried by neutral partons which are identified with gluons, the mediators of the strong force. Direct experimental evidence for the existence of gluons was found in 1979 at DESY via the observation of three-jet events in e^+e^- annihilation [20].

1.1.5 Quantum Chromodynamics

Quantum Chromodynamics (QCD) is a field theory developed in the 1970's to describe the strong interaction between quarks. It is a non-abelian gauge theory based on the SU(3) symmetry group. Quarks carry one of three possible 'color charges' (red (r), green (g) or blue (b)). As a consequence of the non-abelian structure the mediating gauge bosons in QCD called gluons also carry color charge and thus couple to each other. In contrast to QED the QCD coupling constant α_S increases at large distances (low Q^2) and is small at small distances (large Q^2), which is known as asymptotic freedom. The scale dependence in leading order perturbation theory is given by [21]

$$\alpha_S(Q^2) = \frac{12\pi}{(33 - 2n_f)\ln(Q^2/\Lambda^2)} \; , \tag{1.20}$$

where n_f is the number of active quark flavors. The QCD scale parameter Λ determines the energy scale at which α_S becomes small and has been measured to be (100 - 300) MeV. At large Q^2 values α_S decreases logarithmically and when $\Lambda^2 \ll Q^2$ perturbative QCD (pQCD) can be applied.

In QCD the naive QPM model as described in the previous section needs to be modified due to the coupling of quarks to gluons. Quarks may radiate gluons which in turn may split into

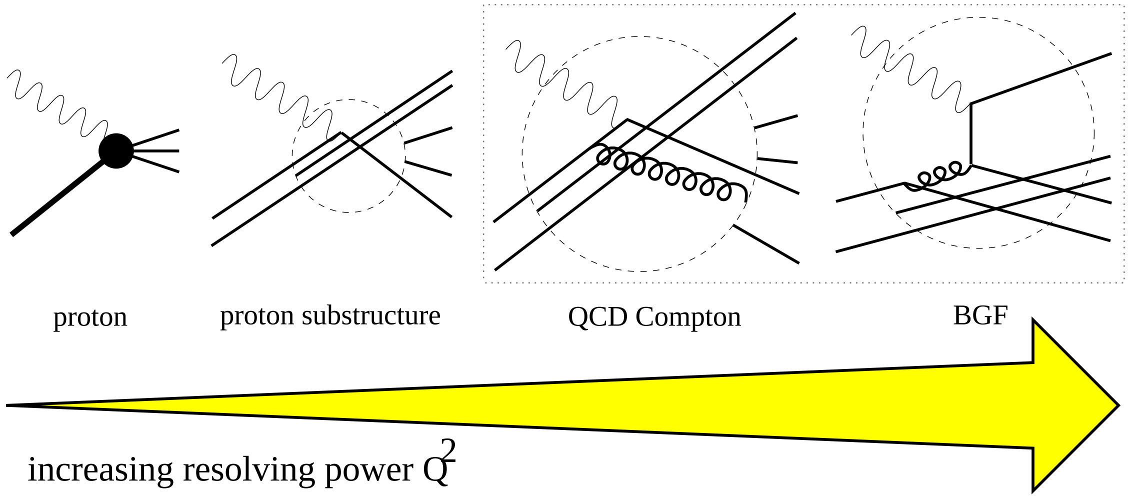

Figure 1.2: Schematic diagram of scaling violations. The quark momentum densities depend on Q^2 which determines the resolution power of the probing photon. Processes such as gluon radiation or quark-antiquark splitting can be resolved with increasing Q^2.

$q\bar{q}$-pairs. In this case the number of partons increases while the average momentum per parton decreases. With increasing Q^2 more and more of these fluctuations can be resolved (compare Fig. 1.2). In the low Q^2 region the valence quarks which have relatively large x values dominate. At large Q^2 values gluon radiation leads to an increase in the number of quarks with low x values and correspondingly to a depletion of the high x region. In fact, at low x a rapid increase of F_2 with increasing Q^2 has been observed [22, 23] while F_2 decreases at large values of x (see Fig. 1.3). This logarithmic Q^2 dependence of F_2 for fixed x is known as scaling violations.

Gluon radiation also results in a transverse momentum component of the quarks which can consequently couple to longitudinally polarized photons. The Callan-Gross relation is thus no longer satisfied exactly and F_L is larger than zero.

1.1.6 Evolution equations

Since the distributions of quarks and gluons in the proton are dominated by non-perturbative effects the inclusive ep cross section σ_{ep} can not be calculated from first principles in QCD. However, the QCD factorization theorem allows to separate the short distance contribution which is calculable in pQCD from the non-perturbative long distance contribution:

$$\sigma_{ep}(x, Q^2) = \sum_{i \in partons} f_{i/p}(x, \mu_F^2) \otimes \sigma_{ei}(x, Q^2, \mu_F^2) \; . \tag{1.21}$$

The σ_{ei} cross sections describe the short distance (hard) interactions. The parton density functions (PDFs) $f_{i/p}$ have to be determined experimentally. They are specific to the type of hadron but independent of the hard interaction. The factorization scale μ_F determines the separation line between what is considered as the long range inner dynamics of the proton ($f_{i/p}$) and the dynamics of the hard lepton-parton interaction (σ_{ei}).

The PDFs depend on the choice of the renormalization scheme. The modified minimal subtraction scheme of dimensional regularization, $\overline{MS}$, and the DIS scheme are the most frequently used. In the DIS scheme the corrections to all orders are absorbed into the PDFs and choosing $\mu_F^2 = Q^2$ the structure function F_2 is defined by $F_2(x, Q^2) = x \sum_i e_i^2 f_i(x, Q^2)$.

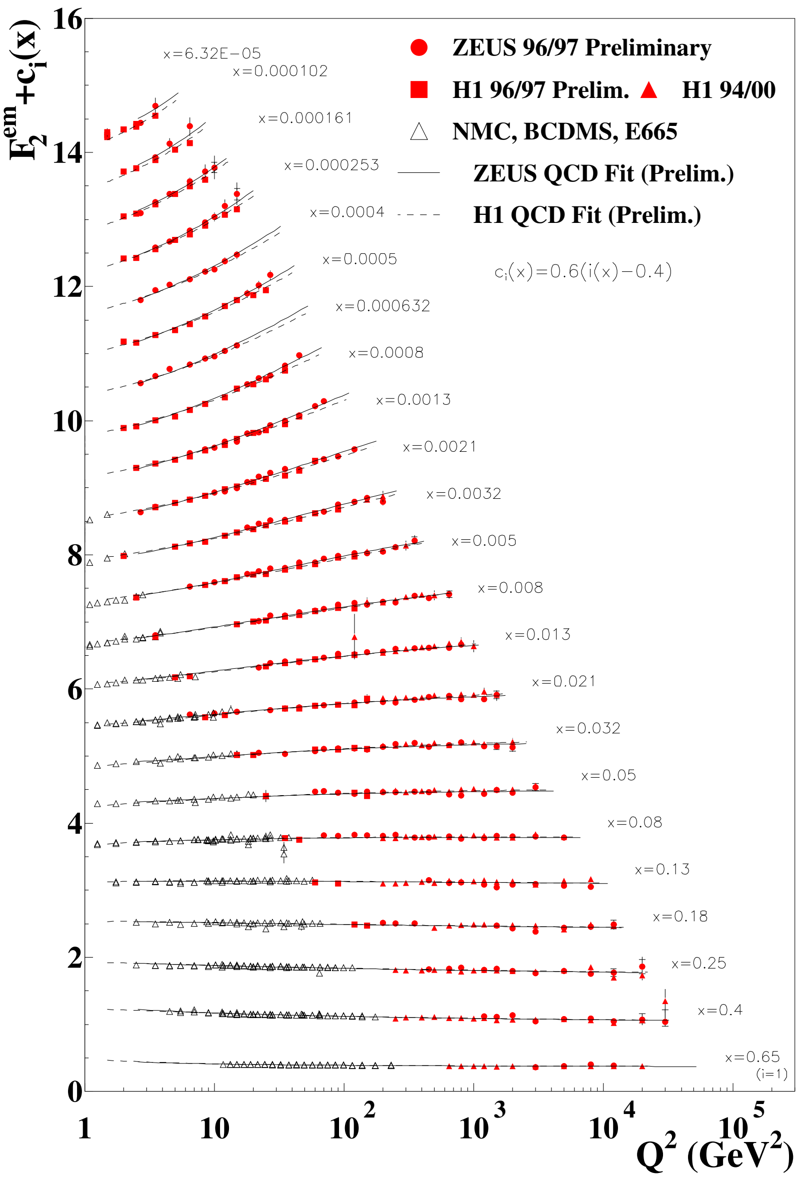

Figure 1.3: The structure F_2 as a function of Q^2 for fixed values of x. Results from the H1 and ZEUS are shown together with fixed target results and NLO QCD fits. For $x \approx 0.1$ F_2 is constant as q^2 changes by 4 orders of magnitude. For smaller x values F_2 is observed to increase logarithmically with Q^2.

Since $\sigma_{ei}(\mu_F^2)$ can be calculated perturbatively in QCD for any scale and the physical observable σ_{ep} must be independent of the arbitrarily chosen scale μ_F^2 the change of the PDFs with changing scale can also be calculated. This leads to the so called evolution equations. In the perturbative calculation of σ_{ei} approximations have to be applied which are valid in certain regions of x and Q^2.

The DGLAP[4] evolution equations [24, 25, 26] are a set of coupled integro-differential equations. They allow to determine the PDFs and thus the DIS cross section for any value of Q^2 within the range of applicability of pQCD if the PDFs are known as a function of x for a particular value Q_0^2.

Introducing the splitting functions $P_{ij}(\xi)$ which describe the probability for $q \to qg$, $g \to qq$

[4]Dokshitzer, Gribov, Lipatov, Altarelli and Parisi

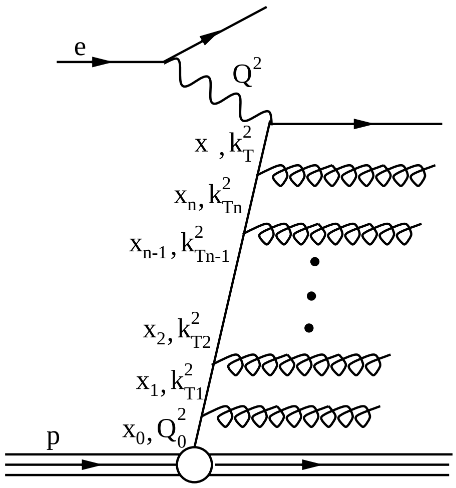

Figure 1.4: Notation of a ladder diagram of n gluon emission.

and $g \to gg$ parton branching where the daughter parton i carries a momentum fraction ξ of the mother parton j the DGLAP equations can be written as:

$$\frac{\mathrm{d}q_i(x,Q^2)}{\mathrm{d}\ln Q^2} = \frac{\alpha_s(Q^2)}{2\pi}\int_x^1 \frac{\mathrm{d}z}{z}\left[q_i(z,Q^2)P_{qq}\left(\frac{x}{z}\right) + g(z,Q^2)P_{qg}\left(\frac{x}{z}\right)\right] \tag{1.22}$$

$$\frac{\mathrm{d}\overline{q}_i(x,Q^2)}{\mathrm{d}\ln Q^2} = \frac{\alpha_s(Q^2)}{2\pi}\int_x^1 \frac{\mathrm{d}z}{z}\left[\overline{q}_i(z,Q^2)P_{qq}\left(\frac{x}{z}\right) + g(z,Q^2)P_{qg}\left(\frac{x}{z}\right)\right] \tag{1.23}$$

$$\frac{\mathrm{d}g(x,Q^2)}{\mathrm{d}\ln Q^2} = \frac{\alpha_s(Q^2)}{2\pi}\int_x^1 \frac{\mathrm{d}z}{z}\left[\sum_{i=1}^{n_f}(q_i(x,Q^2)+\overline{q}_i(x,Q^2))P_{gq}\left(\frac{x}{z}\right) + g(z,Q^2)P_{gg}\left(\frac{x}{z}\right)\right] \tag{1.24}$$

The splitting functions $P_{ij}(\xi)$ are calculable in pQCD. In the leading logarithmic approximation (LLA) contributions of the form $(\alpha_s \ln Q^2)^n$ are summed up to all orders n. The $(\alpha_s \ln Q^2)^n$ terms are associated with ladder diagrams of the type shown in Fig. 1.4 where a chain of n gluons is emitted and the successive gluon transverse momenta k_T are strongly ordered along the chain, i.e. $Q_0^2 \ll k_{T1}^2 \ll .. \ll k_{Tn}^2 \ll Q^2$. The approximations leading to the DGLAP equations are valid for large Q^2 and not too small x such that $\alpha_S(Q^2)\ln\frac{1}{x} \ll \alpha_S(Q^2)\ln(Q^2/\Lambda^2) \lesssim 1$.

For small values of x the DGLAP approximations cease to be valid since $\ln\frac{1}{x}$ terms have been neglected in the derivation of the DGLAP equations. For this regime of small x and finite Q^2 the BFKL[5] equation [27, 28, 29] which sums up terms proportional to $(\alpha_s \ln\frac{1}{x})^n$ appears to be better suited. It takes into account ladder diagrams where the longitudinal momentum fractions x_i with respect to the proton energy are strongly ordered, i.e. $x_0 \gg x_1 \gg .. \gg x_n \gg x$. No ordering on k_{Ti} is imposed.

The BFKL equation has been derived for the gluon distribution $xg(x,Q^2)$ which dominates at low x. Given $xg(x,Q^2)$ at some fixed $x = x_0$ as a function of Q^2 it provides an evolution to other x values. With the unintegrated gluon density $f_g(x,k_T^2)$ defined by $xg(x,Q^2) = \int_0^{Q^2}(dk_T^2/k_T^2)f_g(x,k_T^2)$ the BFKL equation is given by

$$-x\frac{\partial f_g(x,k_T^2)}{\partial x} = \frac{3\alpha_S}{\pi}k_T^2\int_0^\infty \frac{dk_T'^2}{k_T'^2}\left[\frac{f_g(x,k_T'^2)-f_g(x,k_T^2)}{|k_T'^2-k_T^2|} + \frac{f_g(x,k_T^2)}{\sqrt{4k_T'^4+k_T^4}}\right] \equiv K\otimes f_g\ . \tag{1.25}$$

[5]Balitskii, Fadin, Kuraev and Lipatov

1.2 Diffraction

The term diffraction is derived from optics, where it describes the deflection of a beam of light by an obstacle whose dimensions are comparable to its wavelength. In high energy particle physics it was first used to describe small angle elastic hadron-hadron scattering of the type: $a + b \to a + b$. Later it was generalized to processes where one (single dissociation: $a + b \to X + b$) or both (double dissociation: $a+b \to X+Y$) colliding hadrons are transformed into multi-particle final states without exchange of quantum numbers (except for angular momentum) between the scattering hadrons. An intuitive physical picture emerges if the projectile is described by a superposition of different wave components which scatter elastically off the target. The outgoing beam will contain a new superposition of the scattered wave amplitudes which in general corresponds to new physical states. Diffraction can be interpreted as the shadow which emerges when scattering a projectile on an extended target.

Through the optical theorem which relates the total cross section to the imaginary part of the forward elastic amplitude,

$$\sigma_{tot} \propto \frac{1}{s}\mathrm{Im}T_{el}(t = 0) \tag{1.26}$$

diffraction is intimately connected with the total cross section. At high energies $\sqrt{s}$ the elastic scattering amplitude in impact parameter (b) space, is purely imaginary and a function of $b/R(s)$ only, where $R(s)$ is the effective interaction radius. From this follows that $\sigma_{el} \propto \sigma_{tot} \propto R^2(s)$. For a general review of diffractive scattering see e.g. [31, 32].

1.2.1 Properties of diffractive processes

A characteristic feature of diffractive scattering is the exponential suppression of the cross section as a function of the square of the momentum transfer, t, between the colliding hadrons. This is reminiscent of diffraction in optics. In even more striking analogy to the optical case a minimum in the diffractive hadron hadron cross section has been found in the region $t \simeq 1 - 2\,\mathrm{GeV}^2$ (see Fig. 1.5). The small t region can be parameterized as

$$\frac{d\sigma^{diff}}{d|t|} \propto e^{-B(s)|t|} \ . \tag{1.27}$$

The slope B is related to the interaction radius R of the target by $B = R^2/4$. It typically increases slowly with energy s which is known as shrinkage of the forward diffractive peak.

The diffractive cross section shows only a weak dependence on the energy $\sqrt{s}$ as expected from the optical analogy where the cross section is given by the size of the scattering obstacle and is independent of the energy of the incoming wave. At high energies the energy dependence of the forward elastic cross section $d\sigma_{el}/d|t|(t = 0)$ can be parameterized as

$$\frac{d\sigma_{el}}{d|t|}(t = 0) \propto s^{2\epsilon} \tag{1.28}$$

and through the optical theorem the energy dependence of the total cross section is given by

$$\sigma_{tot} \propto s^{\epsilon} \ , \tag{1.29}$$

where experimentally $\epsilon \approx 0.08$ was found [36].

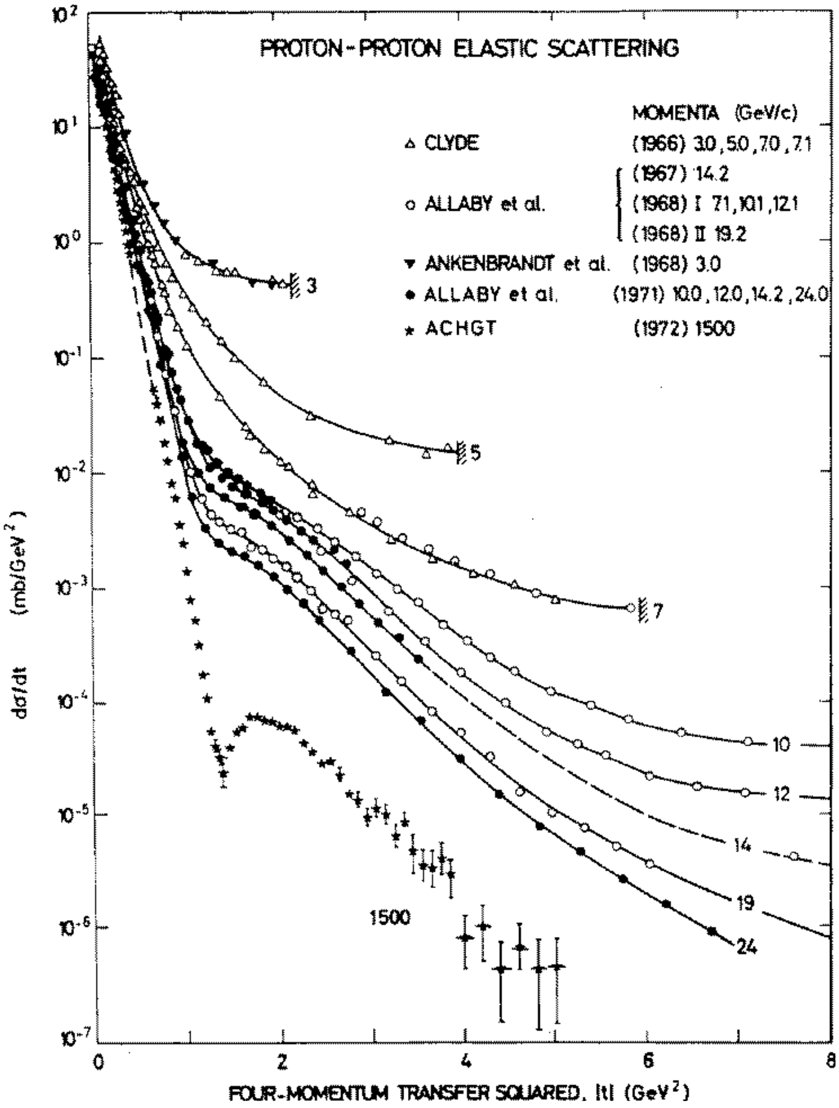

Figure 1.5: Differential proton proton elastic scattering cross section $\frac{d\sigma}{d|t|}$ for different values of the square of the center of mass energies s.

An additional characteristic feature for single dissociation diffractive processes of the form $a + b \to X + b$ is that small masses M_X are preferred and the cross section falls off with the mass of the system X like (compare Fig. 1.6)

$$\frac{d\sigma^{ab\to Xb}}{dM_X^2} \propto \frac{1}{M_X^n} \quad , \quad n \approx 2. \tag{1.30}$$

The preference for small masses M_X is a consequence of the fact that diffractive scattering requires coherence between the incoming and the outgoing waves. This coherence condition can be translated to the following criterion

$$\frac{M_X^2}{s} \lesssim \frac{1}{2m_a R} , \tag{1.31}$$

where R is the longitudinal interaction radius in the rest frame of the target b. Since R is in the order of ~ 1 fm $= 5$ GeV^{-1} one gets for pp scattering $\frac{M_X^2}{s} \leq 0.1$.

In diffractive processes which are of the general form $a + b \to X + Y$ no quantum numbers are exchanged in the t-channel which implies for partonic processes that no color charge is

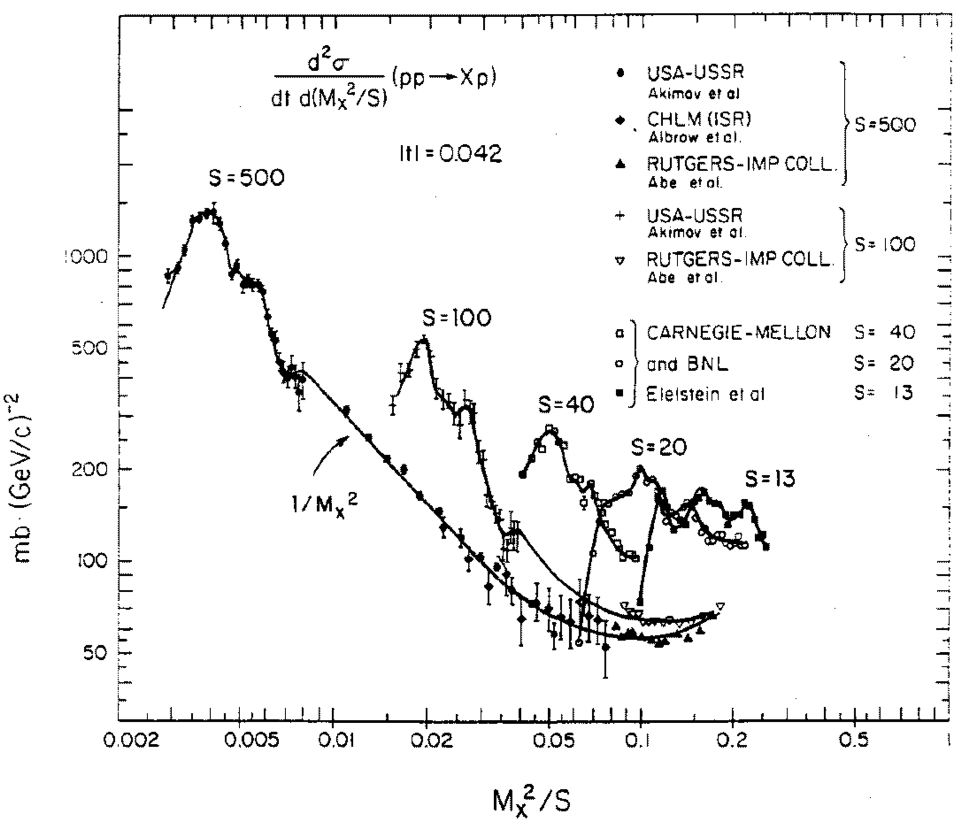

Figure 1.6: The differential cross section for the inelastic diffractive process $pp \to Xp$ as a function of the scaled diffractive mass M_X^2/s.

exchanged. Therefore, there is no color field operating between the two outgoing systems X and Y and they will in general be well separated in phase space. This behavior is most obvious in elastic and single dissociation diffractive events where at least one of the incoming particles preserves its identity and emerges from the collision with a large fraction of its initial energy. Diffractive events are thus characterized by a large rapidity gap in the final state. The rapidity $\mathcal{Y}$ of a particle with energy E and longitudinal momentum $p_{||}$ is defined as

$$\mathcal{Y} = \frac{1}{2}\ln\frac{E + p_{||}}{E - p_{||}}\,, \tag{1.32}$$

which can be approximated by the pseudorapidity $\eta = -\ln\tan(\theta/2)$ in the limit where the particle mass m is small.

Due to the lack of a hard scale diffractive processes in hadron-hadron scattering are predominantly a soft phenomenon which therefore is not directly accessible to perturbative QCD calculations.

1.2.2 Regge formalism

Regge theory was developed in the 1960's based on the formalism of analytical continuation of the scattering amplitude into the complex angular momentum plane [33]. It successfully describes the energy dependence of the total hadron-hadron interaction cross section and certain

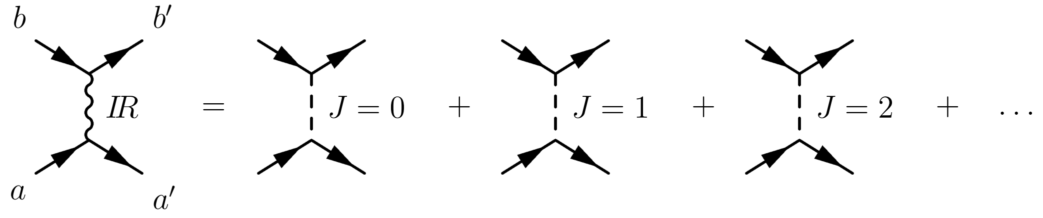

Figure 1.7: Schematic representation of the exchange of a Reggeon as a superposition of many particles with different spin.

properties of elastic and diffractive scattering. Since the Regge formalism is based on fundamental properties of quantum-mechanical wave scattering it is a suitable tool for the description of processes which are not accessible to perturbative QCD calculations. In the following some fundamental predictions of Regge theory are reviewed [30, 34].

Consider elastic hadron-hadron scattering of the type $ab \to ab$ with four-momenta a,b in the initial state and a',b' in the final state. The cross section is a function of the center of mass energy squared $s = (a+b)^2$ and the four-momentum transfer $t = (a-a')^2$. In Regge theory the elastic hadron-hadron scattering of the type $ab \to ab$ is described by t-channel exchange of one or more Reggeons. A Reggeon is equivalent to a superposition of many particles with the same quantum numbers except for spin (see Fig. 1.7). In the Chew-Frautschi plot [35], where the spin J of a particle is plotted as a function of the mass squared $m^2 = t$, the particles corresponding to a specific Reggeon lie on a Regge trajectory (see Fig. 1.8). These trajectories can be approximated by straight lines

$$\alpha(t) = \alpha(0) + \alpha' t \, . \tag{1.33}$$

The slope α' is typically close to 1 GeV^{-2}. The intercept $\alpha(0)$ of trajectories corresponding to known particles is typically in the range 0 - 0.5, for instance $\alpha_\pi(0) \approx 0$, $\alpha_\rho(0) \approx 0.5$.

I. Elastic cross section

According to Regge theory the transition amplitude T of a process where a Reggeon with a trajectory $\alpha(t)$ is exchanged can be written as

$$T(s,t) \stackrel{s\to\infty}{\longrightarrow} \gamma(t) \left(\frac{s}{s_0}\right)^{\alpha(t)} \, . \tag{1.34}$$

The cross section of the elastic scattering process $ab \to ab$ is expressed as

$$\frac{d\sigma^{el}}{dt} \propto \frac{|T(s,t)|^2}{s^2} \propto \beta^2(t) \cdot \left(\frac{s}{s_0}\right)^{2\alpha(t)-2} \, . \tag{1.35}$$

The observed exponential decrease of $d\sigma/dt$ with increasing t leads to the parameterization $\beta(t) = e^{-Bt}$. Substituting this and (1.33) into (1.35) the differential cross section can be written as

$$\frac{d\sigma^{el}}{dt} \propto \left(\frac{s}{s_0}\right)^{2\alpha(0)-2} e^{\{2B+2\alpha' \ln(s/s_0)\}t} \, . \tag{1.36}$$

The derivative α' determines the logarithmic dependence of the exponential t-slope as a function of s.

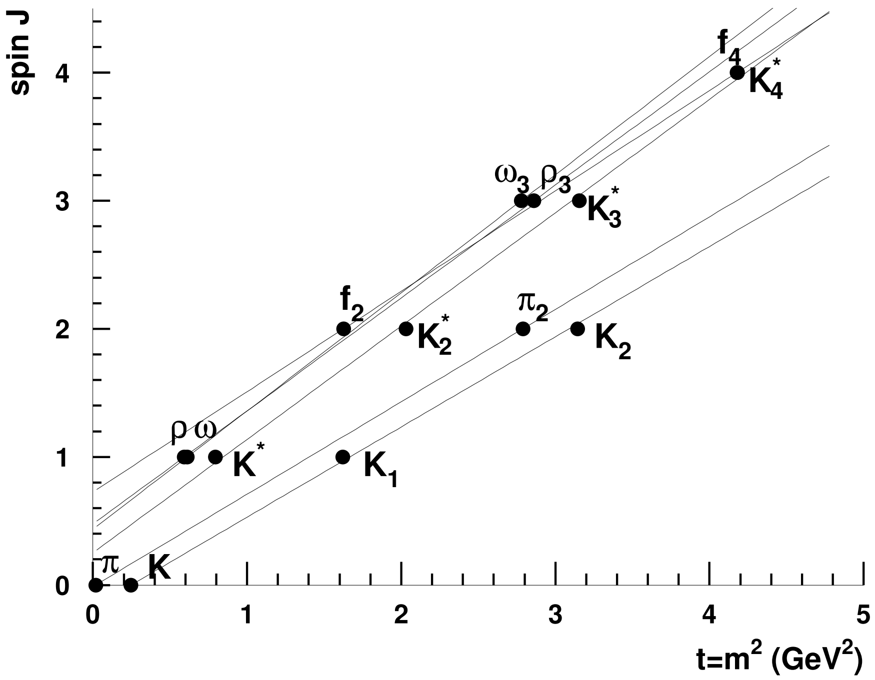

Figure 1.8: Chew-Frautschi plot: Spin J versus mass squared for different mesons. The lines are linear fits and correspond to Regge trajectories.

The above results should be compared to the predictions of a scattering process mediated by the exchange of only one meson of mass M and spin J. In this case one expects for large s and small t the scattering amplitude to behave like $T(s \to \infty, t = const) \propto s^J$. The comparison with Eq. 1.34 shows that the summation over many particles lying on a Regge trajectory damps the rapid rise with s predicted for the exchange of a single particle with $J > 1$, in agreement with experiment.

II. Total cross section and the Pomeron

Using the optical theorem (Eq. 1.26), which relates the total cross section to the forward elastic scattering amplitude, the energy behavior of the total hadron-hadron scattering cross in Regge theory is given by

$$\sigma_{tot} \propto s^{\alpha(0)-1} \; . \tag{1.37}$$

The total cross sections for pp, p$\bar{\text{p}}$, γp and $\gamma\gamma$ scattering are plotted as a function of $\sqrt{s}$ in Fig. 1.9. At high energies a similar energy dependence for these processes can be seen which also applies to other hadron-hadron scattering processes not shown in Fig. 1.9. The fall off at low energies in Fig. 1.9 can be explained by the exchange of Regge trajectories corresponding to known particles. However, the slowly increasing cross section at high c.m. energies requires a Regge trajectory with $\alpha(0) \gtrsim 1$, while all known trajectories of existing particles have $\alpha(0) \lesssim 0.5$. In order to describe the data in the Regge framework a new trajectory named Pomeron ($I\!P$) after Pomeranchuk has been introduced [38], with $\alpha_{I\!P}(0) \approx 1$. The Pomeron has the quantum numbers of the vacuum and is generally regarded as the mediator in diffractive scattering.

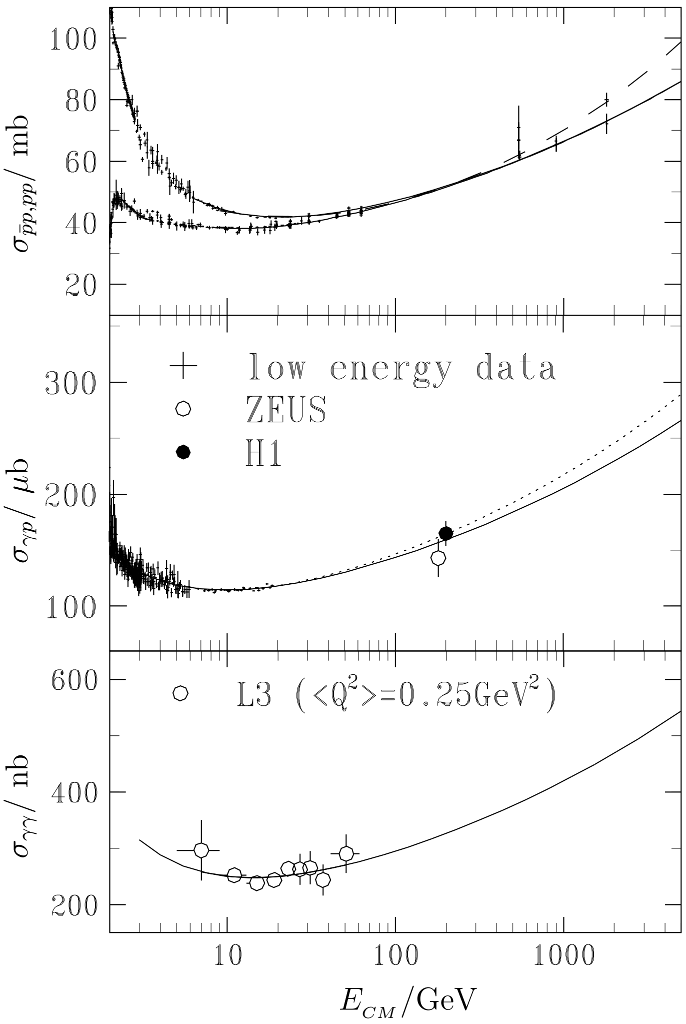

Figure 1.9: Total cross sections for pp (p$\bar{\text{p}}$), γp and $\gamma\gamma$ scattering as a function of the center of mass energy E_{CM}. The curves represent the DL parameterization with $\alpha_{I\!P}(0) = 1.0808$ (solid), $= 1.112$ (dashed) and $= 1.088$ (dotted).

Total hadron-hadron scattering can conveniently be described by the sum of a Reggeon and a Pomeron contribution. Donnachie and Landshoff [36] fitted all available hadronic data to the parameterization

$$\sigma_{tot} = A\, s^{\alpha_{I\!R}(0)-1} + B\, s^{\alpha_{I\!P}(0)-1} \, . \tag{1.38}$$

The parameters A and B depend on the particular process while global values for $\alpha_{I\!R}(0) \approx 0.55$ and $\alpha_{I\!P}(0) \approx 1.08$ are able to fit all considered data. A recent fit including newer data yielded $\alpha_{I\!P}(0) \approx 1.096$ [37].

III. Triple Regge formalism

Now consider the diffractive single dissociation process $a + b \to X + b$. In the Regge limit defined as t small and $s/M_X \to \infty$ the double differential cross section can be written as

$$\frac{d^2\sigma^{ab}}{dtdM_X^2} = \sum_{k,l} \frac{\beta_{ak}(0)\beta_{bl}^2(t)g_{kll}(t)}{16\pi s} \left(\frac{s}{M_X^2}\right)^{2\alpha_l(t)} \left(M_X^2\right)^{\alpha_k(0)} \; , \tag{1.39}$$

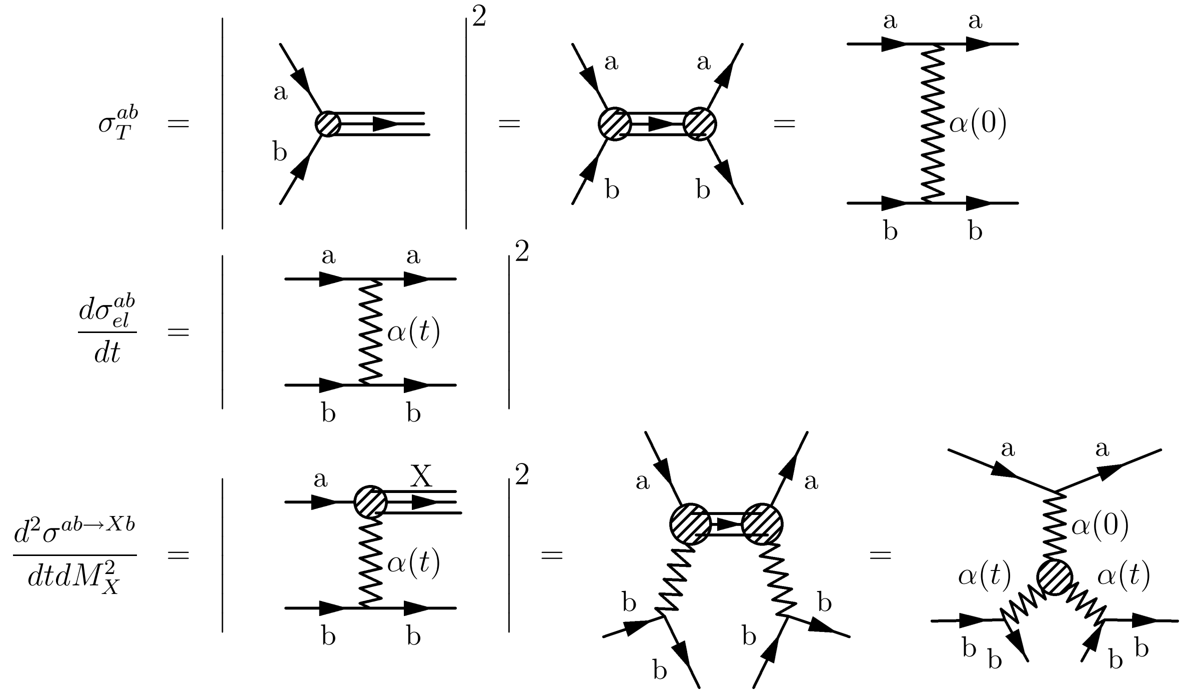

Figure 1.10: Diagrams illustrating the relation between total, elastic and inelastic diffractive cross section in the triple Regge formalism.

where β and g are vertex functions and the sum runs over all contributing Regge trajectories. Equation 1.39 is based on Mueller's generalization of the optical theorem [39], which relates the total cross section of the process $a + b \to X + b$ to the amplitude of the three-body forward elastic scattering. The term g_{kll} is called the 'triple Regge coupling'. The relation between the cross sections for total, elastic and inelastic diffraction is illustrated in Fig. 1.10.

By design, the Pomeron trajectory dominates in diffractive processes. Therefore, parameterizing the Pomeron trajectory as $\alpha_{I\!P}(t) = 1 + \epsilon + \alpha' t$, Eq. 1.39 becomes

$$\frac{d^2\sigma^{ab\to Xb}}{dtdM_X^2} = \frac{\beta^2_{aI\!P}(0)\beta_{bI\!P}(t)g_{I\!PI\!PI\!P}(t)}{16\pi}\frac{1}{M_X^2}\left(\frac{s}{M_X^2}\right)^{2\epsilon}\left(M_X^2\right)^{\epsilon} . \quad (1.40)$$

Assuming as in the elastic case $\beta_{hI\!P}(t) = \beta_{hI\!P}(0)e^{bt}$ and $\epsilon = 0$ one obtains

$$\frac{d^2\sigma^{ab\to Xb}}{dtdM_X^2} \approx \frac{A}{M_X^2} e^{\{2b+2\alpha' \ln(s/s_0)\}t} , \quad (1.41)$$

recuperating the characteristic diffractive behavior i.e. approximate constancy with s, an exponential t-slope which shrinks with s and a M_X dependence $\propto 1/M_X^2$.

1.2.3 Diffraction in photoproduction

Photoproduction at HERA refers to processes where the electron is scattered under a small angle emitting a quasi-real photon with $Q^2 \approx 0\,GeV^2$, which then interacts with the proton. Already the first γp scattering experiments in the 1960's [40] showed striking similarities to hadron-hadron interactions, most notably seen in the s-dependence of the total cross section (compare Fig. 1.9). A possible explanation is provided by the Vector Dominance Model (VDM) which assumes a hadronic structure of the photon [41, 42, 43]. The photon can fluctuate into a $q\bar{q}$ state, which means that the photon appears as a superposition of a bare photon $|\gamma_b\rangle$ and hadronic states $|h\rangle$

$$|\gamma\rangle = \sqrt{Z_3}|\gamma_b\rangle + \sqrt{\alpha}|h\rangle \ , \tag{1.42}$$

where α is the fine structure constant and $\sqrt{Z_3}$ assures the correct normalization. Conservation laws require that the hadronic states $|h\rangle$ have the same quantum numbers as the photon $|\gamma\rangle$. The original VDM developed in the 1960's assumes that $|h\rangle$ is composed of the three lightest vector mesons ρ^0, ω and ϕ and the bare photon $|\gamma_b\rangle$ does not contribute to the γ hadron interaction. Later, several generalized vector dominance (GVD) models included more constituents for $|h\rangle$.

The lifetime of a given hadronic fluctuation $|h_V\rangle$ of the photon can be estimated by the uncertainty principle to be

$$t_f \approx \frac{2E_\gamma}{Q^2 + m_V^2} \ , \tag{1.43}$$

where m_V is the mass of the vector meson V. In the proton rest frame the Vp interaction time t_i is approximately given by $t_i = 2R_p$, where R_p is the radius of the proton. For small values of Q^2 and m_V^2 where $t_f > t_i$ the γp scattering can be regarded as a fluctuation of the photon into a vector meson V followed by a Vp hadronic interaction.

In this picture photoproduction is predominantly a hadronic interaction and therefore should also lead to diffractive processes. These diffractive processes can be classified as follows:

quasi elastic	:	$\gamma p \to Vp$	$(V = \rho^0, \omega, \phi)$
photon dissociation	:	$\gamma p \to Xp$	$(X \neq \rho^0, \omega, \phi)$
proton dissociation	:	$\gamma p \to VY$	$(Y \equiv$ 'excited' proton$)$
double dissociation	:	$\gamma p \to XY$	

Figure 1.11 illustrates the contributing processes in the VDM picture.

Both HERA experiments ZEUS [44] and H1 [45] have studied the single photon dissociation diffractive contribution in the photoproduction regime. The energy range covered is an order of magnitude larger than for fixed target experiments [46]. The energy dependence as well as the M_X dependence were found to be in good agreement with predictions from the triple Regge formalism. The ZEUS analysis estimated the fraction of the total photoproduction cross section due to single diffractive photon dissociation in the mass range $m_\phi^2 < M_X^2 < 0.05\,W^2$ to be $13.3 \pm 0.5 \pm 3.6\%$. Studying the M_X distribution at a fixed value of $W = 200$ GeV ZEUS obtained a value of

$$\alpha_{I\!P}(0) = 1.12 \pm 0.04 \pm 0.08 \ , \tag{1.44}$$

in agreement with values from hadron-hadron data. In addition ZEUS has measured the corresponding t distribution using the Leading Proton Spectrometer [47]. The slope was found to be

$$B = 6.8 \pm 0.9^{+1.2}_{-1.1} GeV^{-2} \ , \tag{1.45}$$

in agreement with expectations based on results from pion-proton scattering experiments.

1.2.4 Diffraction in DIS

For a fixed photon energy highly virtual photons have a shorter fluctuation time into $q\bar{q}$ states than real photons (see Eq. 1.43). Therefore, in deep inelastic scattering diffraction is expected

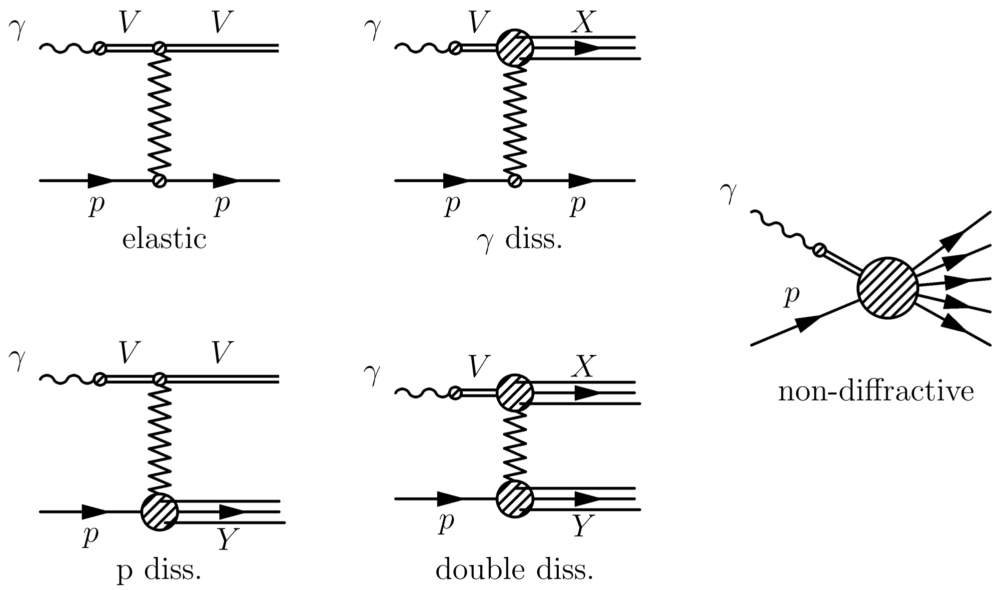

Figure 1.11: Diagrams illustrating the classification of diffractive processes in γ^*p scattering. Diagram for elastic, photon dissociation, proton dissociation and double dissociation diffractive processes are shown. For comparison a diagram for a non diffractive process is also shown.

to play a less prominent role. The discovery of large rapidity gap events in NC DIS processes by ZEUS [48] and later by H1 [49] therefore came as a surprise. This class of events could not be explained by the then available DIS Monte Carlo generators. In standard DIS events rapidity gaps between the proton remnant and the current jet which originates from the parton struck by the virtual photon are exponentially suppressed due to parton radiation in the resulting QCD color field. In diffractive events, however, a color singlet object is exchanged. Parton radiation between the current jet and the proton remnant which in general escapes through the beam pipe is strongly suppressed. The following diagrams illustrate the characteristic topologies of diffractive and non-diffractive NC DIS events.

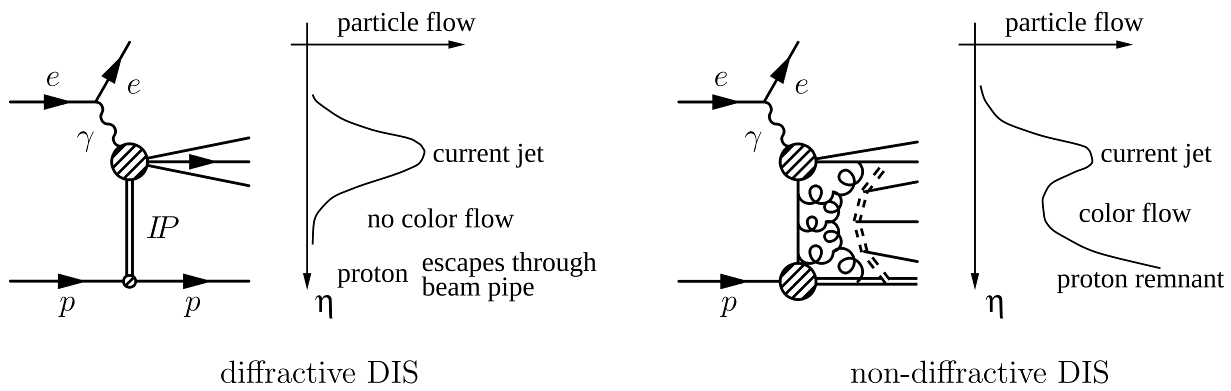

As discussed above the Regge formalism successfully describes many global features of diffractive interactions. However, it provides no insight into the structure of the Pomeron and the nature of its interactions. In QCD the Pomeron can be thought of as a color singlet system of partons such as two gluons. In order to study the partonic nature of the Pomeron an interaction

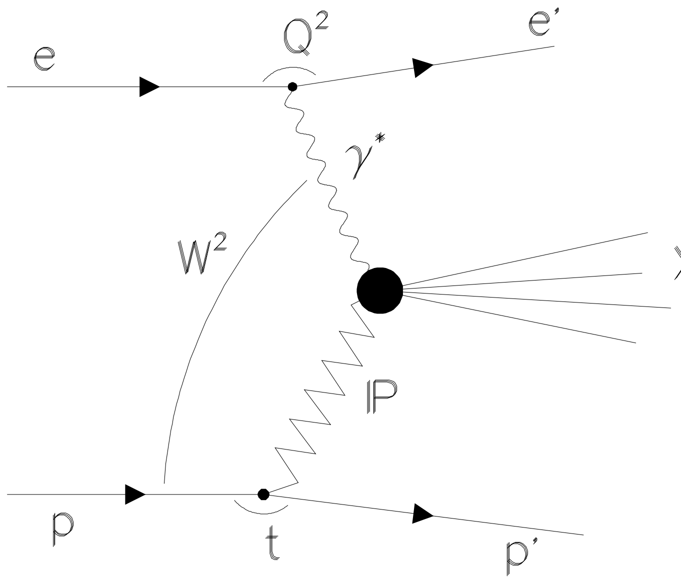

Figure 1.12: Diagram of a diffractive event where the virtual photon dissociates.

containing a hard scale is needed. For instance, high p_T-jets in diffractive events from hadron-hadron collisions as first observed in [50] provide such a high scale. Deep inelastic scattering, where the photon virtuality Q^2 provides a hard scale and where Q^2 and the $\gamma^* p$ center of mass energy W can be varied over a wide range in a well defined manner in a single experiment, promises an ideal testing ground for QCD models of diffractive scattering.

I. Kinematic variables

Diffractive events in DIS are of the general form

$$e(k) + P(p) \rightarrow e'(k') + P'(p') + X, \tag{1.46}$$

where X denotes the final state originating from the dissociated photon and P' the final state proton (see Fig. 1.12). If the proton dissociates into higher mass states it will be denoted by N. For a complete description of diffractive events further variables in addition to the usual DIS variables x and Q^2 are introduced. The square of the four momentum transfer between the virtual photon and the proton is defined as

$$t = (p - p')^2. \tag{1.47}$$

The mass M_X of the hadronic system system X produced by the photon dissociation is a second independent variable.

Alternatively, the kinematics can also be expressed in terms of $x_{I\!P}$ and β which are defined as

$$x_{I\!P} = \frac{(p-p')\cdot q}{p\cdot q} \approx \frac{M_X^2+Q^2}{W^2+Q^2} \quad \text{and} \tag{1.48}$$

$$\beta = \frac{Q^2}{2(p-p')\cdot q} = \frac{x}{x_{I\!P}} \approx \frac{Q^2}{M_X^2+Q^2}\ , \tag{1.49}$$

(1.50)

where the approximations hold for small values of t. In a model where a Pomeron is exchanged in the t-channel $x_{I\!P}$ measures the fraction of the proton momentum carried by the Pomeron and β corresponds to the momentum fraction of the struck quark within the Pomeron.

II. Diffractive structure function

Diffractive structure functions can be defined in analogy to inclusive DIS and the four-fold differential diffractive cross section can be expressed as [51]

$$\frac{d^4\sigma^{diff}}{dx_{I\!P}dtdQ^2dx} = \frac{2\pi\alpha^2}{xQ^4}\left[\left(1+(1-y)^2\right)F_2^{D(4)} - y^2 F_L^{D(4)}\right](1+\delta_Z)(1+\delta_r)\,, \tag{1.51}$$

where δ_Z and δ_r denote small corrections due to Z^0 exchange and radiative corrections. The contribution from F_L is expected to be small in the kinematic range addressed in this thesis and has been neglected. When t is not measured an integration over t is performed and $F_2^{D(3)}$ is defined through

$$\frac{d^3\sigma^{diff}}{dx_{I\!P}dQ^2dx} = \frac{2\pi\alpha^2}{xQ^4}\left[1+(1-y)^2\right]F_2^{D(3)}(\beta, Q^2, x_{I\!P})\;, \tag{1.52}$$

where F_L and the δ_i are neglected as above.

In Pomeron type models it is expected that the diffractive structure function factorizes into two parts

$$F_2^{D(4)}(x, Q^2, x_{I\!P}, t) = f_{I\!P/p}(x_{I\!P}, t)\cdot F_2^{I\!P}(\beta, Q^2)\;, \tag{1.53}$$

where $f_{I\!P/p}(x_{I\!P}, t)$ describes the Pomeron flux emitted from the proton and $F_2^{I\!P}(\beta, Q^2)$ is the Pomeron structure function describing the $\gamma I\!P$ vertex. In Regge models the Pomeron flux is expected to behave like

$$f_{I\!P/p}(x_{I\!P}, t) \approx f(t)\cdot(1/x_{I\!P})^{2\alpha_{I\!P}(t)-1}\;. \tag{1.54}$$

In the model by Ingelman and Schlein [51] the Pomeron consists of partons like a standard hadron. Here the virtual photon probes the internal parton content of the Pomeron. In analogy to the proton structure function $F_2^p(x, Q^2)$ the Pomeron structure function $F_2^{I\!P}(\beta, Q^2)$ can then be interpreted as the probability to find a parton within the Pomeron which carries a momentum fraction β of the Pomeron.

1.2.5 Models of Diffraction in DIS

I. Aligned jet model

The presence of diffraction in DIS was first predicted by Bjorken and Kogut [53] based on the 'aligned jet model' (AJM). The virtual-photon proton interaction is considered in the proton rest frame. In this frame the photon fluctuates into a $q\bar{q}$-state which undergoes hadronic interactions with the proton as in the Vector Dominance Model. However, if all configurations of the hadronic fluctuation were to contribute to the total γ^*p cross section $\sigma^{tot}_{\gamma^*p}$ in a universal manner, σ_{γ^*p} would be Q^2 independent leading to scaling violation of the structure function $F_2 \propto Q^2\sigma_{\gamma^*p}$. Bjorken suggested to overcome the scaling violation by requiring that only $q\bar{q}$ configurations where the p_T of the $q(\bar{q})$ relative to the photon axis is small (aligned jet configurations) contribute to the $\gamma^* p$ cross section. The low-p_T configurations correspond to extended, hadron like objects, which give also rise to a substantial diffractive cross section.

In QCD models there is a simple explanation for the above suppression [59, 61, 63]. The effective color charge of small size $q\bar{q}$-states is small due to screening of one parton by the other and consequently the interaction is suppressed. This phenomenon is called color transparency.

II. QCD inspired models

Since the first observation of diffractive events in DIS at HERA many attempts have been made to develop QCD based models of diffraction. The most popular approaches can roughly be classified as follows

Regge factorization and QCD: This class of models follows the idea of Ingelman and Schlein [51]. The diffractive cross section is assumed to factorize into a Pomeron flux of the proton and a γ-Pomeron interaction. The Pomeron is assumed to have a partonic structure which has to be determined experimentally. The Q^2 evolution of the parton distributions is generally assumed to be given by the DGLAP equations. The assumption on the initial parton distribution at a small starting scale Q_0 differs between several models. The Pomeron flux is usually obtained using Regge inspired fits to data.

Perturbative QCD and Color dipole approach: The simplest realization of the Pomeron in QCD is a color singlet two gluon state [54]. In perturbative QCD approaches [55, 56, 57] the virtual photon fluctuates into a $q\bar{q}$ or $q\bar{q}g$ state. The interaction with the proton is calculated as a t-channel exchange of a color singlet two gluon state. The models differ in the treatment of QCD corrections and in the choice of the gluon density in the proton.

In the color dipole approach the $q\bar{q}$ fluctuation of the photon interacts with the proton as a color dipole first advocated by Nikolaev et al. [58]. In [59] this concept was extended to more complicated hadronic states. The calculation is performed in a kinematic regime where perturbative QCD is applicable and then extrapolated into the soft region.

Saturation model: The Saturation model developed by Golec-Biernat and Wüsthoff [60] is related to the color dipole models. It considers saturation effects occurring when the photon wavelength $1/Q$ reaches the size of the proton at small Q^2. A second kind of saturation appears in the low x region where the parton density is very high and recombination effects limit a further growth of the density. A simple ansatz for the dipole-proton cross section $\hat{\sigma}$ is made:

$$\hat{\sigma} = \sigma_0 \{1 - exp[-r^2/(4R_0^2(x))]\} , \tag{1.55}$$

where r denotes the transverse $q\bar{q}$ separation, R_0 is a x-dependent saturation scale $R_0^2(x) = (x/x_0)^\lambda$ in GeV^{-2} and σ_0, x_0 and λ are free parameters. The inclusive $\gamma^* p$ cross section for transverse (T) and longitudinally (L) polarized photons is given by

$$\sigma_{T,L}(x, Q^2) = \int d^2r \int_0^1 dz |\Psi_{T,L}(z, r)|^2 \hat{\sigma}(x, r^2) , \tag{1.56}$$

where z is the longitudinal momentum fraction of the photon carried by the quark and $\Psi_{T,L}$ is the photon wave function. The cross section for diffractive DIS can then be written as

$$\frac{\sigma^D_{T,L}}{dt}(t=0) = \frac{1}{16\pi} \int d^2r \int_0^1 dz |\Psi_{T,L}(z,r)|^2 |\hat{\sigma}(x,r^2)|^2 \; . \tag{1.57}$$

After determining the free parameters σ_0, x_0 and λ from fits to total $\gamma^* p$ cross sections the diffractive cross section can be predicted. The model is found to reproduce the measured diffractive cross section surprisingly well [61].

Soft color interactions and semi classical approach: Motivated by the observation of a close similarity between the x and Q^2 dependence of the diffractive and the inclusive DIS cross section at small x the model of soft color interactions (SCI) [62] assumes that the same hard partonic processes underlie both cross sections. In the proton rest frame the photon fluctuates into a $q\bar{q}$-state which interacts with the proton. After this hard interaction the $q\bar{q}$ pair propagates through the color field of the proton. Through the exchange of soft gluons, which do not affect the kinematics of the process, the color of the $q\bar{q}$ pair changes randomly. The probability that the $q\bar{q}$ pair, which is originally produced in a color octet state, evolves into a color singlet state is $P = 1/9$ given by the statistical weight factor accounting for all possible color states. In the case that a color singlet state is created there is no color flow between the $q\bar{q}$ pair and the proton remnant. The color singlet state fragments independently of the proton remnant yielding a gap in rapidity, which is a characteristic feature of diffractive events. The SCI model predicts that the ratio of the diffractive and the non-diffractive DIS cross section is $\approx 1/9$ independent of Q^2 and W in agreement with experiment.

The semi classical approach [63] is based on the SCI model. The interaction of the $q\bar{q}$-state with the color field of the proton is treated in the eikonal approximation. Also, higher Fock states in the photon wave function such as $q\bar{q}g$ states are included in the calculations.

Chapter 2

The ZEUS detector at HERA

2.1 The HERA Accelerator

HERA, the Hadron Elektron Ring Anlage (Fig.2.1) [64], is the world's first lepton proton collider, located at the DESY laboratory in Hamburg, Germany. Construction began in 1984. It was commissioned in 1991 and data taking started in spring 1992. HERA is designed to accelerate electrons or positrons up to 30 GeV and protons up to 820 GeV energy, yielding a center of mass energy of $\sqrt{s} = 314$ GeV.

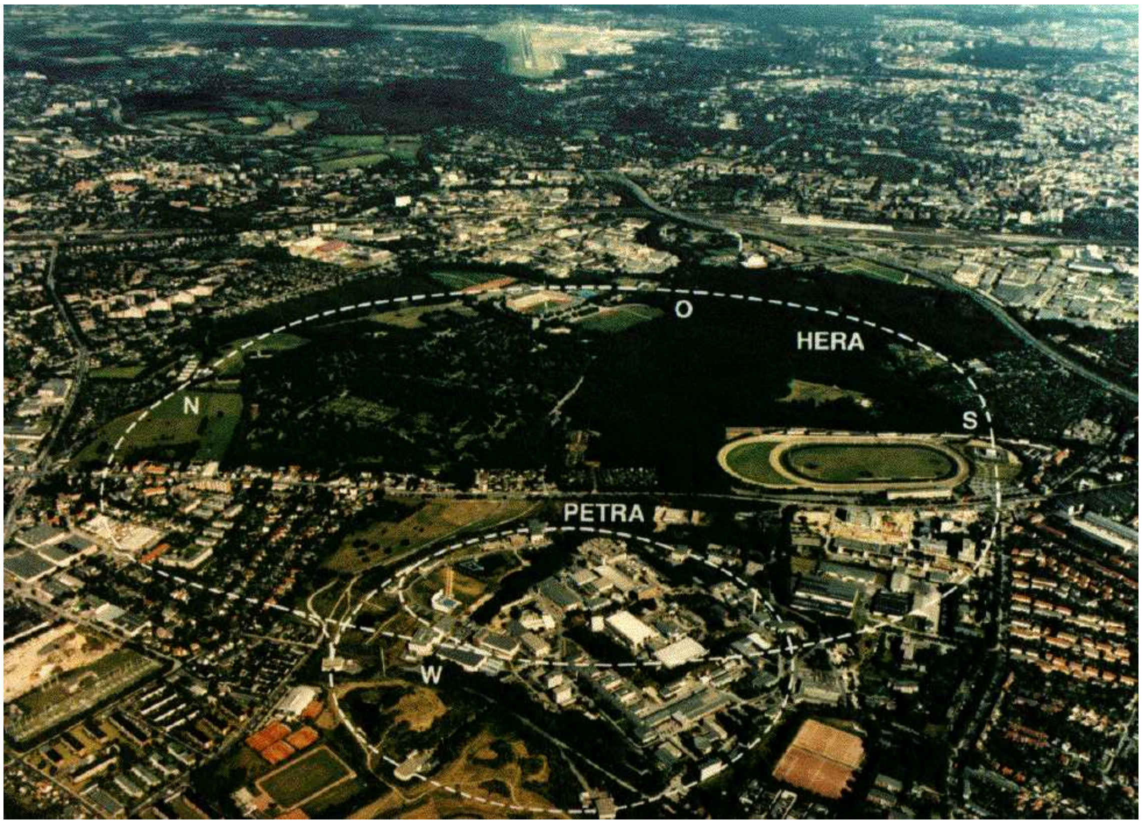

Figure 2.1: Aerial view of DESY and the surrounding area in Hamburg, Germany. The location of the accelerators PETRA (enclosing the DESY site) and HERA are indicated by dashed lines.

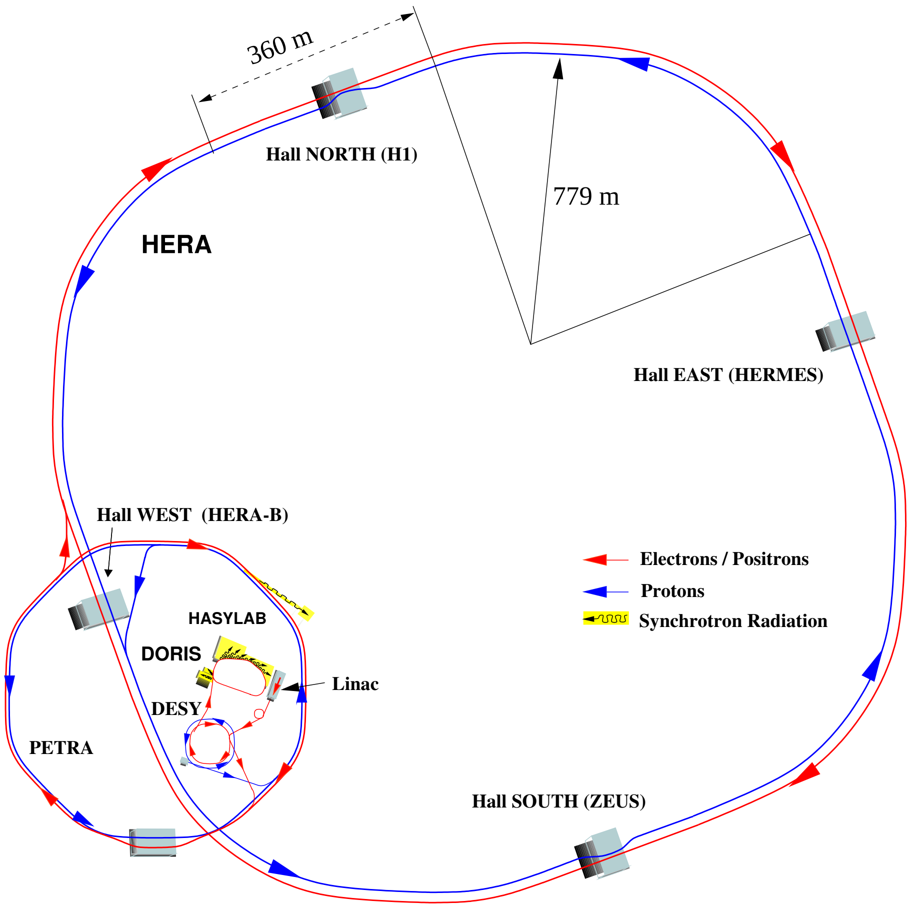

Figure 2.2: The HERA accelerator complex. Four experiments are located in the experimental halls South (ZEUS), West (HERA-B), North (H1), and East (HERMES).

In the two collider experiments, H1 and ZEUS, the beams are brought to collision at zero crossing angle. Two fixed-target experiments: HERMES and HERA-B, make use of the electron and proton beams, respectively. HERMES studies the spin structure of the nucleon by scattering longitudinally polarized electrons off polarized gas jet targets such as hydrogen, deuterium or ^{3}He. Transversely polarized electrons are turned into longitudinally polarized electrons using spin rotators. The HERA-B experiment is designed to measure $\mathcal{CP}$-violation in the $B^0\overline{B^0}$-system. It uses collisions of the proton beam halo with a wire target for the production of B-mesons.

Figure 2.2 shows a schematic layout of the HERA accelerator complex. Two separate rings for electrons and protons, located in a 6.3 km long tunnel 15-30 m underground, use conventional and superconducting magnets respectively.

The proton accelerator chain starts with a 50 MeV H^- linear accelerator. Before injection into the DESY III synchrotron ring, the electrons are stripped off the H^--ions. After subsequent acceleration to 7.5 GeV and 40 GeV in DESY III and PETRA II, respectively, the protons are injected into the HERA storage ring where they are accelerated to their final energies.

The electron injection starts with a 500 MeV linear accelerator filling the positron injection accumulator (PIA). In DESY II and PETRA II the electrons are accelerated to 7.5 GeV and 12 GeV, respectively, and then transferred to HERA where they are accelerated to 27.5 GeV.

HERA can be filled with up to 210 electron and 210 proton bunches with 96 ns spacing. In

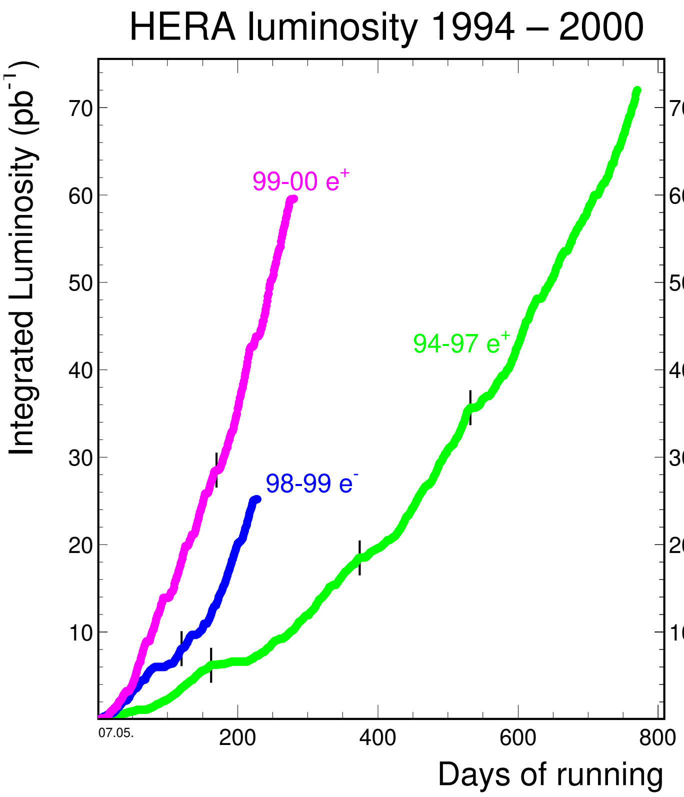

Figure 2.3: Integrated luminosity delivered by HERA during data taking periods 1994 - 2000 (until Mai 2000). From 1994 to 1997 protons were accelerated to 820 GeV. During the following two periods 920 GeV protons were used.

practice not all bunches are filled (in 1998-99 HERA was operated with typically 174 colliding bunches of each species). Noncolliding (unpaired) bunches allow to estimate the beam related background and empty bunches can be used to measure cosmic ray background rates.

From mid 1994 to 1997 HERA accelerated positrons instead of electrons due to lifetime problems which have been attributed to capturing of positively charged dust. During the 1997/1998 shutdown new vacuum pumps have been installed which significantly reduced this problem. This allowed HERA to run with electrons during the data taking period used for this analysis. Also in 1998, HERA increased the proton beam energy from the design value of 820 GeV to 920 GeV. The integrated luminosities for these 3 running periods are shown in Fig. 2.3.

The design parameters and performance of HERA during the 1998-1999 electron data taking period are summarized in table 2.1.

[1] noncolliding bunches
[2] total of 8 months luminosity running in 99 with e^- and e^+.

HERA parameters	Design Values		Values of 1998/99	
	$e^{\pm}$	p	e^{-}	p
Circumference (m)	6336			
Energy (GeV)	30	820	27.6	920
Center-of-mass energy (GeV)	314		318	
Injection energy (GeV)	14	40	12	40
Maximum current (mA)	58	160	37	99
Number of bunches	210	210	174+15[1]	174+6[1]
Time between bunch crossings (ns)	96			
Horizontal beam size (mm)	0.301	0.276	0.200	0.200
Vertical beam size (mm)	0.067	0.087	0.054	0.054
Longitudinal beam size (mm)	8	110	8	170
Max. specific luminosity ($cm^{-2}s^{-1}mA^{-2}$)	$3.6 \cdot 10^{29}$		$9.9 \cdot 10^{29}$	
Max. inst. luminosity ($cm^{-2}s^{-1}$)	$1.5 \cdot 10^{31}$		$1.2 \cdot 10^{31}$	
Integrated luminosity per year (pb^{-1})	35		47[2]	

Table 2.1: HERA design parameters and performance during 1998/99 electron running.

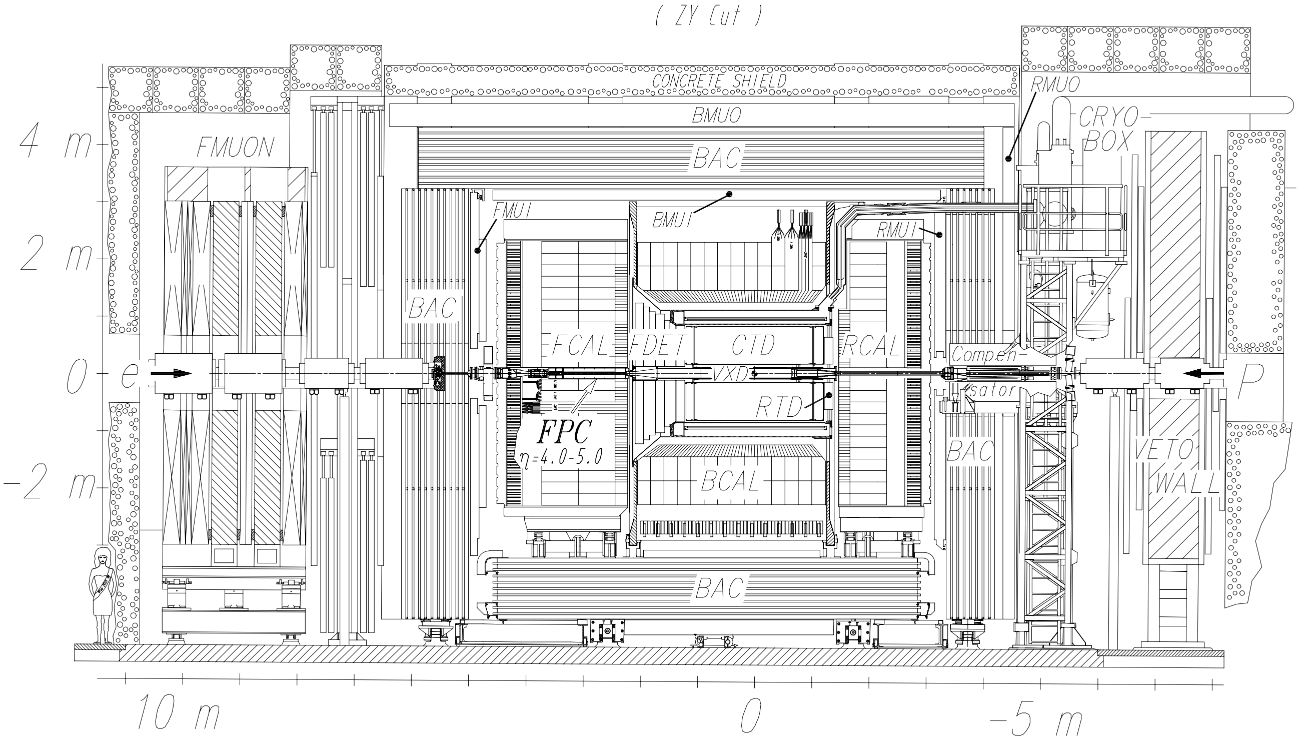

Figure 2.4: longitudinal cut of the ZEUS detector

2.2 The ZEUS detector

The ZEUS detector is a general purpose magnetic detector designed to study many different processes of electron-proton scattering at HERA. The design reflects the forward-backward asymmetry of the ep final-state resulting from the difference in the energy of the electron and proton beams. ZEUS is built and operated by a collaboration of more than 400 physicists from 51 institutes in 12 different countries and has been in operation since 1992. Since then, several detector upgrades have been carried out as a consequence of the physics and technical understanding gained during the first years of data taking.

The ZEUS coordinate system is defined as a right-handed orthogonal system with the origin at the nominal interaction point (IP), the Z-axis pointing in the proton beam direction (defining the forward direction), the Y-axis pointing upwards and the X-axis pointing horizontally towards the center of HERA. Thus, the polar angle θ of the proton beam is $0°$ and of the electron beam is $180°$. The azimuth angle ϕ is measured with respect to the X-axis.

Figures 2.4 and 2.5 show a longitudinal and a transverse cut of ZEUS. A brief overview of the main components is given below followed by a more detailed description of some components essential for this analysis. For a more complete description refer to [65].

In the center of ZEUS, the central tracking detector (CTD) [66] surrounds the interaction point. In the forward and rear directions additional tracking information is provided by the FTD/TRD and RTD chambers. The FTD consists of three sets of planar drift chambers with transition radiation detectors (TRD). The RTD is made of one planar drift chamber with three layers. The whole tracking system is surrounded by a superconducting magnet providing a 1.43 T magnetic field.

Surrounding the tracking system a compensating high resolution Uranium Calorimeter (CAL) is installed [68, 69, 70]. The calorimeter is divided into a forward (FCAL), barrel (BCAL) and

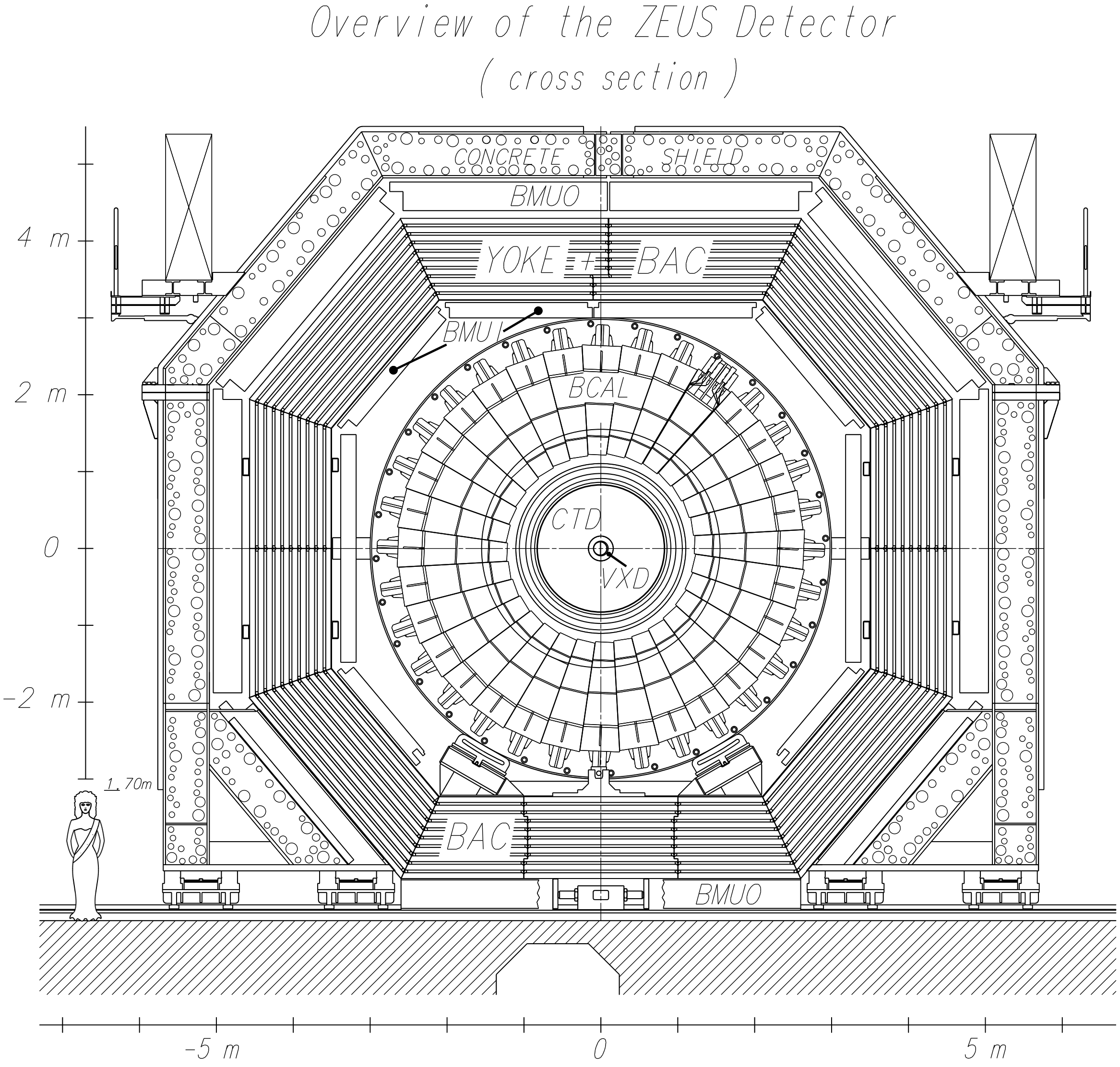

Figure 2.5: cross section of the ZEUS detector

rear (RCAL) section. In order to detect electrons at very low scattering angles, a beam pipe calorimeter (BPC) [71] has been installed on two sides of the beam pipe in the rear direction. In the forward direction a Forward Plug Calorimeter (FPC) has been installed in the beam pipe hole of the FCAL, extending the calorimetric coverage by one unit in pseudorapidity η[1]. The FPC is described in detail in chapter 3. Attached to the front face of the RCAL a Small Angle Rear Tracking Detector (SRTD) covers an area of roughly $\sim$ 34 cm radius around the beam pipe. In addition a presampler is attached to the front face of the calorimeter. It consists of a 5 mm thick scintillator layer and is used to estimate the amount of energy loss in the inactive material in front of the calorimeter. In RCAL and FCAL a hadron-electron separator (HES) consisting of a plane of 3×3 cm^2 silicon diodes is installed after 3 radiation lengths.

The CAL is surrounded by an iron yoke which provides a return path for the magnetic field flux and serves as absorber for the backing calorimeter (BAC) which measures energy leakage from the main calorimeter. Limited streamer tube chambers are located inside (FMUI, BMUI, RMUI) and outside (FMUON, BMUON, RMUON) of the yoke. Together with the magnetic

[1]The pseudorapitidy is defined as $\eta = -ln(tan\frac{\theta}{2})$.

field in the yoke, which is enhanced by additional copper coils to 1.6 T, these chambers are part of the muon detection system.

Outside the main detector in the forward direction the leading proton spectrometer (LPS) [72] is installed very close to the beam at distances Z = 24 - 90 m from the interaction point. It consists of 6 silicon strip detector stations which measure protons scattered at small angles. Final state neutrons are measured by the forward neutron calorimeter (FNC) [73], a lead/scintillator calorimeter installed at Z = 105.6 m .

In the electron beam direction two small lead/scintillator calorimeters (LUMIE, LUMIG) installed at Z = -34 m and -104 m measure outgoing electrons and photons for the determination of the luminosity and for tagging of $Q^2 \sim 0$ events with $0.2 < y < 0.6$ as well as radiative events. Additional taggers have been installed at Z = -8 m and -44 m to identify $Q^2 \sim 0$ events by detecting the scattered electron in the energy range of $1 < E_{e'} < 3$ GeV and $21.5 < E_{e'} < 26$ GeV, respectively.

The time interval of 96 ns between bunch crossings in HERA leads to a nominal beam crossing rate of 10 MHz. The rate of events observed by the detector is at the level of a few 100 kHz, resulting mainly from beam halo particles and beam gas scattering. A three-level trigger system selects specific event types. In order to keep the amount of data written to tape at a manageable level the rate of the accepted events is at the 5-10 Hz level.

2.2.1 The Central Tracking Detector (CTD)

The central tracking detector (CTD) [66] is a cylindrical drift chamber which measures the direction and momentum of charged particles and the energy loss dE/dx used for particle identification. Its active volume ranges from Z = -100 cm to Z = 104 cm with an inner radius of 19 cm and an outer radius of 78.5 cm and covers polar angles of $15° < \theta < 164°$. There are 576 cells with 8 sense wires each, organized in 9 radial superlayers (see Fig. 2.6). The wires of the odd numbered superlayers are parallel to the beam axis, whereas the even numbered ones are inclined by $\sim 5°$. This allows to determine the Z-position with an accuracy of 2 mm. Additionally, layers 1, 3 and 5 are equipped with a Z-by-timing system (resolution $\sigma_Z \sim 4$ cm), mainly used for trigger purposes. The CTD is filled with a gas mixture of $Ar/CO_2/C_2H_6$: 85/13/2.

The position resolution achieved in r-θ is 190 μm. This results in a transverse momentum resolution of (p_t in GeV) [74]

$$\frac{\sigma(p_t)}{p_t} = 0.0058 \cdot p_t \oplus 0.0065 \oplus 0.0014/p_t \ , \tag{2.1}$$

where the symbol $\oplus$ indicates that the three terms are added in quadrature. The first term results from the position resolution, whereas the second and third ones are due to multiple scattering before and inside the CTD, respectively. The Z-position of the vertex for medium and high multiplicity events can be reconstructed with an accuracy of $\lesssim 2$ mm.

2.2.2 The Uranium Calorimeter (CAL)

The main ZEUS calorimeter is a high resolution uranium-scintillator calorimeter (CAL) [68, 69, 70]. It is the most essential detector for the reconstruction of the ep-scattering final state and plays a crucial role in the present analysis.

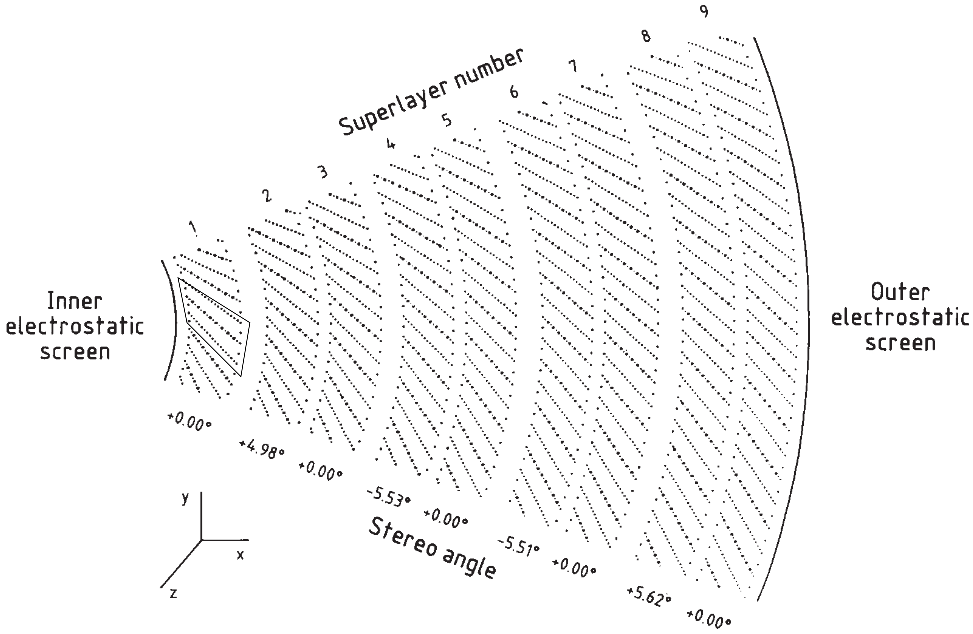

Figure 2.6: Layout of a CTD octant. Each octant has nine superlayers with the even numbered ones inclined with respect to the beam axis ('Stereo angle').

The CAL is a sampling calorimeter consisting of alternating layers of 3.3 mm $\hat{=}$ 1 X_0 depleted uranium as absorber medium and 2.6 mm organic scintillator[2] as active material. The thicknesses have been optimized to achieve a compensating calorimeter, where the response to electromagnetic and hadronic particles of equal energy is the same ($e/h = 1$, see section 3.2). In this way optimum accuracy for the absolute value and resolution of hadron energies is achieved. The CAL energy resolution measured under test beam conditions is for electrons

$$\frac{\sigma_E}{E} = \frac{18\%}{\sqrt{E/\text{GeV}}} \oplus 2\% \tag{2.2}$$

and for hadrons

$$\frac{\sigma_E}{E} = \frac{35\%}{\sqrt{E/\text{GeV}}} \oplus 1\% \;. \tag{2.3}$$

The calorimeter consists of a forward (FCAL), a barrel (BCAL) and a rear (RCAL) section covering the angular regions shown in Tab. 2.2.2. Taking into account the 20×20 cm^2 hole for the HERA beam pipe in the FCAL and the 8×20 cm^2 beam hole in the RCAL[3], the calorimetric coverage is $> 99.8\%$ of 4π sr. The coverage in the forward direction is extended further by the installation of a forward plug calorimeter (FPC) in the forward beam hole (see chapter 3). The calorimeter is vertically (FCAL and RCAL) and radially (BCAL) subdivided into modules (Fig. 2.7), which themselves are subdivided into towers of approximate transverse dimensions of 20×20 cm^2. Longitudinally, the towers are segmented into an electromagnetic (EMC) and two (RCAL only one) hadronic sections. The EMC section of each tower consists of four 5×20 cm^2 (RCAL: two 10×20 cm^2) cells, whereas the HAC sections consist of only one cell. The BCAL is projective in ϕ and the EMC section also in θ. FCAL and RCAL however are

[2] SCSN-38 polystyrene

[3] In 1995 the RCAL modules above and below the beampipe hole have been moved closer together reducing the hole from 20×20 cm^2 to 8×20 cm^2.

	FCAL	BCAL	RCAL
η-range	3.8 - 1.0	1.1 - (-0.74)	(-0.72) - (-4.2)
θ-range	$2.5°$ - $39.9°$	$36.7°$ - $129.1°$	$128.1°$ - $178.4°$
EMC rad. length X_0	25.9	22.7	25.9
total abs. length λ	7.14	4.92	3.99

Table 2.2: Angular acceptance and longitudinal depth of the CAL

non-projective. The scintillator light of each cell is transported to two photomultiplier tubes (PMT) via separate wave-length-shifter plates on two opposite sides of the cells. Summing the signals of both PMTs, the response is independent of the point of incidence of particles. The comparison of the two signals allows to determine the horizontal impact position. The excellent time resolution of the CAL, being smaller than 1 ns for energy deposits > 4.5 GeV, allows to reduce the beam related background at the trigger level.

The constant signal resulting from the radioactive decay of ^{238}U (half-life $4.5 \cdot 10^9$ years) is used as a reference to calibrate the calorimeter to better than 1%. The PMTs and the readout electronics are additionally calibrated using LED and LASER and test pulses.

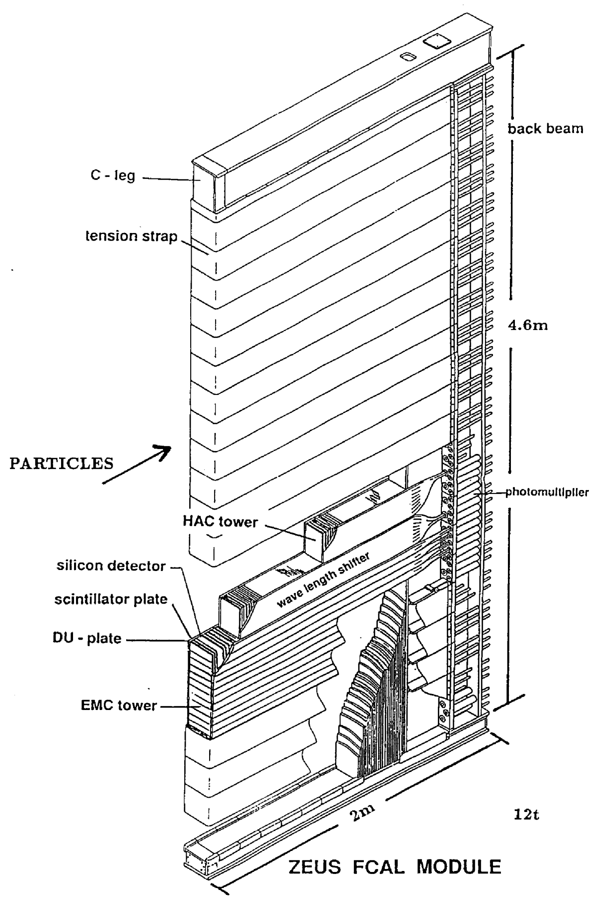

Figure 2.7: Layout of a FCAL module. It is longitudinally subdivided into one EMC and two HAC sections, which in turn are divided into cells. Each cell is read out by two wavelength shifter bars on opposite sides.

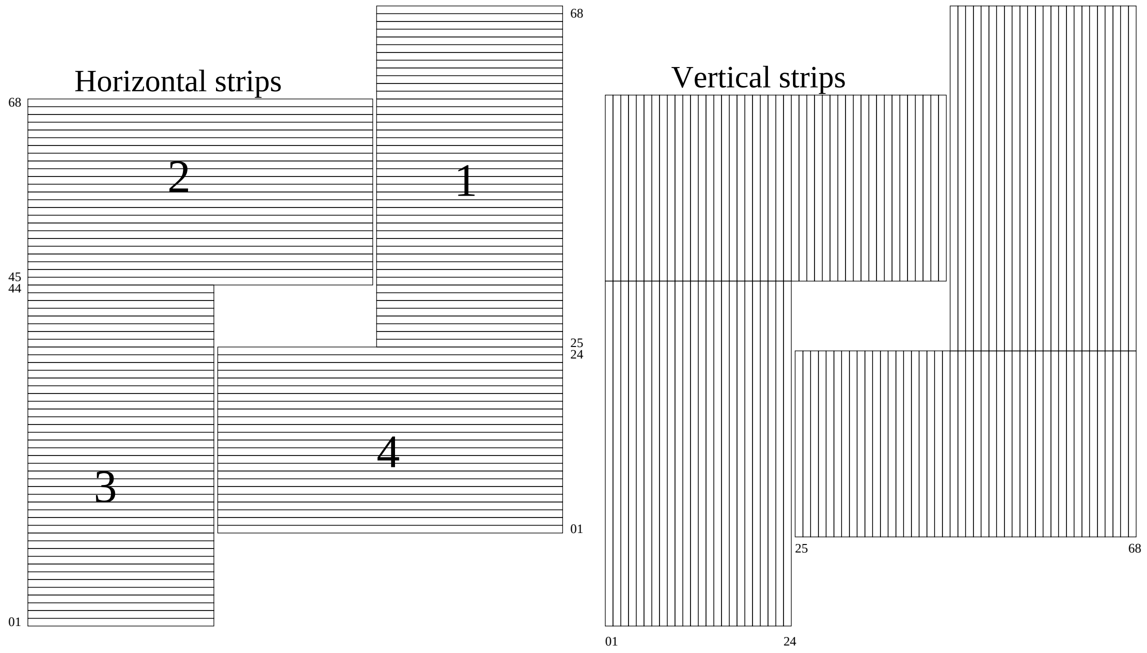

Figure 2.8: Orientation and numbering scheme of the strips of the two SRTD planes. The strip size is 0.98 cm × 24(44) cm.

2.2.3 The Small Angle Tracking Detector (SRTD)

In order to improve the measurement of the energy and angle of the scattered electron for low Q^2 events, a Small Angle Tracking Detector (SRTD) has been installed in 1994 [75]. It is attached to the front face of the RCAL and covers approximately an area of 34 cm radius around the beam pipe (Fig. 2.8). The SRTD consists of a horizontal and a vertical layer of 1 cm wide and 0.5 cm thick scintillator strips. Position and pulse height information is provided via optical fiber and photomultiplier readout. The SRTD is used to measure the electron impact position as described in section III..

Electrons which loose energy through showers in the dead material in front of the calorimeter in general deposit more energy in the SRTD than nonshowering electrons. The measured energy deposit in the SRTD can therefore be used to correct for this energy loss. The SRTD also provides a fast time measurement (resolution $\sim$ 2 ns), which is used to reject background events at the trigger level.

2.2.4 The Electron-Hadron Separator (HES)

For isolated electrons the electromagnetic and hadronic sections of the calorimeter provide good electron identification (see section: 7.3.1). In order to improve the identification of electrons inside jets an electron-hadron separator has been installed in RCAL and FCAL. It consists of 3×3 cm^2 silicon diodes placed at a longitudinal depth of 3 radiation lengths X_0 which corresponds to the approximate position of the electromagnetic shower maximum. The separation between electrons and hadrons is based on the fact that the hadronic interaction length is 20 times larger than the electromagnetic radiation length. Hadrons therefore produces a smaller HES signal.

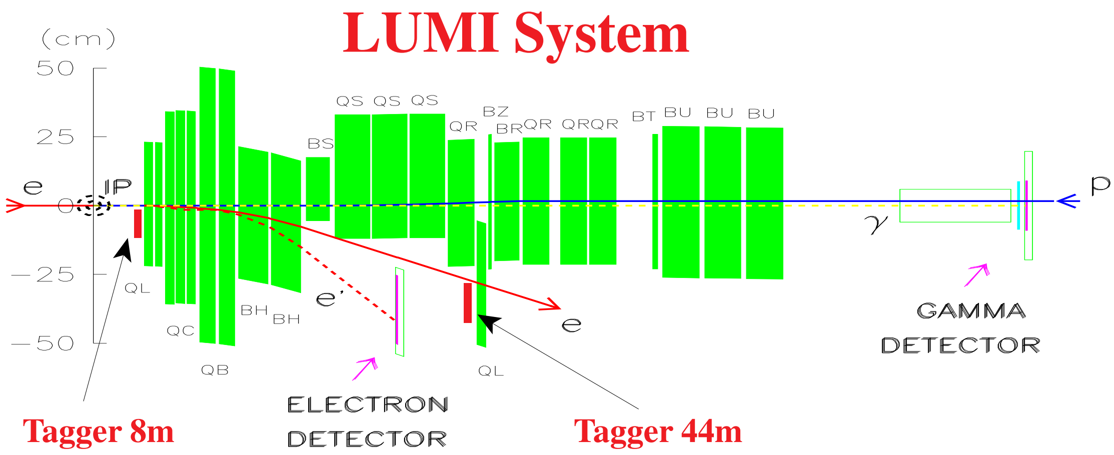

Figure 2.9: Location of ZEUS detectors in negative Z-direction. Shown are the gamma (LUMIG) and electron detectors (LUMIE) used for the luminosity measurement together with the electron taggers at Z = −44 m and Z = −8 m.

The fine segmentation of the HES can also be used to improve the position resolution for electromagnetic particles in the calorimeter as described in section II..

2.2.5 The Luminosity measurement (LUMI)

Since the event rate $\dot{N}$ is related to the Luminosity $\mathcal{L}$ and the cross section σ by $\dot{N} = \mathcal{L} \cdot \sigma$, an accurate knowledge of $\mathcal{L}$ is crucial for cross section measurements. In ZEUS, $\mathcal{L}$ is determined by measuring the rate of bremsstrahlung events produced by the Bethe-Heitler process $ep \rightarrow e\gamma p$ [76]. The cross section for this process has been calculated with an accuracy of 0.5%.

Electrons which have lost part of their energy through bremsstrahlung are deflected from the nominal beam orbit by the magnetic field of HERA (Fig. 2.9). In the energy range 0.2 E_{beam} < $E_{e\prime}$ < 0.8 E_{beam} they are detected by a lead scintillator calorimeter (LUMIE). The LUMIE detector also allows to tag photoproduced events with $0.2 < y < 0.6$ and $Q^2 < 0.001$ GeV^2.

Photons produced by bremsstrahlung at angles $\theta_\gamma < 0.5$ mrad exit the beam-pipe through a Cu - Be window at Z = -82 m and are detected in the LUMIG calorimeter at Z = -106 m. The energy resolution of this lead scintillator calorimeter was determined to be $18\%/\sqrt{E(GeV)}$ under test beam conditions. In order to shield it against low energetic photons from synchrotron radiation a carbon lead filter with an adjustable thickness between 0.5 and 3.5 r.l. has been installed in front of the LUMIG detector, which increases the energy resolution to $23\%/\sqrt{E(GeV)}$. The background due to bremsstrahlung of electrons on rest gas molecules has to be subtracted statistically using unpaired electron bunches. The impact position of the photons is reconstructed with an accuracy of $\sim$ 2 mm using scintillator fingers embedded in the calorimeter at a depth of 7 X_0. The LUMIG calorimeter is also used to tag photons from initial state radiation events.

Although originally a coincidence measurement between the electron and the photon was planned the rate of the photons alone provides a precise measurement of the luminosity [77].

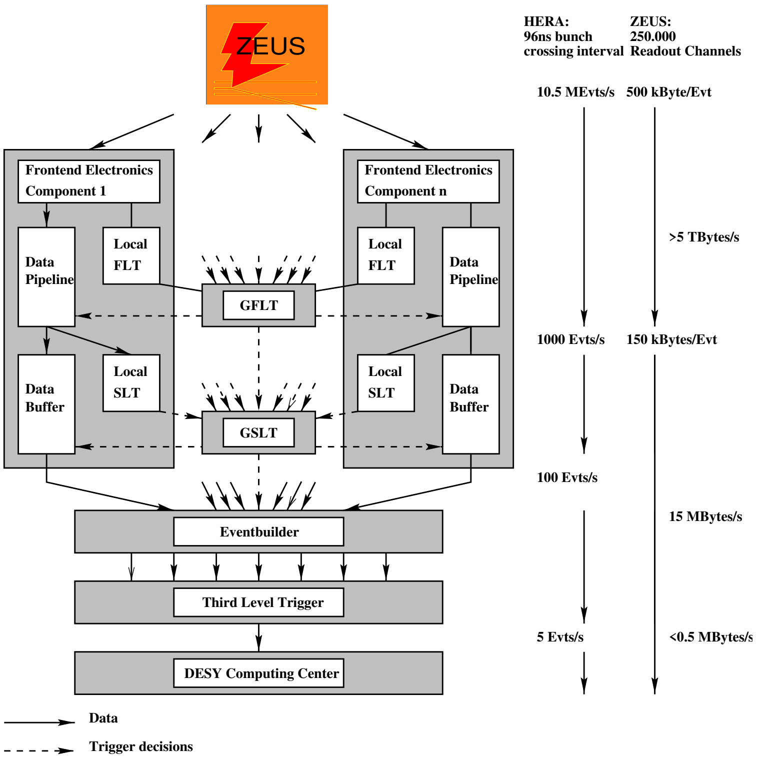

Figure 2.10: Schematic diagram of the ZEUS trigger and data acquisition system.

2.2.6 The ZEUS Data Acquisition System

While the rate of interesting ep physics events in the ZEUS detector is of the order of a few Hz, the rate of background events, dominated by upstream interactions of the proton beam with the residual gas, is in the order of 10 - 100 kHz. Taking into account a raw data size of 0.5 MB and a maximum writing speed of $\sim$ 0.5 MB/s, this requires a sophisticated rate and data reduction system. In ZEUS a three level trigger system accomplishes this task (Fig. 2.10).

The First Level Trigger (FLT) reduces the rate to below 1 kHz: hardware based triggers in each detector component provide a trigger decision within 2 μs after beam crossing to the Global First Level Trigger (GFLT). Within 4.4 μs the GFLT decides whether the event is to be fully digitized and transfered to the Second Level Trigger (SLT).

The SLT is designed to reduce the trigger rate to 50-100 Hz. Typically, the SLT decision takes 30 μs introducing a $\sim$2% dead time (at a GFLT rate of $\sim$ 0.6 kHz). On the SLT level a transputer network calculates objects like track momenta or calorimeter clusters, which allow a more restrictive trigger decision.

If an event is accepted by the SLT, all detector components send their data to the Event Builder, which combines the data and writes it into the final data format. The Third Level Trigger (TLT) performs part of the offline analysis on a farm of Silicon Graphics CPUs. The TLT accepts events at a rate of a few Hz. These events have a typical data size of $\sim$ 100 kB and are written to disk at the DESY computing center via a fiber-link (FLINK) connection. From here they are available for offline reconstruction and analysis.

Chapter 3

The Forward Plug Calorimeter

3.1 Introduction

In 1998 a Forward Plug Calorimeter (FPC) was installed into the 20×20 cm^2 forward beam hole of the ZEUS uranium calorimeter (see Fig. 3.1). With a 6.3 cm diameter inner hole it extends the calorimetric coverage in pseudorapidity from $\eta \leq 4.0$ to $\eta \leq 5.0$.

The FPC vastly increases the physics potential for the study of DIS diffractive scattering and is therefore a crucial component for the present analysis. Diffractive processes are of the type

$$\gamma^* p \rightarrow XN$$

where the system X (N) results from diffractive dissociation of the virtual photon (proton). The maximum mass of the system X up to which diffractive events can be separated from nondiffractive processes and hence the study of diffractive events is feasible depends on the calorimeter coverage in forward direction. Despite a 99.7% solid angle coverage of the uranium calorimeter only a fraction of the hadronic final state is detected. The rest escapes mainly through the forward beam hole due to the asymmetric collision of 920 GeV protons and 27.6 GeV electrons. After the extension in η the accessible mass range increased by a factor of 1.7 such that M_X^2 values up to $\approx 0.03 \cdot W^2$ can be reached.

3.2 Basic calorimetry

Calorimeters are massive detectors used to measure particle energies. The particle that is to be measured deposits all its energy in the detector volume. A small fraction of that energy is transformed into a measurable signal (e.g. scintillation light, Cherenkov light or ionization charge). Provided that this fraction is constant the signal is proportional to the energy of the incident particle.

Two kinds of calorimeters are employed in high energy physics: homogeneous and sampling calorimeters. Homogeneous calorimeters such as leadglass detectors consist of a uniform medium which serves both as the absorber and as the readout medium.

In sampling calorimeters two different materials, usually arranged in a sandwich-like structure, are used for energy dissipation and measurement. The passive absorber medium in general

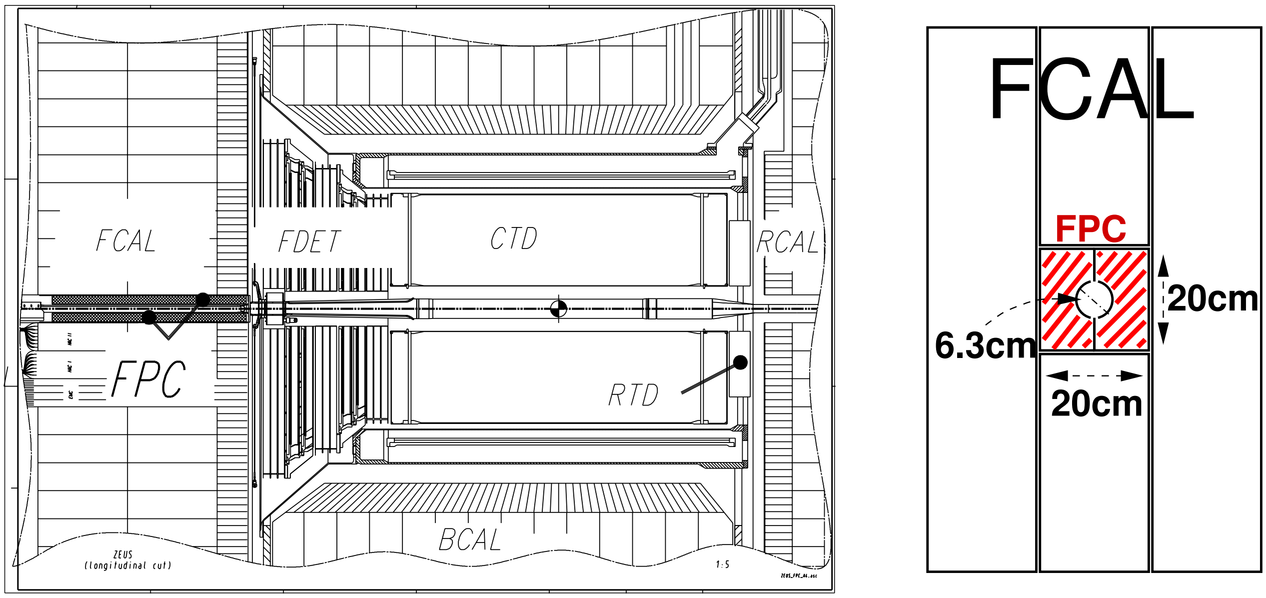

Figure 3.1: Longitudinal cut of the inner part of the ZEUS detector and front view of the forward calorimeter. The FPC is installed into the 20×20 cm^2 beam hole of the FCAL.

consists of a high density material like Pb or U. The total depth of the absorber medium is chosen to ensure complete energy deposition up to the highest expected energies taking into account spatial constraints. Common choices for the readout medium are liquid Ar, where the ionization charge is measured directly, and scintillators with subsequent detection of the produced light in photomultipliers (PMTs).

The properties of sampling calorimeters depend on the fraction of energy deposited in the readout material, called sampling fraction R^i:

$$R^i = \frac{E^i_{readout}}{E^i_{readout} + E^i_{absorber}}, \tag{3.1}$$

where $E^i_{readout}$ and $E^i_{absorber}$ denote the energies deposited in the readout and absorber medium for the incident particle type i. For the FPC with 15 mm Pb and 2.6 mm plastic scintillator the sampling fraction for electrons has been determined using the MC described in 4.1 to be $R^e = 1.6\%$.

The measurable signal is generally induced by the ionization energy dE/dx deposited in the readout medium by charged particles as described by the Bethe-Bloch equation [82, 83, 87]:

$$-\frac{dE}{dx} = \frac{N_A}{4\pi\epsilon_0}\frac{e^4}{m_e c^2}\frac{z^2}{\beta^2}\frac{Z}{A}\left[\ln\frac{2m_e c^2\beta^2}{I^2(1-\beta^2)} - \beta^2\right] \quad \text{with} \ \ \beta = \frac{v}{c}\ , \tag{3.2}$$

where m_e is the electron mass, ze and v are the charge and velocity of the ionizing particle, N_A is the Avogadro constant, Z and A are the atomic number and mass of the medium and x is the path length in the medium measured in g/cm^2. The mean excitation energy I is approximately given by $I = 10eV \cdot Z$.

The sampling fraction R and the final calorimeter signal are often normalized to those of a hypothetical minimum ionizing particle (mip).

Although muons are frequently used to approximate mips, the signal ratio μ/mip is equal to unity only near momenta of 300 MeV and larger than unity otherwise. For high energy muons this is due to the relativistic rise of dE/dx and to additional effects like bremsstrahlung, e^+e^- pair production and nuclear interactions [84].

3.2.1 Electromagnetic showers

The processes involved in electromagnetic (e.m.) showers are well known and calculable in the framework of QED. At energies above 10 MeV e.m. cascades are dominated by bremsstrahlung and e^+e^- pair production. The mean energy loss of electrons due to bremsstrahlung over a path length x in g/cm^2 is determined by the radiation length X_0:

$$E(x) = E_0 \cdot e^{-x/X_0}, \tag{3.3}$$

where E_0 is the incident particle energy. The radiation length X_0 can be parameterized as [87]:

$$X_0 = \frac{716.4 \text{ g cm}^{-2} \text{ A}}{\text{Z(Z+1)} \ln(287/\sqrt{Z})}. \tag{3.4}$$

For Pb $X_0 = 0.56$ cm is obtained.

In the early stage of the e.m. shower development, where the energies of the individual shower particles are above 10 MeV, the number of particles (N_e) on average doubles after one radiation length X_0 while the mean particle energy $\langle E_e \rangle$ is halved:

$$N_e = 2^{x/X_0} \quad , \quad \langle E_e \rangle = E_0/N_e = E_0 \cdot 2^{-x/X_0} \; . \tag{3.5}$$

At lower energies other energy loss processes contribute. For electrons ionization becomes the dominating process but also Møller and Bhabha scattering as well as e^+e^- annihilation contribute. For photons Compton scattering and the photo-electric effect contribute; the latter is dominant for high Z materials such as Pb. The critical energy E_c at which the energy loss due to ionization and bremsstrahlung are equal depends on the atomic number Z of the material and can be approximated by:

$$E_c = \frac{800 \text{ MeV}}{Z + 1.2}. \tag{3.6}$$

For Pb $E_c \approx 10$ MeV is obtained.

The mean transverse and longitudinal shower profile is governed by the high energy part of the cascade and scales with X_0. The depth t_m of maximum energy deposition increases logarithmically with the incident particle energy and is approximately 6 X_0 for 10 GeV electrons. The lateral shower size is mainly determined by multiple scattering. The shower consists of a high energy core region and a low energy halo. The width of the shower distribution scales with the Moliere radius R_M, which is given by:

$$R_M = X_0 E_s / E_c \quad \text{with} \quad E_s = \sqrt{4\pi/\alpha} m_e c^2 = 21.2 \text{ MeV} \; . \tag{3.7}$$

On average, only 10% of the energy deposition lies outside a cylinder with radius R_M.

The signal ratio e/mip is typically 0.67 in contrast to the naive expectation of 1. The reason is mainly the energy loss behavior of γ's with energies below 1 MeV. In Pb roughly 40% of the ionization energy is due to shower particles with energies below 1 MeV. At these energies the photo-electric effect dominates the energy loss of photons. Due to the Z^5 dependence of this cross section low energy γ's, which are produced in the high Z absorber medium, interact, in general, inside the absorber before reaching the readout medium. The energy carried by these γ's is therefore not detected. Thus the total signal produced by an incoming electron is reduced compared to that of a minimum ionizing particle with the same total energy deposition and the ratio e/mip is smaller than 1.

3.2.2 Hadronic showers

The appropriate length scale for hadronic showers is the nuclear interaction length λ, given roughly by:

$$\lambda = 35 \text{ g cm}^{-2} \text{ A}^{1/3}. \tag{3.8}$$

The value for Pb is $\lambda = 17.1$ cm. The depth required for containment of a certain energy fraction increases logarithmically with the incident energy. For 10 GeV hadrons 95% of their energy is contained in about 5 λ for a calorimeter which is infinitely wide in transverse dimensions.

The detailed description of hadronic cascades is far more complex than of e.m. showers since a wide variety of processes contribute to the shower development [88, 89].

In the early stage of hadronic cascades (usually the first interaction length) a strongly fluctuating number of π^0s is produced. Since π^0s decay into γ's the energy carried by these π^0s (f_{em}) is deposited in form of e.m. showers. The mean value of f_{em} increases slowly with the incident particle energy E:

$$\langle f_{em}(E) \rangle \approx 0.1 \ln E(GeV) \; . \tag{3.9}$$

For the purely hadronic part of the shower, a fraction of the deposited energy does not produce any measurable signal. For example, weakly interacting particles such as ν's generally escape from the detector. More importantly, most of the energy spent in breaking up nuclei will not be visible. Therefore, the average response to the pure hadronic shower component h_{intr} will in general be less than the response to an e.m. shower of the same energy ($e/h_{intr} > 1$), which implies that the total response to hadrons will be less than the response to electrons of the same initial energy ($e/h > 1$). The relation between e/h and e/h_{intr} is given by

$$e/h(E) = \frac{e}{\langle f_{em} \rangle \cdot e + (1 - \langle f_{em} \rangle) \cdot h_{intr}} = \frac{e/h_{intr}}{1 - \langle f_{em}(E) \rangle \cdot (1 - e/h_{intr})} \; . \tag{3.10}$$

Compensation i.e. $e/h = 1$ is desirable for hadronic calorimeters not only in its own right. As will be seen in section 3.2.3, if $e/h \neq 1$ the linearity and energy resolution are strongly degraded for hadronic particles.

In order to understand how compensation can be achieved in sampling calorimeters with high Z absorber material (U or Pb) and plastic scintillator as readout medium the shower development of the pure hadronic shower contribution in such calorimeters will be discussed in some detail.

shower component i	f_i
ionization (mainly protons)	43 %
nuclear de-excitation γ's	3 %
neutrons (< 20 MeV)	12 %
invisible (binding + recoil) energy	42 %

Table 3.1: Energy fractions f_i carried by various shower components i in a hadronic shower initiated by a 5 GeV proton incident on a Pb block neglecting the e.m. contribution (results of a simulation performed by Wigmans [88]).

I. High energy part of the hadronic shower development

When a high energy hadron collides with a nucleus, the most likely process to occur is spallation which consists of an intranuclear cascade followed by a de-excitation step. The incoming hadron makes quasifree collisions with nucleons which in turn hit other nucleons inside the nucleus. At high enough energies π's and other hadrons may be created. Some of the particles of the intranuclear cascade reach the boundary of the nucleus and escape. This can lead to the production of energetic protons and neutrons at ratios corresponding to their ratio inside the target nucleus. In the de-excitation step nucleons, mainly neutrons, are evaporated until the excitation energy is less than the binding energy of one nucleon. The remaining energy is emitted in the form of γ-rays of typically a few MeV. Depending on the type of material also nuclear fission can occur.

The resulting particles initiate a hadronic cascade resulting in more hadrons with lower energy. At energies below $\sim$ 20 MeV the Coulomb barrier suppresses the emission of charged particles and neutrons are the only hadrons produced.

In these nuclear interactions a widely fluctuating energy fraction f_{loss} (typically $\langle f_{loss} \rangle \approx 40\%$ at $E_{incident} = 5$ GeV) is deposited in form of nuclear binding energy and target recoil energy which are not observed in the detector. In case of Pb the average binding energy needed to free a nucleon is $\sim$ 7.6 MeV.

The remaining energy fraction $(1 - f_{loss})$ is shared between different shower components. The fraction of energy carried by ionizing charged hadrons (f_{ion}), soft neutrons (f_n) and soft γ's (f_γ) from nuclear de-excitation as obtained by a simulation [88] are listed in table 3.1.

II. Calorimeter response to hadronic shower components

The calorimeter response to hadronic showers depends on the fraction of energy carried by the individual shower components (f_{ion}, f_n, f_γ) and on the response to ions, neutrons and γ's (ion/mip, n/mip, γ/mip) which are summarized in table 3.2. The e/h_{intr} ratio can be written as

$$e/h_{intr} = \frac{e/mip}{f_{ion} \cdot ion/mip + f_n \cdot n/mip + f_\gamma \cdot \gamma/mip} \,. \tag{3.11}$$

The contributions from ionizing particles and γ's of nuclear origin account for roughly 50% of the deposited energy. While ion/mip is close to 1, typically $\gamma/mip \approx 0.4$ since low energetic γ's are mostly absorbed in the high Z absorber by the photo-electric effect (see section 3.2.1).

shower component i	i/mip
e.m. energy (e.g. π^0 decay)	≈ 0.6
ionization	≈ 1
nuclear de-excitation γ's	≈ 0.4
neutrons (< 20 MeV)	tunable, typically up to 2 (depending on sampling fraction)

Table 3.2: Typical efficiency i/mip to convert the energy carried by shower component i into measurable signal (normalized to mip) in sampling calorimeters with scintillator readout.

III. Response to soft neutrons

The soft neutron component ($E_n^{kin} < 20$ MeV) plays a crucial role in compensating calorimeters since the number and energy of these neutrons is correlated with the amount of energy lost as nuclear binding energy. For uranium as absorber material typical yields are 33 evaporation neutrons per GeV of hadronic shower energy for $E_{incident} = 10$ GeV [89]. The kinetic energy carried by these soft neutrons amounts to $\approx 12\%$ of the hadronic shower energy. However, if this energy can be converted into a measurable and large signal (i.e. $n/mip \gg 1$) the binding energy loss can be compensated for and $e/h = 1$ can be achieved.

In high Z materials neutrons undergo elastic and inelastic (n,xn) collisions with the target nuclei. In inelastic collisions more neutrons and soft γ's from de-excitation processes are produced, where as before the γ's contribute little to the measurable signal. The last 1-2 MeV of the neutron's energy are predominantly lost in elastic collisions where an energy fraction

$$\langle \Delta E/E \rangle = 1/(A+1) \tag{3.12}$$

is transfered to the target recoil with nuclear number A. Therefore, in the high Z absorbers little energy is lost. However, in materials like plastic scintillators which contain a substantial amount of hydrogen ($A = 1$) the energy transfer is highly effective. The energy spectrum of these recoil protons is very soft with a typical mean free path of 20 μm in scintillator. Therefore, these protons deposit most of their energy via ionization inside the scintillator. In contrast to the energy deposition by other shower components this contribution is not sampled, i.e. it does not scale with the relative thicknesses of readout and absorber media. In a 3.3 mm ^{238}U / 2.6 mm organic scintillator calorimeter neutrons with energies of a few MeV deposit about 50% of their energy in the scintillator (i.e. $R^n(E_n < 20\,\text{MeV}) \approx 0.5$), compared to 10% for mips (i.e. $R^{mip} \approx 0.1$). For fixed scintillator thicknesses the ratio n/mip increases with increasing absorber thickness since the sampling fraction for mips R^{mip} decreases stronger with increasing absorber thickness than the sampling fraction for low energy neutrons $R^n(E_n < 20\,\text{MeV})$. Due to saturation and recombination effects inside the scintillator the light output does not increase linearly with the energy deposition at high ionization densities [90]. Since recoil protons produce high density ionization this reduces the effective signal enhancement. Nevertheless, in effect n/mip values up to 2 can be achieved.

Once neutrons are thermalized they are captured by the surrounding absorber nuclei releasing binding energy in form of γ's of typically 6 MeV. The signal response is suppressed by the small γ/mip ratio at these low energies. In spite of that, due to their large number, neutrons may produce a sizable contribution also in this way. However, the signal due to captured neutrons is delayed by 0.1 - 1 μsec. Therefore, long signal integration times would be needed to include this contribution.

IV. Conclusions

As a result of these considerations, the n/mip ratio of calorimeters with hydrogen in the readout medium depends on the sampling fraction and is in general considerably larger than 1. By tuning the relative thickness of absorber and readout medium one can achieve $e/h = 1$ for certain combinations of absorber and readout materials. Compensation has been achieved with calorimeters using 3.3 mm ^{238}U / 2.6 mm organic scintillator ($e/h \lesssim 1.03$ for $p_h > 2$ GeV [91]) and 10 mm Pb / 2.5 mm organic scintillator ($e/h \approx 1.05$) [92].

3.2.3 Energy resolution

The energy resolution of calorimeters is determined by several factors: sampling fluctuations, intrinsic fluctuations, detector imperfections and, for hadronic calorimeters, deviations of the signal ratio for electrons and hadrons (e/h) from unity. The first two contributions are of statistical nature and therefore scale as $1/\sqrt{E_0}$ with the energy E_0 of the incident particle. The qualitative behavior of sampling fluctuations can be understood as follows. The mean number of ionizations in the readout medium N_{ion} is given by $N_{ion} = R \cdot E_0/E_{ion}$ where E_{ion} is the mean energy deposition required to ionize the readout medium and $R \cdot E_0$ is the energy deposited in the readout medium. The measured signal and thus the reconstructed energy E is proportional to N_{ion}. Poisson statistics thus leads to:

$$\frac{\sigma_E}{E} \sim \frac{\sigma_{N_{ion}}}{N_{ion}} = \frac{1}{\sqrt{N_{ion}}} \propto \frac{1}{\sqrt{E_0}}. \tag{3.13}$$

Intrinsic fluctuations refer to event-to-event variations of the many competing energy loss processes. This adds major contributions to the total energy resolution mainly for hadronic calorimeters, where large fluctuations of the fraction of undetected energy occur (see section 3.2.2). The energy resolution for hadronic particles is therefore inevitably worse than for e.m. showers.

If the e/h ratio differs from 1 (for most calorimeters $e/h > 1$) a term $\sigma_E^{e/h\neq 1}$ is added to the energy resolution of hadronic calorimeters which does not scale with $1/\sqrt{E_0}$. In hadronic showers a strongly fluctuating fraction of energy f_{em} goes into e.m. showers initiated by π^0s (see section 3.2.2). The fluctuations of f_{em} are large and are not suppressed at high incident energies E_0 since the fraction f_{em} for a particular event is mainly determined by the nature of the first interaction of the incoming particle with the calorimeter material. If $e/h \neq 1$ the measured calorimeter signal depends on f_{em} and the fluctuations of f_{em} lead to a contribution $\sigma_E^{e/h\neq 1}/E$ to the total energy resolution which is almost independent of the energy of the incident particle E_0 ($\sigma_E^{e/h\neq 1}/E \sim const(E_0)$). The resolution at high energies E_0 is therefore dominated by $\sigma_E^{e/h\neq 1}$. In addition, the energy dependence of $\langle f_{em}(E)\rangle$ causes non-linearities in the signal response of non-compensating (i.e. $e/h \neq 1$) calorimeters.

Two different strategies facing this problem have been used in high energy calorimeters. The first is based on the observation that the characteristic dimensions of e.m. and hadronic shower components are very different. Software corrections using different weighting factors for narrow and wide showers can be applied for calorimeters with $e/h \neq 1$ and sufficiently high transverse and longitudinal segmentation [85]. The second solution consists in the construction of a compensating calorimeter [86], where $e/h = 1$ is achieved intrinsically by an appropriate choice of type and size of readout and absorber medium (see section 3.2.2). This solution in principle

	e.m. section	hadronic section
absolute calibration uncertainty	5 %	5 %
cell–to–cell variations	5 %	5 %
position resolution for hadrons	1 cm	3 cm
σ_E/E for multihadron systems	$100\,\%/\sqrt{E[GeV]} \oplus 10\,\%$	

Table 3.3: Requirements on the performance of the FPC

offers the best energy resolution. The ZEUS uranium-scintillator calorimeter is compensating with $e/h \lesssim 1.03$.

Various detector deficiencies also contribute to the energy resolution of real calorimeters. Noise in the readout chain mainly affects the low energy measurement ($\sigma_E^{noise}/E \propto 1/E$). Detector non-uniformities ($\sigma_E^{nonunif}/E \propto const(E_0)$) and energy leakage out of the detector volume (in general: $\sigma_E^{leak}/E \propto \log(E_0)$) contribute particularly at high energies.

3.3 FPC requirements and design

3.3.1 FPC requirements

Since the purpose of the FPC is to extend the measurement of the hadronic final state in the ZEUS detector a good capability for hadronic energy measurement at energies ranging from few 100 MeV up to 1 TeV is required. An e/h ratio of 1 is aimed for. The energy resolution requirements, however, are moderate. A hadronic resolution of $\sigma_E/E = 100\ \% \ / \ \sqrt{E[GeV]} \ \oplus \ 10\ \%$[1] was considered to be sufficient. A position resolution of < 3 cm for hadrons is adequate to limit the uncertainty on the transverse momentum measurement. Since a large fraction of the hadronic showers is shared between the FPC and the surrounding FCAL the nuclear interaction length (λ(FPC) = 20 cm) has been chosen to be similar to the FCAL value (λ(FCAL) = 21 cm), which is expected to give a similar longitudinal shower depth in FCAL and FPC. This reduces fluctuations in the shower development. The performance requirements for the FPC are summarized in Table 3.3 [93].

3.3.2 FPC design and construction

The FPC has been built as a lead-scintillator sandwich calorimeter read out by wave length shifter (WLS) fibers and photomultipliers (PMT). This concept has been investigated in [94, 95, 96].

A front view of the FPC is shown in Fig. 3.2. The active part of the FPC has outer dimensions of $192 \times 192 \times 1080$ mm^3. The 63 mm diameter central hole accommodates the new reduced HERA beampipe. The FPC is mechanically subdivided into two identical half modules. They are attached to the bottom and top half parts of the innermost FCAL module, respectively. The FCAL halves and therefore also the FPC halves are moved apart during beam injection in order to reduce the radiation dose on the calorimeters.

[1] Here, $\oplus$ stands for addition in quadrature.

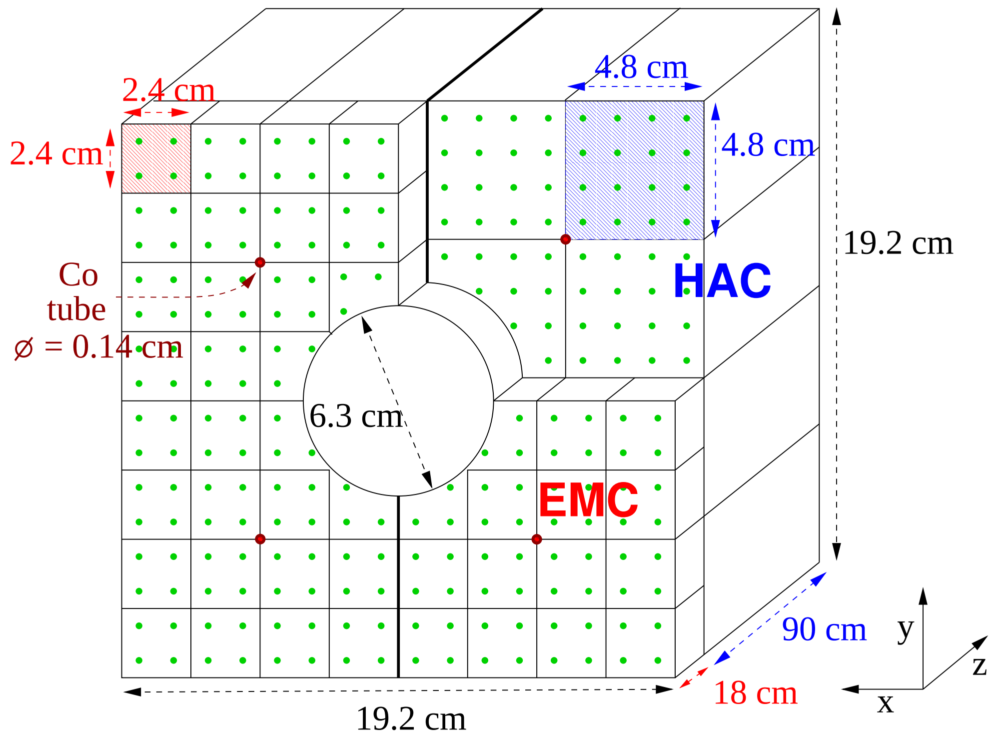

Figure 3.2: Front view of the FPC. The readout cells and the position of WLS fibers are shown. One hadronic readout cell is behind 2×2 electromagnetic cells, except for the cells near the beam hole.

In the FPC, 15 mm thick lead plates alternate with scintillator layers of 2.6 mm. The WLS fibers have a diameter of 1.2 mm and pass through 1.4 mm diameter holes in the lead and scintillator layers. The holes are located on a 12 mm square grid. The FPC has 232 holes of this type. In addition, there are 4 brass tubes (1.4 mm inner diameter) which are used to guide a ^{60}Co source, placed on the tip of a long steel wire, for monitoring the calibration of the FPC cells. Taking into account the WLS fibers and the fiber holes in the lead plates, the effective lead to plastic ratio by volume is 5.2:1. Based on the results obtained with a lead-scintillator

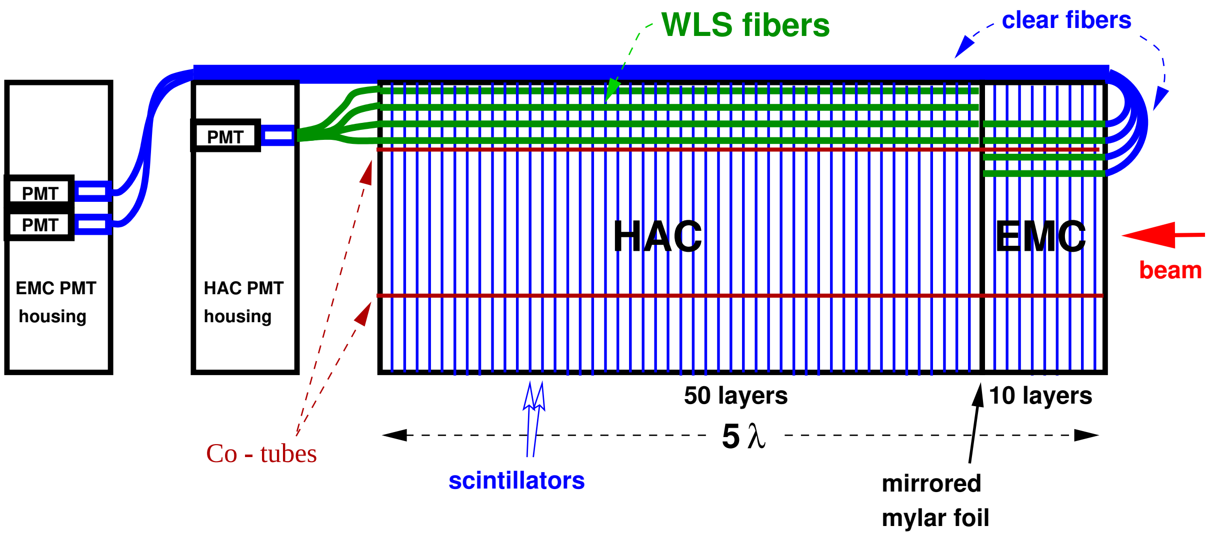

Figure 3.3: Schematic side view of the FPC. The horizontal lines indicate the positions of the WLS fibers and of the tubes for the ^{60}Co source.

	EMC	HAC	total
length [mm]	180	900	1080
layers	10	50	60
X_0	26.5	133.0	159.5
λ	0.9	4.5	5.4
cells	60	16	76
transverse dimensions [mm]	192×192		
layer structure [mm]	Pb: 15, scint: 2.6 tyvek: 0.4		
effective thickness [mm]	Pb: 14.84, plastic: 2.86		
Moliere radius [mm]	20		

Table 3.4: Summary of FPC parameters.

calorimeter of similar composition [92] the FPC is expected to be compensating ($e/h = 1$).

With the chosen layer structure, the radiation length $X_0 = 0.68$ cm and nuclear absorption length $\lambda = 20$ cm are similar to those of the FCAL (viz. $X_0(\text{FCAL}) = 0.74$ cm, $\lambda(\text{FCAL}) = 21.0$ cm).

The FPC is longitudinally subdivided into an electromagnetic (EMC) and a hadronic (HAC) section which are read out separately (see Figs. 3.2 and 3.3). The EMC section consists of 10 layers of lead and scintillator corresponding to 26.5 X_0 and 0.9 λ. The HAC section consists of 50 layers resulting in 5.4 λ for the complete FPC (see table 3.4).

The scintillator layers consist of tiles and form cells which are read out individually (Fig. 3.2). The cell cross sections are 24×24 mm^2 in the EMC, commensurate with the Moliere radius of 2 cm, and 48×48 mm^2 in the HAC section. The 8 (4) innermost cells in EMC (HAC) surrounding the beam hole follow the circular shape given by the beam hole.

The polystyrene based scintillator SCSN81T2 from Kuraray was chosen in order to optimize light yield and achieve good radiation stability [97]. The scintillator tiles were wrapped with 0.2 mm thick tyvek paper in order to improve the light collection efficiency and suppress light coupling between neighboring cells.

The WLS fibers of the EMC are connected to clear fibers (1.4 m length) which transport the light to the PMTs placed behind the FPC (Fig. 3.3). The clear fibers are bent by 180° at the front of the EMC, and are guided to the PMTs in the rear by two ducts situated on either side of the FPC. The WLS fibers of the HAC section transport the light directly to the PMTs. All 4 (16) fibers corresponding to an EMC (HAC) cell are connected to the same PMT through a light-mixing bar in order to smooth non-uniformities at the PMT surface. An additional fiber is connected to each PMT through the same light-mixer bar in order to inject LED and laser light pulses used to monitor the stability of the PMTs and the readout electronics. At the other end of the WLS fibers a reflective aluminized mylar foil is placed to avoid light losses. The total number of readout channels is (EMC + HAC): 60 + 16 = 76.

For the WLS fibers the material Y11200(dc) from Kuraray has been chosen. It has a polystyrene core and a double cladding (PMMA and fluorinated PMMA) which produces a substantial increase in light output compared to a single clad fiber. Its absorption spectrum matches well the SCSN81T2 emission spectrum.

Hamamatsu R5600U PMTs are used in the FPC. This PMT type which uses metal channel dynodes is relatively insensitive to magnetic fields and its small dimensions ($16 \times 16 \times 16$ mm^3)

are well suited for the limited space available around the hole of the FCAL. Tests done prior to the FPC construction showed that it fulfills well the constraints on dynamic ranges placed by the required FPC performance in the HERA environment [93]. The mean number of photoelectrons (pe) for the FPC was measured with the LED to be 45 pe/GeV for the EMC and 55 pe/GeV for the HAC section [98].

The PMTs are placed inside ARMCO magnetic iron blocks whose shape and transverse size is similar to that of the lead plates. This reduces the magnetic field at the PMT position such that the PMT response is not affected by the magnetic field inside the ZEUS detector. This had been tested using an FPC prototype [103]. The blocks are placed behind the hadronic section (see Fig. 3.3). The EMC PMTs are arranged in their support frames in such a way that they do not line up with their respective calorimeter cell. This avoids that muons traversing the FPC create Cherenkov light in the light-mixing bar corresponding to the EMC cell they have hit.

After the installation in ZEUS, the PMTs have been connected to a high voltage system based on a Cockroft-Walton generator [99]. At a typical operation voltage of 900 V an average charge of 4.4 pC arrives at the front end electronics per 1 GeV deposited energy.

The readout system of the FPC uses the design developed for other ZEUS calorimeter subcomponents [100], which itself closely follows the concept originally developed for the main ZEUS calorimeter [101]. The FPC PMT pulse is sent to a trigger sum card where 20% of the charge is split off and is used in the first level trigger [102]. The remaining signal is integrated and shaped in the analog cards. Due to the large dynamic range required a high and a low gain signal are provided and processed. The shaped signal is then sampled at a rate of 96 ns synchronized with the HERA bunch crossing and stored in a 5 μs deep analog pipeline. In case of a positive GFLT trigger decision 8 samples per FPC channel are digitized in a 12 bit ADC. These allow a precise reconstruction of the integrated PMT charge and the signal arrival time (time resolution < 1 nsec).

Chapter 4

Detector Simulation

4.1 Simulation of the FPC measurements performed at CERN

For the analysis of the CERN-test data the FPC has been simulated with a detailed Monte Carlo program (MC) using the GEANT 3.21 package [78]. GEANT is a general purpose MC which allows the simulation of all relevant physics processes for electromagnetic, muonic and hadronic interactions in arbitrary geometries of any element or compound. The simulated energies range from 10 keV to 10 TeV.

The FPC has been implemented as a sampling calorimeter consisting of scintillator and absorber layers (section 3.3.2). The density of the absorber layers has been adjusted in order to account for the tyvek layer and for the holes left for the WLS fibers. The fibers have not been included in the simulation. Saturation and recombination effects inside the scintillator are taken into account according to the model by Birks [90]. The light attenuation in the WLS fibers is taken into account using the measurement of the attenuation function $f_{att}(z)$ with the ^{60}Co source as described in section 5.8.3. The scintillator signal S_{sci} is thus given by:

$$S_{sci} = \int f_{att}(z) \cdot E_{sci}(z) dz, \tag{4.1}$$

where $E_{sci}(z)$ is the energy deposited in the scintillator at a given z position. Photostatistics and electronic noise are simulated by appropriate smearing with a Poisson and a Gaussian distribution. The cross talk has also been included according to the measurements (see section 5.3). In the simulation, the FPC has been positioned between FCAL modules as in the CERN-test setup described in section 5.1 (see also Fig. 5.1).

For the simulation of the reconstructed energy E_{rec}^{MC} the effective attenuation length λ_{att} and the sampling fraction R have been defined as:

$$\lambda_{att} = \frac{\int f_{att}(z) \cdot E_{sci}(z) dz}{\int E_{sci}(z) dz} \tag{4.2}$$

and

$$R = \frac{\langle E_{sci} \rangle}{\langle E_{sci} \rangle + \langle E_{abs} \rangle} \ , \tag{4.3}$$

where $\langle E_{sci} \rangle$ and $\langle E_{abs} \rangle$ are the mean energies deposited inside the scintillator and the absorber of the FPC. Using these definitions, E_{rec}^{MC} is given by:

$$E_{rec}^{MC} = \frac{1}{R \cdot \langle \lambda_{att} \rangle} S_{sci} \ , \tag{4.4}$$

where $\langle \lambda_{att} \rangle$ is the mean of λ_{att} for a given particle type and energy.

The accuracy of the simulated response to electrons and muons has been estimated to be about 3%. For pions the accuracy of the simulated energy signals, which have been determined with the hadronic package GHEISHA [79], is about ±10%.

4.2 Monte Carlo simulation of the ZEUS detector

The ZEUS detector simulation package MOZART [65] provides a description of all major detector components. The ZEUS trigger decision is based on the signals from the detector components and is simulated by the program ZGANA.

The MOZART program uses the general purpose simulation packages GEANT 3.13 and GHEISHA. In order to describe the test beam data measured with the CAL modules, some modifications have been implemented. In particular, GEANT 3.13 + GHEISHA failed to describe correctly the measured e/h ratio and the energy resolution of hadrons showing discrepancies up to 30% [80]. Two fast, tunable shower terminators have been developed [81], which have been adjusted to describe the testbeam data with an agreement of better than 5%. The E/M terminator operates on e^-, e^+ and γ with kinetic energies below 200 MeV. The neutron terminator acts on the evaporation energy of excited nuclei and on neutrons with kinetic energies below 50 MeV. These shower terminators reduce the execution time of the simulation program by a factor ~ 15.

The FPC has been implemented in the MOZART package using the same type of shower terminators. Since the internal structure of the FPC is different from that of the CAL, a different set of parameters [1] has been chosen. In order to compare this simulation program to test beam data, the FCAL geometry in MOZART has been adjusted to the CERN test setup (section 5.1). Figure 4.1 shows the comparison of the mean energy deposition in FPC and FCAL as a function of incident beam energy. Good agreement for all combinations is observed. Note that only $\sim 92\%$ of the beam energy is recovered; the remaining 8% are lost mainly due to energy leakage into uninstrumented regions above and below the FPC in the CERN test setup. The comparison for the energy resolution is shown in Figure 4.2. The measured FPC energy resolution is reasonably well described by the MC. When adding the FCAL prototype signal to the FPC signal small discrepancies in the order of 5-10% are found.

[1] Tunable parameters are: sampling fraction and resolution for E/M and neutron terminators as well as the mean free path for the neutron terminators

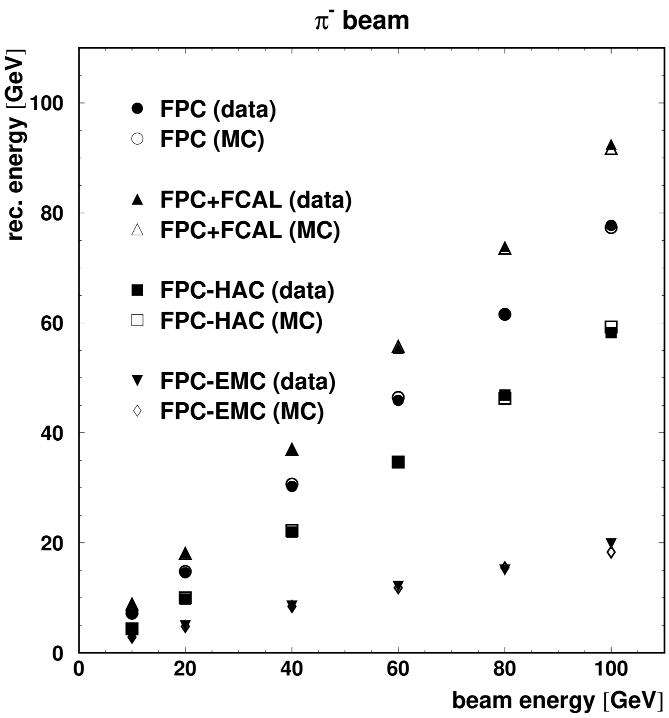

Figure 4.1: The mean of the reconstructed energy in FPC, FPC+FCAL, FPC-HAC and FPC-EMC for π^- is shown as a function of the beam energy. The results of the Monte Carlo for the CERN-test geometry (see Fig. 5.1) are shown in comparison with test beam data.

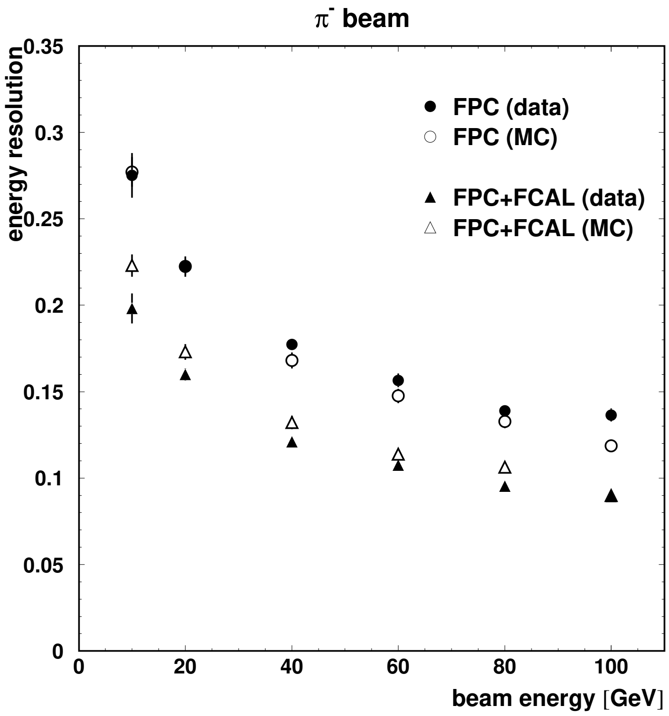

Figure 4.2: The energy resolution for π^- in FPC and FPC+FCAL prototype is shown as a function of the beam energy. The results of the Monte Carlo for the CERN-test geometry are shown in comparison with test beam data.

Chapter 5

Calibration and performance of the FPC

The performance of an FPC-type calorimeter was first tested with a prototype of the FPC. The prototype is identical in design to the final FPC and corresponds to one half of an EMC section. The readout system was instrumented for a 3×3 cluster of cells and tested at DESY in spring 1997 with electron beams ranging from 1 to 6 GeV [103].

In September 1997, prior to the installation in ZEUS, the completely equipped FPC was tested at CERN using electron, muon and pion beams covering an energy range from 10 to 100 GeV [106]. The performance parameters of the FPC have mainly been determined based on the CERN test beam. Low energy data from the DESY test beam has been used where appropriate.

5.1 CERN Test beam setup

The CERN beam test of the FPC was performed at the X5 beam of the SPS [104]. The FPC was installed between modules of the FCAL prototype, see Fig. 5.1. These uranium-scintillator calorimeter units are similar to the ones installed in ZEUS [91] (see section 2.2.2). This setup allowed the energy sharing between FPC and FCAL to be studied.

The combined FPC and FCAL prototype setup was placed on a structure, which could be moved in the X and Y directions in order to vary the impact point of the particle beam at the calorimeter. The beam line defined the Z direction.

A Delay Line Wire Chamber (DLWC) in front of the FPC provided precise information on the charged particle position (see Fig. 5.2). The relative position of the FPC detector with respect to the DLWC coordinates has been established to within about 1 mm. Cuts on DLWC coordinates were used in the offline analysis in order to select particles hitting a given region of the detector.

A defocused beam was used to obtain events covering a wide region of the FPC. The trigger was defined by requiring signals in both scintillator counters (b_1 and b_2) placed in front of the FPC. Behind the FPC an additional counter (b_5) was installed mainly for offline identification of muons.

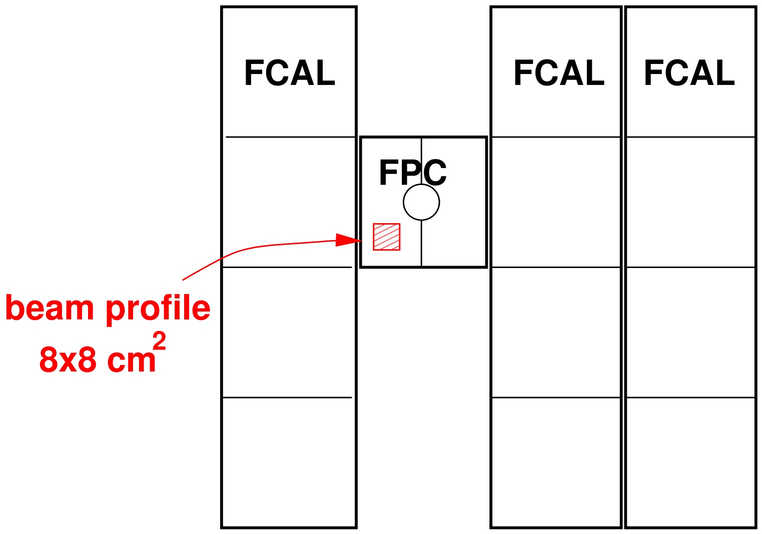

Figure 5.1: Front view of the FPC at the test beam site, surrounded by three FCAL modules.

5.2 FPC Calibration

The calibration of the FPC requires the determination of the pC-to-GeV conversion factors which relate the PMT signals (in pC) to the energy deposited in the corresponding FPC cells. Since hadronic showers are in general not fully contained in the FPC alone, the energy deposits detected in the FPC and the surrounding FCAL modules have been added appropriately. After calibration, the reconstructed energy in the FPC corresponds to the particle energy deposited in the FPC which is typically less than the original particle energy, the side-leaking energy being measured with the FCAL.

The calibration has been performed using the CERN test beam data. Since no adequate reference signal is available to calibrate the FPC in the ZEUS environment, this calibration has also been used after the installation of the FPC in ZEUS. This is justified by the fact that the identical readout system has been used in the testbeam and in the ZEUS environment and the same ^{60}Co source is used to monitor the stability of the calibration in the testbeam and after installation in ZEUS (see section 5.8.1).

The HV setting of the PMTs was determined at the beginning of the CERN test beam and has since been kept constant. The HV values were tuned such that equal signal responses to monoenergetic electron (muon) beams were obtained in all EMC (HAC) channels. The

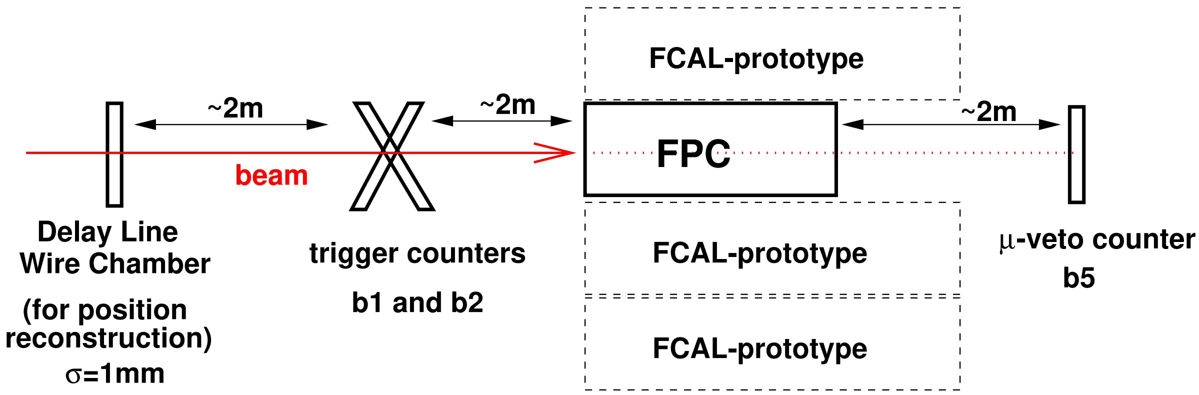

Figure 5.2: Top view sketch of the beam test setup.

absolute calibration and a more precise cell-to-cell calibration for EMC and HAC channels has been obtained offline as described below.

5.2.1 Calibration of the EMC section

A data set obtained with 60 GeV beam electrons distributed over the complete FPC surface has been used for the calibration of the EMC cells. In an iterative procedure the calibration constants c_i have been adjusted such that the mean of the reconstructed energy

$$E_{FPC} = \sum_{i \in cells} c_i \cdot S_i^{raw}, \tag{5.1}$$

where S_i^{raw} is the measured PMT charge corresponding to cell i, is independent of the point of incidence. The absolute calibration has been adjusted to the beam energy. For the edge cells correction factors of 2 - 5 % have been applied which effectively reduce the beam energy taking into account the energy leaking out of the FPC as estimated by MC (section 4.1).

The uncertainty on the EMC calibration is dominated by statistics and is estimated to be 2%.

5.2.2 Calibration of the HAC section with muons

Since the shower of pions is not fully contained in the FPC and the amount of leakage is not reliably described by the available MC, 100 GeV muon test beam data has been used for the calibration of the HAC cells. The absolute energy scale for muons also has been established with MC. The uncertainty in the simulation of muons is smaller than for pions.

The response to 100 GeV muons has been simulated with the MC described in section 4.1. Equation 4.4 has been used for the simulation of the reconstructed energy E_{rec}^{MC}. The sampling fraction R required in Eq. 4.4 has been determined with electrons. The MC uncertainty on R for hadrons is of the order of 10%. Assuming that the FPC is compensating ($e/h = 1$), the sampling fraction for electrons and hadrons have to agree.

In the HAC section the mean effective attenuation $\langle \lambda_{att} \rangle$ due to the WLS fibers is substantially different for muons and pions. While muons deposit energy practically uniformly along their path, pions, on average, deposit a large fraction of the energy at the beginning of the HAC section. Since the WLS fibers are read out at the end of the HAC section the attenuation effect is larger for light produced at the beginning of the HAC section than for light produced at the end of the HAC section. Fig. 5.3 shows the λ_{att} distribution in the HAC section for 100 GeV muons and 20 GeV pions as well as the dependence of λ_{att} on the incident particle energy. In order to optimize the hadronic energy measurement $\langle \lambda_{att} \rangle$, as determined for 20 GeV pions, has been applied in the simulation used for the calibration of the HAC section.

For a sample of 100 GeV muons hitting the FPC at the center of each HAC cell the summed signal of all HAC cells has been studied. The distributions have been fitted to a Landau function convoluted with a Gaussian function, which takes into account photostatistics and electronic noise. The calibration constants have been computed in order to adjust the peak values - obtained from a fit of data signals - to the peak values determined with a fit to E_{rec}^{MC}.

Since the distribution of the muon signal is not Gaussian (see Fig. 5.4), the ratio of the mean and the peak value depends on the exact shape of the distribution. Therefore, it is crucial that

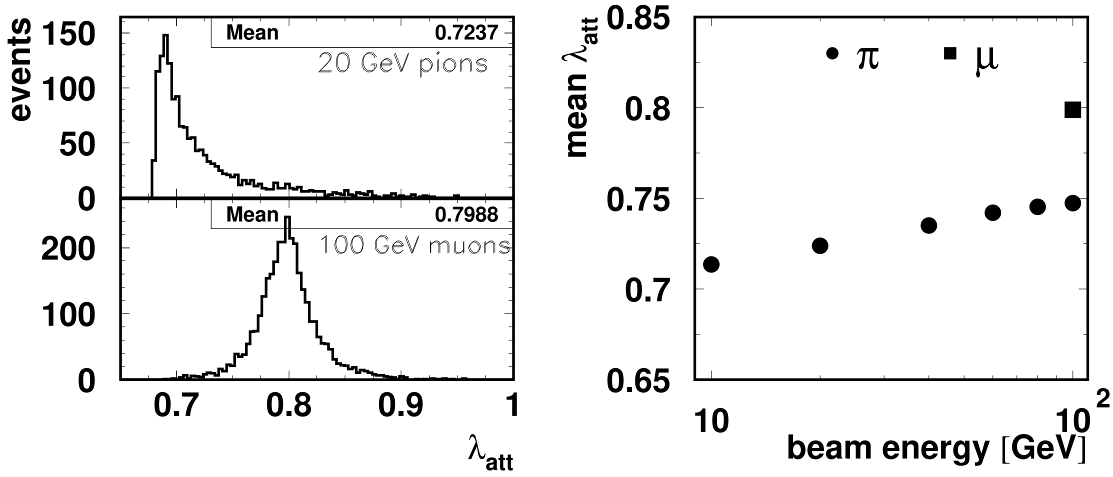

Figure 5.3: left: The distribution of the effective light attenuation in the WLS fibers in the HAC section λ_{att}^{HAC} is shown for 100 GeV muons and 20 GeV pions. right: The mean λ_{att}^{HAC} value is plotted as a function of the incident beam energy.

the shape is well described by the MC. After calibration, a good overall agreement is observed for the HAC section, as can be seen in Fig. 5.4.

The calibration method presented above assumes that the FPC is compensating ($e/h = 1$). According to measurements with calorimeters of similar type [92] and the analysis of pion test beam data (section 5.2.3) the deviation of e/h from unity is estimated to be 5% or less.

Ignoring the uncertainty on the e/h ratio the accuracy of the absolute calibration of the HAC section has been estimated to be 5%. This error is dominated by the uncertainty on the MC

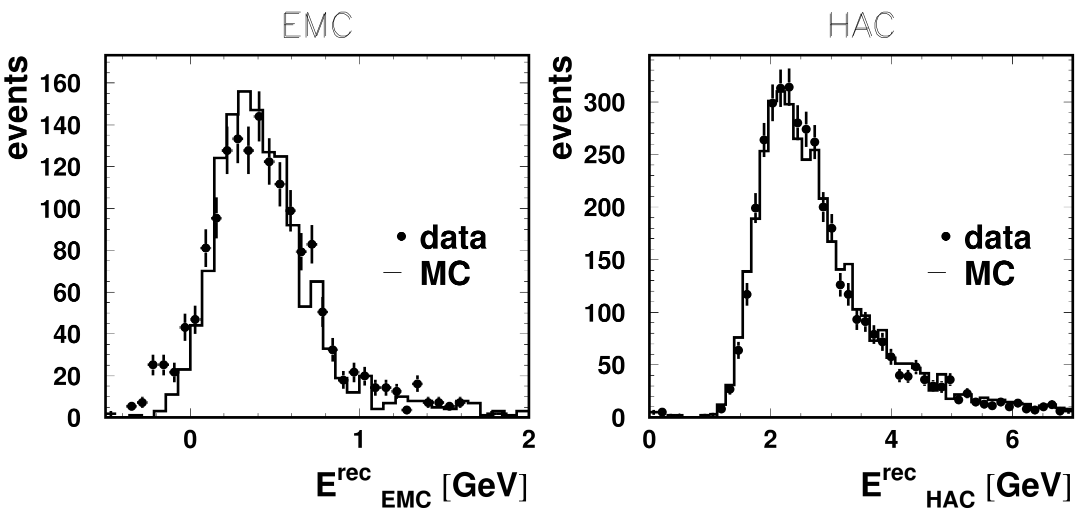

Figure 5.4: The reconstructed energy measured in the EMC and HAC sections of the FPC for 100 GeV muons is shown for data (points) and MC (histogram).

prediction for the relative signal of muons and electrons.

5.2.3 Calibration cross check using pion data

The calibration of the HAC section using muon data involves some uncertainties since it uses a MC. As a cross check, an independent calibration scheme using pion test beam data has been developed [107].

In the case of a hermetic calorimeter which fully contains hadronic showers the initial beam energy E^{beam} can be reconstructed as:

$$E^{beam} = D(E^{EMC} + C_{HAC} \cdot E^{HAC}) \tag{5.2}$$

where E^{EMC} is the reconstructed energy in the EMC section using the calibration obtained with electrons, E^{HAC} is the uncalibrated energy in the HAC section, C_{HAC} is the HAC calibration constant and $D = (e/h)^{-1}$ takes into account the different response to electrons and hadrons.

Since the FPC is non-hermetic, E^{beam} should be replaced by the energy deposited inside the FPC: E^{dep}. The energy leaking out of the FPC (E^{leak}) and thus $E^{dep} = E^{beam} - E^{leak}$ has to be determined using simulations.

In Eq. 5.2 the two quantities D and C_{HAC} are unknown. Therefore, the pion data sample has been split into two subsamples of approximately equal size, separating hadronic cascades starting in the EMC section (sample 1) from those starting in the HAC section (sample 2). This can be achieved with a cut on E_{EMC}. Fig. 5.5 shows the distribution of E_{EMC} for 40 GeV pions. The Landau type peak at $E_{EMC} \sim 0.5$ GeV is due to the ionization of pions which do not start a hadronic cascade inside the EMC section (sample 2).

In the resulting system of equations:

$$\begin{aligned} D_1(E_1^{EMC} + C_{HAC} \cdot E_1^{HAC}) &= E_1^{dep} \\ D_2(E_2^{EMC} + C_{HAC} \cdot E_2^{HAC}) &= E_2^{dep} \ , \end{aligned} \tag{5.3}$$

the energy leakage and thus E^{dep} depend on the sample type since more energy tends to leak out of the back of the FPC for late showering hadrons. The difference between D_1 and D_2, which in fact is small, can be understood as follows: the relative contributions of the different shower components, namely electromagnetic, charged hadrons and neutrons, depend on the shower depth and are therefore different for the two samples. Since the calorimeter response to the different components differs (see section 3.2.2) this affects the factor D. Equation 5.3 gives:

$$C_{HAC} = \frac{rE_2^{EMC} - E_1^{EMC}}{E_1^{HAC} - rE_2^{HAC}} \ , \tag{5.4}$$

where $r = E_1^{dep}/E_2^{dep} \cdot D_2/D_1$. The quantity r has been determined using the three different codes for the simulation of hadronic interactions accessible in the framework of GEANT [78]: GHEISHA, FLUKA and CALOR. When calculating r, the uncertainties on the prediction of E_i^{dep} which are in the order of 10% cancel to a large extent.

The value of C_{HAC} has been determined for various pion beam energies confirming the calibration obtained with muon data as described in section 5.2.2 within 3%, independent of the beam energy. The systematic uncertainties due to the input from simulation is estimated to be in the order of 3%.

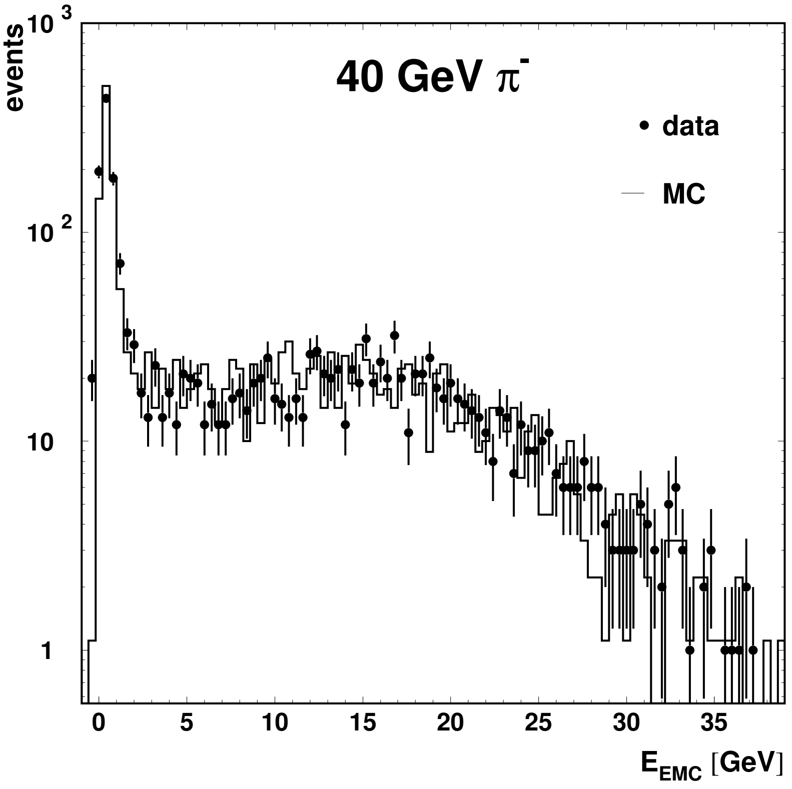

Figure 5.5: Distribution of the FPC EMC response to 40 GeV pions. The Monte Carlo histogram has been produced with the GHEISHA hadronic package.

I. Estimate of e/h

The method presented above allows to estimate the value of e/h. For the complete pion sample a slightly overcompensating value of $e/h = 0.95 \pm 0.03$ has been obtained. However, it should be stressed that in case of the FPC, which is not a hermetic calorimeter, the meaning of e/h is not the ratio of the response to electrons and pions of the same energy. It rather refers to the relative efficiencies for electrons and hadrons of converting energy deposited inside the calorimeter into a measurable signal.

5.3 Cross talk

A cross talk effect has been observed between physically adjacent cells of the FPC in the analysis of the CERN-test data. No cross talk between PMTs or front-end electronic channels has been found. The observed cross talk has therefore been attributed to light being produced in one cell, crossing the tyvek barrier between scintillator tiles and entering the WLS fibers of a neighboring cell. It is known that tyvek is not totally light tight.

The cross talk has been measured using beam muons hitting the 8×8 mm^2 center of each cell. For all pairs of neighboring cells the ratio between the signal of the cell that has been hit and

	EMC	HAC
central cell	73%	81%
each of 4 direct neighbors	5.8%	4.3%
each of 4 diagonal neighbors	1%	0.4%

Table 5.1: The cross talk between neighboring FPC cells is given as the fraction of light collected in the central cell and in the adjacent ones.

the signal in the adjacent cell has been determined. The mean value of this distribution has been taken as the amount of cross talk.

For light produced in the scintillator of a given cell (denoted as the central cell) the fraction of light collected in that same cell and the adjacent cells is shown in Table 5.1.

Using the calibration method described in the previous section, the cross talk affects the lateral shower distribution. The total reconstructed energy, however, is not affected. In order to describe the lateral shower width, the measured cross talk has been implemented in the MC.

5.4 Signal response to electron, muon and pion beams

An outstanding feature of the FPC is the capability to measure electromagnetic and muonic as well as hadronic particles over a wide kinematic range.

5.4.1 Response to electrons

Electron beam data in the energy range between 10 GeV and 100 GeV has been studied. A sample of electrons hitting the FPC uniformly across the 24×24 mm^2 area of an EMC cell has been selected for each available energy. The signal distribution of the reconstructed energy in the EMC section is shown in the top plot of Fig. 5.6 for various beam energies. The distributions have an almost Gaussian shape with some distortions due the effects induced by the WLS fibers (see section 5.7.2). In Fig. 5.7 the fitted Gaussian mean is plotted as a function of beam energy. It is found that 91% of the energy is contained in a 3×3 EMC cell cluster centered around the point of incidence and 99% of the energy is contained in the EMC section of the FPC. About 1% of the energy leaks into the HAC section. The mean signal response scales linearly with the beam energy. In the lower part of Fig. 5.7 the deviations from linearity are plotted, showing agreement with linearity at the level of 1%.

5.4.2 Response to pions

During the CERN beam test, data was taken with negatively charged pions in the energy range between 10 GeV and 100 GeV. The π^- beam had a substantial muon contamination. These muons have been rejected from the data sample by applying the following cuts:

- $E_{b5} < 0.25$ mip
- $E_{FPC} > 0.25 \cdot E_{beam}$

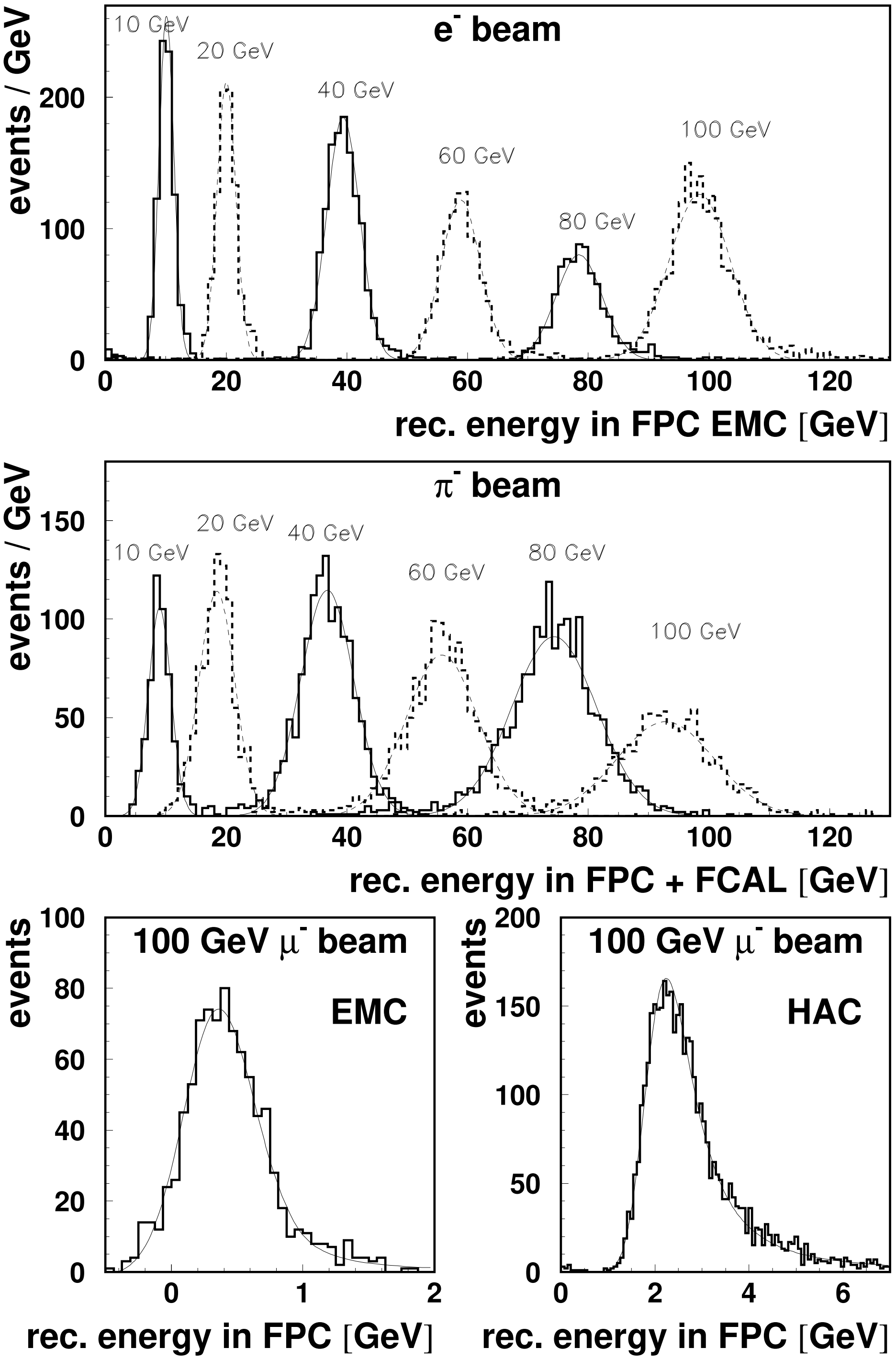

Figure 5.6: The signal distribution of the FPC response to electron, pion and muon test beams is shown. For electrons the reconstructed energy in the EMC section is plotted. For pions the energies in FPC EMC and HAC and in the neighboring FCAL modules have been added. The lower plots show the reconstructed energy for 100 GeV muons separately for the EMC and HAC section.

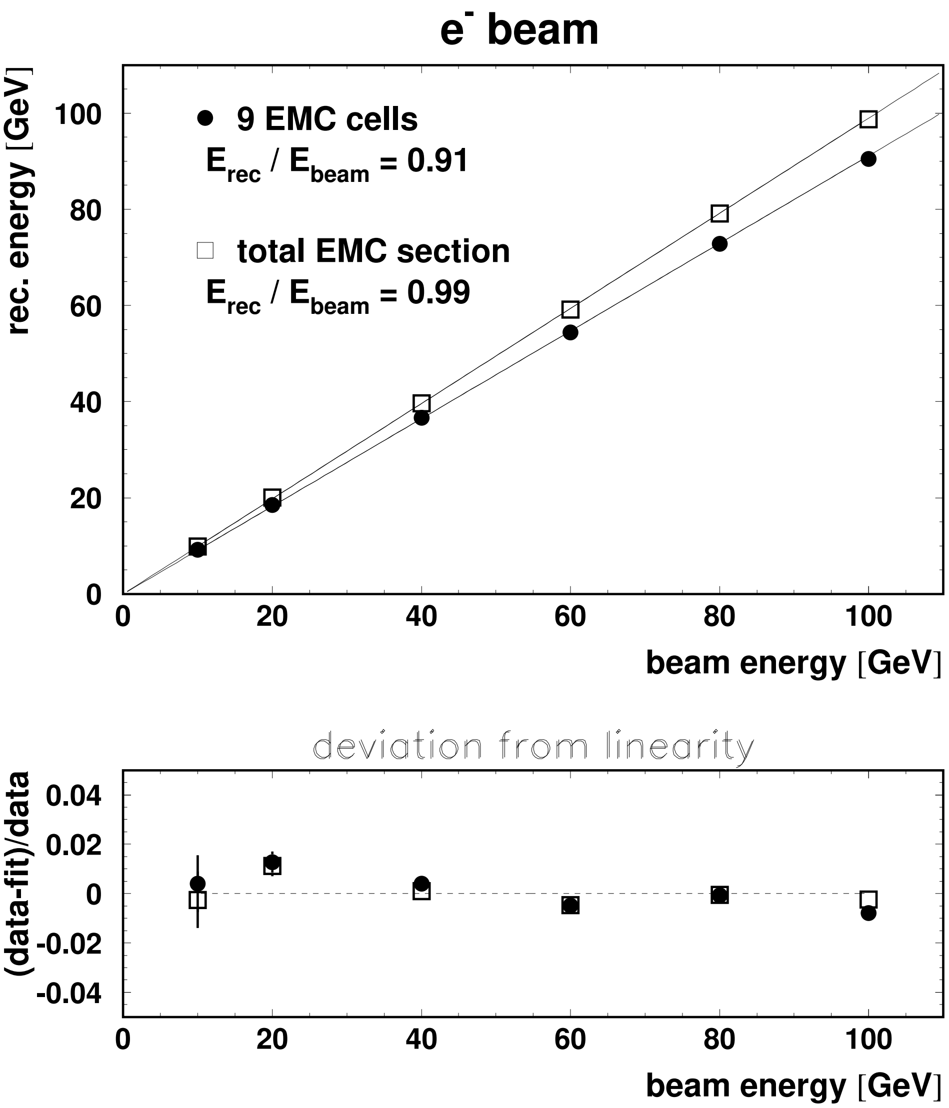

Figure 5.7: The Gaussian mean of the energy measured for electrons in 3×3 cells of the EMC section of FPC and in the complete EMC section are plotted as a function of the beam energy. The lower plot shows the deviations from linearity.

where E_{b5} is the signal measured in scintillating counter b_5 behind the FPC (see Fig. 5.2), 1 mip is the most probable signal deposited in b_5 by a minimum ionizing particle and E_{FPC} is the total energy measured in the FPC. While muons traverse the FPC and induce a mip signal in the b_5 counter, hadronic showers are in general stopped inside the FPC and do not produce a signal in the b_5 counter. However, for high energy hadrons some part of shower may leak out of the back of the FPC. From MC studies it is expected that the ratio of pions that produce a signal in the b_5 counter increases from 0.5% at $E_\pi = 10$ GeV to $\sim 15\%$ at $E_\pi = 100$ GeV.

The π^- signal in the FPC as well as in the FCAL prototype modules has been studied. The distribution of the summed reconstructed energy for FPC + FCAL prototype is shown in the central plot of Fig. 5.6 for different π^- beam energies. The mean of the reconstructed energy measured in FPC + FCAL prototype, FPC alone and FPC HAC is plotted as a function of the

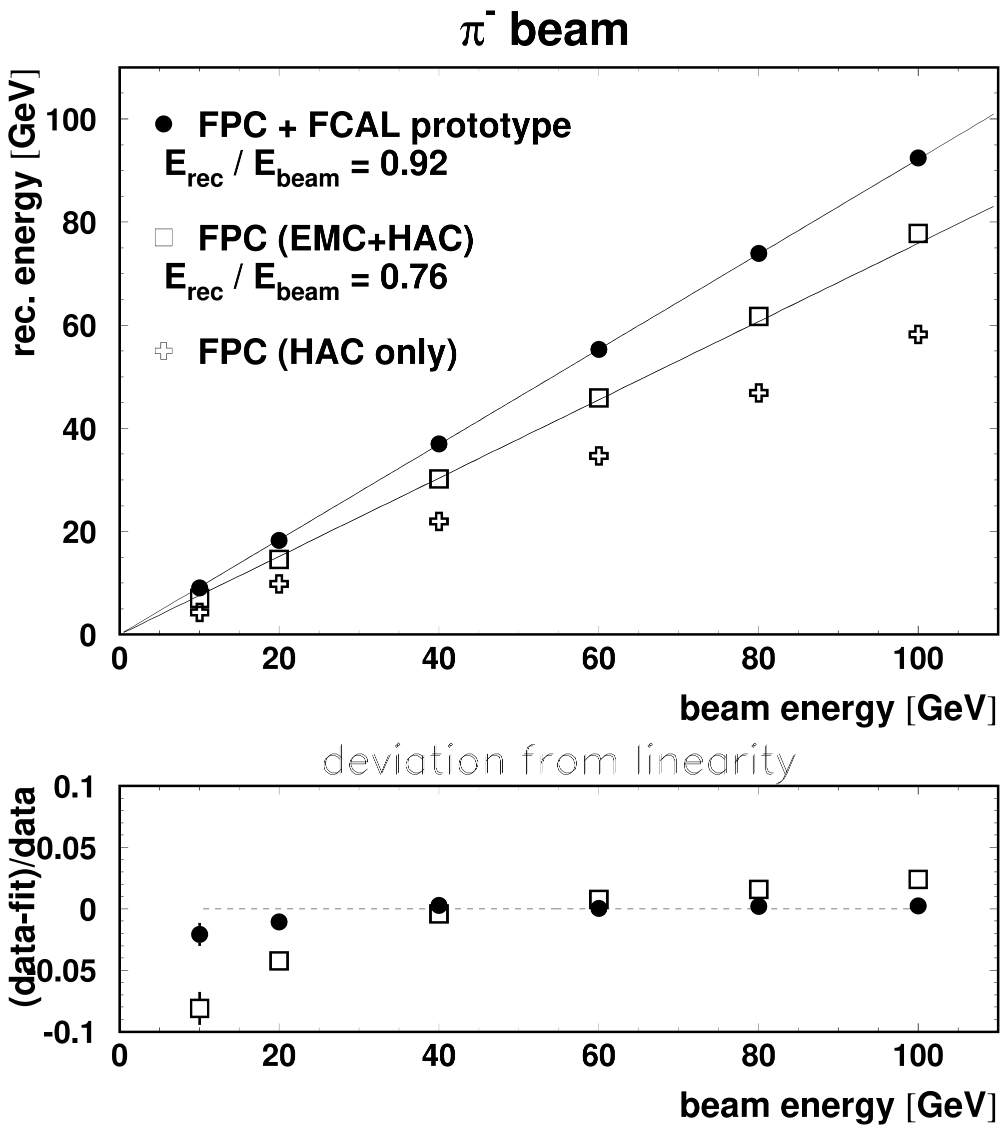

Figure 5.8: The mean energy measured for π^- in the HAC section of FPC, in the complete FPC and in the FPC + FCAL prototype modules are plotted as a function of the beam energy. The lower plot shows the deviations from linearity for FPC alone and of the total FPC + FCAL prototype signal.

beam energy in Fig. 5.8. While only about 76% of the energy is deposited inside the FPC, 92% of the energy is found when adding the signals from FPC and FCAL prototype. A study using the MC described in section 4.2 showed that the missing energy is mainly lost into the vertical gap between the FCAL prototype modules (see Fig. 5.1). In the ZEUS environment where the FPC is completely surrounded by FCAL modules the full energy of the incident particle is reconstructed in FPC + FCAL (see Fig. 5.11).

A linear rise of the measured signal with the beam energy is observed for the combination of FPC + FCAL prototype. The deviations from linearity are smaller than 3% (see Fig. 5.8 bottom). If only the FPC is considered the deviations reach 8% at energies near 10 GeV.

5.4.3 Response to muons

The FPC signal response to muons has been studied with a beam of 100 GeV muons. Since the energy loss of muons at energies below 100 GeV is dominated by QED processes [84] it can accurately be related to that of minimum ionizing particles. The dependence of the deposited energy on the incident particle energy is small. In lead 100 GeV muons deposit $\sim$ 2.5 times more energy than 1 GeV muons [84].

The distributions of the reconstructed energy measured in the EMC and HAC of the FPC are shown in Fig. 5.6(bottom). Since the energy loss of muons is mainly due to ionization the distributions have a Landau shape [105]. A Landau function convoluted with a Gaussian function, which takes into account photostatistics and electronic noise, has been fitted to the muon signals. The peak values were found to be 300 and 2200 MeV for the EMC and HAC section, respectively. Naively, one might expect that the ratio of the energies in HAC and EMC scales with the longitudinal depth of each section, i.e $E_{HAC}/E_{EMC} = d_{HAC}/d_{EMC} = 5$. There are two reasons for the observed deviation from this simple scaling behavior. Firstly, the peak value of a Landau distribution does not scale with the material thickness since the ratio of the peak and the mean value of a Landau type distribution depends on the thickness of the material. Secondly, high energy muons have small e.m. shower contributions initialized by high energetic knock-on electrons. These need some path to develop and the deposited energy is therefore somewhat delayed leading to a larger energy deposit in the HAC section.

Since the FPC has been calibrated with electrons which have a different sampling fraction than muons (see section 3.2.1) the reconstructed energy is higher than the energy deposited by the muon. The reconstructed energy E^{μ}_{rec} is related to the deposited energy E^{μ}_{dep} via $E^{\mu}_{dep} = e/\mu \cdot E^{\mu}_{rec}$.

5.5 Energy resolution

5.5.1 Energy resolution for electrons

Data from the CERN test beam as well as low energy data taken with the FPC prototype in the DESY test beam have been used for the study of the electron energy resolution of the FPC. Electrons hitting the FPC uniformly across the 24×24 mm^2 surface of a complete EMC cell have been selected. The signals of a cluster of 3×3 EMC cells centered around the point of incidence have been added. The energy resolution σ_E/E has been determined as the ratio of the root mean square (RMS) and the mean of the signal distribution. It takes into account the tail in the signal distribution which results from a signal enhancement around the WLS fiber region discussed in section 5.7.2. The solid points in Fig. 5.9 show the energy resolution as a function of beam energy. The data is fitted to the quadratic sum of a sampling and a constant term:

$$\frac{\sigma_E}{E} = \frac{a}{\sqrt{E}} \oplus b, \tag{5.5}$$

where E is in GeV. The result of this fit is a = 0.34 GeV$^{1/2}$ and b = 0.07.

In order to measure the intrinsic energy resolution neglecting the nonuniformities due to the WLS fibers, electrons hitting an 8×8 mm^2 area at the center of one EMC cell have been selected. In this way the beam impact point is kept away from WLS fibers. Since the resulting

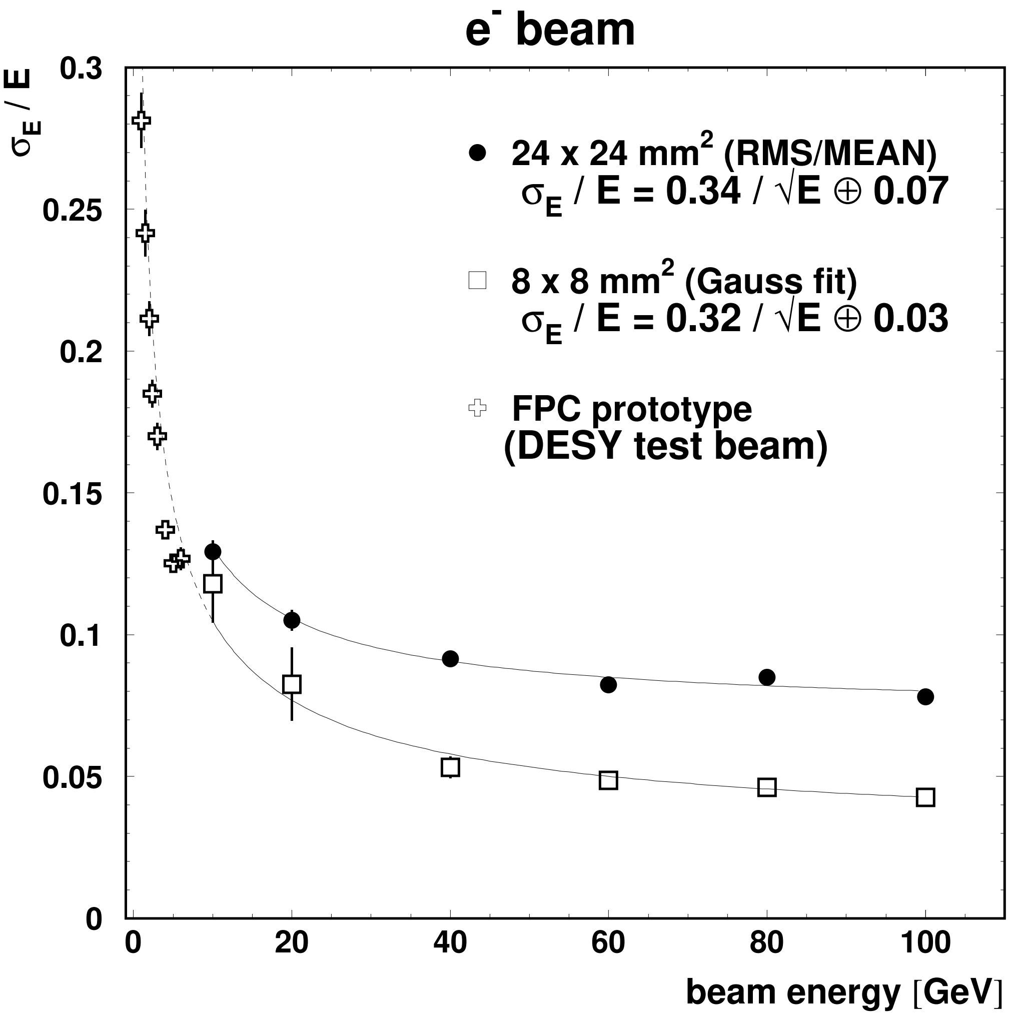

Figure 5.9: FPC energy resolution for electrons. For the solid points the energy resolution is calculated as the ratio RMS/MEAN of the signal distributions from electrons hitting the FPC uniformly across an EMC cell (24×24 mm^2). The open points are obtained from a Gaussian fit using electrons hitting a 8×8 mm^2 square at the center of an EMC cell. FPC prototype data is shown for comparison.

signal distribution is Gaussian, the ratio $\sigma/mean$ of a Gaussian fit has been used for the energy resolution. The result is plotted as open points in Fig. 5.9 as a function of beam energy. Fitting the data to Eq. 5.5 results in: a = 0.32 GeV$^{1/2}$ and b = 0.03. As expected, the constant term is significantly reduced.

The energy resolution points determined at low energies with the FPC prototype have not been included in the fit shown in Fig. 5.9. They are systematically below the fitted curve. A fit to the FPC prototype data (not shown) yields a sampling term of a = 0.30 GeV$^{1/2}$. Since the fibers connecting the scintillator tiles with the PMTs are much shorter in the FPC prototype [103], the light is less attenuated and thus the contribution of photoelectron statistics to the energy resolution is reduced. The fluctuations due to photoelectron statistics have been studied using LED data. For the FPC EMC cells an average value of 45 photoelectrons per 1 GeV reconstructed energy has been measured. This corresponds to a contribution to the

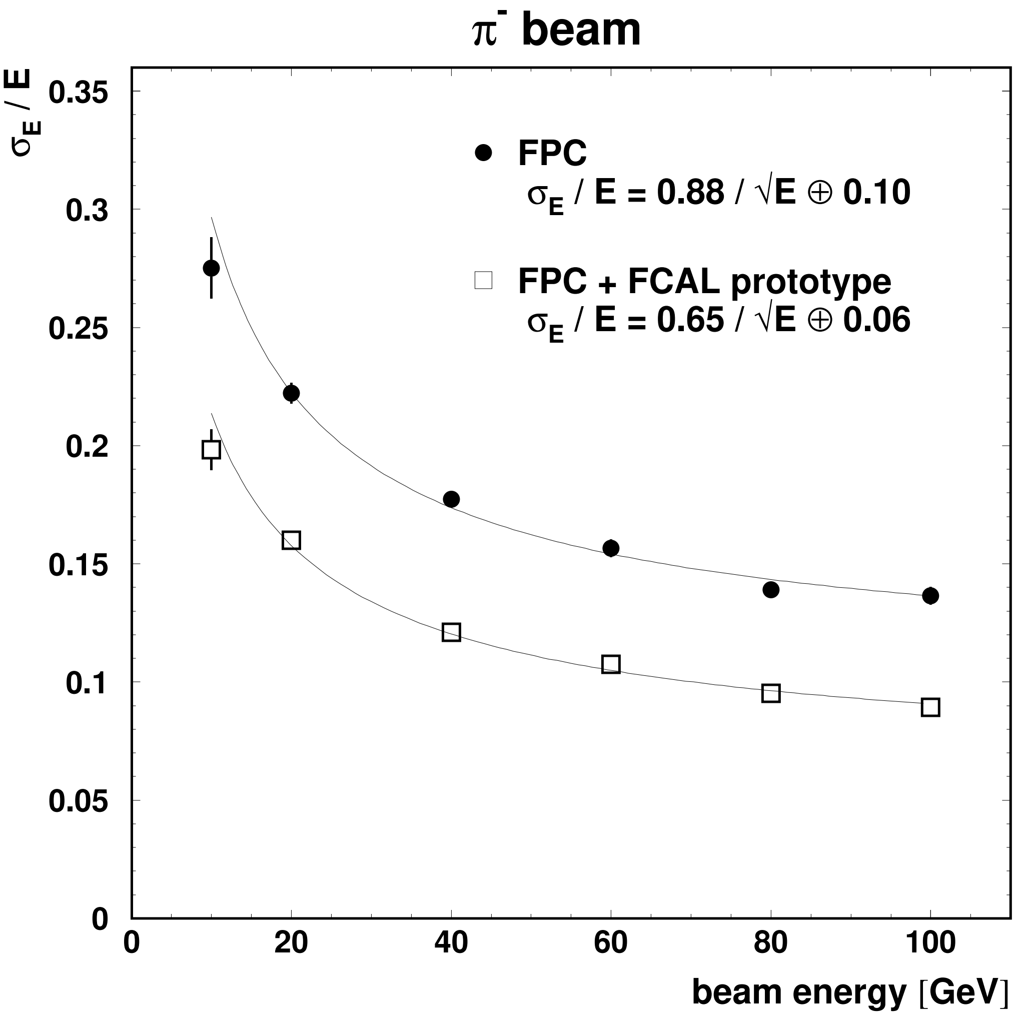

Figure 5.10: Energy resolution (σ_E/E) for π^- as measured by FPC alone (solid points) and FPC + FCAL prototype (open points) as a function of beam energy.

energy resolution of about $0.15/\sqrt{E}$.

5.5.2 Energy resolution for pions

Figure 5.10 shows the measured energy resolution for π^- as a function of energy for FPC alone and FPC + FCAL prototype. Each point is the result of a Gaussian fit to the corresponding π^- distribution shown in Fig. 5.6. The data has been fitted to Eq. 5.5, yielding a sampling term of $a = 0.65$ GeV$^{1/2}$ and a constant term of $b = 0.06$ for the combination of FPC and FCAL prototype.

The measured resolution is affected by transverse leakage into the gap between the FCAL prototype modules (see Fig. 5.1). In the ZEUS environment the FPC is completely surrounded by FCAL modules. As a result there is no transverse leakage except into the beam hole. This effect has been studied using the MC described in section 4.2. The FCAL geometry has been implemented according to (i) the FCAL prototype modules installed in the CERN testbeam area and (*ii*) the environment in ZEUS. The results are shown in Fig. 5.11. A significant improvement in the energy resolution is observed when the FPC is completely surrounded by FCAL modules; a fit to Eq. 5.5 yields $a = 0.59$ GeV$^{1/2}$ and $b = 0.06$. Note, that the resolution obtained from the MC for the combination of FPC and FCAL prototype yields $a = 0.70$ GeV$^{1/2}$ and $b = 0.07$, which is slightly worse than the values obtained from data.

Longitudinal leakage losses out of the back of the FPC (5λ) significantly affect the energy resolution for high energy hadrons. A tail at low energies is expected in the reconstructed energy distribution. Due to large muon contamination in the π^- beam this low energy tail could not be studied with CERN beam data. Instead, the MC described in section 4.2 has been used to study this effect. In order to exclude the effect of transverse leakage the MC has been implemented with FCAL modules completely surrounding the FPC which corresponds to the environment in ZEUS. The lower plot in Fig. 5.12 shows the FPC + FCAL response to 100 GeV π^-s. A tail at low energies is visible. Defining the energy resolution as the ratio RMS/MEAN of the π^- signal distribution takes into account the effect of this tail. In the upper plot of Fig. 5.12 the energy resolution as calculated from a Gaussian fit (solid points) is compared to the energy resolution given by RMS/MEAN (open points). The longitudinal leakage losses substantially degrade the energy resolution for high energy π^-. The open points have been fitted to

$$\frac{\sigma_E}{E} = \frac{a}{\sqrt{E}} \oplus b \oplus c \cdot \ln(E) \ , \tag{5.6}$$

where E is in GeV. The logarithmic term takes into account the effect of longitudinal leakage. The results of this fit are a = 0.53 GeV$^{1/2}$, b = 0.11 and c = 0.03.

5.6 Shower width and position resolution

5.6.1 Shower width for electrons

The fine transverse segmentation of the EMC section of the FPC allows to study the profile of the energy deposition of electrons. The ratio of energy deposited in a given EMC cell of mean distance d to the point of incidence and the total energy deposited in the EMC section have been measured. The mean values for electron beams of 10 GeV and 60 GeV are plotted in Fig. 5.13 as a function of the distance d. The shower profile is practically independent of the beam energy. One observes a roughly exponential decrease as a function of distance. This is expected since the lateral shower profile of dE/dx for electrons can be approximated by a function peaking at the point of incidence with exponentially decaying tails. About 54% of the energy is reconstructed in the central cell of the shower while MC (see section 4.1) predicts 71%. Only when the cross talk discussed in section 5.3 is included in the MC a good description of the data is achieved (see Fig. 5.13).

5.6.2 Position resolution for electrons

As shown in the previous section the shower profile of electrons is governed by exponential tails. Therefore, linear position reconstruction algorithms yield non-optimum resolution and systematic biases. The following algorithm, proposed in [108, 109] has been used for the FPC.

- A cluster of EMC cells containing the highest energy deposition is searched for.

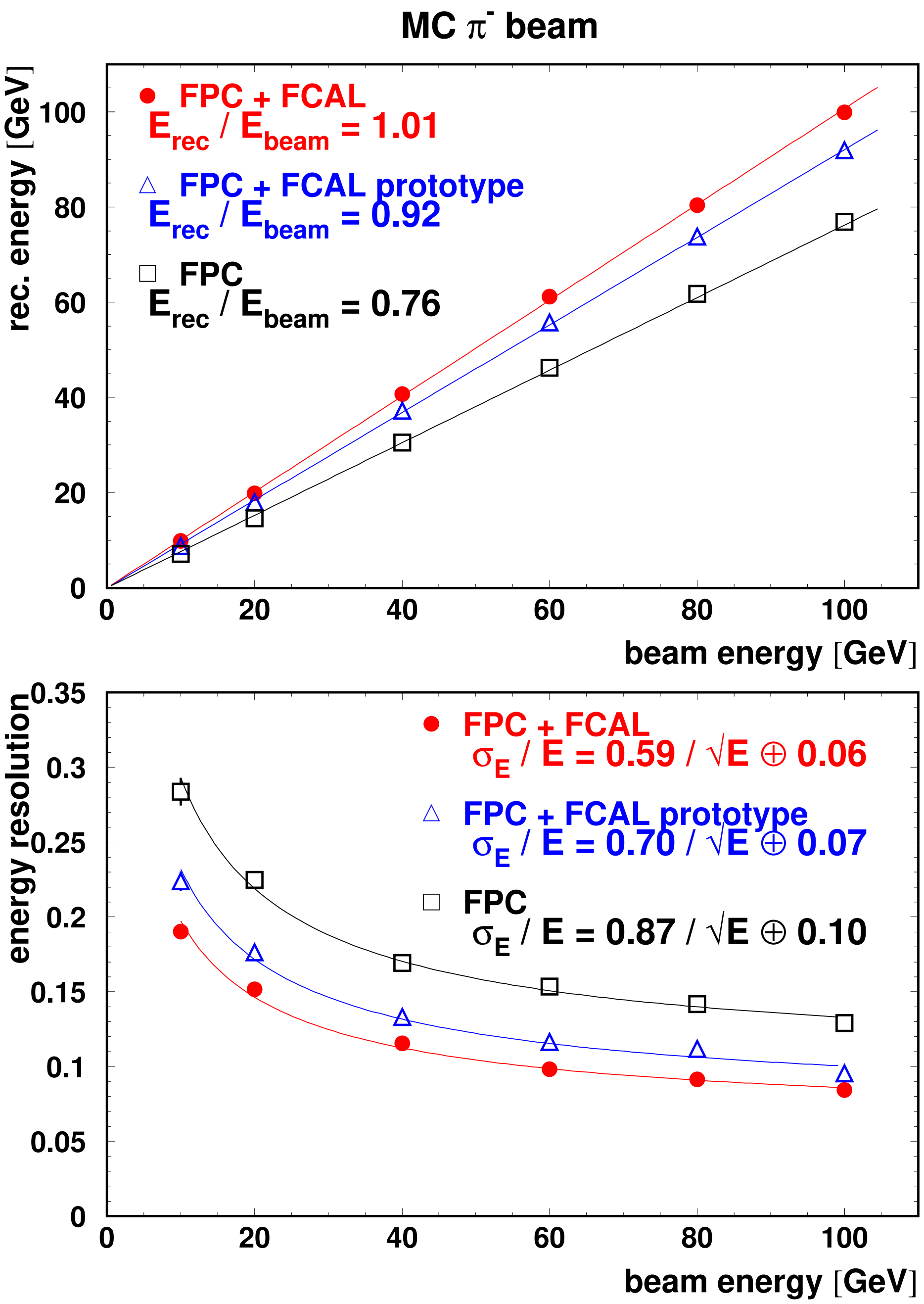

Figure 5.11: The FPC performance for π^- is shown for the case where the FPC is placed between FCAL prototype modules as shown in Fig. 5.1 or where the FPC is completely surrounded by FCAL modules. The results have been obtained using the MC described in section 4.2. *Upper plot*: The mean reconstructed energy in the FPC, FPC + FCAL prototype (CERN testbeam setup) and FPC + FCAL (ZEUS environment) as a function of the incident beam energy. *Lower plot*: Energy resolution (σ_E/E) for the above combinations.

- The reconstructed position $\vec{X}$ for the cluster is then calculated as:

$$\vec{X} = \frac{\sum_{i=1}^{N} w_i \vec{X}_i}{\sum_{i=1}^{N} w_i} \tag{5.7}$$

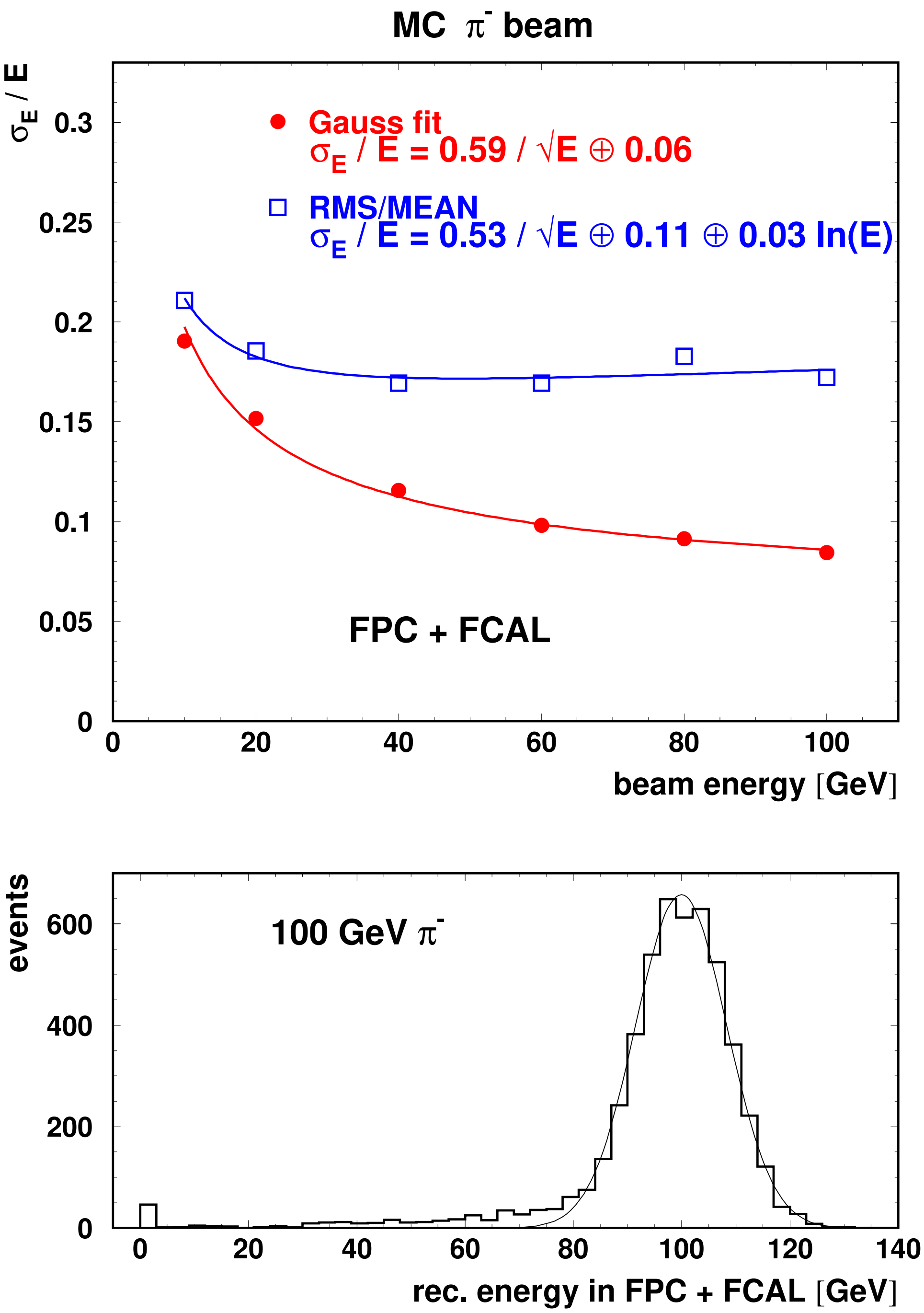

Figure 5.12: MC study of the effect of longitudinal leakage losses on the energy resolution (σ_E/E) for pions. *upper plot*: For the solid points the energy resolution has been determined using a Gaussian fit to the signal in FPC + FCAL. The open points have been calculated as the ratio RMS/MEAN which is sensitive to the low energy tail due to longitudinal shower losses. *lower plot*: The response to 100 GeV π^- in FPC + FCAL is shown.

where the weights w_i are given by:

$$w_i = \max(0, \ln(E_i/\sum_{j=1}^{N} E_j) + W_0), \tag{5.8}$$

$\vec{X}_i$ is the position of the center of cell i and E_i is the energy reconstructed in that cell.

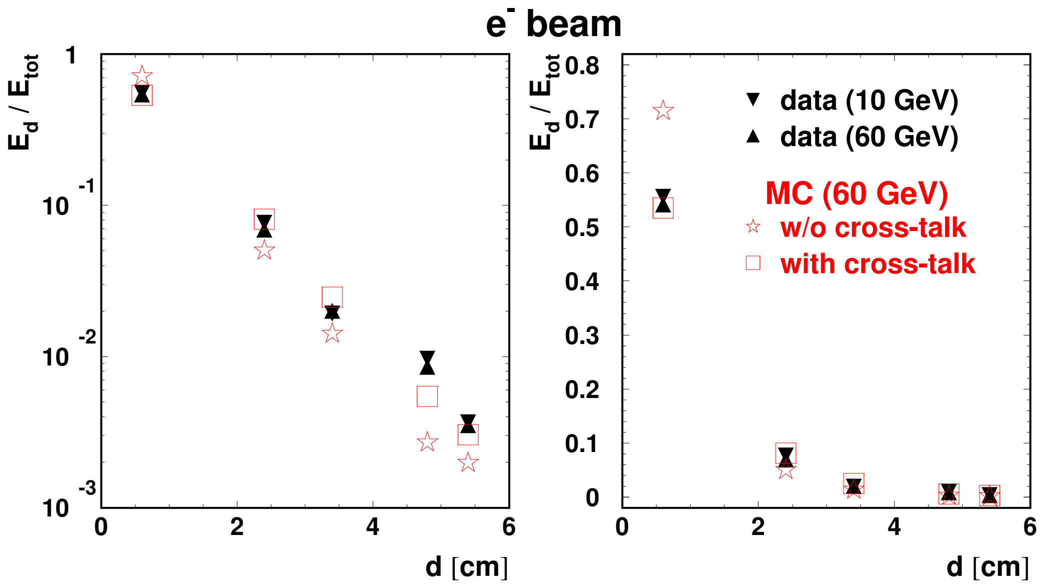

Figure 5.13: The shower width for electrons of 10 GeV and 60 GeV is compared to MC predictions with and without including cross talk effects. The energy fraction deposited in a cell of mean distance d from the impact point is plotted as a function of d in a logarithmic (left plot) and a linear scale (right plot).

The cutoff value W_0 determines the energy above which a cell is considered in the algorithm. The larger the value of W_0 the larger is the weight of low energy tails. This reduces systematic biases but increases the influence of shower fluctuations and thus worsens the resolution. Following MC studies a value of $W_0 = 4$ has been chosen for EMC cells.

To study the performance of the above algorithm the Y coordinate Y_{rec} of the reconstructed position $\vec{X}$ has been compared to the position Y_{DLWC} given by the DLWC. Due to the symmetry of the FPC, similar results are obtained for X_{rec}. In Fig. 5.14 it can be seen that systematic biases are below 0.3 cm except for the outermost EMC cells, where the shower is not fully contained in the FPC.

For FPC cells which are neither at the outer edge of the FPC nor near the beam hole a Gaussian has been fitted to the distribution of $\Delta Y = Y_{rec} - Y_{DLWC}$. In Fig. 5.15 the resulting $\sigma_{\Delta Y}$ is plotted as a function of beam energy. The data is fitted to the functional form:

$$\sigma_y = a/\sqrt{E} \oplus b, \tag{5.9}$$

where E is in GeV, yielding a = 10 mm and b = 1.6 mm.

5.6.3 Position resolution for pions

For the position reconstruction of pions the HAC information has been included and the same algorithm as for electrons has been used. Due to the larger dimensions, a cutoff parameter $W_0 = 2$ has been chosen for the HAC cells. Although the hadronic shower is not fully contained in the FPC a reasonable position reconstruction is achieved using FPC information only. The

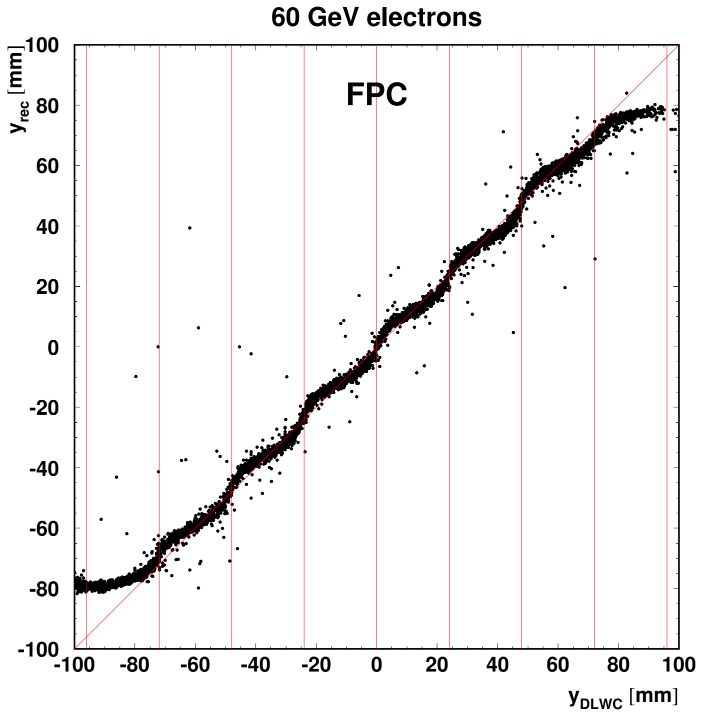

Figure 5.14: The reconstructed position for 60 GeV electrons is plotted vs. the DLWC position. The vertical lines indicate the EMC cell boundaries.

upper set of points in Fig. 5.15 shows the position resolution obtained for pions. A fit to Eq. 5.9 yields a = 22 mm and b = 3.3 mm.

When only EMC cells or only HAC cells are used to obtain the barycenter, the resolution degrades as shown in Table 5.2. For the set of EMC cells, only events which deposit more than 20% of the energy in the EMC section are considered and the RMS is used instead of the sigma from the Gaussian fit.

5.7 Effect of WLS fibers on the signal response

5.7.1 Signal uniformity

The uniformity of the response across the surface of a FPC cell is affected by the presence of the WLS fibers. As discussed in [96] a photon produced in a scintillator is reflected inside the scintillator tile by total reflection and by the tyvek wrapping. The probability to hit a

Cells used	$a\,(\mathrm{mm}\cdot\mathrm{GeV}^{1/2})$	$b\,(\mathrm{mm})$
EMC + HAC (σ)	22 ± 3	3.3 ± 0.5
HAC (σ)	50 ± 4	2 ± 3
EMC ($E_{EMC} > 0.2 \cdot E_{beam}$, RMS)	74 ± 8	9.6 ± 0.9

Table 5.2: π^- position resolution using different sets of cells, with the resolution σ taken either from a Gaussian fit or from the value of RMS. The resolution has been parameterized as the quadratic sum of a sampling term a and a constant term b.

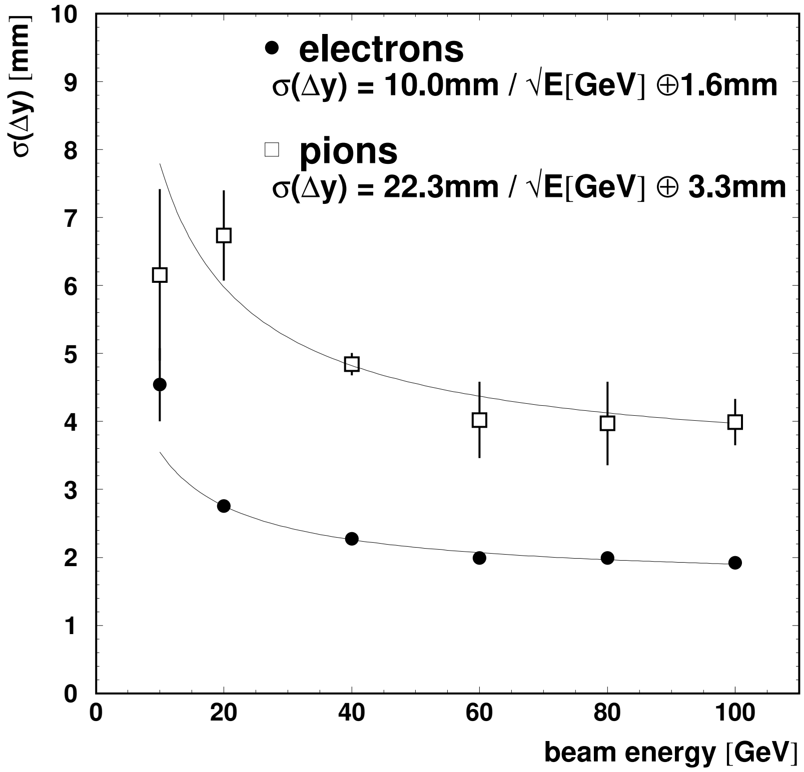

Figure 5.15: The position resolution for electrons and pions is plotted as a function of the beam energy.

WLS fiber before being absorbed inside the scintillator material or being lost due to the limited reflectivity of the tyvek depends on the geometry. Light produced in scintillator regions close to a WLS fiber is collected with higher efficiency than in other regions.

The effect of the enhanced FPC response to particles incident close to a WLS fiber has been studied using high energy electrons for which the energy resolution (σ_E/E) is best. In Fig. 5.16 the FPC response to 100 GeV electrons is shown as a function of the point of incidence. The average response is enhanced by $\sim$ 15% in regions close to the WLS fibers. This effect is slightly reduced for runs where the FPC was tilted by 1.7° (compare Fig. 5.16 top and bottom) corresponding to the mean angle of incidence of beam particles coming from the ZEUS interaction point.

Using a set of runs with focused 3 GeV test beam electrons taken with the FPC prototype in the DESY test beam, a 2 dimensional scan of an EMC cell has been obtained which is shown in Fig. 5.17. The signal enhancement around the 4 WLS fibers is clearly seen.

A decrease of the signal of about 15% has been found at the position of the brass tube used for ^{60}Co scans (see section 5.8.1) at x $\approx$ 0 cm and y $\approx$ -1.7 cm.

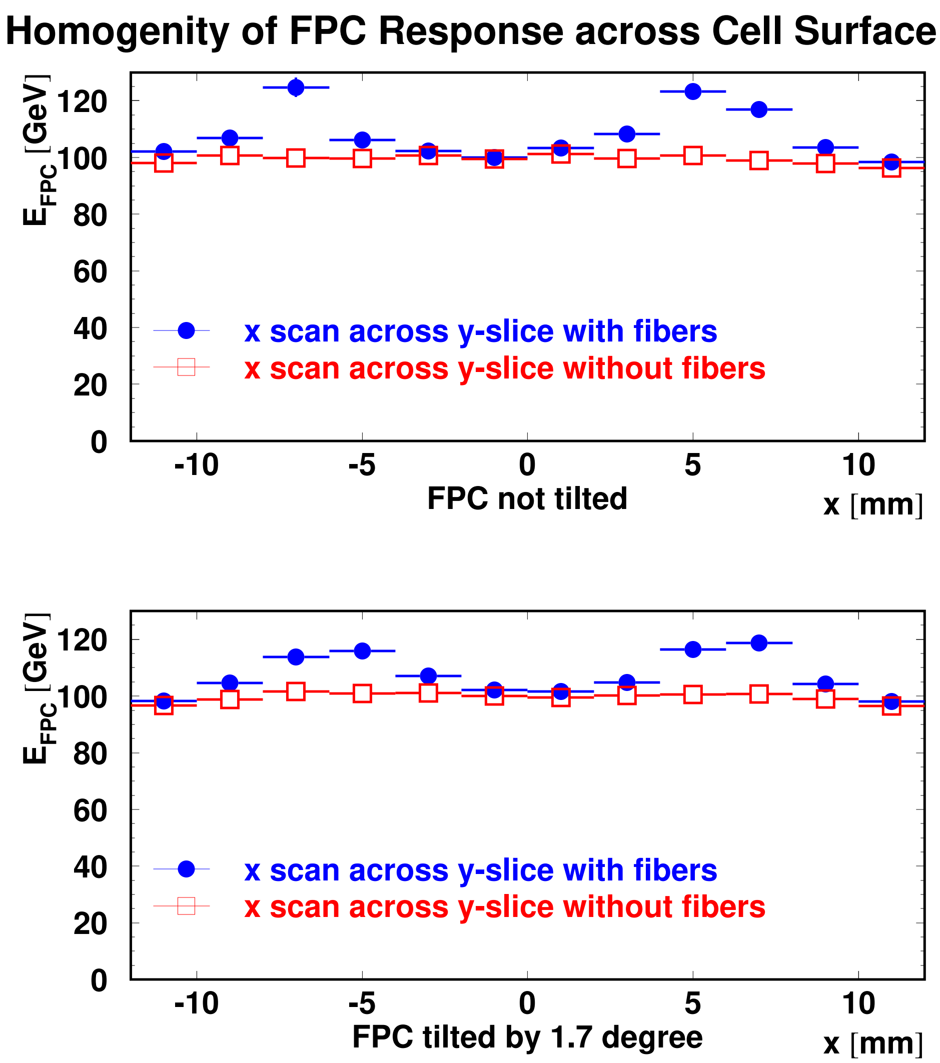

Figure 5.16: The energy measured by the FPC, E_{FPC}, for 100 GeV electrons is plotted as a function of the position of incidence. Two 3 mm wide bands (measured in Y-direction) of position of incidence have been selected, one crossing the WLS fibers (solid dots), the other avoiding the fibers (open squares). In the upper plot the FPC surface has been perpendicular to the beam axis while in the lower plot it has been tilted by 1.7°.

5.7.2 Effect on the energy resolution

The enhancement of the signal in the fiber regions also affects the energy resolution of the FPC as seen in Fig. 5.18. The distribution of the total reconstructed energy, E_{FPC}, shows a tail towards higher energies. The right plot of Fig. 5.18 shows the positions of electrons selected from this tail, as measured by the DLWC. These electrons hit the FPC close to one of the four WLS fibers of the cell. The energy resolution obtained using the RMS and the mean value ($\langle E \rangle$) of the distribution is RMS/$\langle E \rangle = 8$ %, while a resolution of 5% is obtained from a Gaussian fit, which is insensitive to the high energy tail.

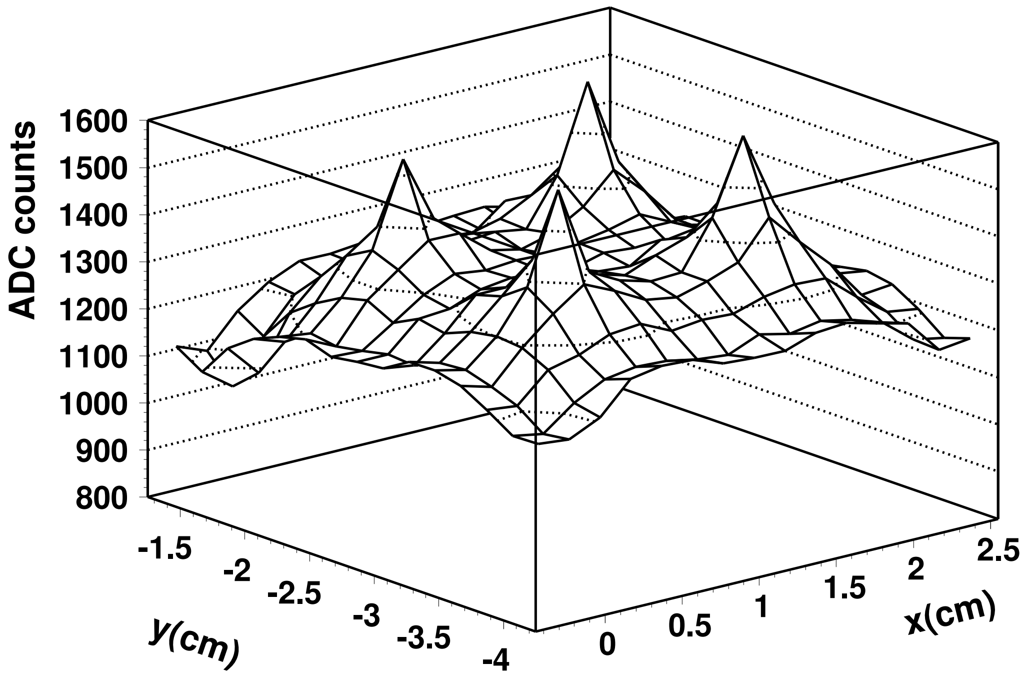

Figure 5.17: The mean signal response as a function of beam incidence position is shown for 3 GeV electrons.

5.7.3 Tunneling of electrons into the HAC section

For electrons of less than 100 GeV, more than 99% of their energy is absorbed in an infinitely wide block of 26.6 X_0 depth. However, electrons hitting the WLS fibers start to shower much later than those incident on the lead. Since the fibers in the EMC section correspond to only $0.4\,X_0$, electrons can traverse the EMC section through the fibers and deposit their energy in the HAC section. For a data sample where electrons are uniformly distributed in the transverse plane, about 2% of the events show more than 10% of the incident energy in the HAC section. These events are also concentrated near the positions of the WLS fibers (see Fig. 5.19). When the FPC is tilted by 1.7° this fraction of electrons reduces to 0.3% (see Fig. 5.20).

5.8 Monitoring of stability

5.8.1 The ^{60}Co monitoring system

A monitor system using a ^{60}Co source, similar to the one used for the ZEUS uranium calorimeter [110, 111], has been developed for the FPC. It allows the detection of changes in the performance of the scintillator tiles and the WLS fibers as well as drifts in the gain of the PMTs. Measuring the ratio of response to ^{60}Co and to beam particles allowed to transport the absolute and cell-to-cell calibration constants from the CERN test beam to ZEUS and to monitor the stability of the calibration.

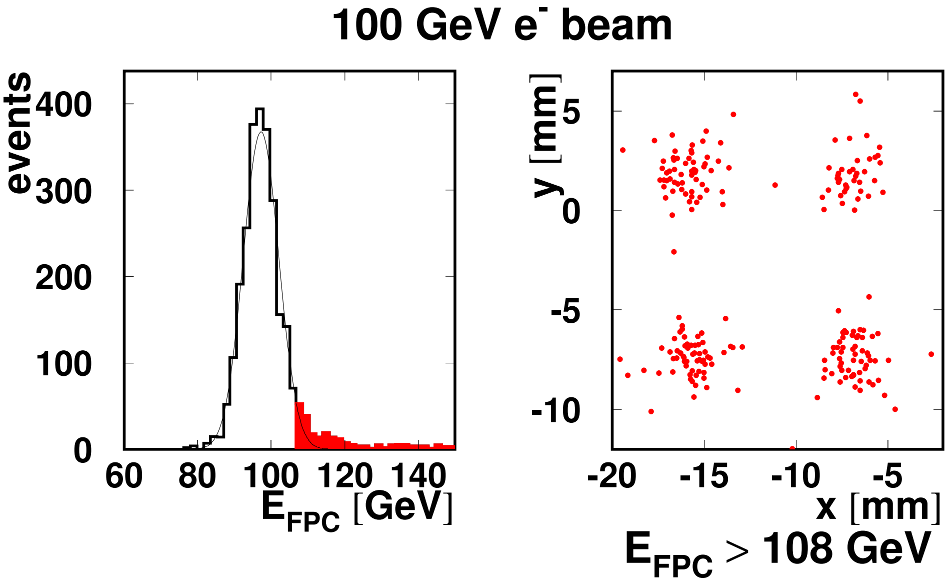

Figure 5.18: The left picture shows the distribution of E_{FPC} for 100 GeV electrons hitting the FPC uniformly across an EMC cells. A tail towards higher energies is present (shaded area). In the right plot the positions of electrons as measured by the DLWC are shown for the events in the tail. These electrons hit the FPC close to one of the four WLS fibers in the cell.

5.8.2 ^{60}Co setup

A 1 mCi pointlike ^{60}Co source is attached to the tip of a steel wire. For safety reasons the wire and the source are enclosed inside a stainless-steel tube. This source wire can be inserted

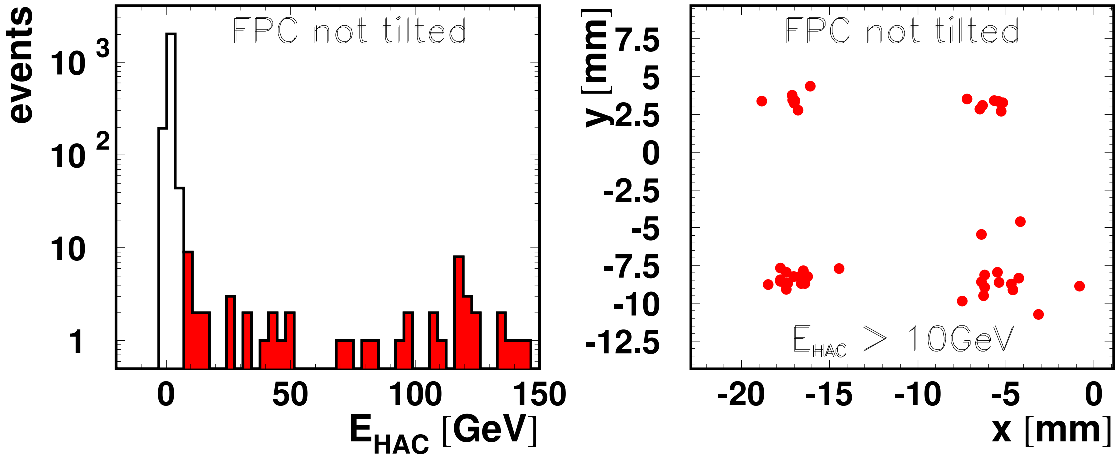

Figure 5.19: The energy deposited in the HAC section of the FPC by 100 GeV electrons is plotted for vertical incidence. The plot on the right shows the impact position of electrons depositing more than 10 GeV in the HAC section (shaded area on the left plot).

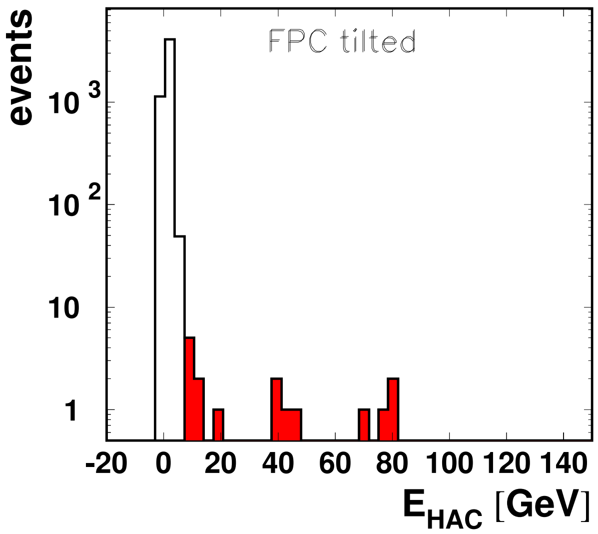

Figure 5.20: The energy deposited in the HAC section of the FPC by 100 GeV electrons is plotted for the FPC tilted by 1.7°.

into brass tubes of 1.4 mm inner diameter inside the FPC. The brass tubes run parallel to the WLS fibers at the center of each FPC quarter (see Fig. 3.2). The ^{60}Co source irradiates the scintillators of the FPC with 1.173 MeV and 1.332 MeV photons (see Fig. 5.21).

A PC-controlled motor moves the ^{60}Co source wire in steps of 0.6 mm through the FPC. At each step the PMT currents are read out across 2 MΩ resistors by an integrating, voltage sensitive ADC. The measurement is repeated 500 times and the mean and root mean square (RMS) values are recorded. During a complete scan the source fully traverses the FPC (from EMC to HAC) and the 15 EMC and 4 HAC channels of the corresponding FPC quarter are read out.

The signal as a function of position is shown in Fig. 5.22. The 10 (50) peaks in the EMC (HAC) part correspond to positions where the source is next to a scintillator. When the source

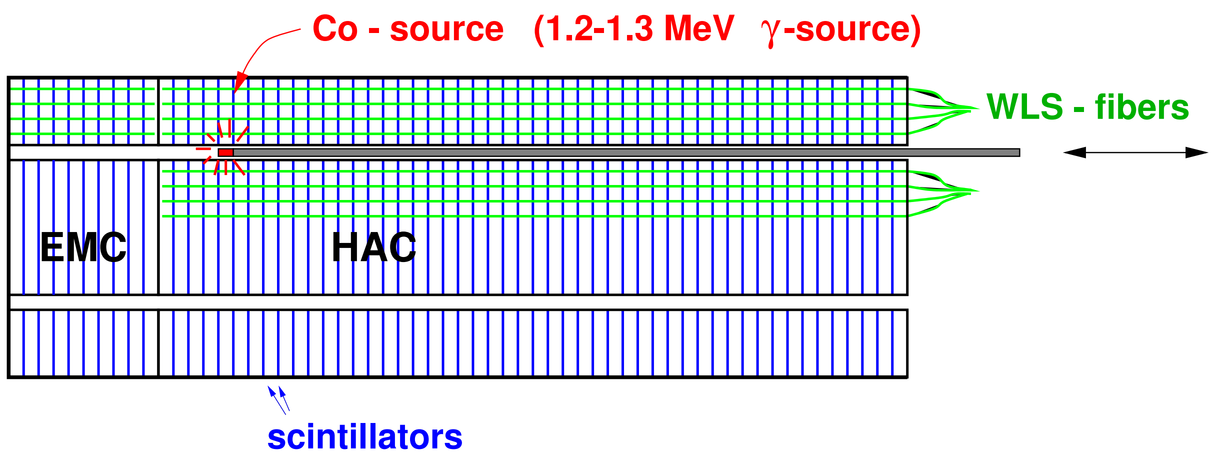

Figure 5.21: Schematic drawing of the FPC with inserted ^{60}Co source

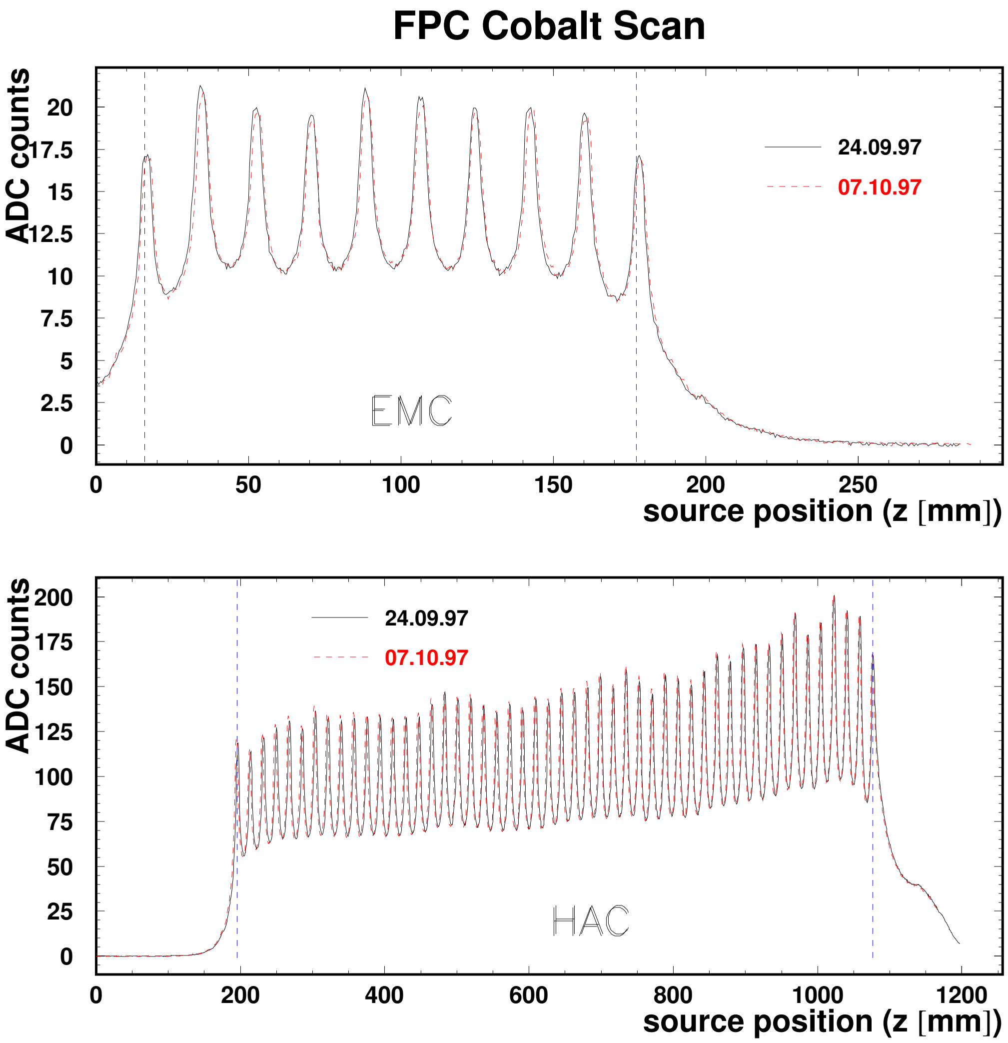

Figure 5.22: The measured ^{60}Co signal in the EMC and HAC sections as a function of the source position. The vertical lines indicate the region of integration used to obtain the value of COMEAN (see section 5.8.4).

is inside a lead layer the photons are partially shielded and the signal drops. The point where the source exits the EMC section and enters the HAC section is clearly seen at $Z \sim 190$ mm.

The maxima of the signals from the individual scintillator tiles fluctuate. This is assumed to be due to differences in the scintillator-WLS fiber light coupling and to differences in the tyvek wrapping and scintillator machining. The overall increase of the signal in the HAC section with increasing Z is due to light attenuation in the WLS fibers: the fibers are read out in the direction of positive Z (see section 5.8.3).

5.8.3 Measurement of the light attenuation in WLS fibers

The change of the peak height with the source position Z in the HAC section (see Fig. 5.22) allows to directly measure the light attenuation length in the WLS fibers. Since the peak height

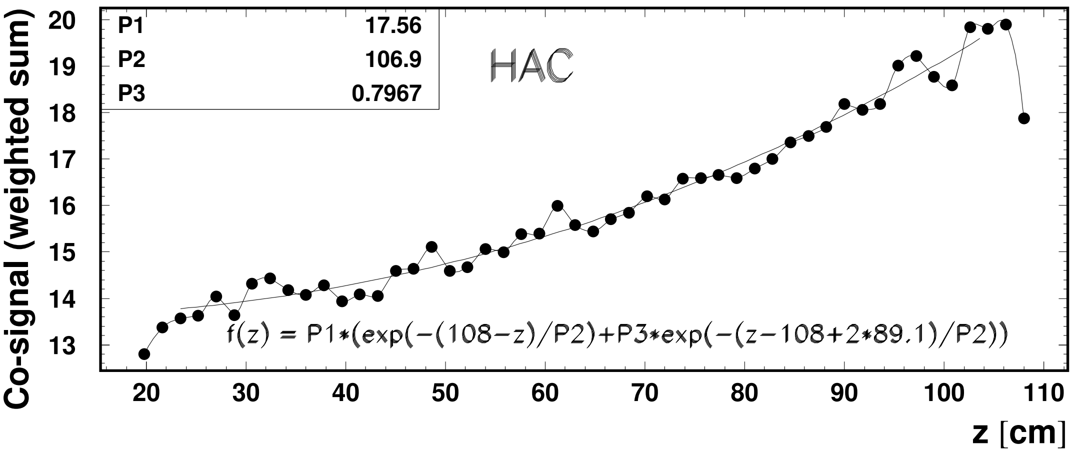

Figure 5.23: The peak height averaged over all cells is plotted as a function of peak position Z (note the suppressed zero). The attenuation length in the WLS fibers is determined with a two exponential fit. The second exponential accounts for the light reflected at the end of the fiber.

is also influenced by the scintillator quality and the light coupling into the WLS fiber, average peak values of all channels have been used (see Fig. 5.23).

The data are fitted by using the function:

$$f(Z) = P_1 \cdot (e^{-(Z_0 - Z)/P_2} + P_3 \cdot e^{-(Z - Z_0 + 2 \cdot L)/P_2}) \tag{5.10}$$

where L = 89.1 cm is the length of the HAC (distance from the reflective mylar foil to the last scintillator layer on the back) and $Z_0 = 108.0$ cm is the Z position where the fiber exits the FPC. In Eq. 5.10 the second exponential accounts for the light reflected at the mylar foil which separates the EMC and HAC sections; P_1, P_2 and P_3 are free parameters in the fit. The attenuation length measured using this method is $P_2 = 107$ cm. The weight of the second exponential function is $P_3 = 0.80$, which indicates that $\sim 80\%$ of the light is reflected by the mylar foil.

5.8.4 Transfer of the FPC calibration to the ZEUS environment

After the installation of the FPC in ZEUS several parameters might have changed as compared to the CERN test beam situation. The external conditions might be different, internal mechanical damage during the transport or during the installation might have occurred and the gain of the PMTs might have changed. These changes affect the calibration determined using the CERN test beam data and have to be corrected for.

The ^{60}Co scans allow to monitor the combination of all these effects and to correct the calibration constants accordingly. In order to quantify the response of each FPC cell to ^{60}Co, the signal induced by the ^{60}Co source is integrated between the bounds shown in Fig. 5.22. The result of the integration is called COMEAN. Figure 5.24 shows COMEAN for 8 different ^{60}Co

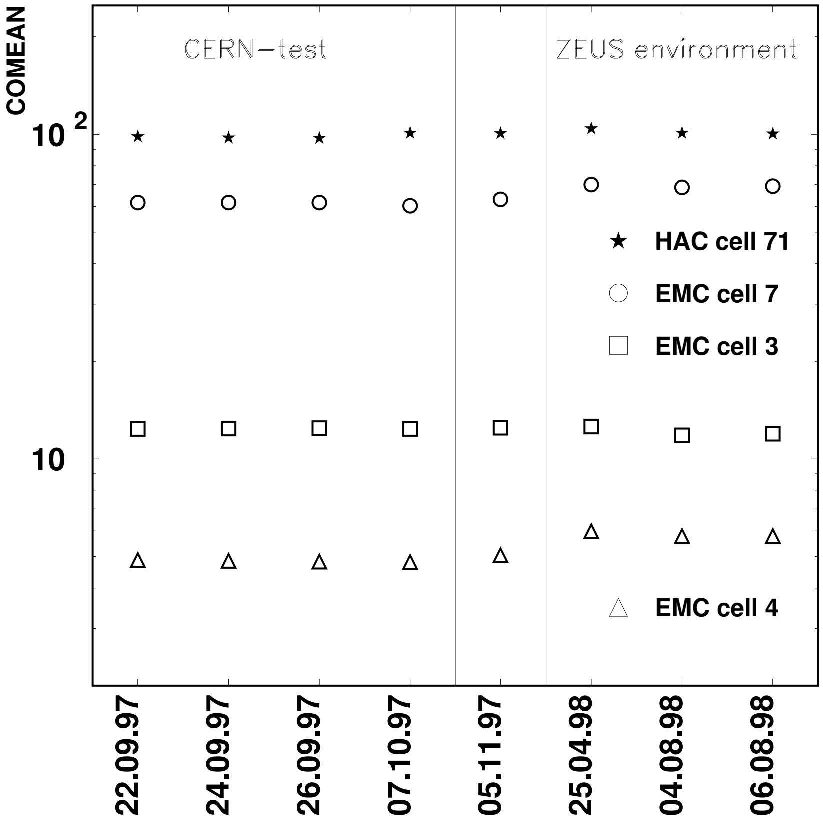

Figure 5.24: The COMEAN values from different ^{60}Co scans, listed by dates, are shown for HAC cell 71 and for three EMC cells at different distances to the cobalt source. According to the classification given in Fig. 5.25 cell 7 belongs to group A, cell 3 to B and cell 4 to C. The values are corrected for the ^{60}Co lifetime.

scans spanning the time from the CERN-test period in September 1997 until the installation of the FPC in ZEUS and the start of luminosity runs in August 1998. The cobalt measurements performed at different dates are corrected for the ^{60}Co lifetime of 7.6 years.

Up to 10% deviations can be observed after the transportation of the FPC to DESY (05.11.97) and after installation of the FPC into the ZEUS environment (25.04.98).

The different signal heights observed for different cells in Fig. 5.24 is due to different distances from the cobalt source. The EMC cells can be subdivided into 3 groups (A,B,C) depending on their distance from the ^{60}Co source (see Fig. 5.25). The distance between the ^{60}Co source and HAC cells is the same for all HAC cells.

The calibration constants for the ZEUS environment have been adjusted such that the ratio R_i of the signal response to electrons of a given energy and the ^{60}Co signal COMEAN be constant. That ratio has been determined for each cell i using electron test beam data and a ^{60}Co scan taken consecutively during the CERN test period. As expected, the value of R_i proved to be the same within a standard deviation of 4% for all cells of the same group as defined in Fig. 5.25.

The additional uncertainty on the calibration due to this procedure has been estimated to be 5%.

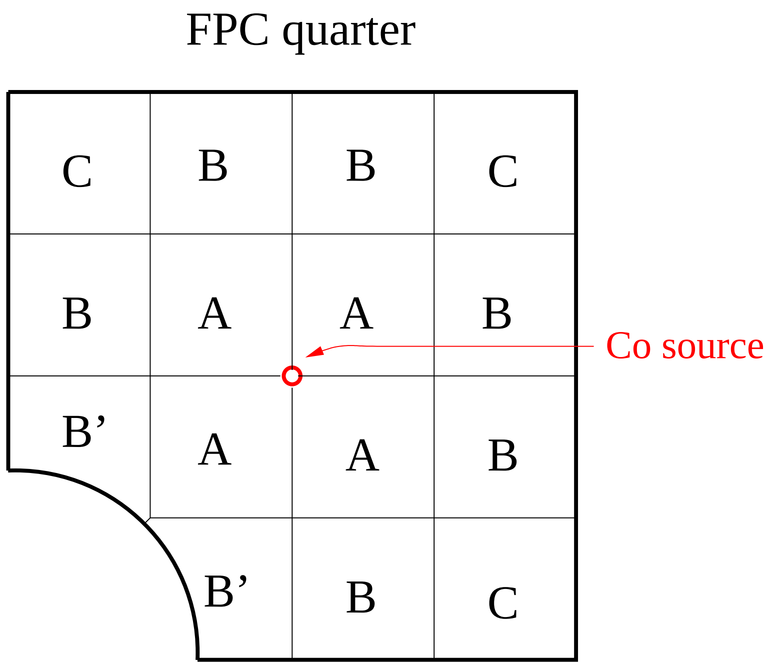

Figure 5.25: Front view of a quarter of the FPC. The EMC cells are classified in three groups depending on their distance to the ^{60}Co source.

5.8.5 Monitoring of the FPC calibration in ZEUS

During the operation of the FPC in ZEUS ^{60}Co scans have been performed at every monthly access day. This data has been used to monitor and correct the longterm calibration of the FPC. Fig. 5.26 shows the value COMEAN for a typical HAC and EMC cell during one year of operation. The fluctuations in response are typically of the order of 5% reaching 15% for about 10% of all channels.

I. Stability cross check with DIS data

The validity of the calibration monitoring and correction using ^{60}Co scans has been cross checked using DIS data. For a sample of DIS events taken with a high Q^2 trigger[1] the mean energy $\bar{E}_i(t)$ reconstructed in cell i has been determined as a function of time t (see Fig. 5.27). The average statistical uncertainty $\delta_{stat,i}$ on each measurement of $\bar{E}_i(t)$ is 8% (3%) for EMC (HAC) cells. The variation $\delta_{calib,i}$ of the calibration of cell i can be determined according to

$$\delta_{calib,i} = \sqrt{\Delta_i^2 - \delta_{stat,i}^2}\ , \tag{5.11}$$

where Δ_i is the RMS of the variation of $\bar{E}_i(t_j)$ with time. After correcting the FPC calibration using the ^{60}Co scans the variations $\delta_{calib,i}$ are less than 7% for all cells. The average value of $\delta_{calib,i}$ is 4% (3%) for EMC (HAC) cells.

[1]The high Q^2 DST bit 12 ($Q^2_{DA} > 80\,\mathrm{GeV}^2$, $y_e < 0.95$, $E_e > 5\,\mathrm{GeV}$) has been used.

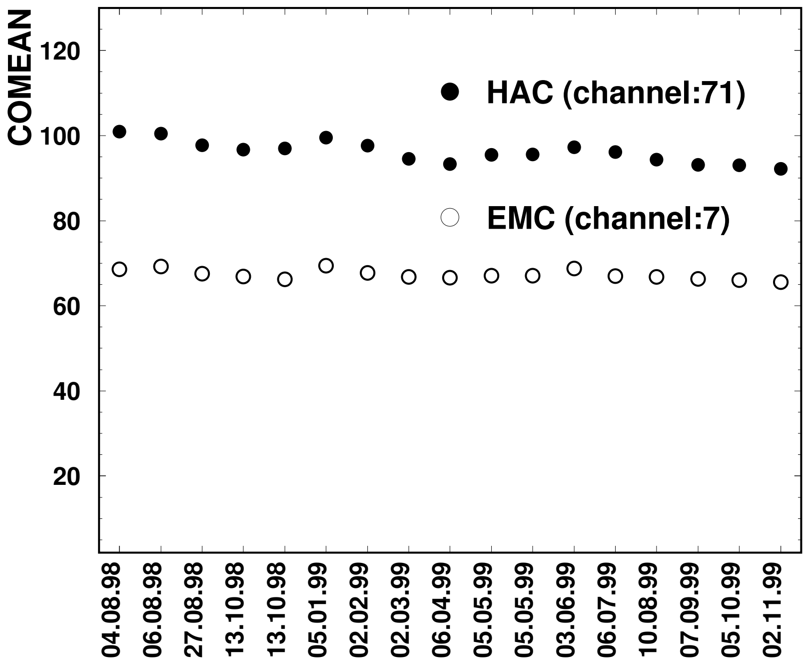

Figure 5.26: The COMEAN values for ^{60}Co scans taken during one year of operation of the FPC in ZEUS are shown for HAC cell 71 and EMC cell 7. The values are corrected for the ^{60}Co lifetime.

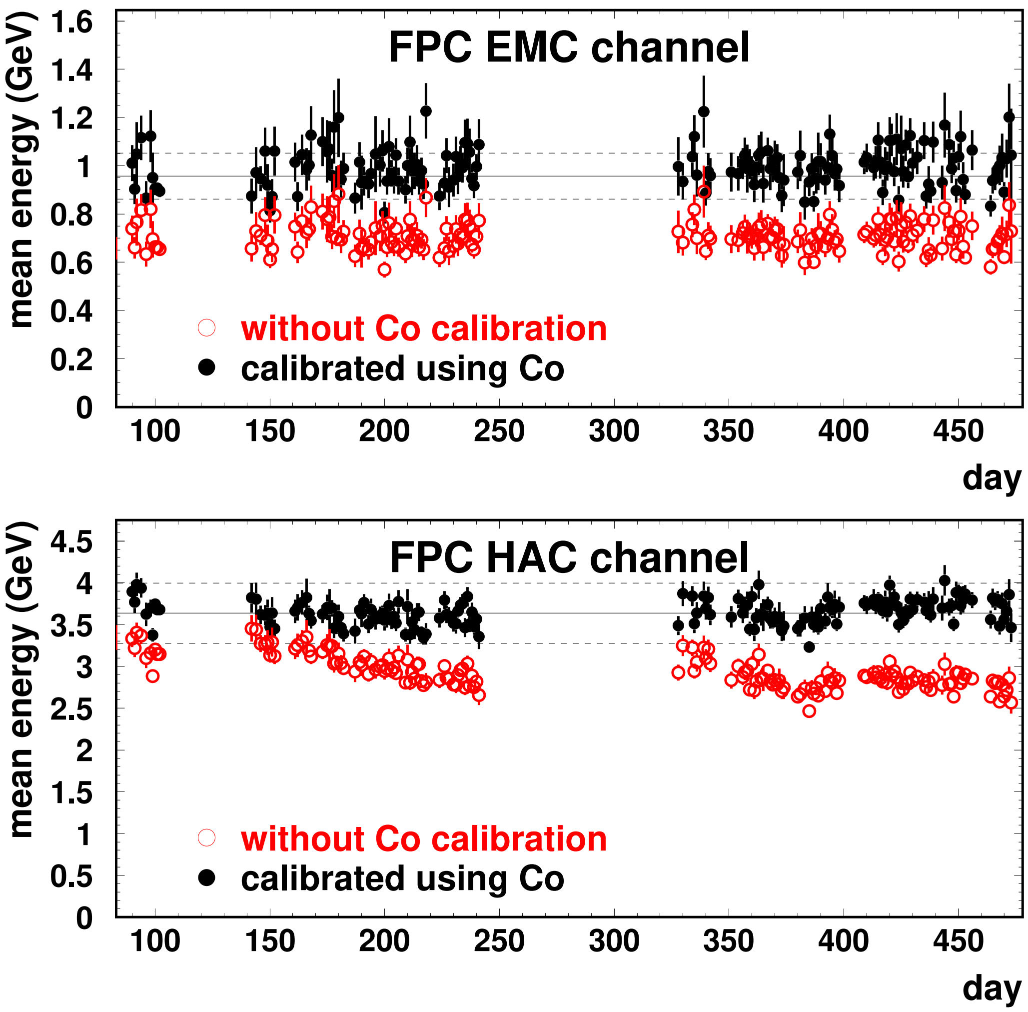

Figure 5.27: The mean energy deposited in a HAC and an EMC cell is shown for a sample of DIS events with $Q^2 > 80\,\mathrm{GeV}^2$ as a function of time. 27.Aug.1998 is defined as day 1. For the solid points the calibration has been corrected using the ^{60}Co measurements, while no correction has been applied for the open points.

Chapter 6

Event Simulation

Simulations are an indispensable tool for the analysis of high energy data. They are used to design and optimize the analysis strategies and allow to correct for acceptance and resolution effects of the detector and trigger system. Both the detailed description of the complete physics process as well as of the detector and the trigger system are highly complex and analytical calculations are far too complicated. Therefore, well established Monte Carlo (MC) techniques are used which simulate the relevant aspects of physics events in the ZEUS detector.

The MC simulation consists of two main parts. In the first part the so called event generator simulates the kinematics and the event topology of electron-proton scattering providing the 4-momenta of all produced particles. In the second step the interaction and detection of the particles generated in the event generator are simulated.

In the following the main concepts of the event generators used in this analysis and their implementations in software packages are described. The ZEUS detector simulation is described in section 4.2.

6.1 DIS event generation

In the present analysis the event generator DJANGOH version 1.1 [112] has been used to simulate DIS $ep \rightarrow eX$ non-diffractive scattering. DJANGOH is interfaced to the MC programs HERACLES [113], LEPTO [114], ARIADNE [115] and JETSET [116] and includes both QED and QCD radiative effects.

Factorization theorems allow to divide the event generation into various steps. The hard scattering process can be separated from the subsequent soft QCD cascades and hadronisation. Figure 6.1 schematically shows the different parts of the DIS event generation described in the following.

In the first step the event kinematics are generated by HERACLES based on parton distribution functions in the framework of the quark parton model. The CTEQ4D [117] parameterization of the parton distributions has been used for this analysis. HERACLES includes leading order QED radiative corrections to the Born level cross section. Figure 6.2 shows the Feynman diagrams of the first order corrections to the lepton line. Radiative corrections coming from the hadron line are smaller than the leptonic ones and are absorbed in the parton distributions.

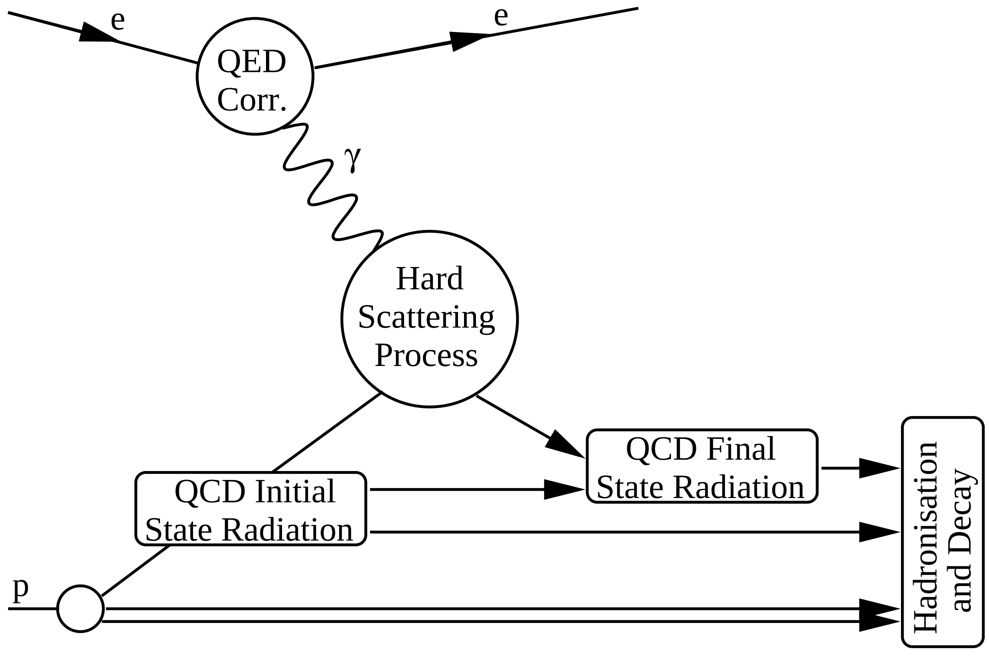

Figure 6.1: Schematic diagram of the different parts of a DIS Monte Carlo generator.

QED radiative effects not only change the Born level amplitudes but also introduce new types of events since additional photons can emerge. These radiated photons affect the relation between the kinematics at the hadronic vertex and the measured event quantities such as the scattered electron angle and energy. The size of the effect depends on the chosen reconstruction method and has to be corrected for.

In the next step QCD cascades are simulated using the color dipole model (CDM) as implemented in ARIADNE. Secondary partons are produced in the color field between the struck quark and the proton remnant. The CDM treats these parton cascades as gluon radiation off color dipoles between two partons with complementary color charge. Splitting of gluons into quark-antiquark pairs is also taken into account. The boson-gluon-fusion (BGF) process which is particularly important at low values of x is not described in this formalism and is therefore added. The combined code is called CDMBGF.

Finally, the colored partons produced in the QCD cascades have to form colorless hadrons. This process is not yet understood from first principles since perturbative calculations are not applicable. The hadronisation therefore has to be described by phenomenological models. The LUND string fragmentation model as implemented in the JETSET program is used to perform the hadronisation. In this model a string of constant energy per unit length (≈ 1 GeV/fm) is formed between a quark q and an antiquark $\bar{q}$. As the $q\bar{q}$ system moves apart the string energy increases until a new $q\bar{q}$ pair can be produced thus breaking the string into two smaller pieces. This break-up process continues until only on-mass-shell hadrons remain. Many of the resulting hadrons undergo weak decays. The corresponding decays are simulated by JETSET according to the known particle decay properties.

6.2 Diffractive event generation

Diffractive processes of the type $e + p \to e + X + p$ are not simulated in the standard DIS event generators. The RAPGAP generator [118] has been used for the simulation of diffractive

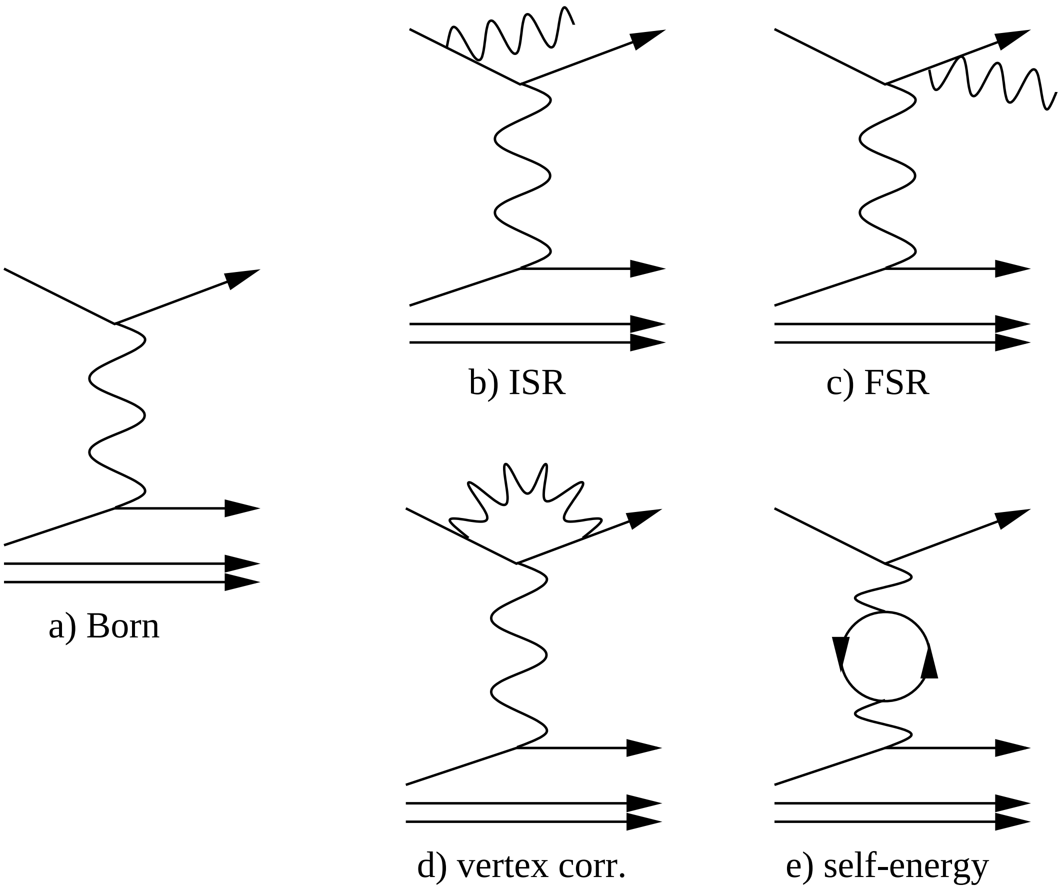

Figure 6.2: Feynman diagrams of the Born level and the LO QED corrections for NC DIS scattering.

DIS events. The inclusive diffractive cross section is parameterized in terms of the diffractive structure function $F_2^{D(4)}(x, Q^2, x_{I\!P}, t)$ introduced in section 1.2.4. In order to simulate QED radiation effects RAPGAP is interfaced with HERACLES. QCD cascades are simulated via leading log parton showers as implemented in the LEPTO program or with the CDMBGF model as implemented in ARIADNE. The hadronisation is performed using the JETSET routines.

6.2.1 RAPGAP with H1 fit

Different approaches exist for the interpretation of the structure function F_2^D in terms of parton distribution functions in analogy to the proton structure function. Using their 1994 data the H1 collaboration has parameterized F_2^D based on the Ingelman and Schlein model of the exchange of a pomeron $I\!P$ with a partonic structure [119]. In order to fit the data a subleading Reggeon $I\!R$ exchange has been assumed in addition to the leading $I\!P$ exchange. The $I\!P$ and $I\!R$ fluxes are taken to have simple Regge motivated forms leading to:

$$F_2^{D(4)}(x, Q^2, x_{I\!P}, t) = \frac{e^{B_{I\!P}t}}{x_{I\!P}^{2\alpha_{I\!P}(t)-1}} F_2^{I\!P}(\beta, Q^2) + \frac{e^{B_{I\!R}t}}{x_{I\!R}^{2\alpha_{I\!R}(t)-1}} F_2^{I\!R}(\beta, Q^2)\ . \tag{6.1}$$

The structure function $F_2^{I\!P}$ is derived from parton distributions which evolve with Q^2 according to the DGLAP equations. The low Q^2 input parton distributions are taken from a QCD fit to data. For the $I\!R$ structure function the parameterization of the pion is taken. The F_2^D

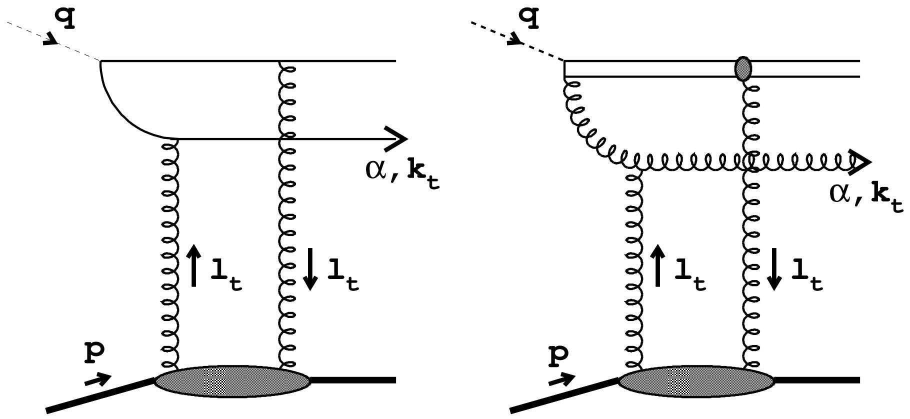

Figure 6.3: Diffractive production of a $q\bar{q}$ and a $q\bar{q}g$ state.

parameterization of H1 has been implemented in RAPGAP and a sample of diffractive events with $Q^2 > 1\,\mathrm{GeV}$ has been generated which will be referred to as RAPGAP sample.

6.2.2 SATRAP

A MC generator based on the saturation model by Golec-Biernat and Wüsthoff [60] introduced in section 1.2.5.II. has been interfaced to the RAPGAP framework. The corresponding event generator is referred to as SATRAP [120]. In the saturation model the photon splits into a $q\bar{q}$ pair which is described by the $\gamma q\bar{q}$ wave function. The $q\bar{q}$ system interacts with the proton with a cross section $\hat{\sigma}_{q\bar{q}}$ which is assumed to be of the form $\hat{\sigma} = \sigma_0\{1 - exp[-r^2/(4R_0^2(x))]\}$, where r is the transverse distance between the quark and the antiquark, $R_0(x)$ defines the saturation radius which is given by $R_0^2(x) = (x/x_0)^\lambda$ and σ_0, x_0 and λ are free parameters. Fluctuations of the incoming photon into a $q\bar{q}g$ state are also taken into account where $\hat{\sigma}_{q\bar{q}} = \hat{\sigma}_{q\bar{q}g}$ is assumed. Using the gluon distribution which is determined by the assumed form of $\hat{\sigma}$, the cross section for the scattering of $q\bar{q}$ and $q\bar{q}g$ states originating from transverse and longitudinal photons has been calculated from the diagrams shown in Fig. 6.3. All free parameters of the model have been determined from fits to HERA total DIS cross section data (i.e. $F_2(x, Q^2)$ data) yielding $\sigma_0 = 23$ mb, $\lambda = 0.29$ and $x_0 = 0.0003$. For the t dependence of the diffractive cross section the form $d\sigma/dt \propto exp(Bt)/B$ with B = 6 GeV^{-2} is assumed.

Due to its good description of the measured total diffractive cross section as a function of Q^2 and W the SATRAP generator has been chosen as the default generator for diffractive events.

The cross section predicted by SATRAP refers to the single dissociation process $\gamma^* p \to Xp$. However, the cross section measured in the present analysis includes processes of the type $\gamma^* p \to XN$ where the proton dissociates into a low mass state N. In order to describe the present data the normalization of SATRAP has to be adjusted. A fit to the measured diffractive cross section yielded a scaling factor of 1.2.

6.2.3 Mixing of diffractive and non-diffractive MC

The topology of the hadronic final state of diffractive and non-diffractive events differs in that diffractive events have lower particle multiplicities. This leads to a difference in the acceptance, i.e. in the probability that an event passes the trigger and offline selection criteria.

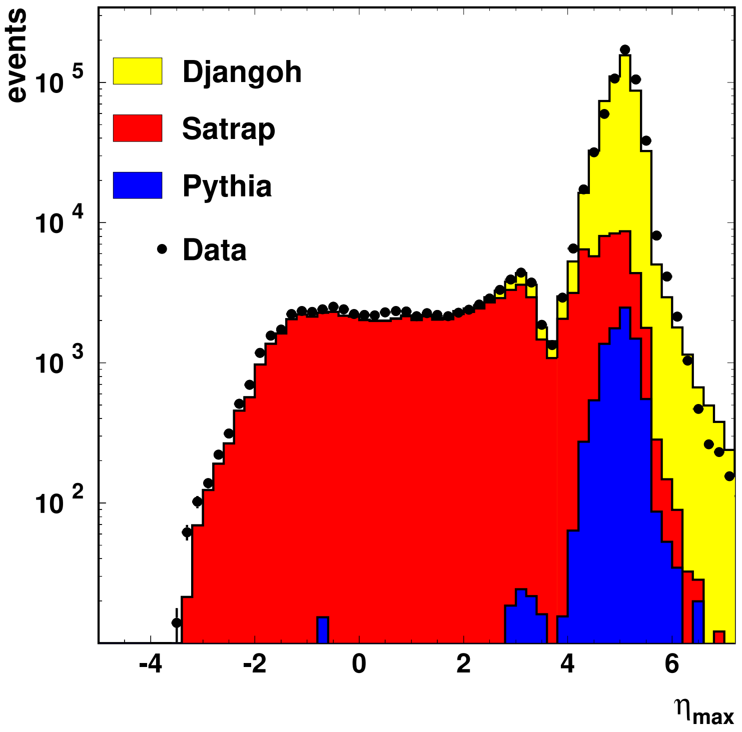

Figure 6.4: The η_{max} distribution for data and MC is shown. The diffractive SATRAP sample is added to the non-diffractive DJANGOH sample according to the procedure described in the text. Also shown is the contribution from photoproduction events simulated with PHYTHIA.

For the extraction of the inclusive cross section (chapter 9) it is therefore important to add the diffractive and non-diffractive MC samples according to the corresponding ratio in the data when computing the acceptance corrections for the data.

The total DJANGOH cross section, which reflects the applied CTEQ4D parameterization of the parton density functions, implicitly includes the diffractive DIS contribution. Therefore, before adding the diffractive sample generated with SATRAP to the DJANGOH sample the latter has to be scaled down such that the total cross section in bins of Q^2 and W does not change with respect to the original cross section generated by DJANGOH. The corresponding scaling factor $\alpha_i^{DJANGOH}$ for each bin i is determined by

$$\alpha_i^{DJANGOH} = 1 - \frac{N_i^{SATRAP}/\mathcal{L}^{SATRAP}}{N_i^{DJANGOH}/\mathcal{L}^{DJANGOH}} \,, \tag{6.2}$$

where N_i^{MC} denotes the number of events generated in bin i and $\mathcal{L}^{MC}$ the generated luminosity.

The distribution of η_{max} is highly sensitive to the ratio of diffractive and non-diffractive events. Here η_{max} is defined as the pseudorapidity of the most forward going energy flow object (see section 7.4.1) measured with an energy of more than 400 MeV. Figure 6.4 shows the η_{max} distribution for data and the combined MC. Good agreement is achieved in the low η_{max} region ($\eta_{max} < 4$) where diffractive events dominate. Some discrepancies can be observed in the high η_{max} (forward) region where the description of the hadronisation of the proton remnant is known to be imperfect. The gap in the distribution around $\eta_{max} = 4$ is due to the fact that no cluster merging is performed between CAL and FPC.

6.3 Generation of photoproduction events

Photoproduction (PhP) represents potentially a serious source of background. In order to estimate the corresponding contamination of the data sample PhP events have been generated using the PYTHIA [116] MC program. The sample has been generated with $Q^2 < 1\,\mathrm{GeV}$ and $y > 0.6$. Events with lower values of y do not enter the data sample since the scattered electron which escapes undetected carries enough energy such that the hadronic system observed in the detector fails the $E - p_Z$ cut.

The PhP MC sample consists of several subsamples which correspond to different production mechanisms with large differences in the hadronic final states [121]. The following processes are considered:

- diffractive PhP processes of the type $\gamma p \to Vp$, $\gamma p \to Xp$, $\gamma p \to VN$ and $\gamma p \to XN$, where V is one of the light vector mesons ρ, ω or ϕ and X (N) is the photon (proton) dissociation system,
- soft non-diffractive processes,
- hard (perturbative) PhP which consists of a direct and a resolved photon component.

The relative contribution of each of these subprocesses has been determined from fits to measured quantities such as the mass of the measured hadronic system M_X, the transverse energy E_T, the maximum pseudorapidity η_{max} and the total calorimeter energy. For subprocesses where ZEUS measurements are available (mainly diffractive processes) the measured cross sections have been used to constrain the contribution of these processes.

In Fig. 6.4 the contribution of photoproduction (PYTHIA) events to the η_{max} distribution is shown. In the low η_{max} region where diffractive events dominate the PhP contribution is observed to be small. The determination of the size of the PhP background is discussed in section 8.3.1.

Chapter 7

Event reconstruction

Measurements of DIS cross sections at HERA require a precise determination of the kinematic event variables such as Q^2 and W introduced in section 1.1.2. The signature of a typical neutral current DIS event in the ZEUS detector is a final state electron of energy E_e' scattered at an angle θ_e with respect to the positive Z-axis (see Fig: 7.1). The hadronic system H consists of the so called current jet originating from the struck quark, the proton remnant which to a large extend escapes through the forward beam pipe and the hadrons emitted in the color field between the struck quark and the proton remnant. The angle γ_h between the current jet and the positive Z-axis corresponds to the polar angle of the struck quark in the naive quark parton model.

In the ZEUS coordinate system as discussed in section 2.2 the initial and final states of the process $e(k) + P(p) \rightarrow e(k^{'}) + H(p^{'})$ can be written as[1]

$$k = \begin{pmatrix} E_e \\ 0 \\ 0 \\ -E_e \end{pmatrix}, \; k^{'} = \begin{pmatrix} E_e^{'} \\ E_e^{'} \sin\theta_e^{'} \cos\phi_e^{'} \\ E_e^{'} \sin\theta_e^{'} \sin\phi_e^{'} \\ E_e^{'} \cos\theta_e^{'} \end{pmatrix}, \quad p = \begin{pmatrix} E_p \\ 0 \\ 0 \\ E_p \end{pmatrix}, \; p^{'} = \begin{pmatrix} E_h \\ p_{X,h} \\ p_{Y,h} \\ p_{Z,h} \end{pmatrix}, \qquad (7.1)$$

[1]Neglecting the masses of the incoming electron and proton.

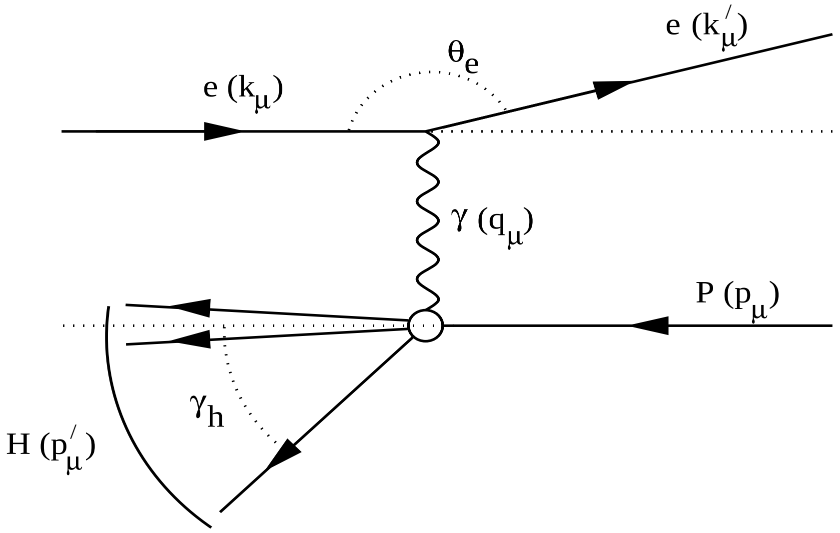

Figure 7.1: Schematic drawing of a NC DIS event.

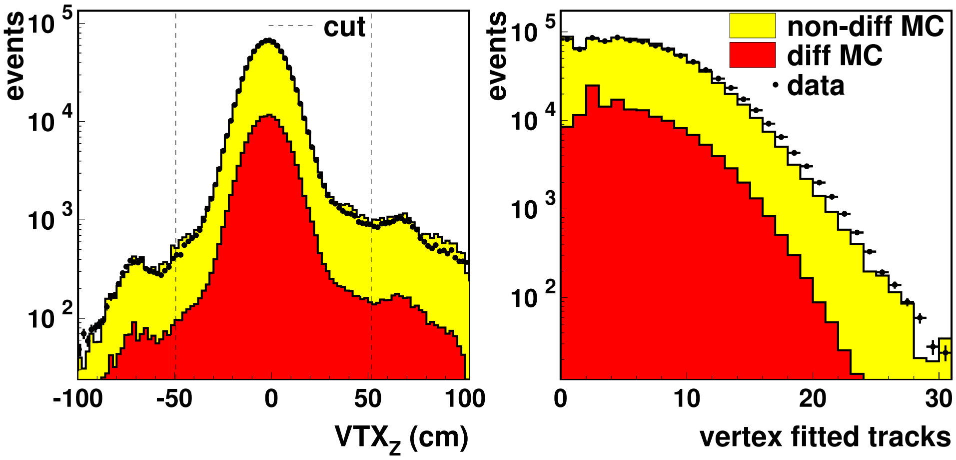

Figure 7.2: The left plot shows the Z component of the vertex measured with the CTD for data and MC. The right plot shows the number of tracks fitted to the vertex. The bin for 0 vertex fitted tracks corresponds to events where no vertex has been measured.

where E_h, $p_{X,h}$, $p_{Y,h}$ and $p_{Z,h}$ denote the 4-vector components of the hadronic system, which are the 4-momentum sums over all final states particles excluding the scattered electron.

As long as the 4-momenta of the electron and the proton in the initial state are known the kinematics of NC DIS events can be determined either from the energy and polar angle of the scattered electron or of the current jet or from any combination of two of these four variables. In the following the measurement of the final state electron and the hadronic system will be described together with a discussion of the methods to extract the kinematic variables.

7.1 Vertex reconstruction

The position of the event vertex is important for the calculation of both the event kinematics and the detector acceptance. For events where either the electron (high Q^2) or the hadronic system (medium and high W) are within the CTD acceptance the event vertex can be measured by fitting the extrapolated CTD tracks to a common vertex [123]. An accuracy of 2 mm has been achieved for the reconstruction of the Z coordinate.

After the final selection cuts an average of 9% of all selected events have no reconstructed vertex (6% of the diffractive events). For events with $Q^2 \lesssim 40\,\mathrm{GeV}^2$ where the electron is emitted outside the CTD acceptance the fraction of events without reconstructed vertex is highly W dependent. In the lowest W bin considered in this analysis (40 GeV $< W <$ 50 GeV) 20% of the events have no reconstructed vertex. For non-diffractive events this fraction drops below 1% for $W >$ 70 GeV. However, for diffractive events with low mass M_X the fraction increases dramatically for $W > 150\,\mathrm{GeV}$. In the highest W and lowest M_X bin the contribution of events without reconstructed vertex is more than 50%. For events with no reconstructed vertex the Z coordinate of the vertex is set to the mean value of the corresponding run. The mean value has been observed to vary within Z = -5 cm and Z = 2 cm.

Since the detector acceptance depends on the vertex position it is important that the MC vertex distribution follows closely that observed in the data. Figure 7.2 shows good agreement between

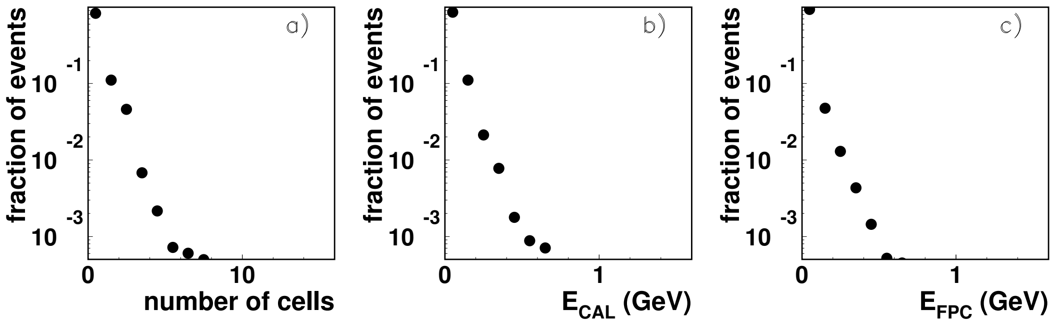

Figure 7.3: For a sample of random trigger events the number of cells and the energy reconstructed in the CAL and in the FPC are shown after applying the noise suppression cuts explained in the text.

data and MC for the reconstructed Z vertex distribution. In addition to the approximately Gaussian peak around Z $\approx$ 0 cm satellite peaks at Z $\approx \pm$ 70 cm can be observed. These originate from protons which spilled over from the main bucket to a neighboring one arriving 4.8 nsec earlier (later).

The number of vertex fitted tracks shows a small excess at high multiplicities (see Fig. 7.2). Nevertheless, a satisfactory overall agreement has been achieved. Most importantly the fraction of events with no reconstructed vertex is well described.

The resolution of the X (Y) vertex position reconstruction is about 1 mm while the size of the beam width is only 200 (50) μm. Therefore, the X and Y coordinates are set to the average value of the corresponding run. The average X coordinate varied between X = +1 mm to X = -1 mm while the Y coordinate was constant at Y $\approx$ +0.4 mm.

7.2 Calorimeter noise reduction

The calorimeter is the main detector component for the measurement of the event kinematics. Noise originating form the electronics and the radioactive decay of the uranium biases the measurement of the hadronic system, in particular the measurement of the hadronic angle γ_h and the mass M_X. It is therefore necessary to develop effective noise suppression algorithms.

The calorimeter noise was studied with random trigger events where no particles traverse the detector and therefore only noise contributes to the detector signal [124]. The noise per calorimeter cell due to the radioactivity of the uranium is centered around zero and has an approximated Gaussian shape with a standard deviation of $\sim$ 18 MeV in the EMC and $\sim$ 27 MeV in the HAC section. At the reconstruction level a noise suppression cut of 60 MeV for EMC cells and 110 MeV for HAC cells is applied to each calorimeter cell.

After this global cut an average of 8 cells with energies above the noise cut remain per event from a total of 5918 cells. These noise cells are mostly due to mini sparks in one of the two PMTs of each cell. Since in this case only one of the two PMTs belonging to a cell fired the absolute value of the imbalance $Imb = \frac{E_l - E_r}{E_{cell}}$ of the energy in the left (E_l) and the right (E_r) PMT is close to 1, where $E_{cell} = E_l + E_r$ is the total energy in the cell. Mini sparks are suppressed by removing single isolated cells with:

$$|Imb| > 0.49 + \frac{0.03GeV}{E_{cell}} . \tag{7.2}$$

In addition, there are cells which have been noisy for certain run periods; they are identified by a significantly higher mean energy or higher firing frequency compared to other cells. These 'known' noisy cells are removed if their energy is less than three sigma above the noise level. This cut is particularly important for cells where one PMT is dead and the cell energy is calculated as $E_{cell} = 2 \cdot E_2$, where E_2 is the energy in the remaining PMT. In this case sparks cannot be removed with the imbalance cut above.

In order to further reduce the noise level a cut of 120 (160) MeV is applied to isolated EMC (HAC) cells. The remaining number of firing calorimeter cells and the distribution of the summed calorimeter energy is shown in Fig. 7.3 (a,b). The number of events with a noise signal in the CAL is reduced below 12%.

The noise in the FPC which is dominated by noise in the PMTs and the readout electronics is treated separately. A cut of 60 MeV is applied to all FPC cells. In addition isolated cells with energy less than 90 MeV are rejected. The FPC energy distribution for random trigger events after these noise reduction cuts is shown in Fig. 7.3(c). The number of events with a noise signal in the FPC after cuts is reduced below 8%.

7.3 Electron identification and reconstruction

A scattered electron in the final state is the characteristic feature of a neutral current DIS event. An efficient identification and a correct reconstruction of the DIS electron is therefore crucial for this analysis.

7.3.1 Electron identification

The identification of the DIS electron is based on the difference between the shower development of electromagnetic and hadronic showers in the calorimeter. Electromagnetic particles deposit their energy mainly in the EMC section of the calorimeter and little or no energy is registered in the HAC section. Also the lateral shower size is in general smaller for electromagnetic showers.

Due to momentum conservation the transverse momentum of the electron $P_{T,e}$ is balanced by the transverse momentum of the current jet $P_{T,h}$. Therefore, for high Q^2 (high $P_{T,e}$) events the electron is well separated from the hadronic system. However, at low Q^2 and high W, where also the current jet is scattered into the rear direction (compare Fig. 7.11), there is some overlap between the hadronic activity and the electron shower, which requires special attention.

In order to achieve optimum separation the energy deposits in the calorimeter are clustered to form islands. Cells which have higher energy than all their neighbors form cluster seeds and all other cells are associated with the neighboring cell of highest energy. The geometry of the calorimeter, including the gaps between the BCAL and the F- and RCAL, is taken into account.

For each island the probability P_{SI} that it was produced by an electromagnetic particle is determined using a neural network algorithm (named SINISTRA [125, 126]) trained with MC. An

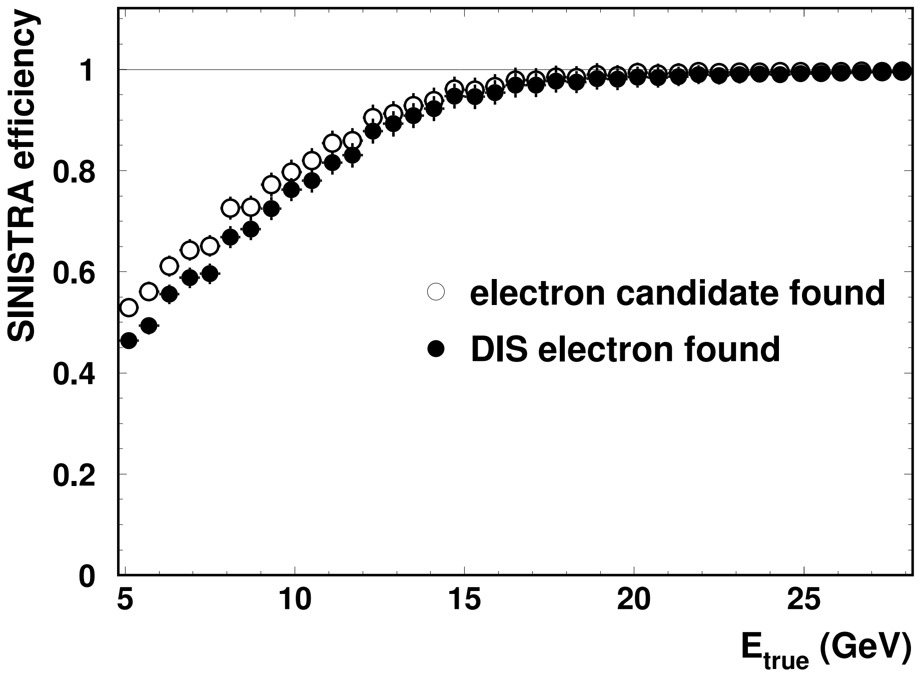

Figure 7.4: The efficiency of the electron finder SINISTRA to find any electron candidate (open points) and the efficiency to find the correct DIS electron (solid points) is plotted as a function of the true electron energy.

island is called an electron candidate if $P_{SI} > 0.9$. The candidate with the highest probability is chosen as the DIS electron. In case of two candidates with equal probability the one with the higher energy is chosen.

In Fig. 7.4 the efficiency to find an electron candidate as well as the efficiency to find the correct DIS candidate is shown as a function of the true electron energy. The efficiency has been determined with a DIS MC sample generated with $Q^2 > 1\,\mathrm{GeV}^2$. In order to determine whether the correct DIS electron was found the angle of the electron candidate is compared with that of the generated electron.

The efficiency to find the DIS electron is $\sim 77\%$ at 10 GeV reaching close to 100 % at 15 GeV. At low energies where some of the hadronic showers look more like electromagnetic showers, the efficiency drops significantly. Also, showering of the electron in the material in front of the calorimeter makes the identification of the electron more difficult.

The main source of islands that are wrongly identified as a DIS electron are photons radiated off the initial state electron under large angles such that they hit the calorimeter. Also electromagnetic showers from $\pi^0 \to \gamma\gamma$ may fake an electron.

7.3.2 Electron position reconstruction

The measurement of the impact position of the electron at the calorimeter surface combined with the event vertex determines the electron scattering angle. The impact position is deter-

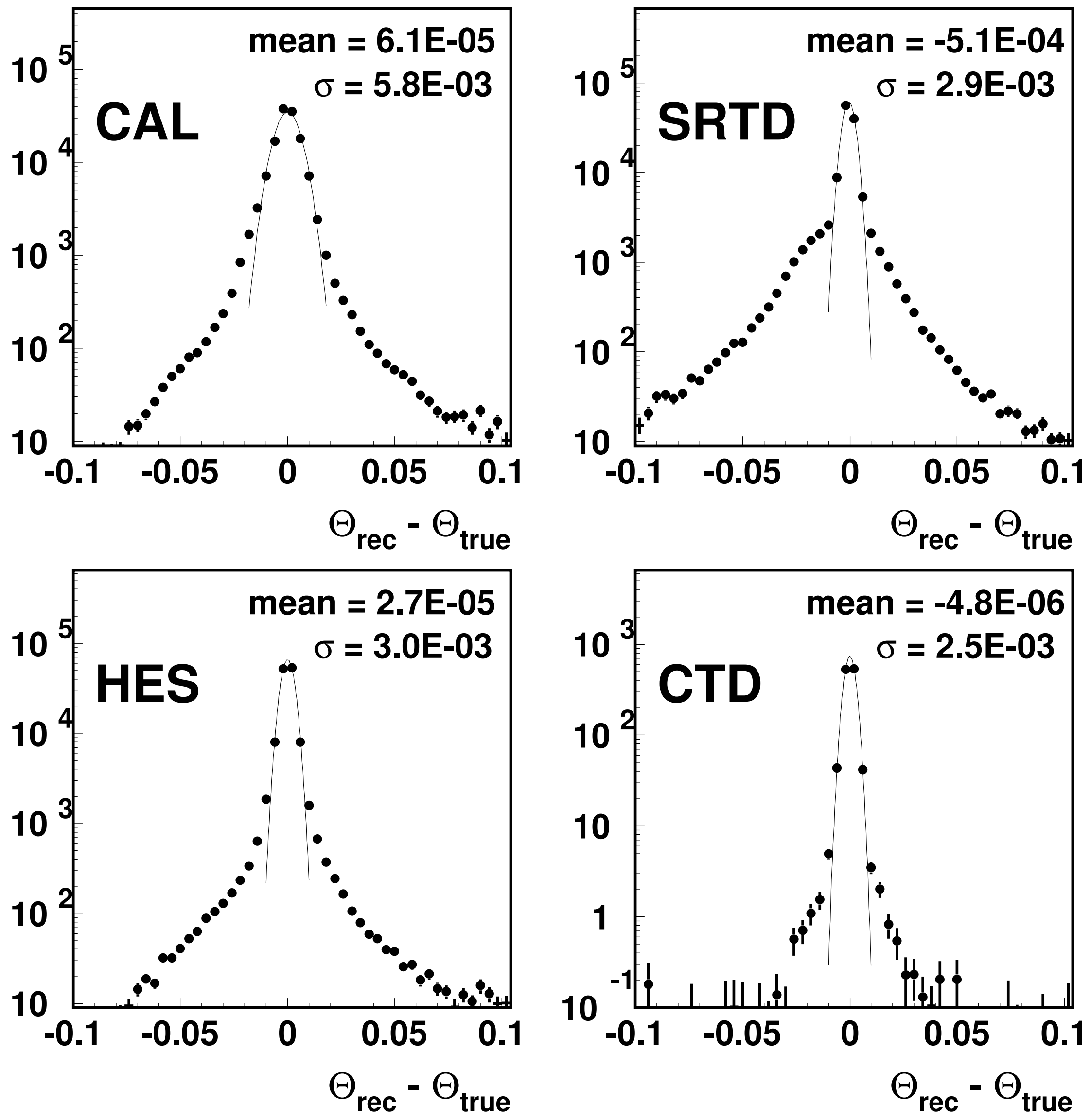

Figure 7.5: The resolution of the scattering angle (in rad) of the electron as measured with the calorimeter, the SRTD, the HES and the CTD.

mined from the calorimeter cells belonging to the electron cluster. The detector components CTD, SRTD and HES are used to improve the measurement of the scattering angle whenever the electron trajectory is within the respective acceptance region. In Fig. 7.5 the resolution of the scattering angle for each of these detectors is compared to that of the calorimeter.

I. Calorimeter position measurement

For the determination of the calorimeter cluster position the ELECPO algorithm [127, 128] is used. The cell with the highest energy and its 8 surrounding neighbor cells are considered. The Y coordinate of the RCAL is calculated as the weighted average of the cell center coordinates using weights proportional to the logarithm of the cell energy. This method is similar to the one used for the FPC position reconstruction described in section 5.6.2.

For the RCAL X coordinate the geometric centers of the cells are corrected using the cell imbalance. Since the light absorption in the scintillator plates is proportional to the distance between the energy deposition and the lightguide on either side of the cell, the imbalance is strongly correlated with the impact position. The corrected cell positions are then combined using the logarithmic weighting method.

The position obtained with the calorimeter has been compared to the position obtained with the SRTD (see below). A resolution of $\sigma_X = 9mm$ and $\sigma_Y = 7mm$ has been found.

II. HES position measurement

In the RCAL region the HES information is used to improve the measurement of the electron impact position. HES diodes which have the highest signal among their neighbor diodes are taken as cluster seeds. Only seeds with a signal corresponding to more than 5 mips are considered. The position of the cluster, which is defined by the seed diode and the 8 surrounding diodes, is calculated using a logarithmic weighting method. The HES position resolution has been studied with test beam measurements and found to be $\sigma_{X,Y} \sim 5mm$.

The HES cluster closest to the calorimeter cluster position is searched for. If the distance between the two is less than 6 cm and the signal of the total HES cluster is more than 40 mips the calorimeter position is replaced by the HES position. The latter condition is fulfilled by about 90% of the electrons. It ensures a high resolution and reduces systematic biases observed at boundaries of the HES acceptance region.

III. SRTD position measurement

In the vicinity of the RCAL beamhole the position measurement is further improved using the SRTD. Due to its fine granularity of 1 cm wide strips it allows to measure the electron impact position with a resolution of $\sigma_{X,Y} \sim 3.5mm$. Further details on the reconstruction algorithm can be found in [129].

If more than one particle hits a SRTD quadrant the matching of the X and the Y hits may not be unique. Matching the wrong pair of SRTD hits leads to long tails in the resolution. The SRTD position is therefore only considered whenever it is within 4 cm of either the calorimeter or the HES position.

The SRTD allows an unbiased measurement of the electron impact position up to 1 cm from the RCAL beam whole as can be seen in Fig. 7.6, while the angles reconstructed with the calorimeter and with the HES show systematic biases close to the RCAL beamhole ($\theta_{RCAL} \sim 3.1$ rad).

IV. Track measurement with the CTD

If the DIS electron is scattered into the acceptance region of the CTD ($Q^2 \gtrsim 100\,GeV^2$) the scattering angle can be determined with high accuracy using the reconstructed track. Whenever

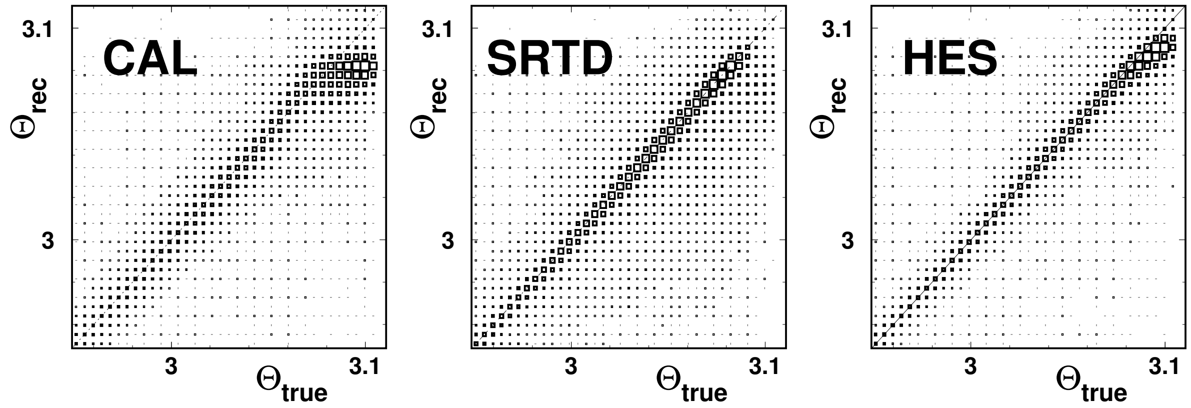

Figure 7.6: The reconstructed (rec) versus the true polar angle (in rad) of the electron is shown for reconstruction by RCAL, SRTD and HES.

a good[2] CTD track is found with a distance of closest approach to the electron cluster in the calorimeter of less than 20 cm, the scattering angle is taken from the track measurement. The CTD provides the best scattering angle resolution of $\sigma(\Delta\Theta) = 2.5$ mrad (compare Fig. 7.5).

V. Alignment studies

For an unbiased measurement of the electron scattering angle it is essential to know the precise position of each relevant detector component. A series of relative alignment studies has been performed using scattered electrons with a good reconstructed position in two detector components. In order to avoid systematic biases at the edges of the acceptance regions the reconstructed electron tracks are required to be within the combined acceptance region of both detector components.

The reference system is given by the CTD. First the HES is aligned with respect to the CTD. Since the position of the HES inside the calorimeter is well know and mechanically stable, no further alignment of the calorimeter is necessary. The SRTD is finally aligned to the HES. An independent check has been performed using the rear tracking detector (RTD) to align the SRTD. The accuracy of the relative alignments was estimated to be in the order of 1 mm.

7.3.3 Electron energy measurement

A precise and unbiased measurement of the electron energy is essential for the reconstruction of the event kinematics. Earlier analyses have shown that the MC does not fully describe all detector details leading to discrepancies between the electron energy distributions in data and MC. Therefore, several corrections have been developed which will be described in the following.

In order to check the accuracy of the energy measurement events with $y_{JB} < 0.04$ and $Q_e^2 < 100$ GeV^2 have been selected[3]. For these so called kinematic peak events the energy of the scattered

[2]A CTD track is considered to be good if it traverses at least 3 superlayers.

[3]For the definition of the reconstruction methods see 7.5.

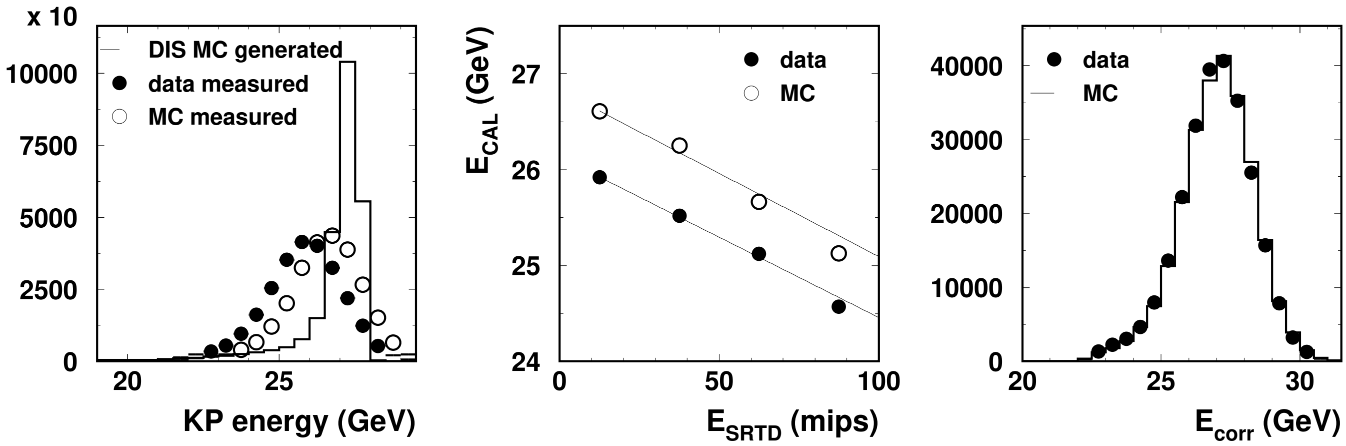

Figure 7.7: Electron energy study using kinematic peak (KP) events in data and MC. *Left*: The generated energy of the scattered electron of KP events is compared to the calorimeter energy. *Center*: The peak calorimeter energy of KP events is plotted as a function of the energy in the SRTD. *Right*: The electron energy after SRTD and energy scale correction for data and MC.

electron is peaked at the electron beam energy. They provide quasi test beam conditions and allow to compare data and MC with high precision.

From the left plot in Fig. 7.7 it can be seen that the distribution of the true electron energy of kinematic peak events is sharply peaked near the beam energy of 27.6 GeV. The tail to lower energies is due to events with initial state photon radiation. The reconstructed calorimeter energy is considerably lower in both MC and data. This is due to energy loss by electrons in interactions with inactive material in front of the calorimeter. The approximately 2% discrepancy between data and MC is thought to be due to an insufficient description of the inactive material in the MC and a small scale problem in the calorimeter.

The amount of energy lost due to showers in the inactive material in front of the calorimeter can be estimated from the energy deposited in the SRTD and the presampler. The energy deposited in these detectors is proportional to the number of traversing particles. The signals are calibrated relative to the signal of a minimum ionizing particle (mip). The energy loss is roughly proportional to the number of particles produced in showers in the inactive material. The electron energy for each event can therefore be corrected using the following linear ansatz:

$$E_{corr} = E_{CAL} + C_{SRTD/PRES} \cdot E_{SRTD/PRES} \ , \tag{7.3}$$

where E_{CAL} is the energy measured in the CAL, $E_{SRTD/PRES}$ is the energy signal recorded in the SRTD or PRES, respectively, $C_{SRTD/PRES}$ is a correction factor and E_{corr} is the corrected energy. Measuring the peak position of kinematic peak events as a function of the SRTD signal the correction factor was found to be $C_{SRTD} = 0.0162$ (0.0172) GeV/mip for data (MC) (see central plot in Fig. 7.7).

Since the presampler in front of the RCAL was not fully operational during the data taking period relevant for the present analysis it has not been used for event by event corrections.

In order to study the energy scale of the RCAL, kinematic peak events[4] with small signals in

[4]For cells with $R_i > 50cm$ the electron energy determined by the double angle method is compared to the

the SRTD and the presampler have been selected. The latter requirement selects non-showering electrons which makes the study independent of the effect of inactive material. Comparing the peak energy in data and MC a correction factor was obtained for each EMC cell. The mean correction factor was found to be 1.01 with cell-to-cell variations of 3% (see [130] for further details). The right plot in Fig. 7.7 shows that after the correction there is good agreement between data and MC.

7.4 Measurement of the hadronic system

The energy E_h and the angle γ_h of the hadronic system are independent variables for the determination of the event kinematics. Also, the separation of diffractive and non-diffractive events is based on the characteristics of the hadronic final state. An accurate measurement of the hadronic system is therefore very important. In this analysis the invariant mass M_X of the hadronic system inside the detector acceptance is of particular importance for the measurement of the diffractive cross section (see 10.3).

7.4.1 The energy flow algorithm

The measurement of the hadronic system is mainly based on the calorimeter information. In the forward region by including the FPC the calorimetric acceptance can be extended up to $\eta = 5$. In the central rapidity region ($-1.75 < \eta < 1.75$) the measurement may be improved including tracking information. The energy measurement is affected by scattering and showering in the inactive material in front of the calorimeter. Low energy particles may not even reach the calorimeter and are therefore lost for the calorimetric measurement. In general, for low energy particles the tracking measurement is more precise than the calorimeter measurement. An energy flow algorithm, also referred to as EFO[5] algorithm, combining calorimeter and tracking information has been developed at ZEUS [131]. For this analysis the EFO algorithm has been extended to include also the FPC. The algorithm will be shortly described in the following.

I. Calorimeter islands

Since particles hitting the calorimeter usually deposit energy in more than one cell, the calorimeter cells are clustered. In a first step all cells are clustered into so-called cell islands by connecting each cell to its neighboring cell with highest energy. Since cell islands are searched for in a local neighborhood only cells belonging to the same calorimeter sections (EMC, HAC1 and HAC2 in FCAL, BCAL, RCAL and FPC) are merged.

The energy deposit of a single particle may be split into separate cell islands. In a second step cell islands are therefore merged to form cone islands. The merging is based on their distance in $\theta - \phi$ space. The maximum distance for which two cell islands are merged has been optimized using MC.

In the FPC-FCAL boundary region it is difficult to cluster energy deposits originating from only one particle due to the high particle multiplicity in that region. For this reason the cone

measured energy.

[5] In the ZEUS jargon the EFO algorithm is often referred to as the ZUFO algorithm.

island clustering is not performed in that region and therefore FPC clusters are not merged to FCAL clusters.

The position of the cone islands is determined using the imbalance of each cell and performing logarithmic weighting as described in section 7.3.2.I. for the calorimeter cluster of the electron.

II. Track-calorimeter matching

In order to match tracks with calorimeter cone islands the tracks are extrapolated into the calorimeter. The distance of closest approach Δ_{DCA} to the cone island is determined. If

$$\Delta_{DCA} \leq \max(r_{min}, r_{isl}) \tag{7.4}$$

the track is matched with the calorimeter island, where r_{isl} is the radius of the island and r_{min} has been tuned to 20 cm.

III. Track or calorimeter cluster

When matching tracks with calorimeter islands different kinds of objects are created which are treated according to the following rules:

- Charged tracks not associated with a calorimeter island are treated as pions.
- Calorimeter islands with no associated tracks are treated as massless neutral particles.
- Islands with three or more tracks pointing to them are counted as one particle with three times the mass of a pion.
- For islands associated with exactly one track the calorimeter information is replaced by the track measurement if the following conditions are satisfied:
  - The track passes at least four CTD superlayers and its transverse momentum is within $0.1 < P_T < 20$ GeV, which ensures good track resolution.
  - The resolution of the momentum p_{trk} measured with the CTD is better than the resolution of the island energy E_{isl} measured with the calorimeter:
    $\Delta p_{trk}/p_{trk} < \Delta E_{isl}/E_{isl}$.
    For hadronic (electromagnetic) particles the tracking resolution is superior for particle energies below 18(13) GeV.
  - $E_{isl}/p_{trk} < 1 + 1.2 \cdot \Delta(E_{isl}/p_{trk})$,
    which suppresses cases where the calorimeter island includes also energy originating from a neutral particle.
- For two tracks associated with one island and one track associated with more than one island the rules are more involved.

The above algorithm produces a set of energy flow objects which are characterized by their energy and three-momentum vector.

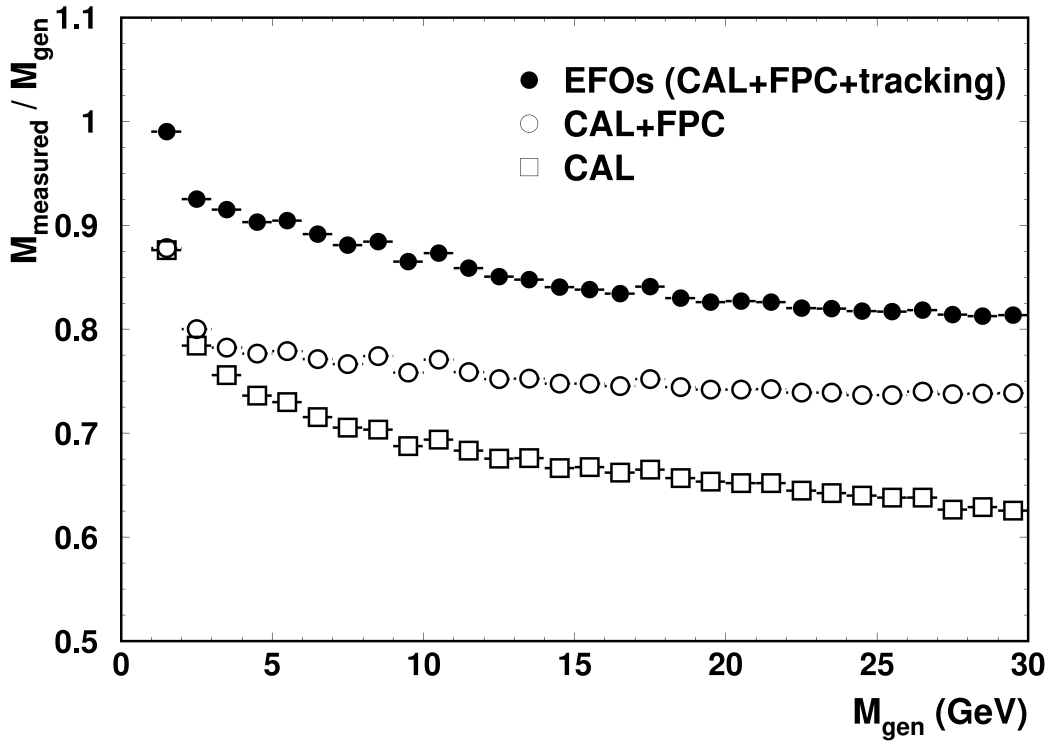

Figure 7.8: The ratio of the measured and generated mass of the hadronic final state M_X as a function of the generated M_X is shown for different reconstruction methods. The mass $M_{X,gen}$ is defined by all particles belonging to the hadronic final state which are emitted with $\eta < 5.5$. For this study the SATRAP diffractive MC was used.

7.4.2 M_X measurement

The invariant mass M_X of the hadronic system observed in the detector is calculated according to:

$$M_X^2 = (\sum_j E_j)^2 - (\sum_j p_{X,j})^2 - (\sum_j p_{Y,j})^2 - (\sum_j p_{Z,j})^2 , \tag{7.5}$$

where the sum runs over all energy flow objects.

The improvement introduced by adding the FPC and the tracking to the CAL information can best be seen by comparing the measurement of M_X using either the EFO algorithm or the CAL information. In Fig. 7.8 the ratio of the measured mass $M_{X,meas}$ and the generated mass $M_{X,gen}$ is shown as a function of $M_{X,gen}$. For this study a diffractive MC sample was used. The mass $M_{X,gen}$ is defined as the invariant mass of all particles belonging to the hadronic final state which are emitted in the pseudorapidity range $\eta < 5.5$.

7.4.3 Energy Scale

The understanding of the energy scale of the detector is of vital importance for an unbiased event reconstruction. A series of studies has shown that the energy scale in the calorimeter is not well described in the MC. This is thought to be mainly due to incomplete description of the dead material in front of the calorimeter. In the RCAL region an energy scale factor as determined with kinematic peak events (see section 7.3.3) has been applied to data separately for each cell. The BCAL energy has been scaled globally by +5% according to the study presented in [132].

In order to check the energy scale after applying the above mentioned scaling of the CAL energy in the data the ratio of the transverse momenta of the electron $p_{T,e}$ and the hadronic system $p_{T,h}$ has been compared between data and MC for different γ_h regions. Since $p_{T,h}$ is nearly balanced by $p_{T,e}$ [6] the ratio $p_{T,h}/p_{T,e}$ is expected to be close to 1. As the electron is measured with much higher precision than the hadronic system the observed deviation from 1 is mainly due to the limitation of the measurement of the hadronic system. The ratio $p_{T,h}/p_{T,e}$ provides a good test of the hadronic energy scale since it can be studied independently for data and MC. Figure 7.9 shows that the energy scale is known to better than 3% which is the uncertainty used for systematic checks.

7.4.4 Electron energy split off

For electrons hitting the RCAL close to the rear beam hole, part of the electromagnetic shower which develops inside the calorimeter material can escape into the beam hole. These shower particles can reenter the calorimeter at the opposite side of the beam hole. The electron clustering algorithm (see section 7.3.1), in general, does not merge this energy deposition with the main electron energy deposition. The leakage energy is therefore considered as hadronic energy. The left plot in Fig. 7.10 shows the average amount of energy identified as hadronic energy in the calorimeter cells around the RCAL beam hole as a function of the electron impact position. For data the hadronic energy around the beam hole increases when the impact position approaches the beam hole. Unfortunately, due to an imperfection in the detector simulation, this effect is not modeled in the MC.

Although the amount of energy thus misidentified as hadronic energy is relatively small (a few 100 MeV, see Fig. 7.10) the effect on the measurement of the hadronic angle is not negligible especially for low W events where the hadronic system is produced mainly in the forward direction. Since the effect is not reproduced in the MC the following cut has been applied to reject this misidentified hadronic energy:

Hadronic energy E_h^{R1} in the first cells around the RCAL beam hole is rejected if:

- the electron impact position (X_e,Y_e) at the RCAL surface is: $|X_e| < 20$cm and $|Y_e| < 15$cm and
- $E_h^{R1} < 1GeV$.

7.5 Reconstruction of kinematic variables

Under the assumption that the energies of the incoming electron and proton are those of the two beams, the event kinematics is overconstraint by measuring energy and scattering angle of

[6] Neglecting the p_T of the proton remnant escaping through the forward beam hole which is small for most of the events.

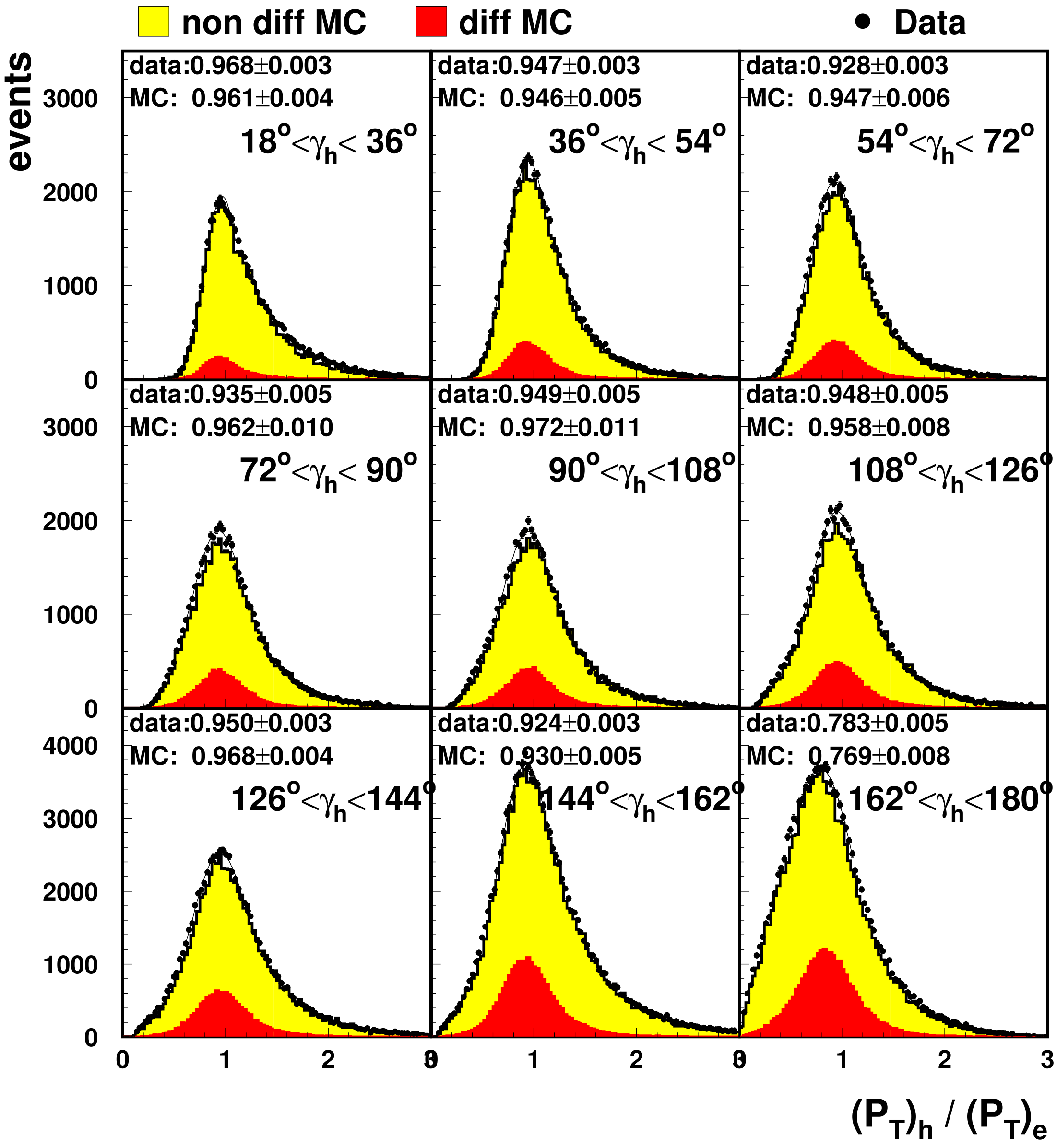

Figure 7.9: The ratio $p_{T,h}/p_{T,e}$ is shown for different regions of the hadronic angle γ_h for data and MC.

both the electron and the hadron system. There are thus several methods to reconstruct the kinematic variables out of the directly measured quantities discussed in the previous sections. Figure 7.11 shows the dependence of Q^2 and W on the energy and angle of the scattered electron and the current jet. The resolution of the kinematic variables depends on the detector resolution and on the chosen reconstruction method and varies strongly over the phase space.

In the following the most common reconstruction methods are introduced and the chosen e, Σ method which provides a satisfactory resolution over the entire phase space relevant for this thesis is discussed.

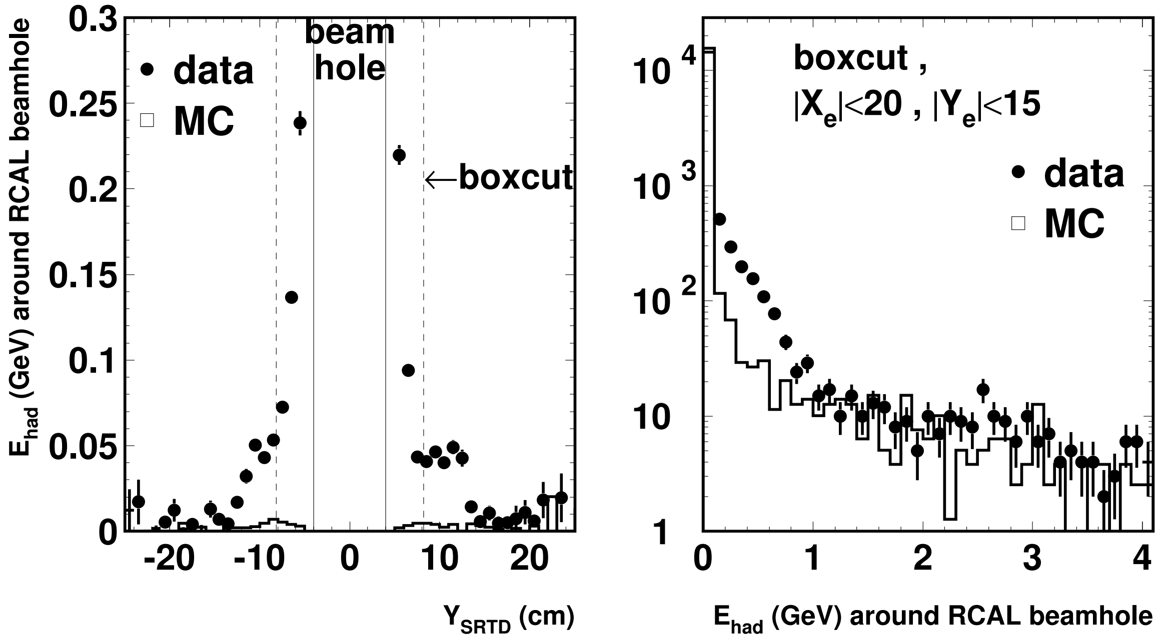

Figure 7.10: *Left*: The energy attributed to the hadronic system in the first cells around the RCAL beam hole is plotted as a function of the electron impact position measured with the SRTD. The following cuts have been applied: $|X_{el,SRTD}| < 10\text{cm}$ and $W_\Sigma < 100\text{GeV}$. The increase of the hadronic energy in the vicinity of the RCAL beam hole is due to showering particles originating from the electron which leak through the RCAL beam hole. The effect is not simulated in the MC. *Right*: For electrons passing the boxcut the hadronic energy around the RCAL beam hole is plotted for data and MC. A significant excess of events with energies below 1 GeV is observed in the data, which is attributed to the above mentioned leakage effect.

7.5.1 The electron method

The electron method uses only the measured electron energy E' and angle θ'_e. Equation 7.1 and 1.7 yield

$$y_{el} = 1 - \frac{E'_e}{2E_e}(1 - \cos\theta'_e) \tag{7.6}$$

$$Q^2_{el} = 2E_e E'_e(1 + \cos\theta'_e) \tag{7.7}$$

$$x_{el} = \frac{E_e}{E_p}\frac{E'_e(1 + \cos\theta'_e)}{2E_e - E'_e(1 - \cos\theta'_e)}, \tag{7.8}$$

As can be seen in Fig. 7.13 the Q^2 reconstruction of the electron method is very precise. However, the reconstruction of W is poor at low values of W. This can be understood from Fig. 7.11 where it can be seen that the dependence of W on θ'_e and also on E' is weak at low W.

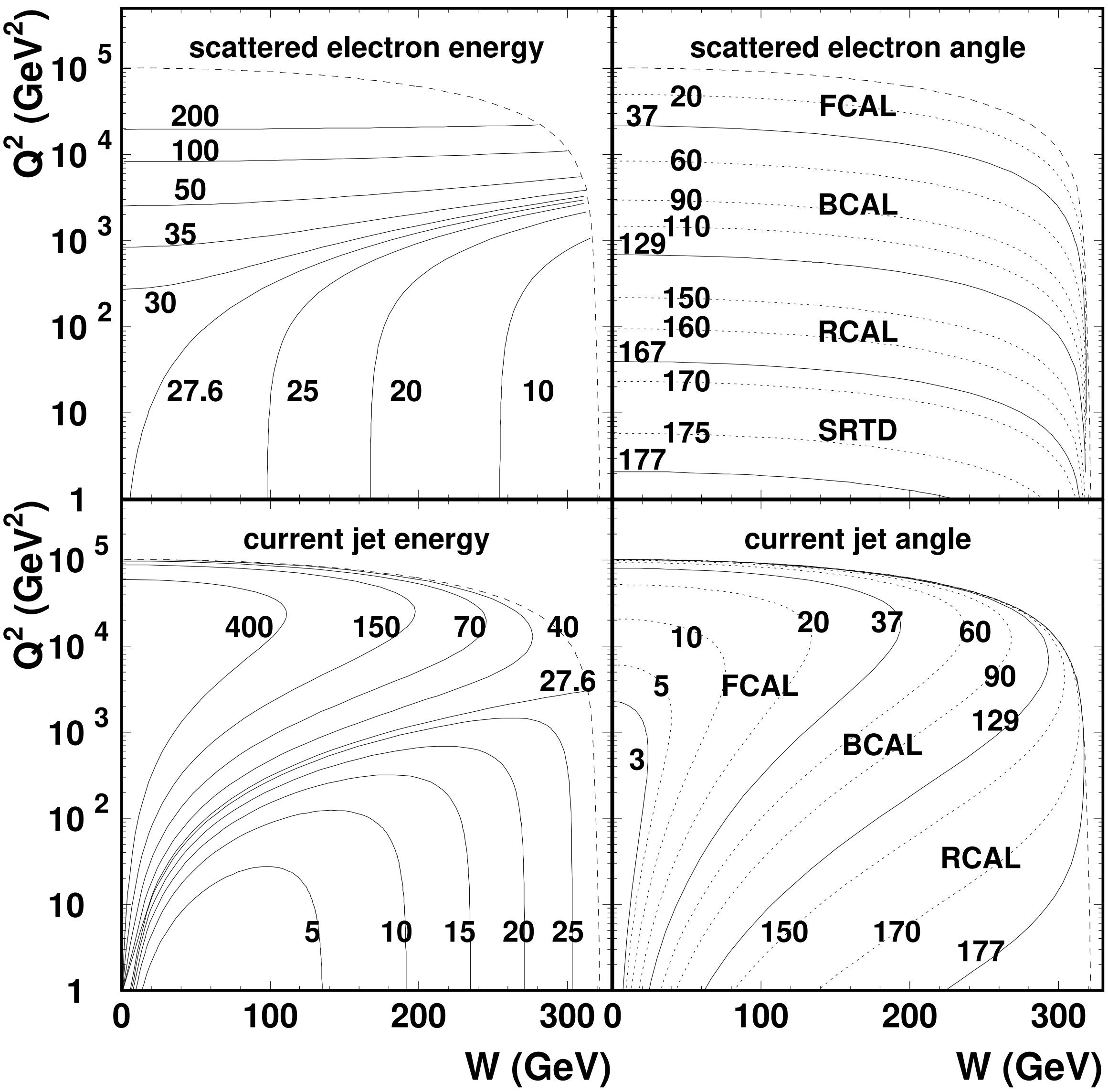

Figure 7.11: Isolines of constant electron energy, constant electron angle, constant current jet energy and constant current jet angle in the (Q^2,W) plane.

7.5.2 The hadron method

Since ZEUS is a 4π detector the kinematic variables can be determined from the measurement of the hadronic system. The variables used by a reconstruction method based on the hadronic system have to be insensitive to fragmentation effects and energy losses in the forward direction since part of the hadronic system escapes through the forward beam hole. Such a method has been developed by Jacquet and Blondel in [133]. It rests on the assumption that the total transverse momentum carried by those hadrons which escape detection through the beam hole in the proton direction as well as the energy carried by particles escaping through the beam hole in the electron direction can be neglected. The method is based on the quantities $\delta_h = (E_h - p_{Z,h})$ and $p^2_{T,h} = p^2_{X,h} + p^2_{Y,h}$ which are measured from the sum over all EFOs according to

$$\delta_h = \sum_j E_j - p_{Z,j} \tag{7.9}$$

$$p^2_{T,h} = (\sum_j p_{X,j})^2 + (\sum_j p_{Y,j})^2 \,. \tag{7.10}$$

The Jacquet-Blondel (JB) method yields

$$y_{JB} = \frac{\delta_h}{2E_e} \tag{7.11}$$

$$Q^2_{JB} = \frac{p^2_{T,h}}{1 - y_{JB}} \tag{7.12}$$

$$x_{JB} = \frac{Q^2_{JB}}{s \cdot y_{JB}}. \tag{7.13}$$

While the resolution of W_{JB} at low values of W is superior to the electron method the Q^2_{JB} reconstruction is poor (see Fig. 7.13).

7.5.3 The double angle method

The double angle (DA) method is based on the measurement of the angles θ'_e and γ_h of the scattered electron and the current jet, respectively [134, 135]. It is motivated by the fact that angles are often measured with better accuracy than energies. In particular the DA method is in first order independent of the energy scale of the detector. The hadronic angle γ_h can be calculated from the hadronic system according to:

$$cos\gamma_h = \frac{p^2_{T,h} - \delta^2_h}{p^2_{T,h} + \delta^2_h}. \tag{7.14}$$

The kinematic variables are then given by:

$$\begin{aligned}
y_{DA} &= \frac{\sin\theta'_e(1-\cos\gamma_h)}{\sin\theta'_e + \sin\gamma_h - \sin(\theta'_e + \gamma_h)} \\
Q^2_{DA} &= 4E_e^2 \cdot \frac{\sin\gamma_h(1+\cos\theta'_e)}{\sin\theta'_e + \sin\gamma_h - \sin(\theta'_e + \gamma_h)} \\
x_{DA} &= \frac{E_e}{E_p} \cdot \frac{\sin\theta'_e + \sin\gamma_h + \sin(\theta'_e + \gamma_h)}{\sin\theta'_e + \sin\gamma_h - \sin(\theta'_e + \gamma_h)}
\end{aligned} \tag{7.15}$$

7.5.4 The Σ-method

So far it has been assumed that the momenta of the incoming beam particles in the interaction are known. This is, however, only the case if there is no QED radiation off the DIS electron. Final State Radiation (FSR) is not a problem since the granularity of the detector is not fine enough to separate the scattered electron and the FSR photon, which is radiated almost collinearly off the scattered electron. In case of Initial State Radiation (ISR), however, a photon of energy E_γ is radiated almost collinear with the initial state electron and escapes through the

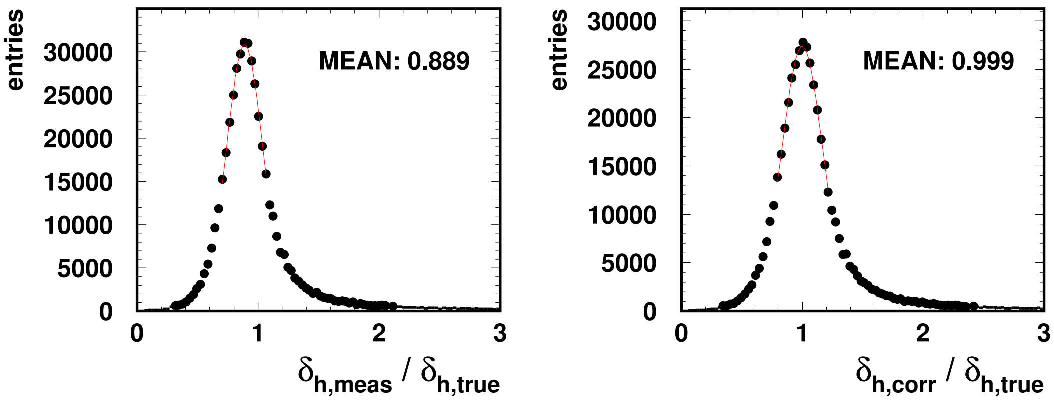

Figure 7.12: The distribution of $\delta_{h,meas}/\delta_{h,true}$ and $\delta_{h,corr}/\delta_{h,true}$ are shown, where $\delta_{h,meas}$ is calculated using EFOs and $\delta_{h,corr} = c_\delta \cdot \delta_{h,meas}$. The mean of a Gaussian fit is given.

rear beam pipe. The electron energy at the interaction vertex is thus reduced to $\tilde{E}_e = E_e - E_\gamma$. While for fully contained events $\Sigma \equiv \delta = \delta_h + \delta_e = E_h - p_{Z,h} + E'_e(1 - \cos\theta'_e)$ is given by $\delta = 2E_e$ it is reduced to $\delta = 2(E_e - E_\gamma) = 2\tilde{E}_e$ for ISR events. The idea of the Σ-method [136] is therefore to replace the scale $2E_e$ in the calculation of y_{JB} by δ:

$$\begin{aligned} y_\Sigma &= \frac{\delta_h}{\delta} \\ Q^2_\Sigma &= \frac{E'^2_e \sin^2\theta'_e}{1 - y_\Sigma} \\ x_\Sigma &= \frac{Q^2_\Sigma}{s \cdot y_\Sigma} \end{aligned} \tag{7.16}$$

At high y the current jet emerges in the rear direction and part of the hadronic system can escape though the rear beam hole. Since this affects δ and δ_h in the same way y_Σ is relatively insensitive to such losses. As can be seen in Fig. 7.13 the resolution of y_Σ is indeed improved with respect to y_{JB}: y_Σ combines the advantages of y_{el} and y_{JB}.

I. δ correction

The left plot in Fig. 7.12 shows the distribution of the ratio $\delta_{h,meas}/\delta_{h,true}$ for a DIS MC sample, where $\delta_{h,meas} = \sum_{i \in EFOs}(E - p_Z)_i$ is calculated using energy flow objects. It can be seen that the distribution peaks significantly below 1. This is mainly due to energy losses in the inactive material which is not recovered by the EFO algorithm. Since δ_h is a crucial quantity when using the JB or the Σ-method a global correction factor $c_\delta = 1.125$ has been applied leading to $\delta_{h,corr} = c_\delta \cdot \delta_{h,meas}$, which peaks around 1 (see right plot in Fig. 7.12). Using $\delta_{h,corr}$ instead of $\delta_{h,meas}$ significantly reduces the bias in the measurement of y_Σ.

Due to its superior resolution the Σ-method has been used for reconstruction of y in the present analysis. For Q^2 the electron method has been chosen due to its simplicity and good resolution.

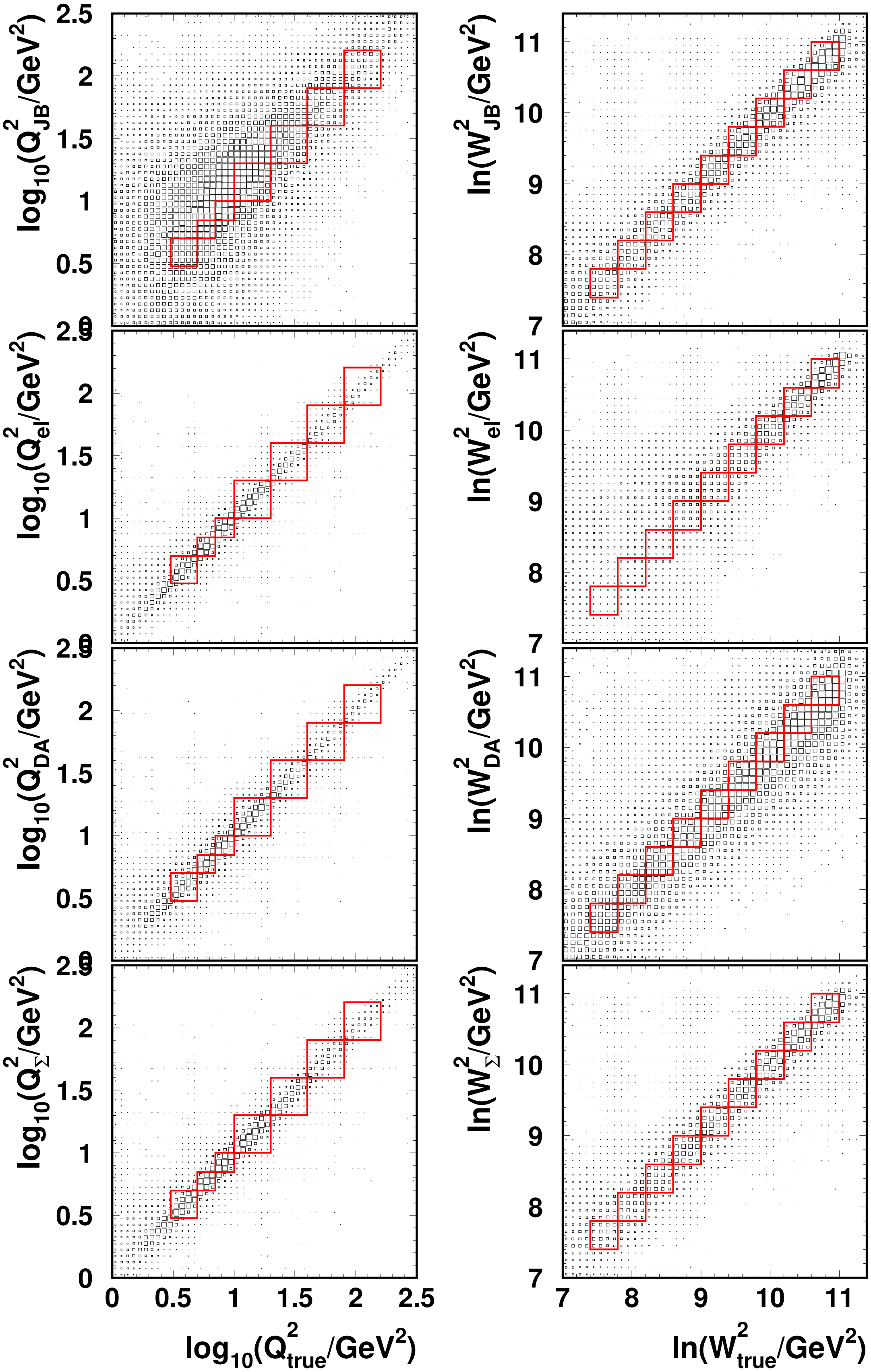

Figure 7.13: The reconstructed values of Q^2 and W are compared to the true values. The electron, the Jacquet-Blondel, the double angle and the Σ-method are shown. The squares indicate the bin size for Q^2 and W. Note that δ_h has been scaled by a factor $c_\delta = 1.125$ both for the JB and the Σ-method.

Chapter 8

Selection of the DIS event sample and background rejection

The data sample analyzed in this thesis corresponds to an integrated luminosity of 4.2 pb^{-1}. It has been taken during the 1998/99 running period when HERA was running with 27.6 GeV electrons and 920 GeV protons.

The final data set is the result of several selection steps filtering DIS events out of the bulk of background events. In the following the trigger preselection and the more stringent offline selection cuts are presented. The remaining background events are either filtered out using specific rejection algorithms or are subtracted on a statistical basis using background MC. This is discussed in the last section of this chapter.

8.1 Trigger preselection

As described in section 2.2.6 the ZEUS experiment uses a three level trigger system to reduce the event rate to a manageable level which can be written to tape. The trigger for neutral current DIS events is based mainly on the requirement of a well reconstructed electron in the calorimeter. Additional cuts on the hadronic final state reduce the background further.

8.1.1 First level trigger

The first level trigger (FLT) criteria relevant for this analysis aim to select events with an electron in the calorimeter. Events are selected if they fulfill one of the following conditions:

- An isolated electromagnetic energy deposition is found in the RCAL AND
  - the total RCAL EMC energy deposit, excluding the cells around the rear beam hole, is greater than 2 GeV OR
  - the total energy deposit in the RCAL EMC including the region around the beam hole is greater than 3.75 GeV OR
  - the total calorimeter energy is above 464 MeV AND the timing of the SRTD is consistent with an ep interaction (which implies an SRTD signal of more than 0.4 mips).

- The RCAL EMC energy outside the cells around the beam hole is greater than 3.4 GeV.
- The BCAL EMC energy is greater than 4.8 GeV AND a good track pattern is found in the CTD.

Background events originating from protons interacting outside the detector are rejected using the timing information of upstream veto counters and the SRTD.

8.1.2 Second level trigger

At the second level trigger (SLT) the background is further reduced by requiring cuts on the energy and timing of the calorimeter. In DIS events particles are emitted from the interaction point and arrive at FCAL and RCAL at times $t \approx 0$. Proton beam related background events, however, deposit energy in the RCAL about 10 ns earlier. This provides an effective handle to reject background events. The time difference between the energy deposit in the upper and the lower half of the calorimeter is used to reject cosmic muon events which in contrast to ep interaction events deposit energy in the upper half of the detector first.

In addition the quantity $\delta = E - p_Z$ is used to reduce the background. At the SLT level δ is calculated as a sum over all calorimeter cells assuming a nominal interaction point at $X = Y = Z = 0$. The quantity δ is conserved by the interaction. Therefore, the initial value

$$\begin{aligned} \delta &= (E - p_Z)_p + (E - p_Z)_e = E_p - E_p + E_e - (-E_e) && (8.1) \\ &= 2E_e = 55.2 \text{ GeV} && (8.2) \end{aligned}$$

should also be measured after the interaction assuming a fully contained event and perfect detector resolution. Particles escaping the detector through the forward beam hole basically have $\delta = 0$ and, therefore, do not affect the measurement of the total δ. Any particle escaping through the rear beam hole, however, decreases δ by two times its energy.

In photoproduced events the electron is scattered under a very small angle and escapes through the rear beam hole. The measurable δ is, therefore, reduced to $\delta = 2(E_e - E_e^{'})$ which can be used to reject photoproduced events with sufficiently large $E_e^{'}$. Also events originating from beam interactions outside the detector volume in general have a δ which is incompatible with a contained DIS event. In order to retain DIS events with an ISR photon escaping through the rear beam hole and hitting the LUMI photon detector the cut on the SLT level is

$$\delta_{SLT} > (29 \text{ GeV} - 2E_\gamma) \,, \tag{8.3}$$

where E_γ is the energy measured in the LUMI photon detector.

8.1.3 Third level trigger

At the third level trigger (TLT) the full event information is available. Therefore, more refined electron finder algorithms can be used to select the events. Events are only accepted if at least one out of 4 electron finders including the SINISTRA algorithm discussed in section 7.3.1 finds an electron with an energy of more than 4 GeV.

The energy of electrons hitting the calorimeter very close to the RCAL beam hole cannot reliably be measured since the electromagnetic shower is not fully contained in the calorimeter.

Due to the Q^{-4} dependence of the cross section the rate of such events is very high. Therefore, the electron is required to hit the calorimeter outside the region $|X| < 12$ cm and $|Y| < 6$ cm. This "12×6" boxcut rejects electrons hitting the RCAL less than 2 cm away from the 20 cm $\times$ 8 cm beam hole.

The δ quantity is calculated at the TLT level using the vertex measured by the CTD and the following cut is applied:

$$\delta_{TLT} > (30 \text{ GeV} - 2E_\gamma) \;, \tag{8.4}$$

In addition tighter timing cuts as well as sophisticated algorithms in order to reject beam-halo and cosmic muons are applied.

After these trigger selection cuts a total of 3.881.192 events is selected.

8.2 Offline selection cuts

The data sample selected by the trigger still contains some remaining background events most of which can be rejected using tighter selection cuts in the offline analysis. In addition, the offline cuts aim to select only well reconstructed events rejecting part of the phase space in which an accurate measurement is not possible. The following cuts are applied in the present analysis:

- $46\,\text{GeV} < \delta < 64\,\text{GeV}$,
  where δ is calculated using the corrected values discussed in the previous chapter:
  $\delta = \delta_{h,corr} + E_e^{corr}(1 - \cos\theta_e)$.
  As already discussed in section 8.1.2 this cut reduces photoproduction and beam-gas background. In contrast to the cut on the trigger level the energy in the LUMI photon detector is not included here. Therefore, this cut also rejects ISR events where the radiated photon carries an energy of $E_\gamma \gtrsim (2E_e - 46\,\text{GeV})/2 = 4.6\,\text{GeV}$.

- $-50\,\text{cm} < Z_{vertex} < 50\,\text{cm}$.
  This cut reduces acceptance uncertainties since the event acceptance is a function of the Z_{vertex} position.

- $E_{CAL,had}^{-RCAL1} \geq 0.4\,\text{GeV}$,
  where $E_{CAL,had}^{-RCAL1}$ is the hadronic energy in the calorimeter excluding the cells around the RCAL beam hole. The aim of this cut is to ensure that a sufficiently large part of the hadronic system is contained in the calorimeter, allowing a measurement well above noise level. The cells around the RCAL beam hole are excluded since the energy of hadrons hitting the RCAL close to the beam hole cannot reliably be measured as part of the shower generated in the calorimeter might escape through the beam hole. This loss strongly affects the determination of δ_h which is a crucial quantity for the reconstruction of the event kinematics. The hadronic energy measurement, therefore, should not be dominated by hadrons hitting the RCAL close to the rear beam hole.

- $y_{JB}^{-RCAL1} > 0.006$,
  where y_{JB}^{-RCAL1} is the usual y_{JB} as introduced in section 7.5 neglecting energy deposited in the calorimeter cells around the RCAL beam hole. At low values of y_{JB} which corresponds to low values of δ_h calorimeter noise, albedo and resolution effects have a large impact on

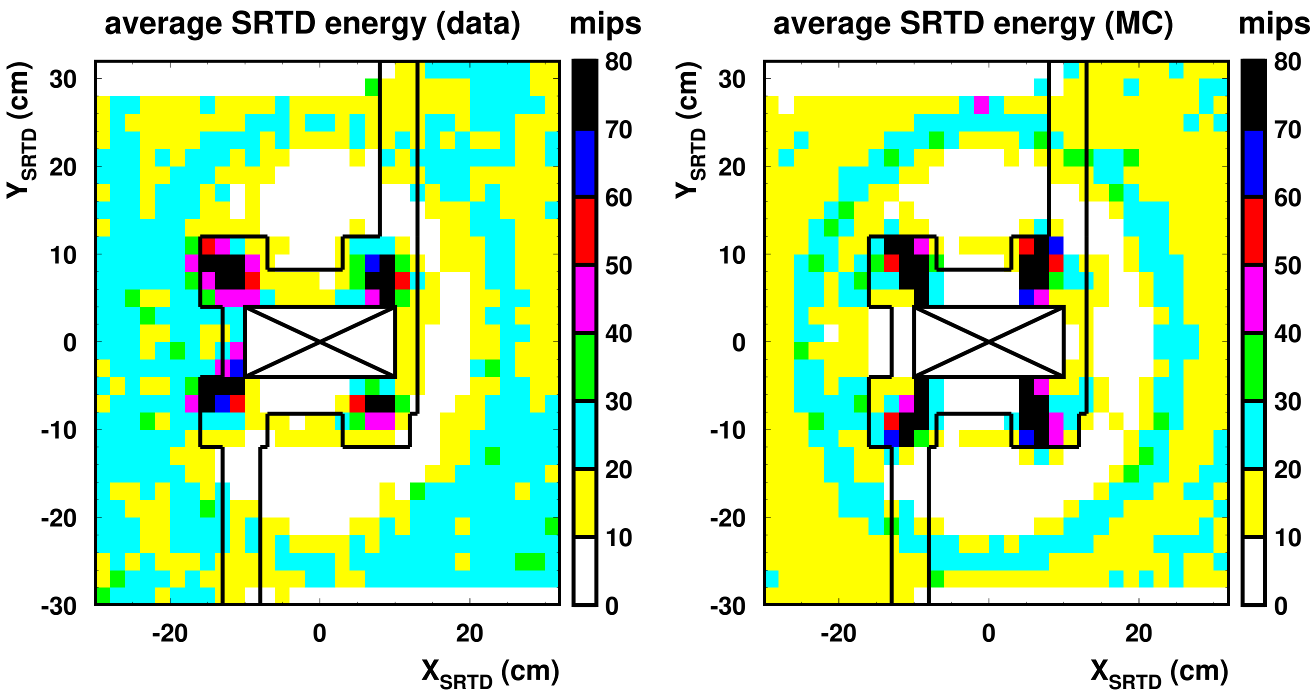

Figure 8.1: The average signal (in mips) in the SRTD as a function of the impact position for data (left) and MC (right). The position of the boxcut which is applied in the offline analysis is indicated. The cross region in the center indicates the beam hole.

the measurement of the hadronic system[1]. The region around the RCAL beam hole is excluded in the calculation of y_{JB}^{-RCAL1} in order not to depend on hadrons for which part of the energy has escaped through the RCAL beam hole.

- $E_e^{corr} > 10\,\mathrm{GeV}$,
  where E_e^{corr} is the corrected energy of the DIS electron found by the SINISTRA electron finder. The cut on the electron energy ensures good purity and efficiency of the electron identification.

- $y_{el} < 0.95$.
  In photoproduced events isolated electromagnetic calorimeter clusters in the FCAL are sometimes misidentified as the scattered electron. Most of these events are characterized by a large value of y_{el} and can, therefore, be eliminated by limiting the maximum value of y_{el}.

- Boxcut:
  In the RCAL region close to the beam hole the reconstruction of the energy and the impact position of the DIS electron is hampered by energy leakage into the beam hole. In order to ensure an accurate reconstruction of the electron a cut on the electron impact position (X_e, Y_e) at the RCAL surface of $|X_e| > 13\,\mathrm{cm}$ and $|Y_e| > 8.2\,\mathrm{cm}$ is applied which ensures a minimum distance to the edge of the RCAL beam hole of 4 cm.

  Furthermore, the electron identification and reconstruction is less precise in the crack region between the north and the south half of the RCAL. Electrons entering the crack

[1] A noise signal of e.g. 120 MeV in the rear direction leads to an error in the measurement of δ_h of $\Delta\delta_h = 0.24$ GeV, which implies $\Delta y_{JB} = 0.0044$. The relative error on y_{JB} is thus substantial for events with $y_{JB} = 0.006$.

region can deposit a substantial amount of energy in the HAC section and thus not be identified as an electron. Also neither the SRTD nor the HES fully cover the crack region which implies a poor reconstruction of the impact position. Therefore, the electron is required to hit the RCAL at least 2.5 cm away from the RCAL crack.

The amount of inactive material in front of the RCAL is in first order proportional to the average signal in the SRTD. Figure 8.1 shows the average SRTD signal as a function of the impact position for data and MC. It can be seen that the amount of inactive material is substantially higher in 4 regions close to the corners of the RCAL beam hole. This material results from copper cooling pipes attached to the rear beam pipe. The exact position and the amount of inactive material differs somewhat between data and MC. The energy correction applied in section 7.3.3 cannot fully compensate these differences. The electron is, therefore, required to hit the RCAL outside the 4 square regions: $(-16 < X < -7, 4 < Y < 12)$, $(3 < X < 12, 4 < Y < 12)$, $(-16 < X < -7, -12 < Y < -4)$ and $(3 < X < 12, -12 < Y < -4)$. The final geometrical boxcut is indicated in Fig. 8.1.

- crazing cut:
  Electrons scattered under small angles might enter the RCAL from within the beam hole. The impact position and also the energy of these "crazing" events are clearly mismeasured. A characteristic feature of such events is that the electron does not pass the SRTD nor the HES thus producing no signal in these detector components. In general, crazing electrons deposit energy only in the cells directly adjacent to the beam hole. Therefore, events are rejected which have no signal related to the electron in the SRTD nor in the HES and have electron energy deposition only in cells around the RCAL beam hole.

After applying the above cuts a total of 928160 events remains in the final data sample.

8.3 Background subtraction

In this section three sources of background are discussed which require special treatment.

8.3.1 Photoproduction background

The largest source of background for the inclusive DIS sample are photoproduction (PhP) events, where the electron is scattered at small angles such that it escapes undetected through the rear beam pipe ($Q^2 \lesssim 1\,\mathrm{GeV}$). Due to the Q^{-4} dependence of the cross section the PhP event rate is very high and therefore needs to be rejected with high efficiency.

Since the electron is not contained in the calorimeter most of the PhP events fail the requirement of an electron candidate found by SINISTRA. However, electromagnetic clusters in the calorimeter originating from e.g. a π^0 in the hadronic final state can be misidentified as an electron.

The cut on $\delta = E - p_Z$ reduces the number of PhP events as discussed in section 8.1.2. However, the cut $\delta > 46\,\mathrm{GeV}$ is effective only for PhP events with $E_e^{'} \lesssim 4.6\,\mathrm{GeV}$, which corresponds to[2] $y \gtrsim 0.83$. Due to resolution effects events of even lower values of y may survive the δ-cut.

[2] For PhP events: $y = 1 - E_e^{'}/E_e$.

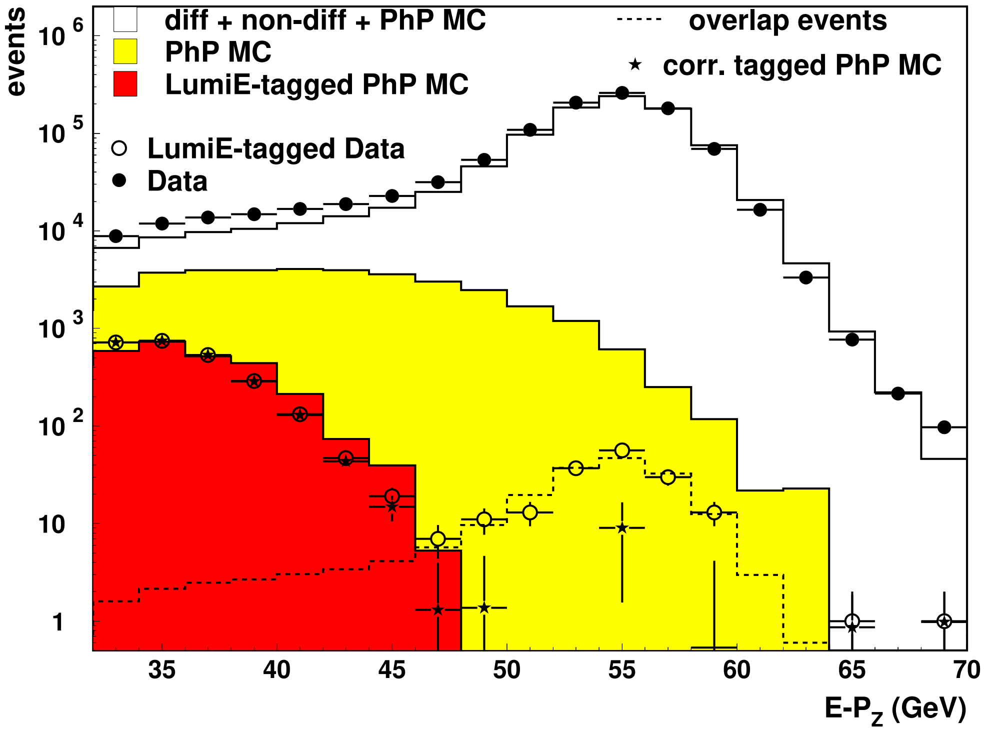

Figure 8.2: The distribution of $\delta = E - p_Z$ for data is compared to the distribution for a PhP MC sample and a combined DIS+PhP MC sample. Also shown are the distributions for events tagged in the LUMIE detector. The dashed histogram indicates the estimated amount of overlaps between a DIS and a bremsstrahlung event.

The remaining PhP contamination can be estimated using a PhP MC sample generated with the PYTHIA event generator. In order to reduce the size of the MC sample events have been generated with $y > 0.6$ since events with lower values of y are strongly suppressed by the δ cut.

Since the cross section of the PhP MC is uncertain the normalization has been determined using PhP data with a tagged electron in the LUMIE detector. Electrons in the energy range $5.5\,\text{GeV} < E_e^{'} < 22\,\text{GeV}$ scattered in the forward direction can be measured in the LUMIE detector. Comparing the number of tagged events in data and MC allows to normalize the MC to the data.

Figure 8.2 shows the $E-p_Z$ distribution of the tagged and the inclusive events in data and MC which pass all selection cuts (except the cut on $E-p_Z$ itself). In this control plot the PhP MC has been added to the DIS MC sample. For the cross section determination, however, the PhP MC is subtracted from the data. As expected the contribution of PHP events is concentrated at low values of $E-p_Z$. In the data sample of LUMIE-tagged events a peak around 55 GeV can be observed. Since the LUMIE detector tags electrons with a minimum energy $E_{e,min}^{'} \approx 5.5\,\text{GeV}$ the maximum $E - p_Z$ is given by $(E - p_Z)_{max} = 2(E_e - E_{e,min}^{'}) \approx 44\,\text{GeV}$. Therefore, the LUMIE-tagged events with $E - p_Z \approx 55\,\text{GeV}$ have to be due to random coincidences between a DIS event and a bremsstrahlung event where the outgoing electron hits the LUMIE detector. The shape of the $E - p_Z$ distribution of these overlap events is expected to be equal to the distribution of the inclusive DIS sample. The contribution of overlap events to the total LUMIE-tagged sample can therefore be estimated by normalizing the inclusive $E-p_Z$ distribution to the tagged sample in the region $50\,\mathrm{GeV} < E - p_Z < 60\,\mathrm{GeV}$ and extrapolating to smaller values of $E - p_Z$. The normalization for the PhP MC has been determined such that the LUMIE-tagged distribution corrected for overlap events agrees in the interval $32\,\mathrm{GeV} < E - p_Z < 40\,\mathrm{GeV}$.

The PhP background is only relevant for the low Q^2 and large W region. The contribution of PhP events to the total number of events amounts to 10% in the worst bin considered in this analysis.

8.3.2 QED Compton rejection

Another source of background are elastic QED Compton events, $ep \rightarrow ep\gamma$. These events consist of an outgoing proton which carries little transverse momentum and an electron which balances the transverse momentum of a photon which is radiated under large angles. Since this process is of pure QED nature it is not simulated in the standard DIS event generators. When both the electron and the photon are detected in the calorimeter they can fake a DIS event with low hadronic mass. It is therefore of significant concern for the diffractive DIS sample. Especially for high Q^2 and low M_X bins, where the diffractive contribution is small, QED Compton events can present a nonnegligible background.

A Compton rejection algorithm has been developed based on the several characteristic features of QED Compton events. Events are rejected on the basis of the following conditions:

- Exactly 2 electromagnetic calorimeter clusters are found with an energy of more than 1 GeV.
- The 2 electromagnetic candidates are back-to-back in azimuth angle.
- There is no vertex fitted track. OR: There is exactly one track which points to one of the electromagnetic candidates.
- The energy in the calorimeter not associated with either of the electromagnetic candidates is less than 0.4 GeV.

The rejection efficiency has been checked using QED Compton MC and was found to be 95% in the kinematic region relevant for this analysis. The probability to reject diffractive DIS events has been found to be less than 0.5% using the diffractive MC sample. In order to account for any remaining contribution the fraction of QED Compton MC events which survive all selection cuts including the QED Compton rejection algorithm is subtracted from the data sample for the cross section determination.

The remaining contribution from QED Compton events is found to be negligible for the low Q^2 region and outside the lowest M_X bin. In the highest Q^2 and lowest M_X bin contributions of up to 10% are observed.

8.3.3 Beam-Gas interactions

Interactions of the electron or the proton beam with rest-gas molecules in the beam pipe are responsible for the beam-gas background. Beam-gas events interacting outside the main detector are rejected effectively using veto counters and timing cuts as described in the previous sections. Remaining e-gas events which originate from interactions within the detector can mimic DIS events with a small hadronic mass and affect the determination of the diffractive cross section.

The contribution from beam-gas events is estimated using unpaired i.e. non-colliding electron and proton bunches. These events have to be scaled with the ratio of the currents in the paired and unpaired bunches. The number of background events for each bin is subtracted from the number of data events.

The background originating from p-gas events is found to be negligible. The contribution from e-gas background events is less than 5% for most bins. Only for some high Q^2 bins where the statistics is low contributions of up to 10% are observed.

Chapter 9

Measurement of inclusive F_2

The measurement of the proton structure function $F_2(Q^2, x)$ is one of the key tasks of the HERA experiments. Precision measurements of F_2 in the kinematic range covered by the present analysis have already been published by the experiments H1 [22] and ZEUS [23]. In the context of this analysis the measurement of F_2 serves as a quality check of the reconstruction of the kinematic variables Q^2 and W and of the background rejection. In addition, the ratio of the diffractive and the total $\gamma^* p$ cross section presented in section 11.4 is evaluated using the F_2 values presented in this chapter. The analysis tools, the kinematic range and the bin definition have been chosen in accordance with the requirements placed by the measurement of the diffractive cross section.

9.1 Unfolding procedure

After the final data selection and background subtraction the measured number of events in each bin in the (Q^2,W) plane does not yet directly reflect the underlying NC ep cross section. The experimentally measured and the corresponding real distributions differ due to the finite resolution of the event reconstruction. Furthermore, the probability to observe an event is limited by the trigger and the offline selection criteria. The procedure to correct the observed number of events for smearing, migration and acceptance effects is commonly called "unfolding".

In general the relation between the number of events g_i produced in a given bin i of true event variables and the number of events m_j observed in bin j of the corresponding measured variables is described by

$$m_j = \sum_i T_{ij} \cdot g_i \; , \tag{9.1}$$

where T_{ij} is called the transfer matrix which can be determined using MC simulations.

The bin-by-bin unfolding method, which is used in this analysis, considers only net migrations into or out of the bin under consideration. The bins are no longer correlated and a single correction factor c_i^{MC} is determined for each bin i using an appropriate MC sample:

$$c_i^{MC} = \frac{N_i^{MC,gen}}{N_i^{MC,rec}} \; , \tag{9.2}$$

where $N_i^{MC,gen}$ is the number of events generated and $N_i^{MC,rec}$ is the number of events reconstructed in bin i. The unfolded number of events $N_i^{data,unf}$ is then given by

$$N_i^{data,unf} = c_i^{MC} \cdot N_i^{data,rec} \,, \tag{9.3}$$

where $N_i^{data,rec}$ is the number of events reconstructed in the data sample.

The bin-by-bin unfolding method requires a good description of the data by the Monte Carlo simulation over the whole kinematic range which contributes to the measured number of events. A good overall agreement between data and MC has been achieved by generating the MC using the CTEQ4D parameterization of F_2, which has been fit to previous results published by H1 and ZEUS.

9.2 Control distributions

Before describing the extraction of F_2 the agreement between data and MC is discussed on the basis of several control distributions. The plots in Fig. 9.1 have been produced applying all selection cuts and restricting the samples to the kinematic range analyzed in this thesis, i.e. $3\,\text{GeV}^2 < Q^2_{el} < 160\,\text{GeV}^2$ and $40\,\text{GeV} < W_\Sigma < 245\,\text{GeV}$. The SATRAP (diffractive) and DJANGOH (non-diffractive) MC sample have been mixed according to the procedure described in section 6.2.3. The photoproduction background has been simulated with PYTHIA and has been added to the DIS MC sample using the normalization determined in section 8.3.1.

The corrected energy of the scattered electron is shown in Fig. 9.1 (a). A small excess of the data can be seen around the peak at 27.5 GeV. However, the shape of the distribution is well described by the MC. As expected the photoproduction background mainly contributes at low values of the electron energy. Figures 9.1 (b) and (c) show the measured angle of the scattered electron and $E - P_Z$ of the electron. Again, good agreement is achieved for the shape of the distributions with a small data excess at large angles Θ_e and around the peak of the $E - P_Z$ distribution at 55 GeV. The $E - P_Z$ (d) and the angle γ_h (f) of the hadronic system show satisfactory agreement between data and MC. In the distribution of the total $E - P_Z$, shown in Fig. 9.1 (e), the data overshoots the MC at the rising edge and undershoots it at the falling edge. This can be interpreted as a shift of the data with respect to the MC by ~ 250 MeV.

The comparison between data and MC of the kinematic variables Q^2 and W as measured with the electron and the Σ-method, respectively, is shown in Fig. 9.2. The Q^2_{el} distribution shows good general agreement. Only at $Q^2_{el} < 5\,\text{GeV}^2$ small ($< 10\%$) deviations can be observed. The distribution of W_Σ shows an access of the data at low W values. However, in the region $W_\Sigma > 40\,\text{GeV}$ the access is less than 5%.

9.3 Bin size and quality

For the measurement of F_2 the same bin definition in Q^2 and W was chosen as for the measurement of the diffractive cross section (see section 10.4). For an unbiased measurement the bins are required to be located in a kinematic region where the event acceptance is sufficiently high. The bin dimensions must be large enough such that an adequate number of events is produced

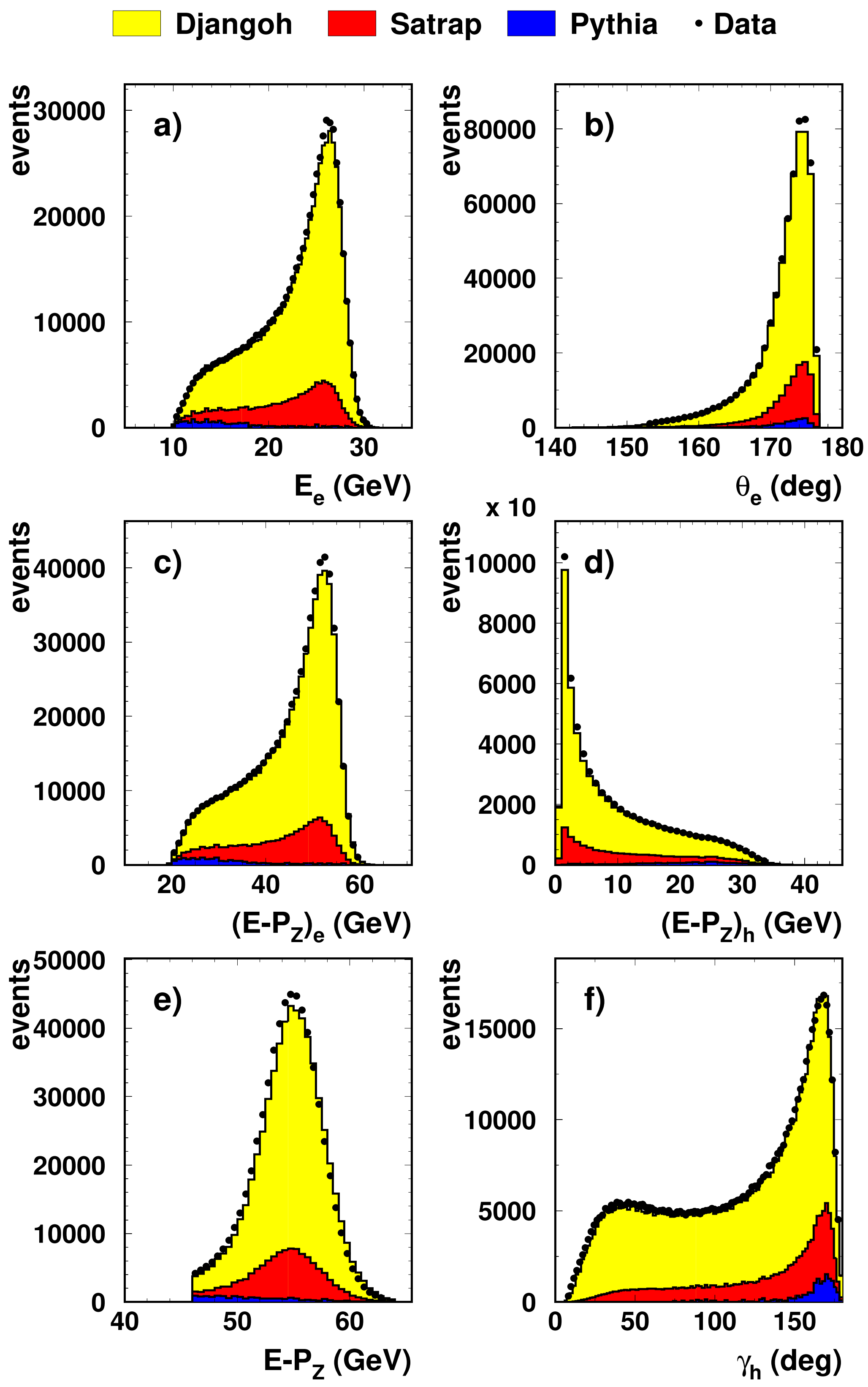

Figure 9.1: Control plots for the scattered electron energy E_e (a) and angle Θ_e (b), $E - P_Z$ of the electron (c), of the hadronic system (d) and of the total event (e) and the angle γ_h of the hadronic system (f).

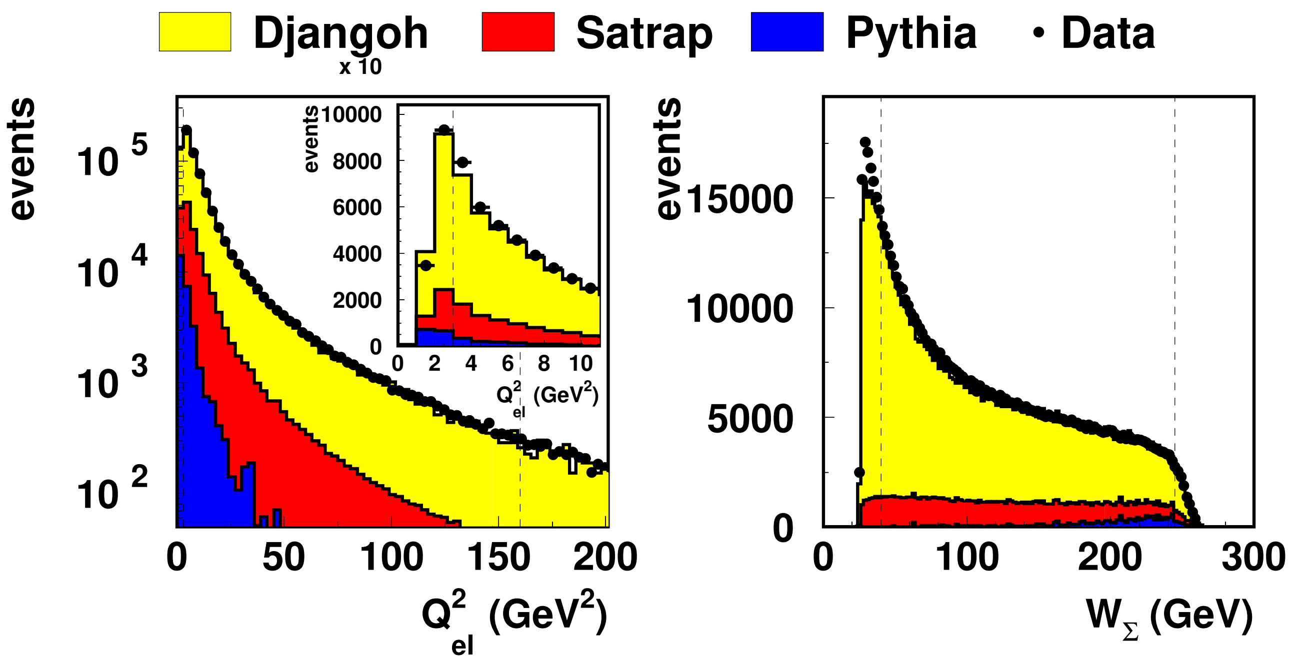

Figure 9.2: Comparison of the Q^2_{el} and W_Σ in data and MC. The dotted lines indicate the kinematic range addressed in the present analysis.

and reconstructed in the same bin. These requirements can be quantified by introducing the bin purity and acceptance defined as

$$purity(i) = \frac{\#\text{ events generated and reconstructed in bin } i}{\#\text{ events reconstructed in bin } i} \tag{9.4}$$

$$acceptance(i) = \frac{\#\text{ events generated in bin } i \text{ and passing the final event selection}}{\#\text{ events generated in bin } i} \tag{9.5}$$

$$\tag{9.6}$$

Figure 9.3 shows the purity and acceptance of each bin in Q^2 and W. The purity which measures the amount of event migration from adjacent bins into the measured bin is generally higher than 30 % except for the lowest bin in W. The acceptance measures the effect of the trigger and offline selection cuts. The geometrical cut applied to the scattered electron limits the acceptance in the low Q^2 region. For $Q^2 > 10\,\mathrm{GeV}^2$ the acceptance reaches values of 80-90%.

9.4 Extraction of F_2

The double differential cross section for the inclusive neutral current deep inelastic ep scattering can be written in terms of the structure function F_2 as

$$\frac{d^2\sigma}{dxdQ^2} = \frac{2\pi\alpha^2}{xQ^4}(1+(1-y)^2)F_2(x,Q^2)\cdot(1-\delta_L \pm \delta_3)\cdot(1+\delta_r)\ , \tag{9.7}$$

where δ_L, δ_3 and δ_r are corrections taking into account contributions from F_L, F_3 and QED radiative effects, respectively, which are expected to be small in the kinematic range addressed

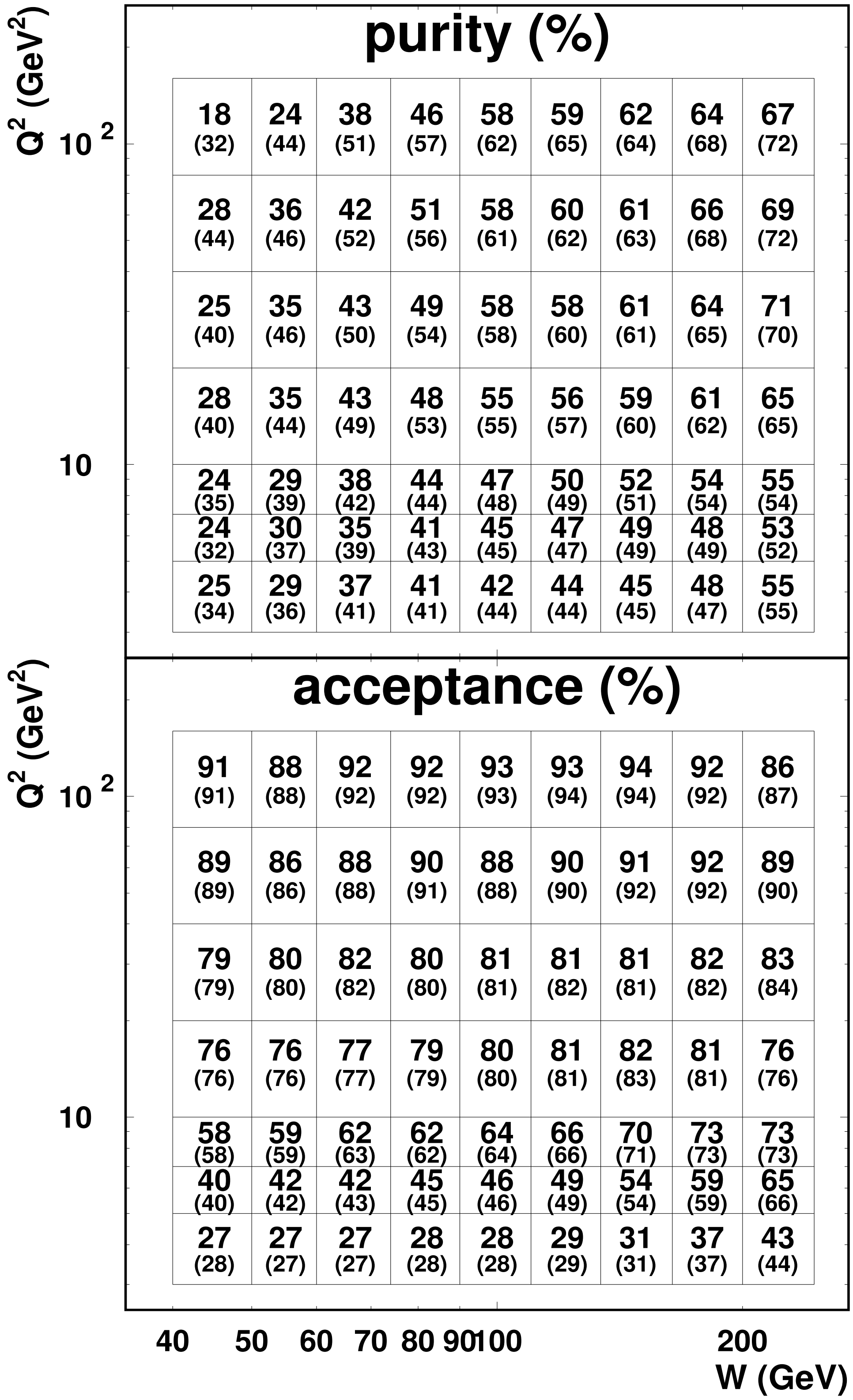

Figure 9.3: Purity and acceptance in % for bins in Q^2 and W. The upper values in each bin denote the purity obtained from the proper mix of diffractive and non-diffractive events. The values in parentheses denote the purity for diffractive events only.

in the present analysis. The number of events produced in a bin i is given by the luminosity $\mathcal{L}$ and the integrated cross section over the region defined by the bin

$$N_i = \mathcal{L} \int \frac{d^2\sigma}{dx dQ^2} dx_i dQ_i^2 = \mathcal{L}\sigma_i \ . \tag{9.8}$$

Assuming that the structure function F_2^{MC}, which was used to generate the MC, adequately describes the x and Q^2 dependence of the data the ratio of the cross section in data and MC can be related to the ratio of the structure functions

$$\begin{aligned} \frac{\sigma_i^{data}}{\sigma_i^{MC}} &= \frac{F_2^{data}(x,Q^2)\frac{2\pi\alpha^2}{xQ^4}(1+(1-y)^2)\cdot(1-\delta_L^{data}\pm\delta_3^{data})\cdot(1+\delta_r^{data})}{F_2^{MC}(x,Q^2)\frac{2\pi\alpha^2}{xQ^4}(1+(1-y)^2)\cdot(1-\delta_L^{MC}\pm\delta_3^{MC})\cdot(1+\delta_r^{MC})} && (9.9) \\ &= \frac{F_2^{data}(x,Q^2)}{F_2^{MC}(x,Q^2)} \ . && (9.10) \end{aligned}$$

In the last step it is assumed that the contributions from F_L, F_3 and radiative effects are correctly simulated in the MC. The ratio of cross sections is then related to the ratio of the number of reconstructed events

$$\frac{\sigma_i^{data}}{\sigma_i^{MC}} = \frac{N_i^{data,unf}/\mathcal{L}^{data}}{N_i^{MC,gen}/\mathcal{L}^{MC}} = \frac{N_i^{data,rec}}{N_i^{MC,rec}} \ , \tag{9.11}$$

where in the second step the bin-by-bin unfolding relations of Eq. 9.2 and 9.3 are used and it is assumed that the MC events are weighted such that $\mathcal{L}^{MC} = \mathcal{L}^{data}$. The number of reconstructed events is given by $N_i^{data,rec} = N_i^{obs} - N_i^{PhP} - N_i^{gas}$, which takes into account the contamination from photoproduction and beam gas events to the number of observed events N_i^{obs}. For the MC the diffractive and non-diffractive samples are added according to the procedure described in section 6.2.3. The structure function F_2 is then evaluated using

$$F_2^{meas}(x,Q^2) = F_2^{MC}(x,Q^2) \cdot \frac{N_i^{data,rec}}{N_i^{MC,rec}} \ . \tag{9.12}$$

Since the structure function F_2^{MC}, which was used to generate the MC, corresponds to the QED Born level cross section (QED radiation effects are simulated by the HERACLES package) Eq. 9.12 automatically yields the Born level corrected result F_2^{meas}.

The measured values of $F_2(Q^2, W)$ are shown in Fig. 9.4 as a function of W in bins of Q^2. For comparison the CTEQ4D parameterization is superimposed. In the smallest Q^2 bin the data overshoots the CTEQ4D values by 5 - 10%. In the remaining region the agreement is satisfactory.

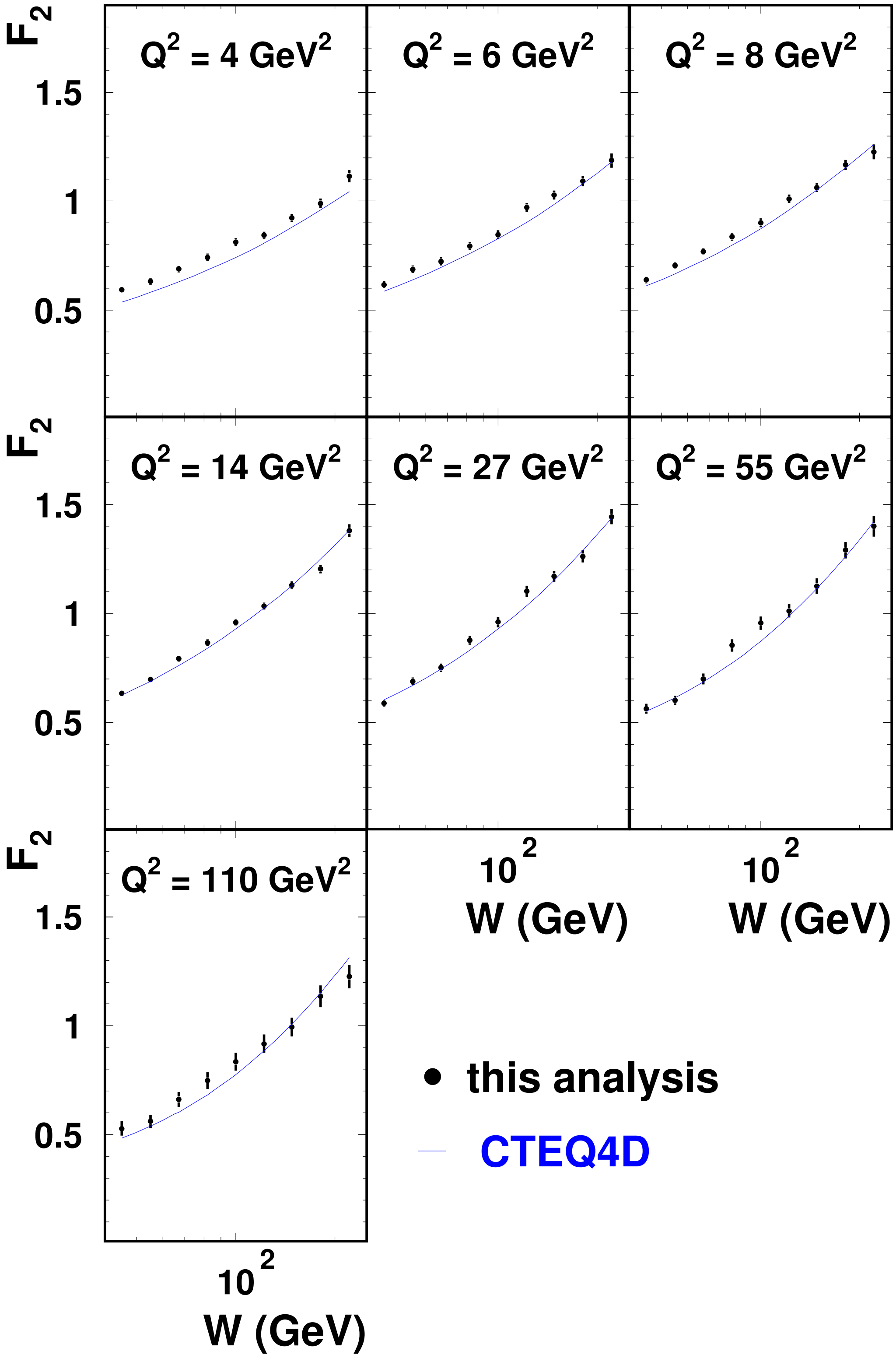

Figure 9.4: The measured values of $F_2(Q^2, W)$ are plotted as a function of W in bins of Q^2. The CTEQ4D parameterization is superimposed for comparison.

Chapter 10

Extraction of the diffractive contribution

In this chapter the extraction of the diffractive contribution to the DIS cross section is presented. Several methods to select diffractive events are discussed first before describing in some detail the method chosen in this analysis in section 10.3. The improvements in the selection procedure resulting from the installation of the FPC are discussed in section 10.3.4. A MC study of the reliability of the extraction method is presented in section 10.6, followed by a discussion of the effect of proton dissociation events.

The dominant mechanism of deep inelastic scattering events is characterized by a color transfer between the struck quark and the proton remnant which is responsible for populating the intermediate rapidity region with hadrons. Rapidity gaps i.e. intermediate regions in which no hadrons are emitted are exponentially suppressed. Diffractive events, however, which are characterized by a color singlet (Pomeron) exchange are of the type

$$e + p \rightarrow e' + X + N \; , \tag{10.1}$$

where the system X is well separated from the outgoing proton system N in the sense that the intermediate rapidity gap is not exponentially suppressed.

10.1 Event selection with the Leading Proton Spectrometer

In a considerable fraction ($\sim$ 20-40%) of diffractive events the outgoing proton system N dissociates into a higher mass multi-particle state. However, the majority of the diffractive events are of the type $e + p \rightarrow e' + X + p'$, where the outgoing proton stays intact. The outgoing proton provides a very clean experimental signature for diffractive events.

Since the transverse momentum p_T of the scattered proton is expected to be small ($p_T \lesssim 1\,\text{GeV}$) the outgoing proton escapes through the forward beam hole in the calorimeter. A fraction of these events can be detected with the Leading Proton Spectrometer (LPS). It measures the momentum vector of the scattered proton using the track deflection induced by the magnets in the proton beam line. The spectrum of $x_L = p'_z/p_z$, where p'_z is the longitudinal momentum of the scattered proton measured with the LPS and p_z is the momentum of the incoming proton,

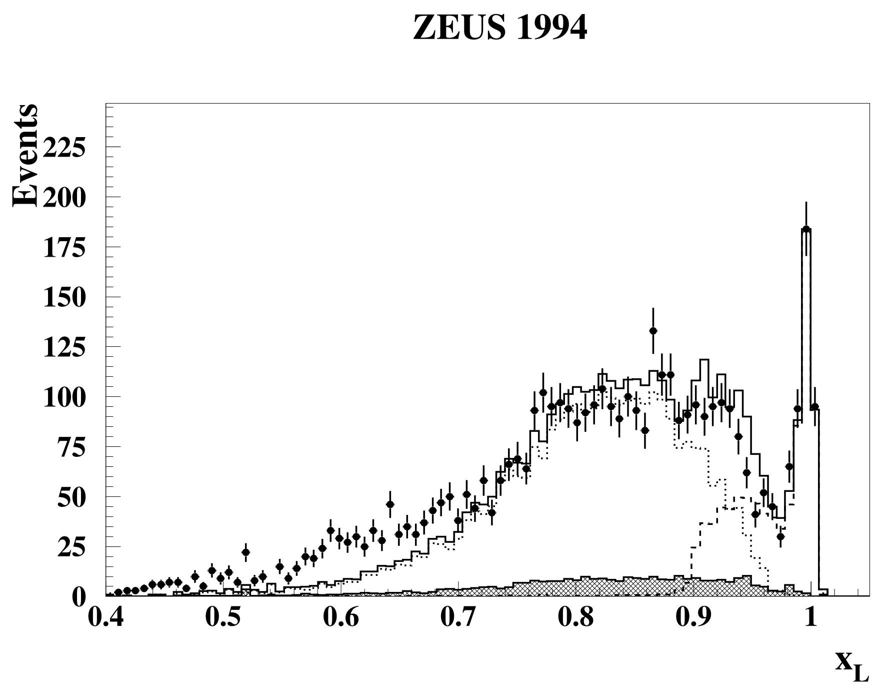

Figure 10.1: The x_L spectrum as measured with the LPS. Overlaid to the data (dots) is the results of fitting the distribution with a sum (full line) of the contribution due to proton dissociation (hashed histogram), of the maximum possible contribution due to pion exchange (dotted line) and of the diffractive signal (dashed line). For details see [137].

is shown in Fig. 10.1. A narrow peak at $x_L \approx 1$ is observed. A clean sample of diffractive events can be selected by requiring $x_L > 0.97$.

The drawback of the diffractive event selection based on the LPS is its limited acceptance which depends on x_L and p_T of the outgoing proton and is typically a few %. For details of the LPS selection see [137].

10.2 Selection of events with a large rapidity gap

The presence of a large rapidity gap between the photon dissociation system X and the scattered proton system p' can be used as a selection criterion for diffractive processes. The first observation of diffractive events in deep inelastic scattering at HERA by ZEUS [48] and H1 [49] was based on the observation of events with a large rapidity gap in the central detector. Figure 10.2 shows the event display of a typical non-diffractive DIS event and a diffractive DIS event with a large rapidity gap in the forward region of the ZEUS detector.

The pseudorapidity η_{max} of the most forward going particle (EFO) which is observed in the main detector is a good measure of the rapidity gap between the system X and the system N since the latter mostly escapes the main detector undetected. Figure 10.3 shows the measured η_{max} distribution. Overlaid are the MC predictions for diffractive and non-diffractive processes. The η_{max} distribution of the non-diffractive sample peaks around $\eta_{max} \approx 5$, which corresponds to the detector limit in the forward direction, and decreases rapidly at lower values of η_{max} [1]. Diffractive events, however, extend to much lower η_{max} values. For $\eta_{max} < 2.5$ the non-

[1] The dip at $\eta_{max} \approx 4$ is due to the fact that no clustering is performed across the boundary between the FCAL and the FPC.

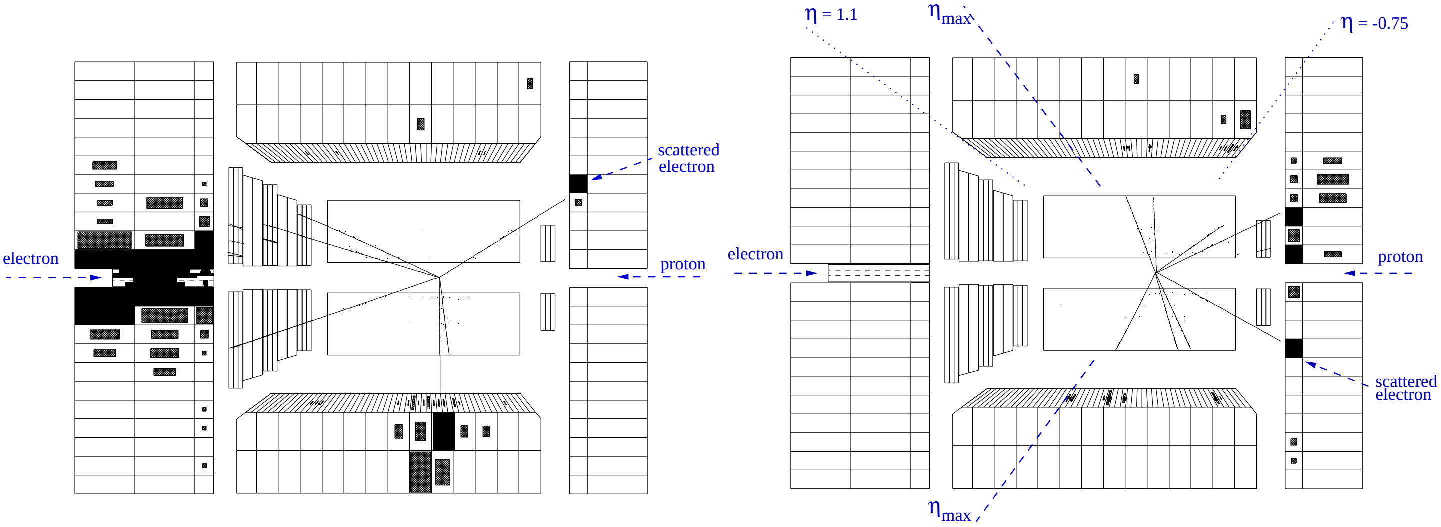

Figure 10.2: *Left*: Event display of a typical non-diffractive DIS event detected in the ZEUS detector. *Right*: Event display of a diffractive DIS event with a maximum rapidity of $\eta_{max} = 0.6$. No activity is observed in the forward region with $\eta > \eta_{max}$.

diffractive background becomes small. Since the detector edge is at $\eta_{edge} \approx 5$ this corresponds to an observed rapidity gap of $\Delta\eta \approx 2.5$. In previous ZEUS analyses using data taken before the installation of the FPC events were selected by requiring $\eta_{max} < 1.5$ [48, 138]. Due to the extended calorimetric acceptance after the installation of the FPC this cut can be relaxed to $\eta_{max} < 2.5$ or even $\eta_{max} < 3$ [139].

The selection method based on a η_{max} criterion cuts into the phase space of diffractive processes, rejecting events where part of the system X is emitted in the forward direction. Extrapolating the measured cross section to the full phase space requires a good understanding of the details of the hadronic final state and is therefore inherently MC dependent. A method which avoids this drawback is presented in the following section.

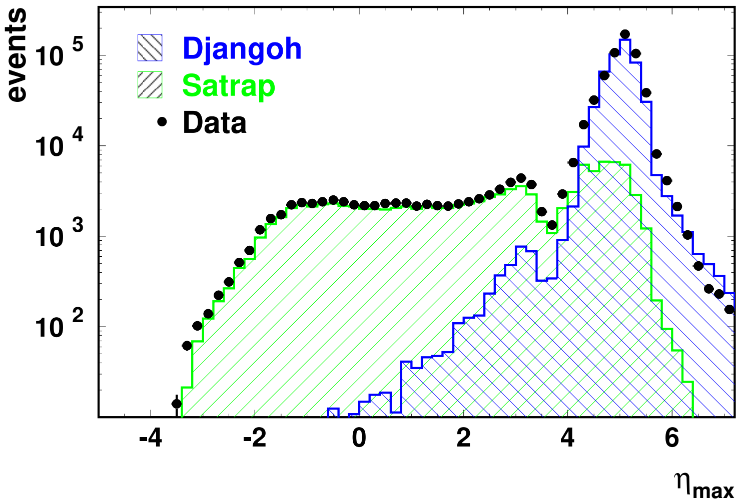

Figure 10.3: The η_{max} distribution for data (dots) is shown. Overlaid is the distribution obtained for the diffractive SATRAP sample and the non-diffractive DJANGOH sample.

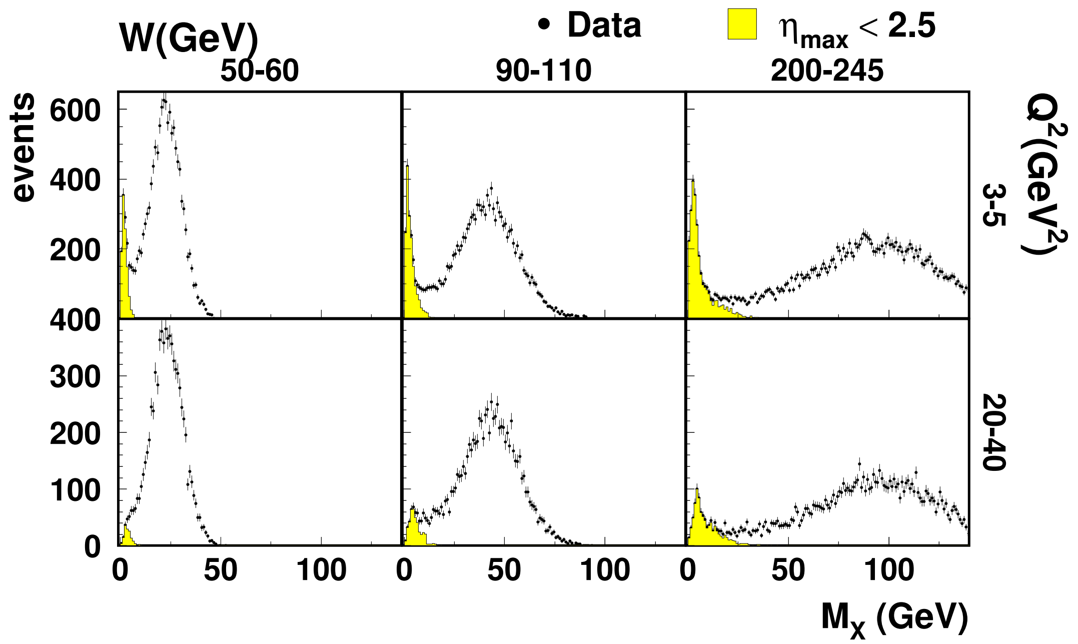

Figure 10.4: The distribution of the measured mass M_X in several (Q^2, W) bins. The shaded areas show the distributions for events with $\eta_{max} < 2.5$.

10.3 The M_X selection method

The M_X method for the selection of diffractive events has been developed by the ZEUS collaboration [140, 141, 142]. Diffractive events are selected based on their characteristic distribution of the invariant mass M_X which is calculated from all particles measured in the central detector excluding the scattered electron.

Figure 10.4 shows the measured M_X distributions for some exemplary (Q^2, W) bins. Most notably in the low Q^2 bins two peaks can be observed. While the position of the lower mass peak is practically independent of W the position of the higher mass peak increases with W. Most of the events in the low mass peak have a large rapidity gap as indicated by the shaded areas which show the contribution from events with $\eta_{max} < 2.5$. The events in the low mass peak are thus identified as being due to diffractive production.

In Fig. 10.5 the mass distribution is plotted in terms of $\ln M_X^2$. The diffractive low mass region, which is mainly populated by events with $\eta_{max} < 2.5$ (shaded area), exhibits a plateau like structure. The non-diffractive high mass region is characterized by a steep exponential fall-off towards lower $\ln M_X^2$ values. The position of the high mass peak scales with $\ln(M_X^2/W^2)$. This can most clearly be seen in Fig. 10.6 where the distribution of $\ln(M_X^2/W^2)$ is plotted for several (Q^2, W) bins.

10.3.1 The M_X distribution of non-diffractive events

The observed characteristics of the $\ln M_X^2$ distribution of the non-diffractive contribution can be understood assuming a uniform and uncorrelated particle emission in rapidity $\mathcal{Y}$ with respect

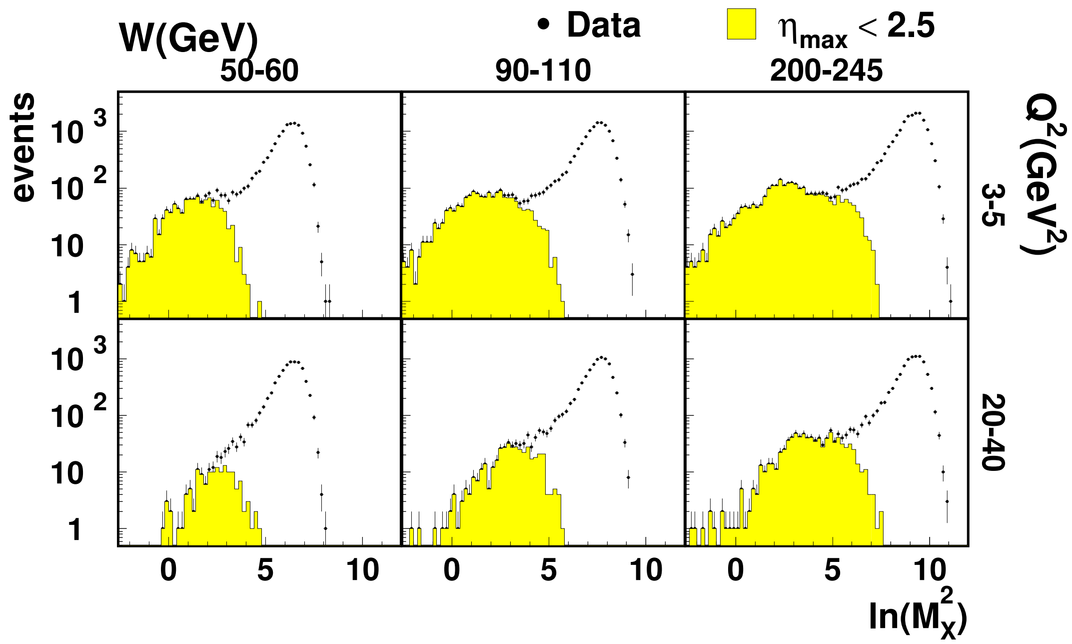

Figure 10.5: The distribution of $\ln M_X^2$ in several (Q^2, W) bins. The shaded areas show the distributions for events with $\eta_{max} < 2.5$.

to the $\gamma^* p$ collision axis [143]:

$$dn/d\mathcal{Y} = \lambda = \text{const} . \tag{10.2}$$

For a uniform $\mathcal{Y}$ distribution between $\mathcal{Y}_{min}$ and $\mathcal{Y}_{max}$ the total center of mass energy W is given by:

$$W^2 = c_0 \cdot \exp(\mathcal{Y}_{max} - \mathcal{Y}_{min}) , \quad \text{with} \;\; c_0 = \text{const} . \tag{10.3}$$

For non-diffractive DIS events only part of the hadronic system with invariant mass W is observed in the central detector due to particle loss through the forward beam hole. The mass

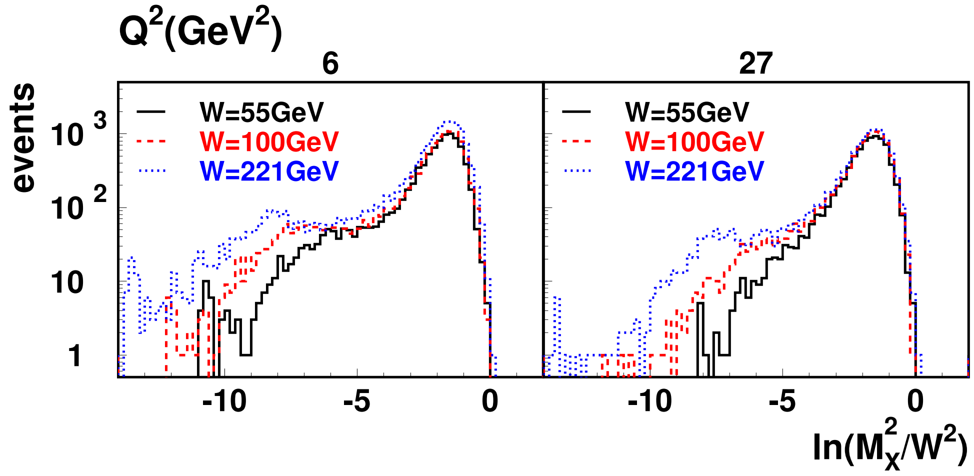

Figure 10.6: The distribution of $\ln(M_X^2/W^2)$ in several (Q^2, W) bins. The non-diffractive peak is observed to scale with $\ln(M_X^2/W^2)$.

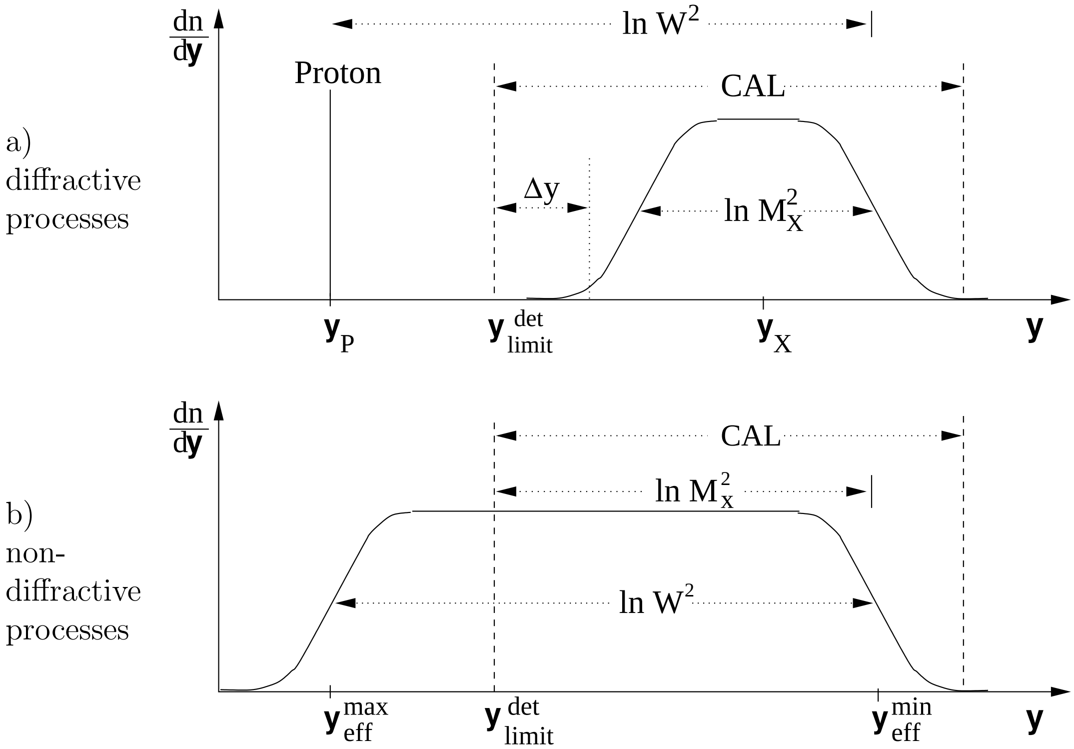

Figure 10.7: Schematic representation of the rapidity distribution for particle emission in a) diffractive and b) non-diffractive events.

M_X of the observed system is given by:

$$M_X^2 = c_0 \cdot \exp(\mathcal{Y}_{limit}^{det} - \mathcal{Y}_{min}) = W^2 \cdot \exp(\mathcal{Y}_{limit}^{det} - \mathcal{Y}_{max}) \ , \qquad (10.4)$$

where $\mathcal{Y}_{limit}^{det}$ denotes the limit of the calorimetric acceptance in the forward direction (see Fig. 10.7). In agreement with the observation this predicts a constant ratio of M_X^2/W^2 i.e. scaling in $\ln(M_X^2/W^2)$.

Due to statistical fluctuations there is a finite probability $P(0)$ that no particle is emitted between $\mathcal{Y}_{limit}^{det}$ and $\mathcal{Y}_{limit}^{det} - \Delta\mathcal{Y}$. Since the particle emission is assumed to be uncorrelated, Poisson statistics predicts $P(0) = \exp(-\lambda\Delta\mathcal{Y})$ resulting in the observed exponential fall-off behavior:

$$dn^{nondiff}/d\ln M_X^2 \propto \exp(b \ln M_X^2) \ , \quad \text{with} \ \ b = \lambda \ . \qquad (10.5)$$

The exponential behavior is expected to extend up to the maximum $\ln M_X^2$ value allowed by kinematics and acceptance. Due to the finite size of the selected W bins and detector smearing effects the exponential fall-off of the $\ln M_X^2$ distribution turns over at $\ln M_X^2 \approx \ln W^2 - \eta_0$, where $\eta_0 \approx 1.8$ was found.

The observed characteristics are well reproduced by standard DIS MC programs. In Fig. 10.8 the $\ln M_X^2$ distribution is shown for events generated with DJANGOH interfaced with ARIADNE at detector and generator level. The generated M_X is defined as the true invariant mass of all particles emitted up to $\eta = 5.5$, which corresponds to the maximum η value up to which a particle can contribute to the measured calorimeter signal. It can be seen that the exponential fall-off persists in the low mass region where diffractive events dominate. The exponential b-slopes extracted from a fit to the $\ln M_X^2$ distributions are practically independent of Q^2 and W (see Fig. 10.9). The average b-slopes obtained from the generator and the detector level distributions are observed to be equal within errors with $\overline{b}_{gen} = 1.84 \pm 0.02$ and $\overline{b}_{det} = 1.86 \pm 0.03$, respectively.

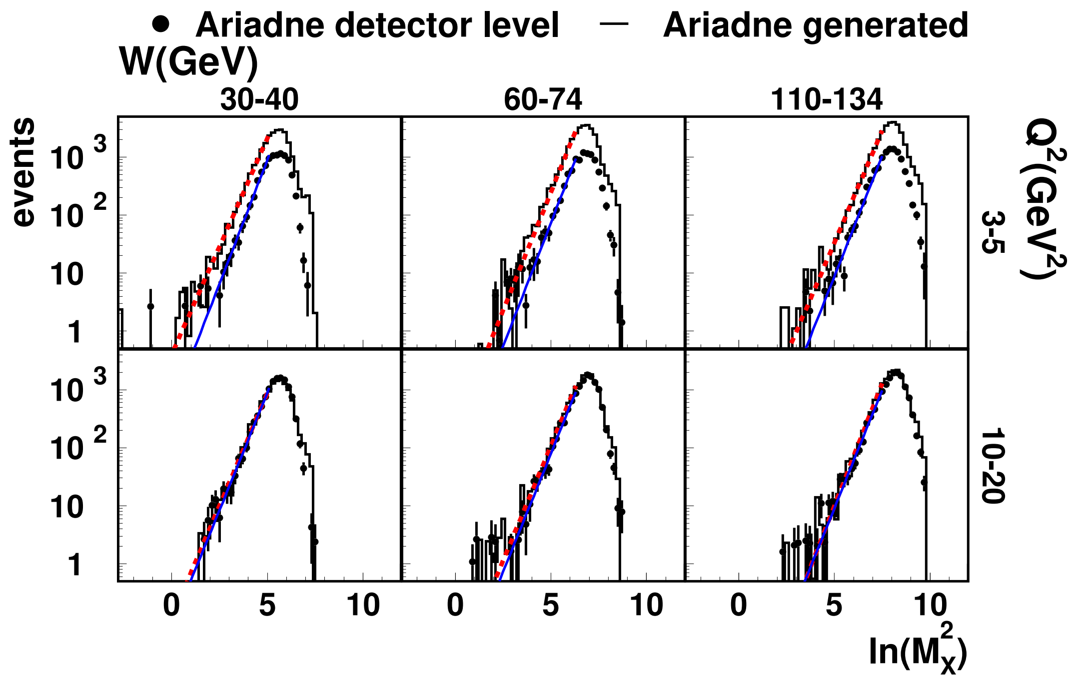

Figure 10.8: Comparison of the $\ln M_X^2$ distribution at generator and detector level for MC events produced with ARIADNE. At the generator level M_X is defined as the true invariant mass of all particles emitted up to $\eta = 5.5$. The straight lines show the result of an exponential fit.

10.3.2 The M_X distribution of diffractive events

In diffractive events the photon dissociation system X is, in general, fully contained in the detector while the proton dissociation system N escapes through the beam hole. For diffractive events generated with SATRAP the mass $M_{X,EFO}$ reconstructed from the energy flow objects in the detector shows a close correlation with the true mass $M_{X,true}$ of the system X as can be seen in Fig. 10.10(a).

Due to energy loss in inactive material and due to loss of particles $M_{X,EFO}$ is on average smaller than $M_{X,true}$. The solid points in Fig.10.10(b) show the average $\ln(M^2_{X,EFO}/M^2_{X,gen})$ as a function of $\ln M^2_{X,EFO}$, where $M_{X,gen}$ is the mass of all particles emitted up to $\eta = 5.5$. In the

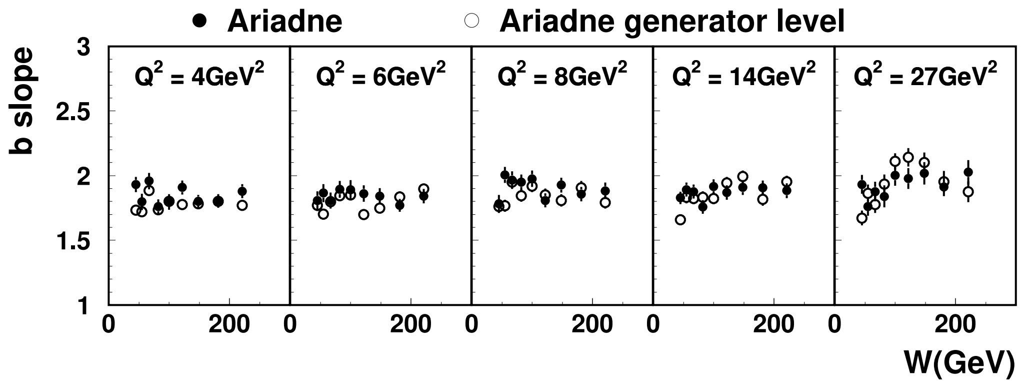

Figure 10.9: The b-slopes obtained from fits to the $\ln M_X^2$ distributions at generator level (open points) and detector level (solid points) for MC events produced with ARIADNE.

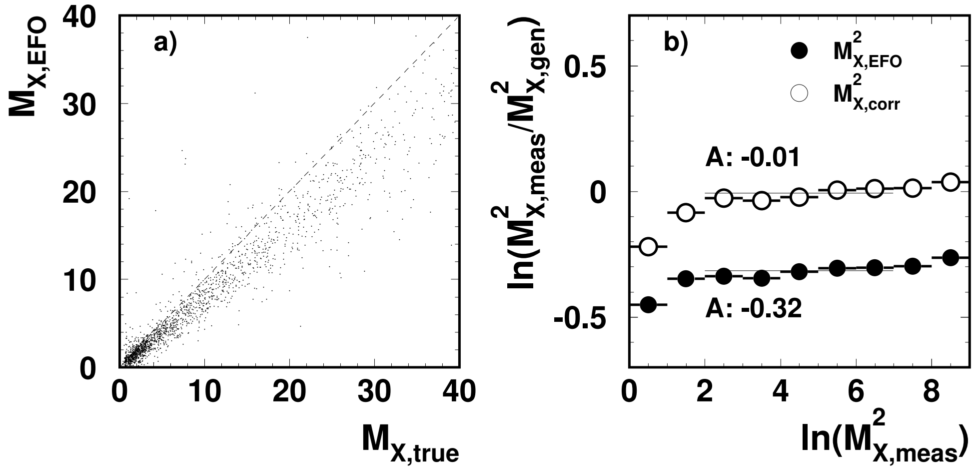

Figure 10.10: (a) For a diffractive MC sample the uncorrected mass $M_{X,EFO}$ is plotted as a function of the true mass $M_{X,true}$. (b) $\ln(M^2_{X,meas})$-$\ln(M^2_{X,gen})$ is plotted as a function of $\ln M^2_{X,meas}$, where $M_{X,gen}$ is the mass of all particles emitted up to $\eta = 5.5$ and $M_{X,meas}$ is the measured mass $M_{X,EFO}$ (solid points) and the corrected mass $M_{X,corr} = f \cdot M_{X,EFO}$ (open points), respectively

mass region $3\,\text{GeV} < M_X < 25$ GeV $\ln(M^2_{X,EFO}/M^2_{X,gen})$ is observed to be shifted by $A = -0.32$. In order to correct for this offset a global correction factor $f_M = \exp(-A/2) = 1.174$ is applied yielding the corrected mass $M_{X,corr} = f_M \cdot M_{X,EFO}$. The result of this correction can be seen in Fig.10.10(b,open points) where $\ln(M^2_{X,corr}/M^2_{X,gen})$ is plotted as a function of $\ln M^2_{X,corr}$.

No attempt is made to apply a M_X dependent correction factor in order not to introduce a bias to the exponential behavior of the non-diffractive contribution. The variation of $\ln(M^2_{X,meas}/M^2_{X,gen})$ with W and Q^2 is found to be small and is therefore neglected.

In Fig. 10.11 the $\ln M^2_X$ for the corrected mass $M_{X,corr}$ is superimposed on the distribution of the true mass $M_{X,true}$ of the system X. Good agreement is observed between the two distributions except for a small distortion at the high mass end. The distribution of $M_{X,corr}$ shows a depletion of events at the high mass end, which show up as an excess at slightly lower mass values. These distortions are caused mainly by particle loss through the forward beam hole. The effect is negligible in the mass range considered in this analysis.

Diffractive dissociation prefers small M_X values with a distribution of the form $dN/dM^2_X \propto 1/(M^2_X)^{(1+n)}$ or

$$dN/d\ln M^2_X \propto 1/(M^2_X)^n \, , \tag{10.6}$$

approximately independent of W. According to observations in diffractive dissociation of pp scattering, $n \approx 0$ is expected for large M_X values, leading to a roughly constant distribution in $\ln M^2_X$. For diffraction processes in DIS this behavior is expected for $M^2_X > Q^2$ which is reproduced by the SATRAP MC as can be seen from Fig. 10.11.

10.3.3 Extraction of the diffractive contribution

The M_X method identifies the diffractive contribution as the excess of events over the exponential fall-off of the non-diffractive background. This allows to extract the diffractive contribution

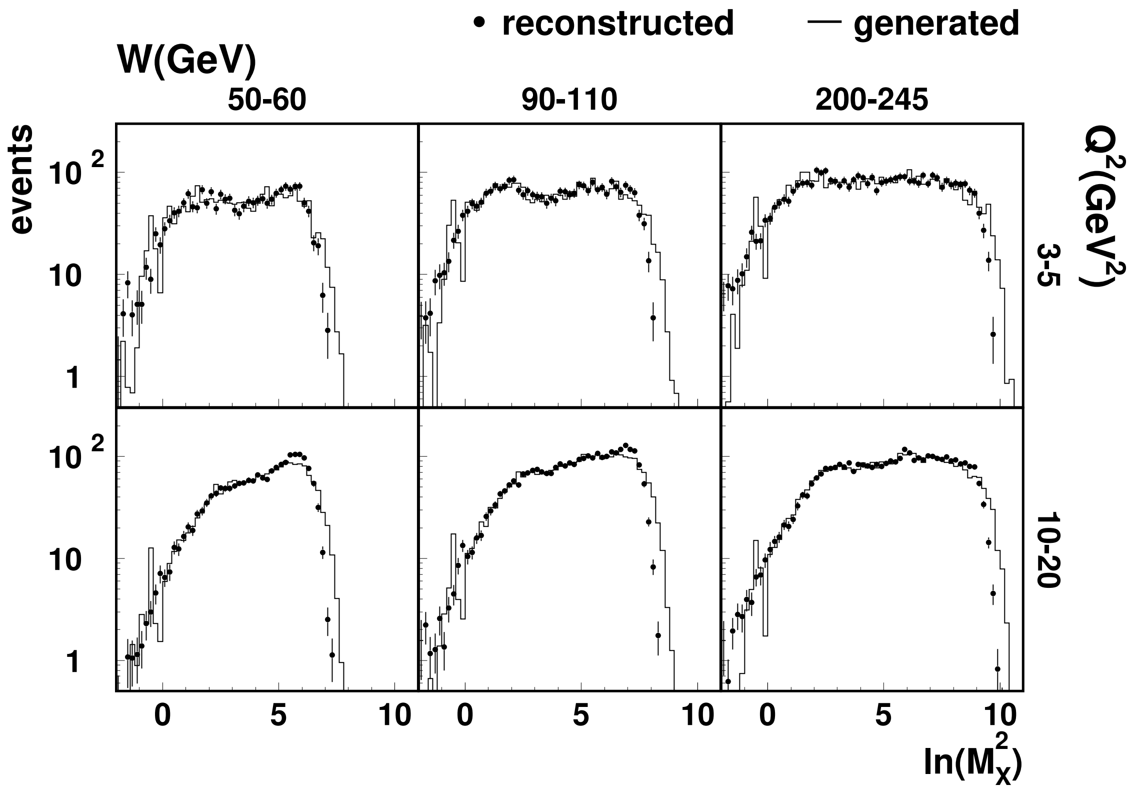

Figure 10.11: The $\ln M_X^2$ distributions for the true mass of the system X (histogram) and the reconstructed mass after correction (points) are shown for different Q^2 and W values. The events were generated with SATRAP.

without assuming its precise M_X dependence. The $\ln M_X^2$ distribution is expected to be of the form

$$dN/d\ln M_X^2 = D + c\exp(b\ln M_X^2)\ , \quad \text{for} \quad \ln M_X^2 \leq \ln W^2 - \eta_0\ , \tag{10.7}$$

where D denotes the diffractive contribution, the second term parameterizes the non-diffractive contribution and c and b are free parameters. The value $\ln W^2 - \eta_0$ is the maximum $\ln M_X^2$ up to which the exponential behavior holds. The parameters c and b are determined from fits to the measured $\ln M_X^2$ distributions in each (Q^2,W) bin. The diffractive contribution N^{diff} is not taken from the fit result for D but is determined by subtracting the non-diffractive contribution $N^{nondiff}$ from the observed number of events N^{obs} according to

$$N^{diff} = N^{obs} - N^{nondiff}\quad , \quad N^{nondiff} = \int_{\ln M_a^2}^{\ln M_b^2} c\exp(b\ln M_X^2)\ d\ln M_X^2\ , \tag{10.8}$$

where M_a and M_b are the M_X bin boundaries. This procedure minimizes the dependence on the parameterization of D.

For the diffractive contribution D four different parameterizations are considered:

$$\begin{aligned} D_{const} &= d_0 & \text{(default)} \\ D_{var} &= d_0(1-\beta)[\beta(1-\beta) + d_1(1-\beta)^\lambda] \\ D_{ext} &= d_0(1-\beta)[\beta(1-\beta) + d_1(1-\beta)^2] \\ D_{mc} &= d_0 \cdot D_{SATRAP}\ , \end{aligned} \tag{10.9}$$

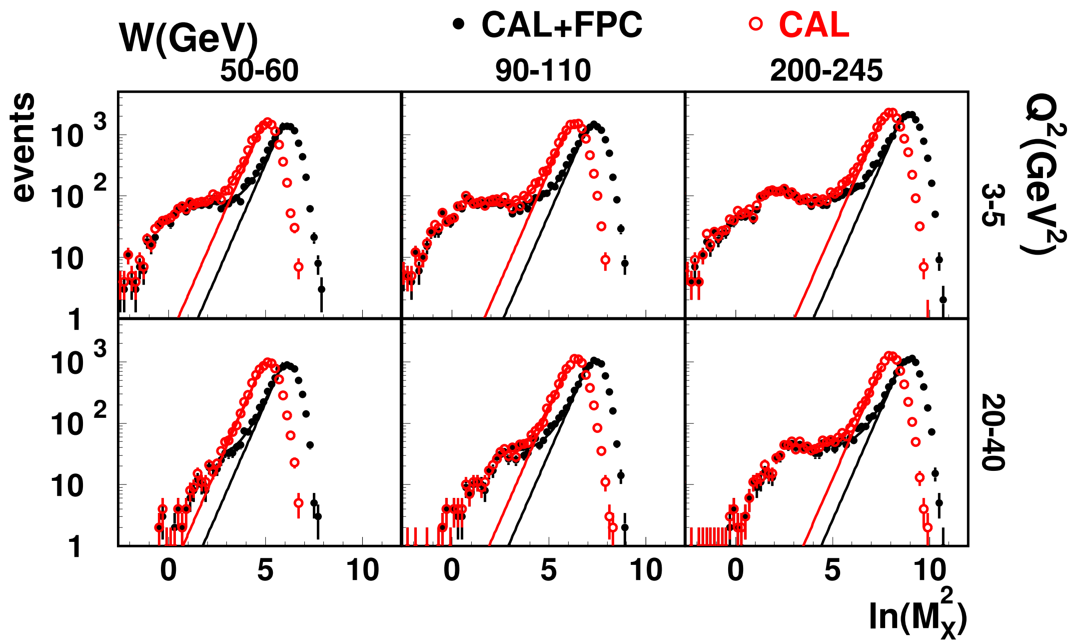

Figure 10.12: The distribution of $\ln M_X^2$ for several (Q^2, W) bins. M_X is determined using CAL+FPC (solid points) and CAL only (open points). The straight lines indicate the non-diffractive contribution from a fit of Eq. 10.7 to either distribution.

where d_0, d_1 and λ are free parameters, β is defined according to Eq. 1.49 and D_{SATRAP} is the normalized shape of the $\ln M_X^2$ distribution at detector level as predicted by SATRAP for a given (Q^2, W) bin. The first parameterization is used in the nominal analysis while the other three are used for systematic checks.

10.3.4 Extension of the kinematic range due to the installation of the FPC

The installation of the FPC has extended the calorimetric coverage of the ZEUS detector by about one unit in pseudorapidity from $\eta \leq 4.0$ to $\eta \leq 5.0$. In Fig. 10.12 the $\ln M_X^2$ distributions measured with the CAL are overlaid to the distributions where CAL+FPC is used to determine M_X. Practically no differences between the distributions are observed in the diffractive low M_X region. However, the non-diffractive peaks are shifted by one unit in $\ln M_X^2$ after including the FPC. For a fixed W bin the upper limit $M_{X,max}$ of the accessible range in M_X, defined as the region where the non-diffractive background amounts to less than 50%, is thus increased to $\ln M_{X,max}^2 = \ln M_{X,max0}^2 + 1$, where $M_{X,max0}$ is the limit before the installation of the FPC. Consequently, the accessible range in M_X is extended by a factor of $M_{X,max}/M_{X,max0} = 1.7$. Alternatively, for a given value of M_X the accessible range in W is extended towards smaller values reducing the lower W limit by a factor of $1/1.7 = 0.6$.

10.4 Reconstruction of diffractive events

The aim of the present analysis is to measure the diffractive cross section as a function of Q^2, W and M_X. The electron method is used for the reconstruction of Q^2 and the Σ-method for the reconstruction of W. This choice ensures good resolution in both variables over the entire measurement region as discussed in section 7.5. The mass M_X is reconstructed using EFOs according to Eq. 7.5 and corrected as discussed in section 10.3.2.

10.4.1 Kinematic range of the measurement

In order to gain new insight into diffraction in DIS it is essential to extend the measured range in W, Q^2 and M_X as far as possible. Limitations are imposed by the detector acceptance, by the resolution and the available event statistics.

The Q^2 range was chosen to be between 3 and 160 GeV^2. The lower Q^2 limit is given by the acceptance of the DIS electron which drops below 25% beyond this limit. The upper limit is dictated by the available number of events. The W-range was set to the region between 40 and 245 GeV. Here, the cut on the minimum energy of the scattered electron of $E_e > 10GeV$ determines the highest accessible W value. The lower end of the W range is limited by the resolution $\Delta W/W$ which is observed to be poor in the low W region.

While the lower M_X region for a given bin in Q^2 and W is dominated by diffractive events the amount of non-diffractive background increases exponentially at higher M_X values as discussed in section 10.3. In order to limit the uncertainties connected with the subtraction of the non-diffractive background the measurement of the diffractive cross section is limited to bins for which the non-diffractive background as determined by the $\ln M_X^2$ fitting procedure amounts to less than 50% of the total number of events in this bin.

10.4.2 Bin selection

The number and size of the bins in the three dimensional space of Q^2, W and M_X are limited by similar requirements as discussed in section 9.3 for the measurement of the inclusive structure function F_2. The number of events in each bin must be large enough to avoid statistical fluctuations. In order to reduce migrations into the measured bins the purity as defined in Eq. 9.4 is required to be larger than 30% for all measured bins. This requirement is fulfilled if the bin size for each of the three kinematic variables is larger than the resolution of the corresponding variable. The acceptance value as defined in Eq. 9.5 is required to be larger than 25% for each bin.

The following bins have been chosen in compliance with the above requirements:

- 7 Q^2 intervals: 3 - 5, 5 - 7, 7 - 10, 10 - 20, 20 - 40, 40 - 80 and 80 - 160 GeV^2 with center values chosen as 4, 6, 8, 14, 27, 55 and 110 GeV^2;
- 9 W intervals equidistant in $\ln W^2$ which provide approximately equal number of events. The bin width is $\Delta \ln W^2 = 0.4$. The center W values are 45, 55, 67, 82, 100, 122, 148, 181 and 221 GeV;

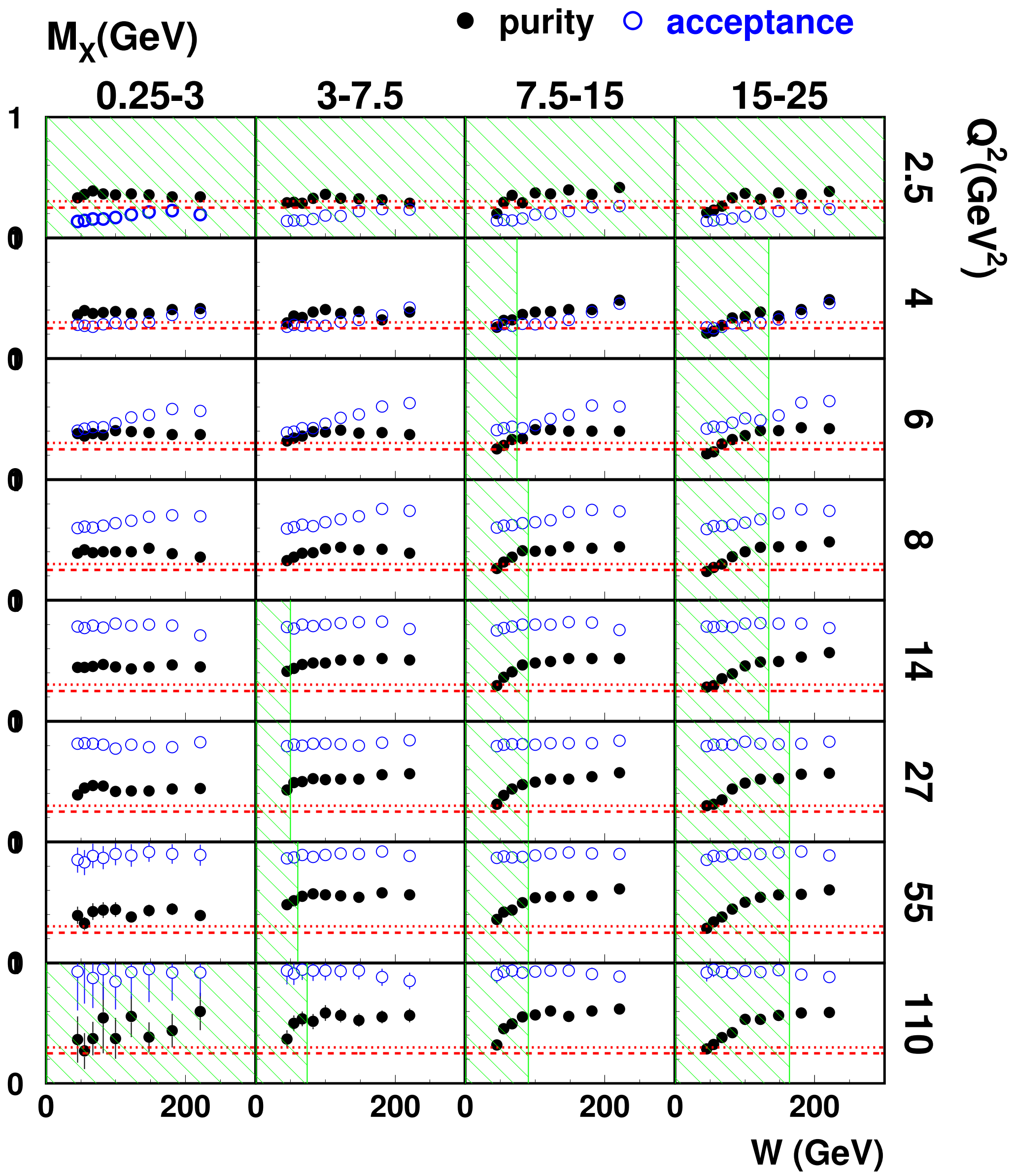

Figure 10.13: The purity (solid points) and acceptance (open points) for diffractive events as determined with the SATRAP MC sample are shown for all bins in Q^2, W and M_X. The horizontal dotted (dashed) line indicates the 30% (25%) threshold. The hashed areas indicate regions which fail at least one of the bin quality criteria explained in the text.

- 4 M_X intervals in the limits: 0.25 - 3, 3 - 7.5, 7.5 - 15 and 15 - 25 GeV with center values 2, 5, 11 and 20 GeV.

The purity and acceptance values for each bin determined with the diffractive SATRAP MC sample are shown in Fig. 10.13. The purity is lager than 30% for all measured bin and is typically 40-50%. The acceptance in the low Q^2 region is limited by the geometrical acceptance of the scattered electron. For $Q^2 > 10\,\mathrm{GeV}^2$ the acceptance reaches values of 80-90%.

10.5 Comparison of data and MC

In Fig. 10.14 the $\ln M_X^2$ distributions for all measured Q^2 and W intervals are shown for data and MC. The MC sample consists of the sum of a diffractive MC sample generated with SATRAP and a non-diffractive sample generated with DJANGOH which are added according to the procedure described in section 6.2.3. Satisfactory agreement between data and MC is obtained for most of the measured range in Q^2, W and M_X without adjusting the MC to the present data. However, in the low W region a small excess of low M_X i.e. diffractive events can be observed. In order to estimate the unfolding uncertainty due to this small discrepancy between data and MC the SATRAP sample is multiplied by a normalization factor in each Q^2 and W bin such that the number of events reconstructed in the M_X range where the non-diffractive background is less than 10% agrees between data and MC.

10.6 Test of the M_X method with MC

A combined diffractive (SATRAP) and non-diffractive (DJANGOH) MC sample is used to (*i*) optimize the technical details of the $\ln M_X^2$ fitting procedure and to (*ii*) test the reliability of the subtraction method, following the strategy developed in [142].

The correct determination of the non-diffractive background requires an accurate determination of the b-slope parameter. The reliability of the b-slope measurement is studied as follows. In a first step, the expected b-slope is determined at the detector level by fitting Eq. 10.7 to the non-diffractive MC sample alone setting $D = 0$. As observed in section 10.3.1 the values of b are within errors independent of Q^2 and W (see Fig. 10.9). The average value is found to be $\overline{b}_{exp} = 1.86 \pm 0.03$.

In a second step, Eq. 10.7 is fit to the combined MC sample using $D = D_{const}$. The fits are performed in the range $\ln(f_q \cdot Q^2) < \ln M_X^2 < \mathrm{Max}(\ln M_X^2)$. The lower fit limit is chosen according to the expectation that the $\ln M_X^2$ distribution of the diffractive contribution is flat for $M_X^2 \gtrsim Q^2$. Best agreement between the measured and the expected b-slope is obtained for $f_q \sim 10$.

The upper fit limit $\mathrm{Max}(\ln M_X^2)$ is the maximum $\ln M_X^2$ up to which the exponential behavior is observed. It scales with W according to $\mathrm{Max}(\ln M_X^2) = \ln W^2 - \eta_0$. The parameter η_0 is determined by performing a fit to the $\ln M_X^2$ distribution for various values of η_0. For $\eta_0 \lesssim 1.6$ the χ^2 probability is observed to drop rapidly. The upper limit is thus chosen to be $\mathrm{Max}(\ln M_X^2) = \ln W^2 - 1.8$.

In Fig. 10.15 the b-slopes obtained from fits to the combined MC sample are compared to the true b-slope values at the detector level for different Q^2 and W intervals. Good agreement is observed for the upper three W and lower four Q^2 intervals. For the remaining bins a systematic shift towards lower b-slopes is observed. This can be understood by looking at Fig. 10.16. For the lower W and higher Q^2 bins the diffractive plateau region is relatively small and the diffractive term D is thus not well constrained in the fit. This leads to a biased b-slope measurement.

Since the b-slope is expected to be independent of Q^2 and W and an unbiased value can only be obtained in a restricted Q^2 and W region an average b-slope, $\overline{b}$, is determined using the upper three W and lower four Q^2 intervals. A value of $\overline{b}_{MC} = 1.81 \pm 0.03$ is obtained which is

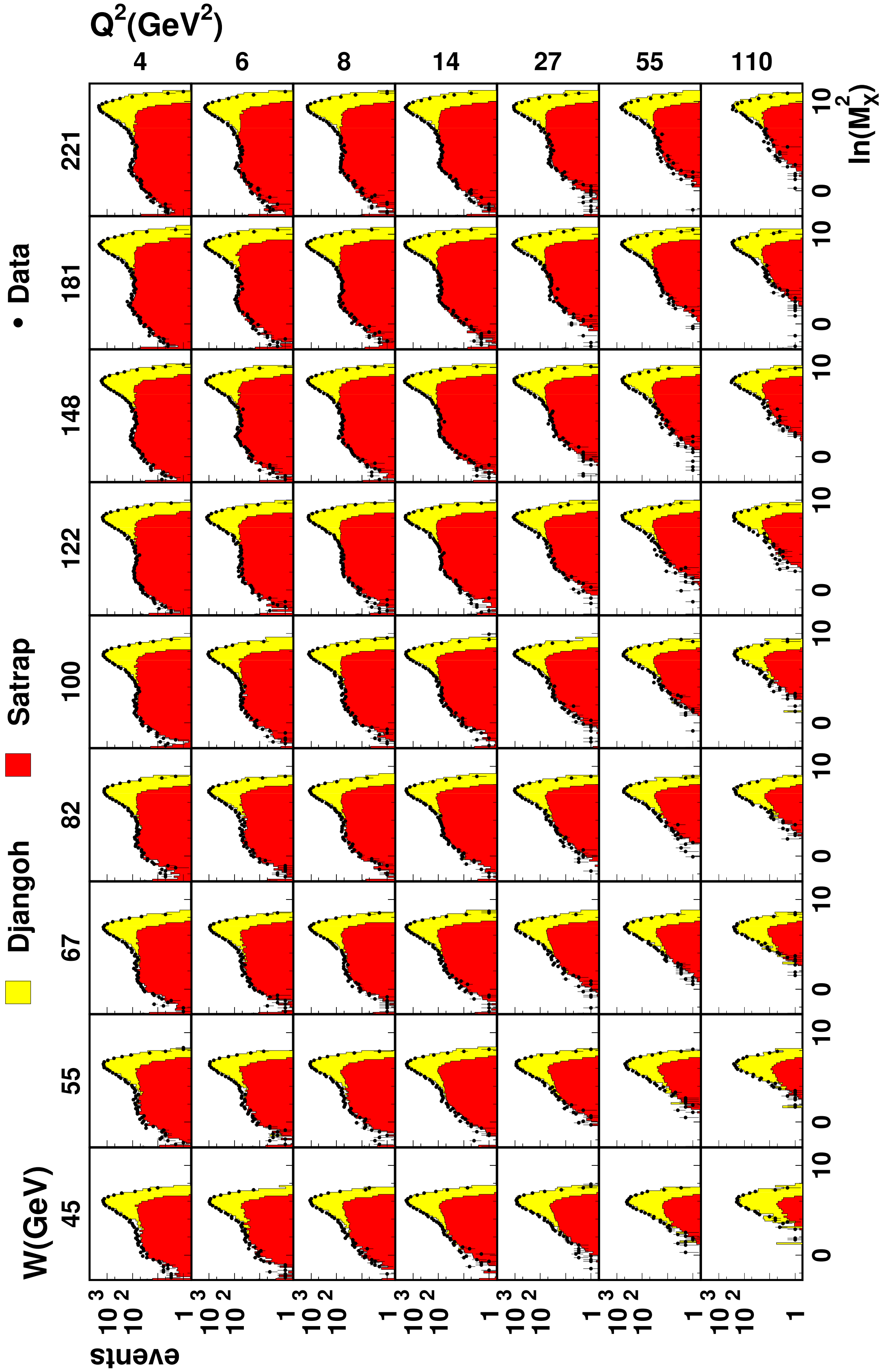

Figure 10.14: $\ln M_X^2$ distributions for all measured Q^2 and W intervals in data (points) and MC (shaded area). The diffractive MC sample generated with SATRAP has been added to the non-diffractive sample generated with DJANGOH according to the procedure described in section 6.2.3.

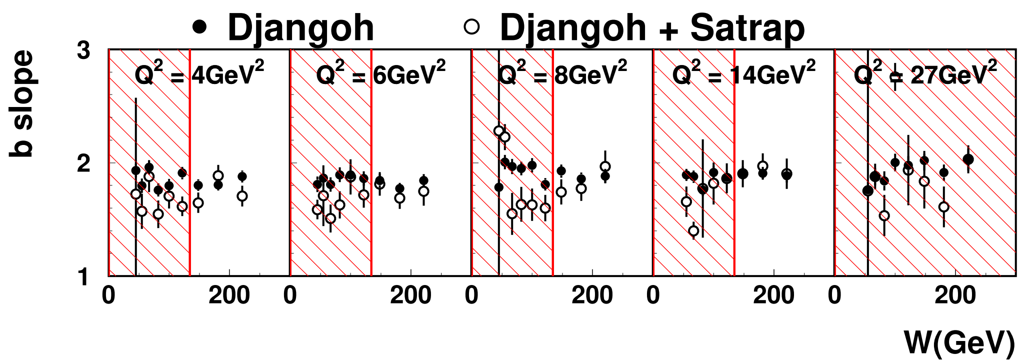

Figure 10.15: The b-slopes obtained from a fit to the combined diff+non-diff MC sample are compared to the true b-slopes obtained from a fit to the non-diffractive MC sample.

within errors compatible with the value $\overline{b}_{exp} = 1.86 \pm 0.03$ found from the fits to the diffractive distributions alone.

For the determination of the non-diffractive contribution in all (Q^2,W) bins the $\ln M_X^2$ fit is repeated using $b = \overline{b}$ as a fixed parameter. The lower fit limit is reduced to $\ln M_X^2 < \ln(f_q \cdot Q^2)$ using $f_q = 1$. This is required in order to obtain a sufficiently large fit range which constrains the diffractive contribution also in the low W and high Q^2 region. The results of the fits are shown in Fig. 10.16 for some exemplary Q^2 and W bins.

Finally, the number of reconstructed diffractive events N_{rec}^{MC} for the combined MC sample is evaluated according to Eq. 10.8. In Fig. 10.17 the obtained values of N_{rec}^{MC} are compared to the number of events N_{SATRAP} originating form the diffractive MC sample alone. The agreement is better than 5% for most bins. For a few high W and high Q^2 bins discrepancies in the order of 10% are obtained.

In conclusion, it has been found that the $\ln M_X^2$ method extracts the correct number of diffractive events for the combined diffractive and non-diffractive MC sample. A fitting procedure has been developed which consists of two steps. In the first step Eq. 10.7 is fit to the $\ln M_X^2$ distributions in a limited Q^2 and W region treating b as a free parameter leading to the common b-slope value $\overline{b}$. In the second step fits are performed for all Q^2 and W bins fixing the parameter b to the common slope $\overline{b}$.

10.7 Contribution from proton dissociation

The contribution from diffractive processes of the type $ep \rightarrow eXN$, where the proton dissociates into a system N, has been studied with EPSOFT2.0 [122]. This MC generator simulates diffractive events based on the triple-Regge formalism and an M_N distribution as measured for diffractive dissociation in pp scattering. For most of the events with masses $M_N \lesssim 2.5\,\text{GeV}$ the system N escapes through the forward beam hole and deposits no energy in the FPC. However, for basically all events with $M_N \gtrsim 4\,\text{GeV}$ the system N deposits energy in the FPC as shown in Fig. 10.18(a). For events where the system N deposits energy in the calorimeter the reconstructed mass $M_{X,rec}$ is significantly larger than the true mass $M_{X,true}$ of the system X (see Fig. 10.18(b)). In general, the reconstructed mass is so large that these events do not contribute to the diffractive sample.

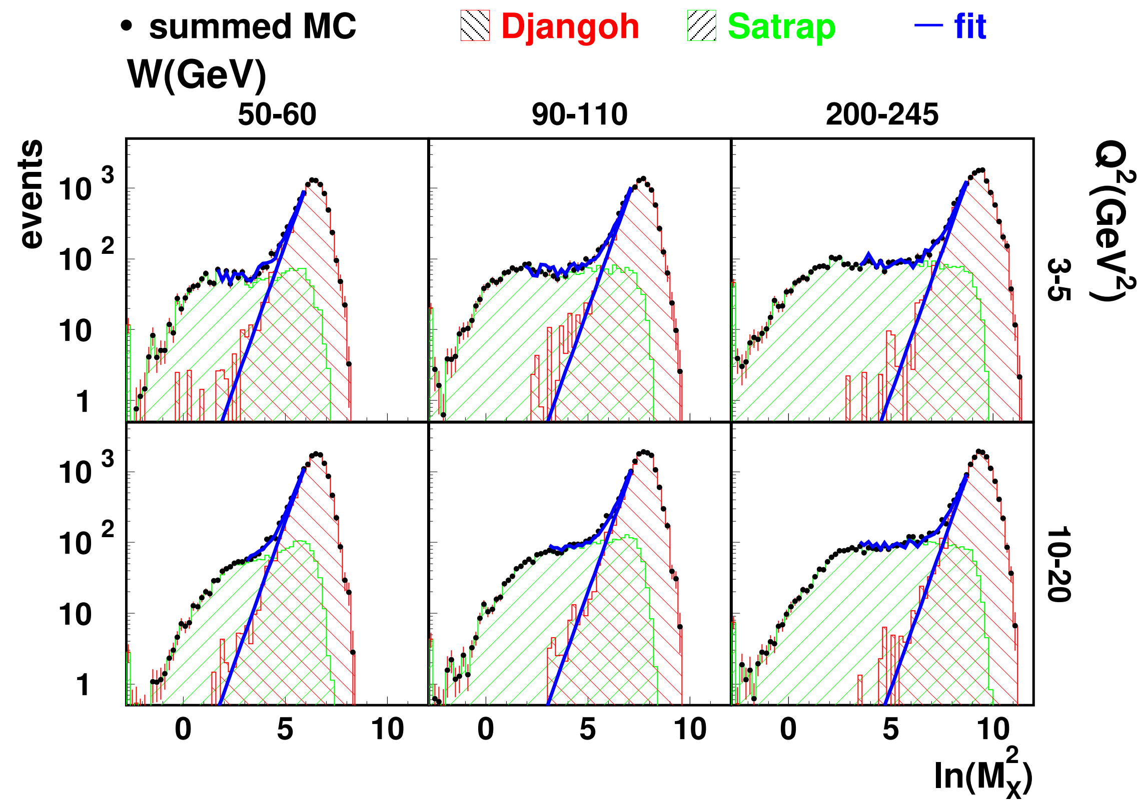

Figure 10.16: The $\ln M_X^2$ distributions of a diffractive (SATRAP) and non-diffractive (DJANGOH) MC sample as well as the combined MC (solid points) are shown. The curves indicate the result of the fit using a fixed b-slope. The straight lines indicate the non-diffractive contribution of the fit.

In Fig. 10.19 the distributions of $\ln M_{X,true}^2$ and $\ln M_{X,rec}^2$ are shown for three different W bins. While the migrations in $\ln M_X^2$ are small at low W, strong migrations are observed for high W values. The contribution from proton dissociation changes the shape of the $\ln M_X^2$ distribution mainly at high W. This might affect the fitting procedure described in section 10.6. In particular the extracted b-slope value might be biased.

In order to decrease the bias on the $\ln M_X^2$ distribution, a cut has been developed that rejects proton dissociation events with a large migration in M_X. The basic idea of this cut is that proton dissociation events where the system N is detected in the calorimeter can be identified by a large rapidity gap $\Delta\eta$ within the measured hadronic system (see Fig. 10.20(*Left*)). The maximum observed rapidity gap $\Delta\eta$ is defined as the largest distance in pseudorapidity η between two consecutive EFOs with energy $E_{EFO} > 0.4GeV$ ordered in η. Since there is a large rapidity gap between the scattered electron and the hadronic system it is important to exclude EFOs which belong to particles that showered off the electron and were not merged with the electron cluster. To this end, EFOs with $E_{EFO} < 1GeV$ that have a distant of less than 36 cm across the CAL surface from the measured DIS electron are excluded from the calculation of $\Delta\eta$. The distribution of $\Delta\eta$ is shown in Fig. 10.20 for data and MC of single diffractive and non-diffractive as well as proton dissociation diffractive events. It can be seen that the distribution for the proton dissociation sample extends to higher values of $\Delta\eta$. Adjusting the normalization of the proton dissociation sample, good description of the data is achieved.

In order to reduce the contribution from proton dissociation events with large migrations in

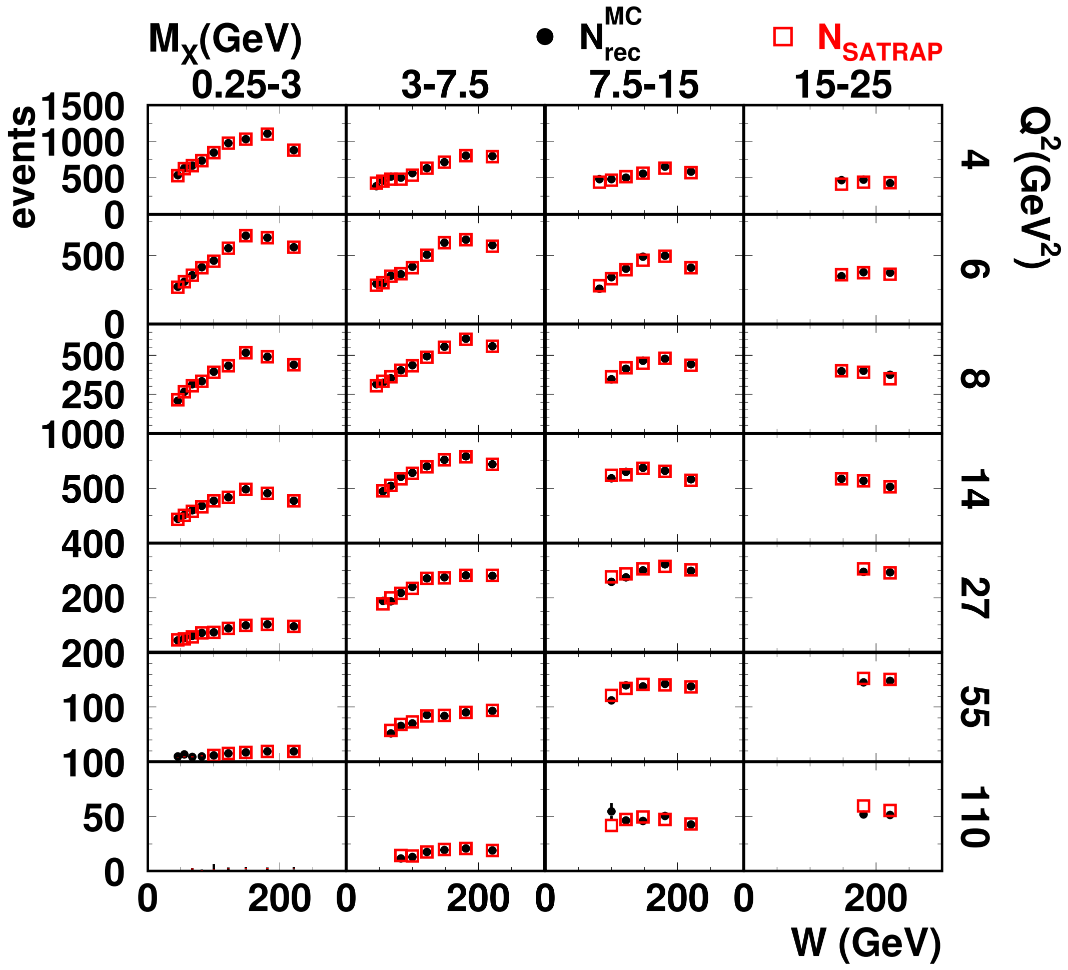

Figure 10.17: The extracted numbers of diffractive MC events (solid points) are compared with the numbers of diffractive events present in the samples (open points).

M_X, events are rejected that fulfill the following two requirements ($\Delta\eta$-cut):

- $\Delta\eta > 2.5$,
- $M_X(\eta < 2.5)/M_{X,rec} < 0.6$,

where $M_X(\eta < 2.5)$ is the invariant mass of all EFOs with $\eta < 2.5$. The value $M_X(\eta < 2.5)/M_{X,rec}$ gives an estimate of how much the measurement of M_X is affected by the contribution from the system N.

The distributions of $\ln M^2_{X,true}$ and $\ln M^2_{X,rec}$ of the EPSOFT proton dissociation sample after applying the $\Delta\eta$-cut are shown in Fig. 10.21. The bias in the distribution of $\ln M^2_X$ is observed to be much reduced.

The determination of the b-slope in data as described in section 10.6 has been repeated with and without applying the $\Delta\eta$-cut yielding a significantly increased value of $b_{\Delta\eta-\mathrm{cut}} = 1.66 \pm 0.02$ compared to $b_{nocut} = 1.51 \pm 0.03$. In the following the $\Delta\eta$-cut is always applied.

The remaining contribution due to proton dissociation events mainly originates from events with a small mass M_N, where the system N is not detected in the calorimeter. For each bin

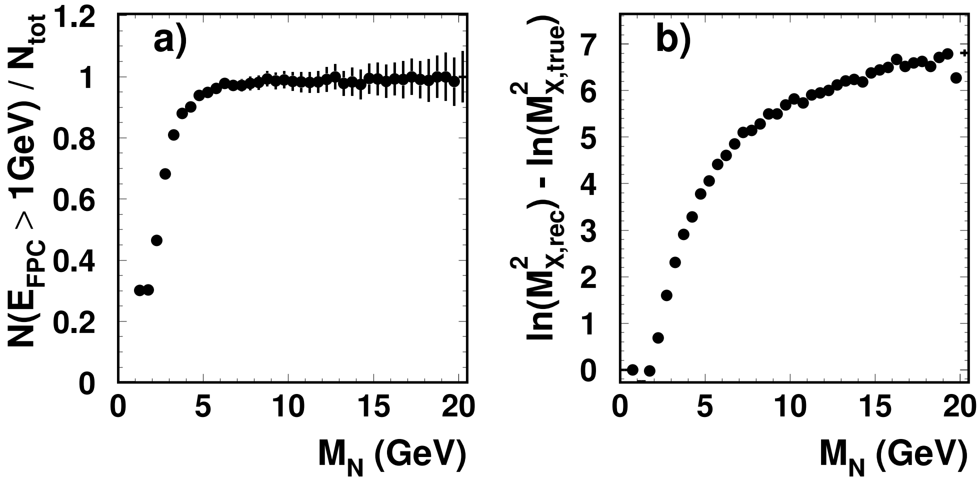

Figure 10.18: Study of $ep \to eXN$ events generated with EPSOFT. (a) The fraction of events with $E_{FPC} > 1$GeV as a function of the mass M_N of the dissociated proton. (b) The logarithmic increase of the reconstructed mass $M_{X,rec}$ compared to the true mass $M_{X,true}$ of the system X as a function of M_N.

in M_X and W there is a value M_N^{acc} such that the measured cross section σ^{meas} corresponds to the diffractive cross section including all proton dissociation events with $M_N < M_N^{acc}$:

$$\sigma^{meas} = \sigma^{ep\to Xp} + \int_0^{M_N^{acc}} \frac{\sigma^{ep\to XN}}{dM_N} dM_N \ . \tag{10.10}$$

From the proton dissociation EPSOFT MC sample M_N^{acc} is estimated to be $M_N^{acc} = 2.7 \pm 0.5$ GeV.

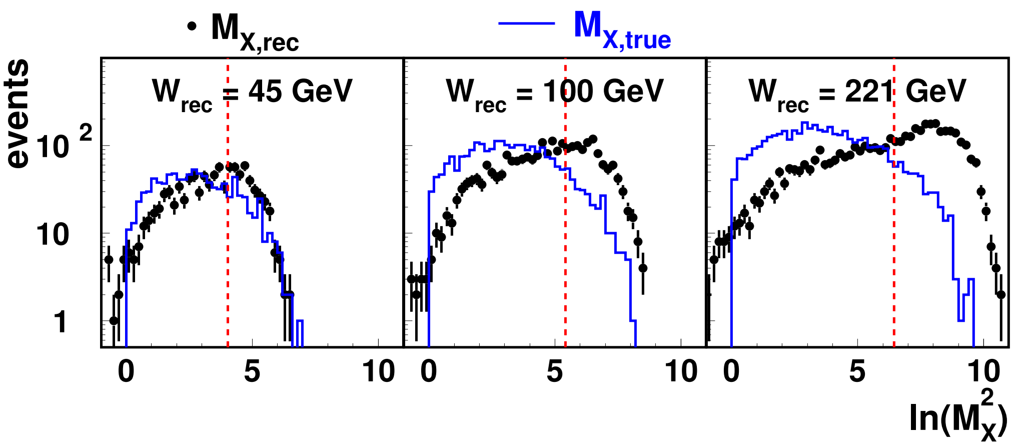

Figure 10.19: The $\ln M_X^2$ distributions of the true (histogram) and reconstructed (points) mass M_X are shown for proton dissociation events generated with EPSOFT in three bins of the reconstructed W value. The dotted line indicates for every W bin the upper limit of M_X considered in this analysis.

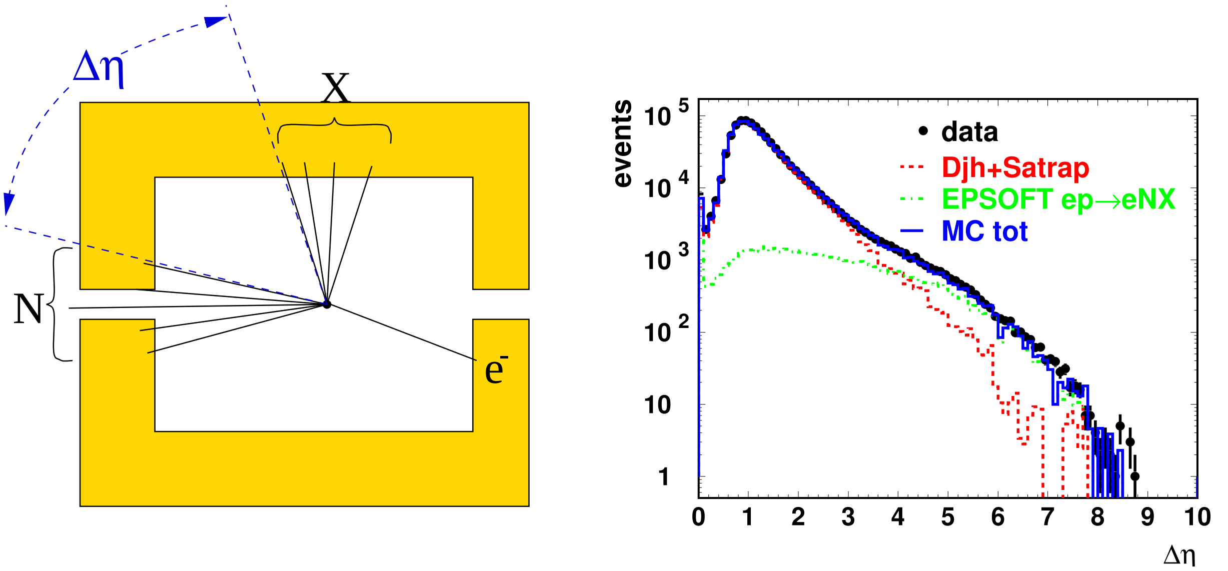

Figure 10.20: *Left*: Schematic representation of the particle flow for proton dissociation diffractive events. If part of the system N is detected in the calorimeter, the rapidity gap $\Delta\eta$ can be measured directly. *Right*: The distribution of the measured $\Delta\eta$ in the data (points) and for different MC combinations.

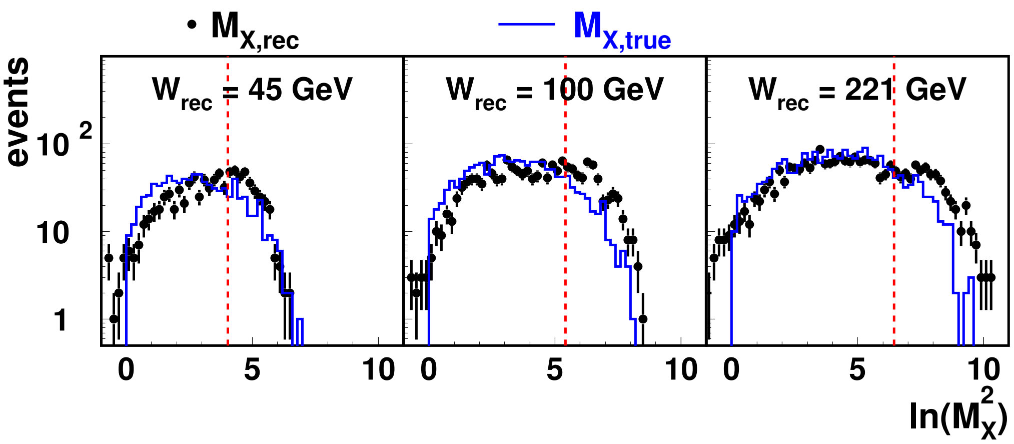

Figure 10.21: The $\ln M_X^2$ distributions of the true (histogram) and reconstructed (points) mass M_X are shown for proton dissociation events generated with EPSOFT after applying the $\Delta\eta$-cut. The dotted lines indicate the upper limit of M_X which is covered in this analysis.

Chapter 11

The Diffractive cross section

11.0.1 The diffractive event sample

The M_X method described in section 10.3 is used to extract the diffractive contribution from the sample of inclusive DIS events which is dominated by non-diffractive events.

According to the procedure developed in section 10.6 the fit to the $\ln M_X^2$ distributions in bins of Q^2 and W is first performed treating the b-slope as a free parameter. The fit is performed for each of the four parameterizations D of the diffractive contribution defined in Eq. 10.9. Following the MC study described in section 10.6 the common b-slope is determined using the three highest W and four lowest Q^2 intervals. For these bins the variations of the b-slopes obtained with the different parameterizations of D are observed to be small (see Fig. 11.1). The average b-slope was found to be $\bar{b} = 1.66 \pm 0.02(\text{stat})$. The values obtained using the other parameterizations of D are in good agreement with the nominal value: $\bar{b}_{var} = 1.70 \pm 0.02$, $\bar{b}_{ext} = 1.68 \pm 0.02$ and $\bar{b}_{mc} = 1.64 \pm 0.02$.

The b-slopes obtained from the data are significantly lower than the values obtained from the MC (compare Fig. 10.15). The value of b depends on the particle multiplicity in the forward direction and cannot be precisely predicted by the available models. It is therefore essential to use the b values obtained from the data. Estimating the non-diffractive background from the MC alone may lead to incorrect cross section results.

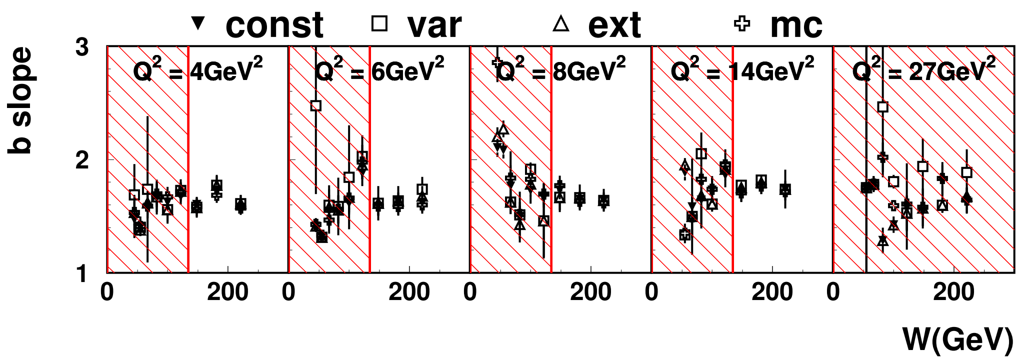

Figure 11.1: The b-slopes obtained from fits to the $\ln M_X^2$ distributions in data using the four different parameterizations for the diffractive contribution D defined in Eq. 10.9. The shaded areas are not considered for the evaluation of the average b-slope.

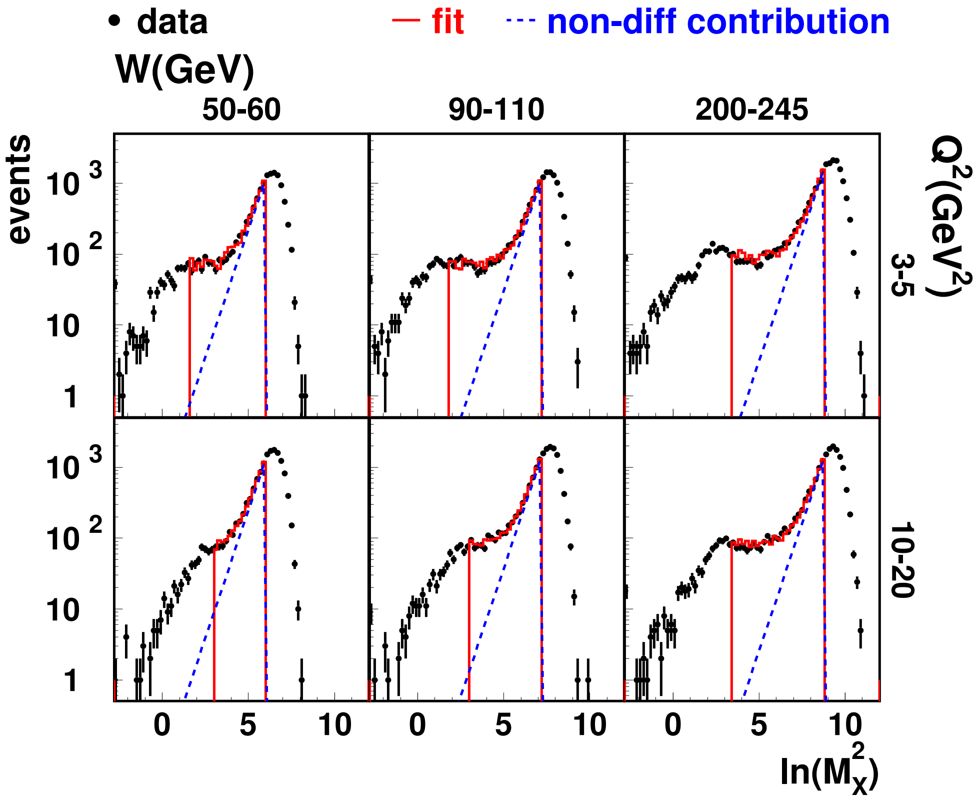

Figure 11.2: The $\ln M_X^2$ distributions in the data are shown for several (Q^2,W) bins. The solid lines show the results of fitting the data with Eq. 10.7 using a fixed slope of $\overline{b} = 1.66$. The dotted lines indicate the non-diffractive contribution as determined by the fit. The vertical lines indicate the fit limits.

In the second step the fit to the $\ln M_X^2$ distributions is repeated using $b = \overline{b} = 1.66$ as a fixed parameter. The results of the fits are shown in Fig. 11.2 for some exemplary bins in Q^2 and W.

The number of measured diffractive events N_{data}^{meas} in each bin is obtained using:

$$N_{data}^{meas} = N_{data}^{obs} - N^{nondiff} - N^{gas} - N^{PhP} - N^{QEDC} \ , \tag{11.1}$$

where N_{data}^{obs} is the number of observed events, $N^{nondiff}$ is the non-diffractive contribution as obtained from the fit, N^{gas} is the contribution from beam gas events and N^{PhP} and N^{QEDC} are the remaining contributions from photoproduction and QED-Compton processes as predicted by the MC.

11.1 Extraction of the diffractive ep cross section

As discussed in section 9.1 the measured number of events is corrected for detector smearing and acceptance effects using the bin-by-bin unfolding method. Using Eq. 9.11 the triple differential diffractive cross section is extracted according to:

$$\frac{d^3\sigma^{meas}(Q^2, W, M_X)}{dQ^2 d\ln W^2 dM_X} = \frac{N_{data}^{meas}}{N_{MC}^{meas}} \cdot \frac{d^3\sigma_{MC}^{Born}(Q^2, W, M_X)}{dQ^2 d\ln W^2 dM_X} \ . \tag{11.2}$$

For the evaluation of N_{MC}^{meas} the diffractive SATRAP MC sample is used which has been generated including QED radiative corrections using HERACLES. The Born level MC cross section $d^3\sigma_{MC}^{Born}(Q^2, W, M_X)/(dQ^2 d\ln W^2 dM_X)$ has been determined with SATRAP turning off QED radiative corrections. The cross section $\sigma_{MC}^{Born}(Q^2, W, M_X)$ and thus $\sigma^{meas}(Q^2, W, M_X)$ is evaluated for the average Q^2 and W values of each bin since its dependence on Q^2 and W inside each bin is smooth and adequately well known. However, the cross section dependence on M_X exhibits large fluctuations within the lower M_X bins due to vector meson resonances. The quoted cross section $\tilde{\sigma}$ corresponds therefore to the value averaged over the M_X bin according to

$$\frac{d^3\tilde{\sigma}(Q^2, W, M_X)}{dQ^2 d\ln W^2 dM_X} = \frac{1}{\Delta M_X} \int_{M_a}^{M_b} \frac{d^3\sigma(Q^2, W, M'_X)}{dQ^2 d\ln W^2 dM_X} dM'_X \,, \tag{11.3}$$

where M_a and M_b are the M_X bin boundaries. In the following σ stands for $\tilde{\sigma}$.

11.2 From ep to $\gamma^* p$ cross section

The cross section of interest to understand the properties of diffractive processes is the $\gamma^* p$ scattering cross section. The total $\gamma^* p$ cross section $\sigma^{\gamma^* p}$ is defined as the sum of the scattering cross sections $\sigma_L^{\gamma^* p}$ and $\sigma_T^{\gamma^* p}$ for longitudinally and transversely polarized photons. Using the Hand convention for the photon flux the $ep \to eXN$ cross section can be related to the $\gamma^* p \to pXN$ cross section by

$$\frac{d\sigma_{\gamma^* p}^{diff}(Q^2, W, M_X)}{dM_X} \equiv \frac{d(\sigma_L^{\gamma^* p} + \sigma_T^{\gamma^* p})}{dM_X} \approx \frac{2\pi}{\alpha} \frac{Q^2}{(1-y)^2 + 1} \frac{d\sigma_{ep}^{diff}(Q^2, W, M_X)}{dM_X d\ln W^2 dQ^2} \tag{11.4}$$

Here, a term $[1 - \frac{y^2}{(1-y)^2+1} \frac{R}{1+R}]$ with $R = \sigma_L^{diff}/\sigma_T^{diff}$ has been neglected. Since R cannot be determined it is set to zero. The effect of a non-zero value of R on the measurement of $\sigma_{\gamma^* p}^{diff}$ is largest for large values of W since $y \approx W^2/s$. In the extreme case of $R \gg 1$ the cross section will increase by at most 18% in the highest W bin. For $W < 170$ GeV the effect is less than 5%.

11.2.1 Systematic errors

The systematic errors of the cross section were estimated by varying several cut, calibration and selection parameters. The resulting changes compared to the nominal analysis were recorded. The systematic checks are listed below and are numerated for reference reasons:

Checks related to the electron measurement:

{1},{2}: The cut on the corrected energy of the scattered electron was lowered (increased) from 10 GeV to 8 (12) GeV. The largest observed changes were less than 6% in the low Q^2 and high W region.

{3},{4}: The size of the fiducial cut (box cut) for electrons hitting the RCAL close to the beam hole was decreased (increased) from 8.2×13 cm to 7×12 (9×14) cm. This cut only affects low Q^2 events. The largest observed errors in the low Q^2 range were less than 8%.

{5},{6}: The effect of the 1% energy scale uncertainty of the scattered electron was tested by decreasing (increasing) the electron energy in data by 1%. The MC sample was left unchanged. The errors were found to be less than the statistical errors for each bin. Only in the high Q^2 bins where the statistics is low changes of more than 10% were observed.

{7},{8}: The alignment uncertainty of the SRTD was found to be ±2 mm. The largest systematic effects are expected to arise in the case where the true position of the upper and the lower halves are shifted in opposite directions with respect to the nominal position. The corresponding uncertainty was estimated by shifting the SRTD halves in the data by 2 mm in y-direction away from (towards) the RCAL beam hole. The largest effect was found to be less than 12% in the lowest Q^2 and W bins.

Checks related to the measurement of the hadronic system:

{9},{10}: The energy scale of the CAL in the data was increased (decreased) by 3% according to the estimated uncertainty. The largest error associated to the CAL energy scale was found to be less than 10%.

{11},{12}: The energy scale of the FPC in the data was varied by ±10% according to the estimated uncertainty. This lead to changes in the measured cross section of up to 8%.

{13}: In order to check the contribution of noise background to the low M_X bins the requirement on the minimum energy associated with the hadronic system in the calorimeter was increased from 0.4 GeV to 1 GeV. The maximum observed changes were in the order of 2%.

{14}: In the nominal analysis the measured values used for the cut on the minimum hadronic energy and on y_{JB} were calculated excluding the RCAL cells closest to the beam hole. As a systematic check these cells where included in the evaluation of the cut values. The associated error was found to be less than 3% in all bins.

Checks related to the background rejection:

{15},{16}: In order to estimate the uncertainty related to the contribution from interactions in the tail of the Z_{Vertex} distribution the cut on Z_{Vertex} was changed from ±50cm to ± 100 (30) cm. Changes of up to 10% were observed in the high Q^2 bins; however, the statistical errors were always larger. In the remaining regions the error was found to be less than 5%.

{17}: The uncertainty connected with the treatment of the photoproduction background was estimated by lowering the cut on the minimum $E - P_Z$ from 46 GeV to 40 GeV. As expected this affected mainly the high W region where changes up to 10% were observed.

Checks related to the $\ln M_X^2$ fitting procedure:

{18},{19},{20}: The $\ln M_X^2$ fitting procedure was repeated using the 3 alternative parameterizations of the diffractive contribution D defined in Eq. 10.9. This leads to significant changes in the cross section only in the lowest considered W bins for each M_X interval. The largest changes of up to 10% were observed when using D_{var}.

{21},{22}: The value of the b-slope which is used as a fixed parameter in the lnM_X^2 fitting was increased (lowered) from b=1.66 to b=1.76 (1.56). This check lead to a systematic increase (decrease) of the cross section in the lowest W for each M_X interval of up to 15%.

{23}: As a systematic check the b-slope which is fixed in the fit of the nominal analysis is treated as a free parameter. Again, significant changes were only observed in the lowest three W bins of each M_X interval. Changes of up to 15% were observed.

{24},{25}: The upper limit of the fit range in lnM_X^2 was increased (decreased) from lnW^2-1.8 to lnW^2-1.6 (2.0) in order to check whether the fit is affected by the rounding-off of the exponential behavior of the non-diffractive background. The largest error was found to be less than 5%.

Checks related to the unfolding procedure:

{26}: The unfolding of the true distributions from the measured ones requires a good description of the data in the MC. Even without reweighting, the available SATRAP MC provides a satisfactory description of the data in the entire phase space under study. In order to estimate the unfolding uncertainty due to differences between data and MC, SATRAP has been reweighted in each bin in Q^2 and W such that the number of events reconstructed in the M_X range where the non-diffractive background is less than 10% agrees between data and MC. The observed changes were generally less than 10%. Only in the high Q^2 and low W region where the diffractive cross section is small and the reweighting procedure is not well constrained changes of up to 20% were observed.

The total systematic error for each bin was evaluated as the quadratic sum of each individual systematic error, separately for the positive and the negative contributions. The total errors included in Fig. 11.3 were obtained as the quadratic sum of the statistical and systematic error. An overall error of 2.5% due to the uncertainty in the luminosity measurement was not included.

11.3 The diffractive cross section $d\sigma^{\gamma^* p}/dM_X$

The results of the differential diffractive cross section $d\sigma^{\gamma^* p \to XN}/dM_X$, $M_N < 2.7$, are presented in Fig. 11.3 as a function of W. The inner error bars denote the statistical errors and the outer bars denote the statistical and systematic errors added in quadrature. For $M_X < 15\,\text{GeV}$ the cross section is observed to rise with the virtual photon proton center of mass energy W.

Also shown in Fig. 11.3 are the published ZEUS results [142] which were obtained using the 1994 data. The highest Q^2 bin with a central value of $Q^2 = 60\,\text{GeV}^2$ is omitted since the bin definition is incompatible with the one of the present analysis. In general, the results of the two analyses agree within errors. However, the rise of $d\sigma/dM_X$ with W tends to be steeper for the 94 analysis.

The kinematic range covered by the present analysis has been substantially increased compared to the ZEUS 94 analysis. The lower Q^2 limit has been extended from $Q^2 = 7\,\text{GeV}^2$ to $Q^2 = 3\,\text{GeV}^2$ adding two additional Q^2 bins. The highest measured M_X value has been increased from $M_X = 15\,\text{GeV}$ to $M_X = 25\,\text{GeV}$ allowing for an additional M_X bin. The measured range

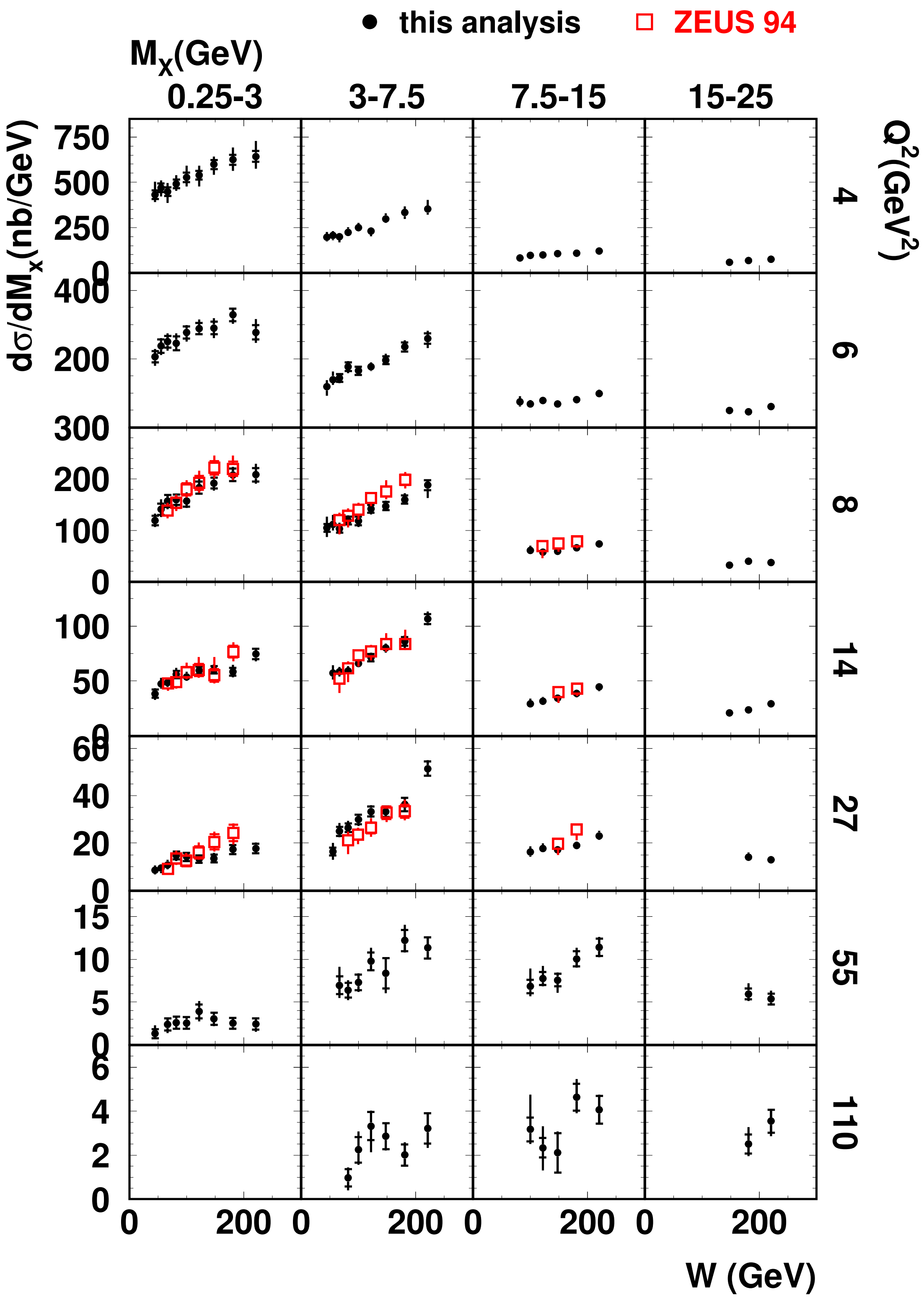

Figure 11.3: The differential diffractive cross section $d\sigma^{\gamma^* p \to XN}/dM_X$, $M_N < 2.7$, is plotted as a function of the virtual photon proton center of mass energy W for all measured Q^2 and M_X values. The inner error bars denote the statistical errors and the outer bars the statistical and systematic errors added in quadrature. An overall 2.5% normalization uncertainty originating form the luminosity measurement is not included. Also shown are the ZEUS results (open points) published in [142].

in W has been extended towards both lower and higher values covering the region $40\,\mathrm{GeV} < W < 245\,\mathrm{GeV}$ compared to $60\,\mathrm{GeV} < W < 200\,\mathrm{GeV}$ for the 94 analysis.

The increase of the measured kinematic range has been possible due to several detector upgrades and an improved understanding of the ZEUS detector. In 1995 the RCAL modules above and below the beampipe have been moved closer together reducing the beam hole in the rear direction from 20×20 cm to 8×20 cm. This led to an increased acceptance for low Q^2 events. The extension of the measured range towards higher M_X and lower W values is a consequence of the installation of the FPC. The increased calorimetric coverage in the forward direction allowed to reduce the non-diffractive background (see section 10.3.4).

The Q^2 dependence of $d\sigma^{diff}_{\gamma^* p}/dM_X$ is shown in Fig. 11.4. A fast decrease with Q^2 is observed for small M_X values. For the larger M_X values the decrease becomes slower, i.e. the relative contribution of high mass diffractive dissociation of the virtual photon grows as a function of Q^2. The difference in the Q^2 dependence for high and low masses M_X is most clearly seen in Fig. 11.5 where the diffractive cross section multiplied by Q^2, $Q^2 d\sigma^{diff}_{\gamma^* p}/dM_X$, is plotted as a function of Q^2. While $Q^2 d\sigma^{diff}_{\gamma^* p}/dM_X$ is independent of Q^2 in the higher M_X bins it is suppressed by about an extra power of Q^2 in the lowest M_X bin.

11.4 Comparison of diffractive and total $\gamma^* p$ cross section

The ratio of the diffractive and the total virtual photon proton cross section,

$$r^{diff}_{tot}(Q^2, W, M_X) = \frac{\int_{M_a}^{M_b} dM_X d\sigma^{diff}_{\gamma^* p}/dM_X(Q^2, W, M_X)}{\sigma^{tot}_{\gamma^* p}(Q^2, W)} , \tag{11.5}$$

is displayed in Fig. 11.6 as a function of W for different M_X and Q^2 values. The diffractive cross section $d\sigma^{diff}_{\gamma^* p}/dM_X$ is integrated over the bin width $M_a < M_X < M_b$ and the total cross section is evaluated from the F_2 data presented in chapter 9 using $\sigma^{tot}_{\gamma^* p}(Q^2, W) = \frac{4\pi^2\alpha}{Q^2(1-x)} F_2(Q^2, W)$.

Within errors the ratio r^{diff}_{tot} is observed to be consistent with W independence as observed in [142]. Combined with the observation of a rising diffractive cross section with W this is in contradiction to the naive expectation. Assuming that the cross section for diffractive photon dissociation at fixed M_X has the same W dependence as the forward elastic cross section, $\gamma^* p \to \gamma^* p$, the optical theorem states that the W dependence of $d\sigma^{diff}/dM_X$ behaves like the square of the W dependence of σ^{tot}. Hence, $d\sigma^{diff}/dM_X$ should be proportional to W^a if $\sigma^{tot} \propto W^{a/2}$. This implies a W dependence of the ratio r^{diff}_{tot} proportional to $W^{a/2}$.

The same W dependence for the diffractive and the total cross section has been predicted in [63] and is well described by the Saturation model introduced in [60].

The Q^2 dependence of r^{diff}_{tot} is shown in Fig. 11.7 for different values of M_X. The ratio r^{diff}_{tot} is averaged over the measured W intervals for each bin in Q^2 and M_X. In the low M_X region r^{diff}_{tot} is observed to decrease rapidly with increasing Q^2. However, for $M_X > 7.5$ GeV the Q^2 dependence of r^{diff}_{tot} becomes flat. This is in agreement with the observation in [138] that the fraction of DIS events with large rapidity gaps (LRG) is roughly constant with Q^2 since the LRG analysis considered events with masses $M_X \gtrsim 4$ GeV.

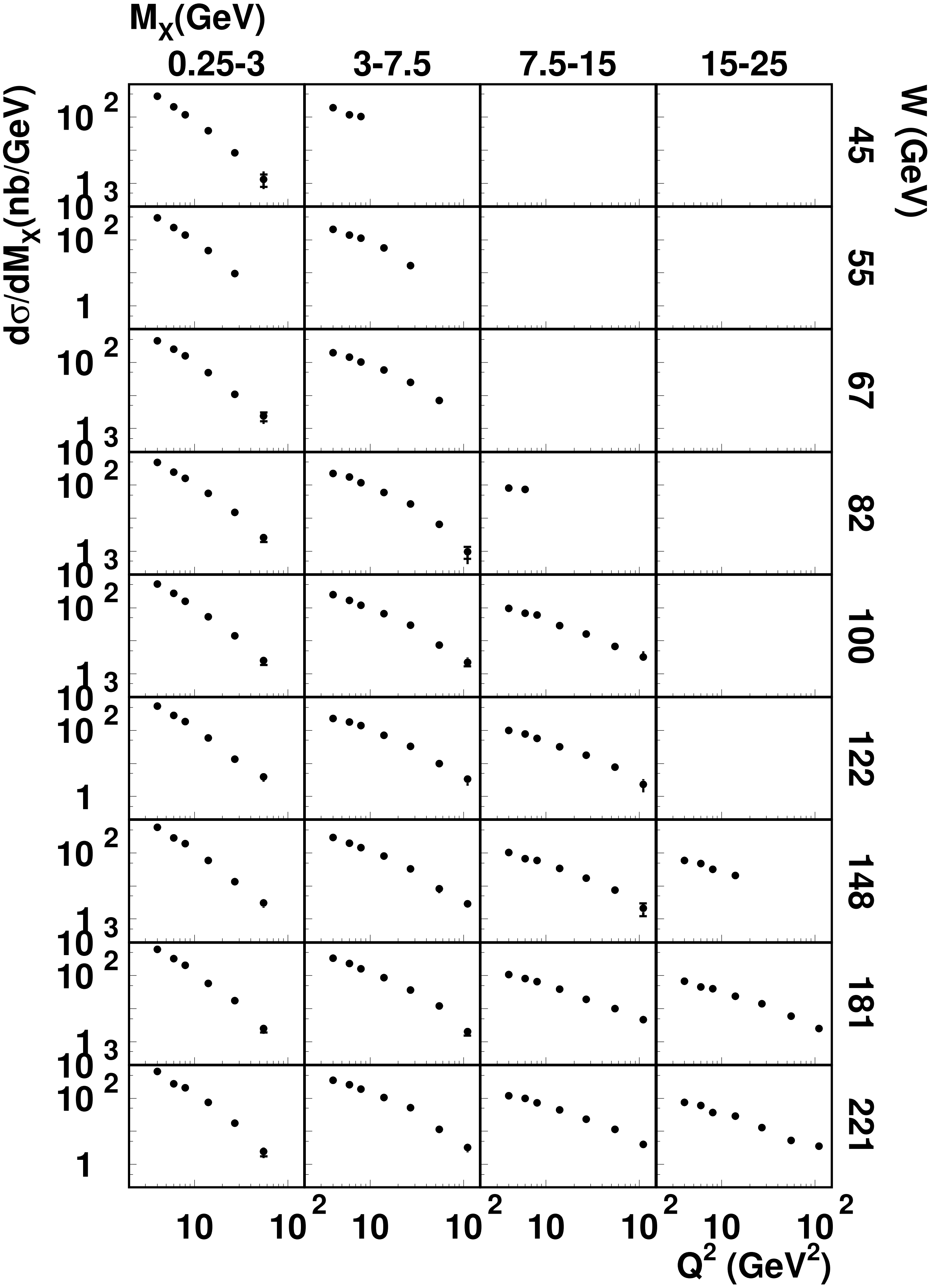

Figure 11.4: The differential diffractive cross section $d\sigma^{diff}_{\gamma^* p}/dM_X$ is plotted as a function of the virtuality Q^2 of the exchanged photon for the indicated M_X and W values.

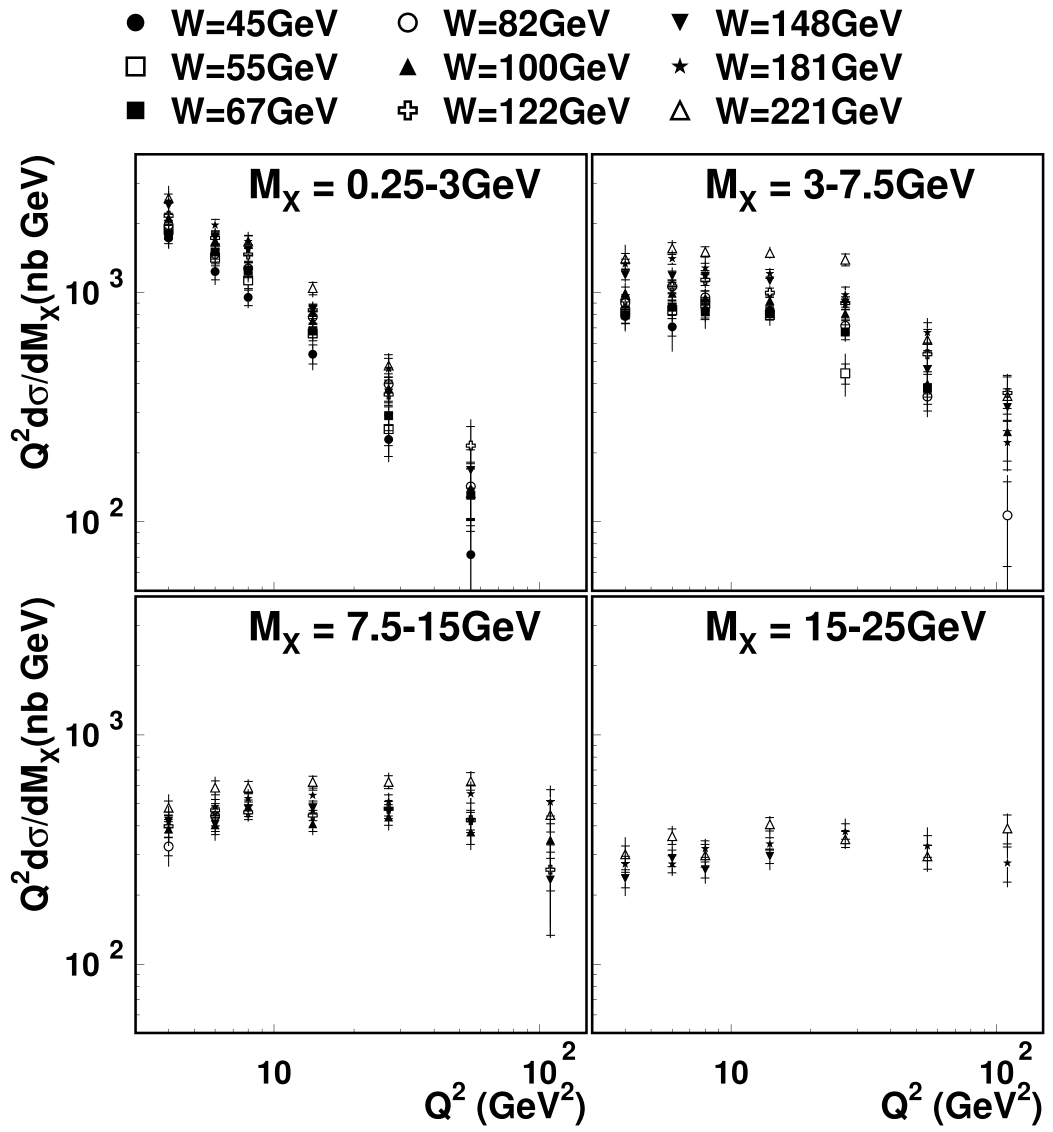

Figure 11.5: The differential diffractive cross section multiplied by Q^2, $Q^2 d\sigma^{diff}_{\gamma^* p}/dM_X$, is plotted as a function of Q^2 for the indicated M_X and W values.

11.5 Diffractive structure function

The concept of a diffractive structure function has been introduced in [51]. It is based on the assumption that diffraction is mediated by the exchange of a colorless object, called a pomeron, which is composed of partons. The diffractive structure function is related to the diffractive cross section by:

$$F_2^{D(3)}(Q^2, \beta, x_{I\!P}) = \frac{1}{4\pi^2 \alpha_{em}} \cdot \frac{Q^2(W^2+Q^2)^2}{2M_X W^2} \cdot \frac{d\sigma^{diff}_{\gamma^* p}(Q^2, W, M_X)}{dM_X}\,, \tag{11.6}$$

where $x_{I\!P}$ is the momentum fraction of the proton carried by the exchanged pomeron and β is the momentum fraction carried by the struck quark within the pomeron (see section 1.2.4). $F_2^{D(3)}$ can be interpreted in terms of parton densities of the pomeron which for diffractive scattering specify the probability to find a parton carrying a momentum fraction $x = \beta x_{I\!P}$ of

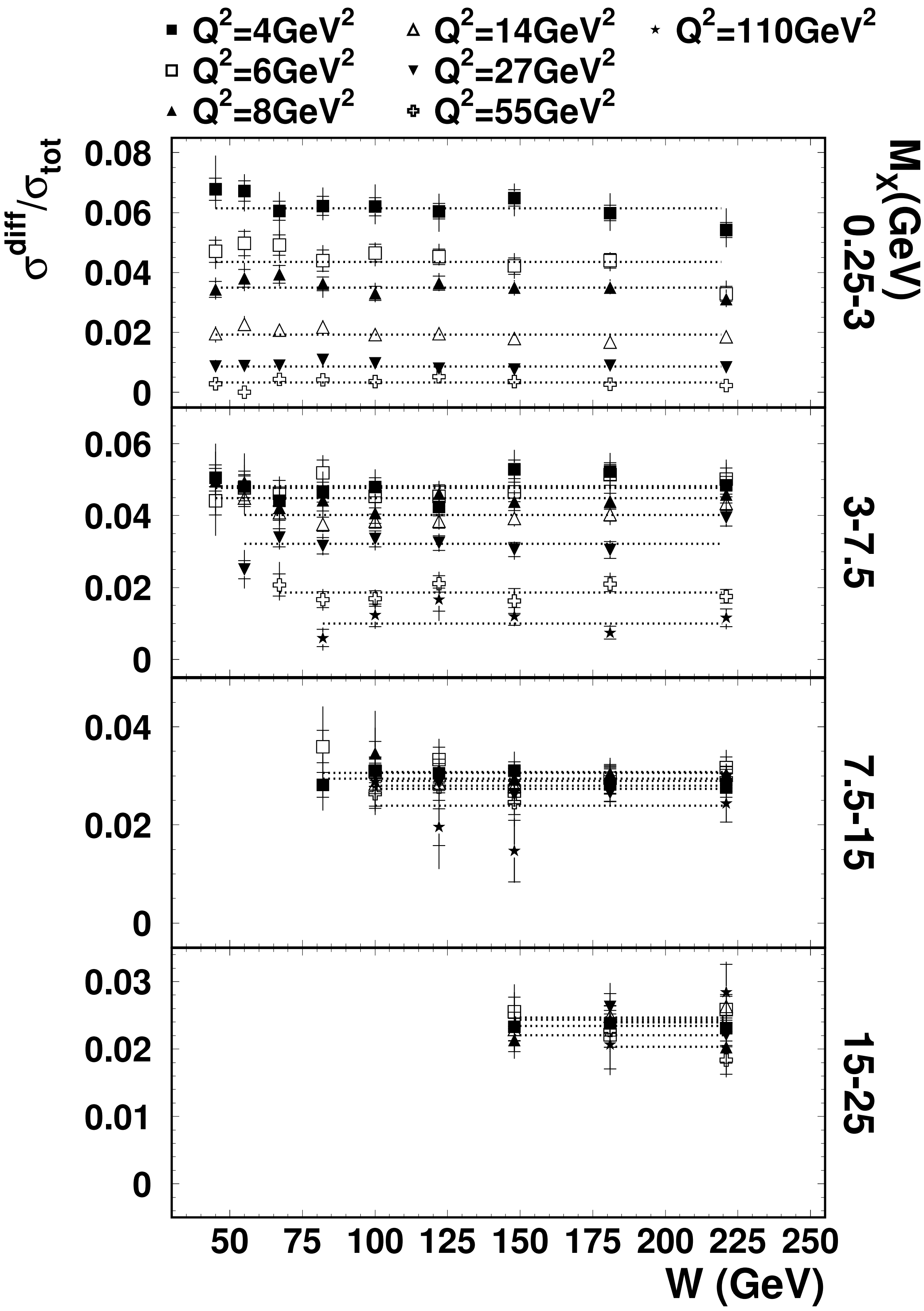

Figure 11.6: The ratio of the diffractive cross section σ^{diff}, integrated over the bin width $M_a < M_X < M_b$, and the total $\gamma^* p$ cross section σ^{tot} is shown as a function of W for different bins of M_X and Q^2. The dotted lines indicate the average values of $\sigma^{diff}/\sigma^{tot}$ in the measured W region for each bin in Q^2 and M_X.

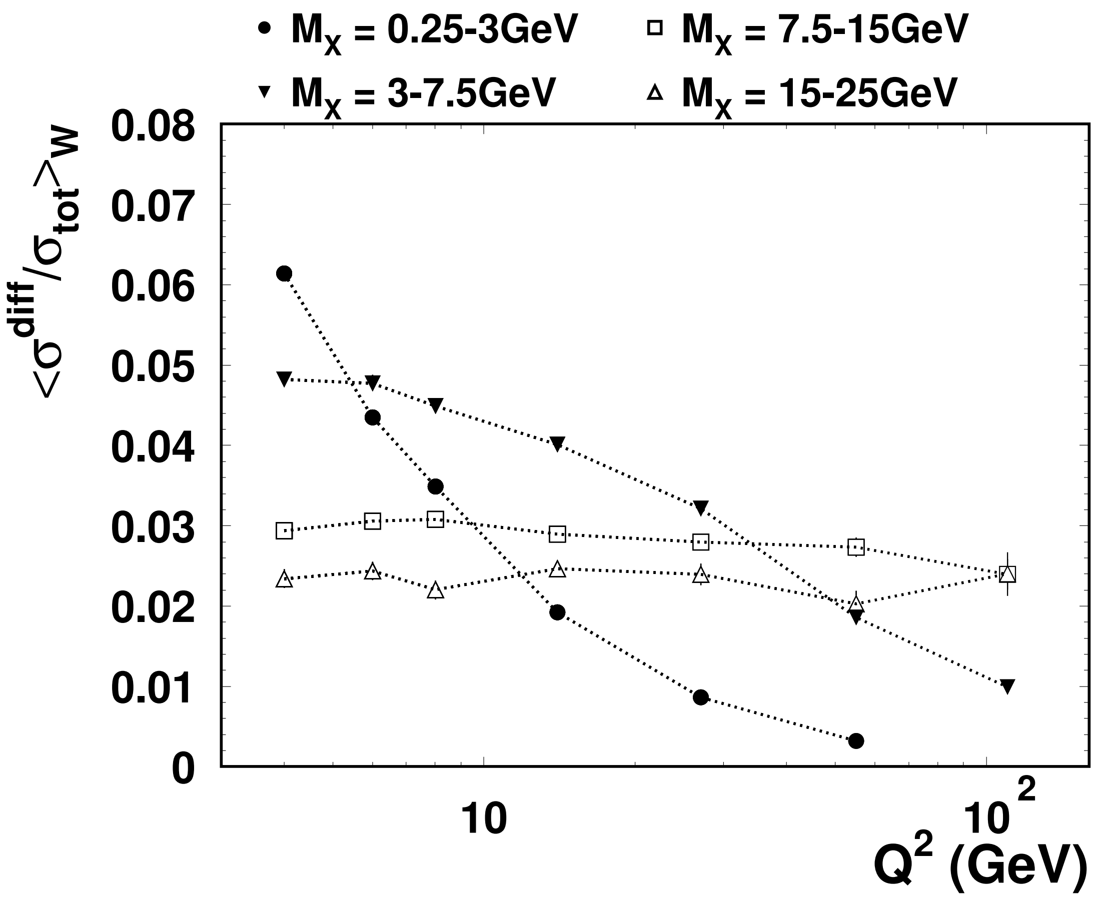

Figure 11.7: The ratio of the diffractive cross section σ^{diff} and the total $\gamma^* p$ cross section σ^{tot} is shown as a function of Q^2 for different bins of M_X. To guide the eye the dotted lines connect points corresponding to the same M_X values.

the proton. For $W^2 \gg Q^2$, which holds for this analysis, the above equation can be rewritten as:

$$x_{I\!P} \cdot F_2^{D(3)}(Q^2, \beta, x_{I\!P}) = \frac{1}{4\pi^2 \alpha_{em}} \cdot \frac{Q^2(M_X^2 + Q^2)}{2M_X} \cdot \frac{d\sigma^{diff}_{\gamma^* p}(Q^2, W, M_X)}{dM_X} . \tag{11.7}$$

The quantity $x_{I\!P} F_2^{D(3)}$ is shown in Fig. 11.8 as a function of $x_{I\!P}$ for different values of Q^2 and β. The data is seen to decrease with increasing $x_{I\!P}$ which reflects the rise of $d\sigma^{diff}_{\gamma^* p}/dM_X$ with W.

In [51] it has been suggested that $F_2^{D(3)}(Q^2, \beta, x_{I\!P})$ should factorize into two terms

$$F_2^{D(3)}(Q^2, \beta, x_{I\!P}) = f_{I\!P/p}(x_{I\!P}) \cdot F_2^{D(2)}(\beta, Q^2) , \tag{11.8}$$

where the pomeron flux factor $f_{I\!P/p}$ depends on $x_{I\!P}$ and the pomeron structure function $F_2^{D(2)}$ depends on Q^2 and β. In order to test this factorization hypothesis the data are fitted with a universal $x_{I\!P}$ dependence. Assuming the flux factor to be of the form $f_{I\!P/p}(x_{I\!P}) = (C/x_{I\!P}) \cdot (x_0/x_{I\!P})^n$ the data are fitted to the form $F_2^{D(3)}(Q^2, \beta, x_{I\!P}) = (C/x_{I\!P}) \cdot (x_0/x_{I\!P})^n F_2^{D(2)}(\beta, Q^2)$. The arbitrary normalization constant C is set to 1 and for x_0 an average value of the measured $x_{I\!P}$, $x_0 = 0.0042$, is chosen. The values $F_x^{D(2)}(\beta_i, Q_i^2)$ for the 27 measured (β_i, Q_i^2) bins and the

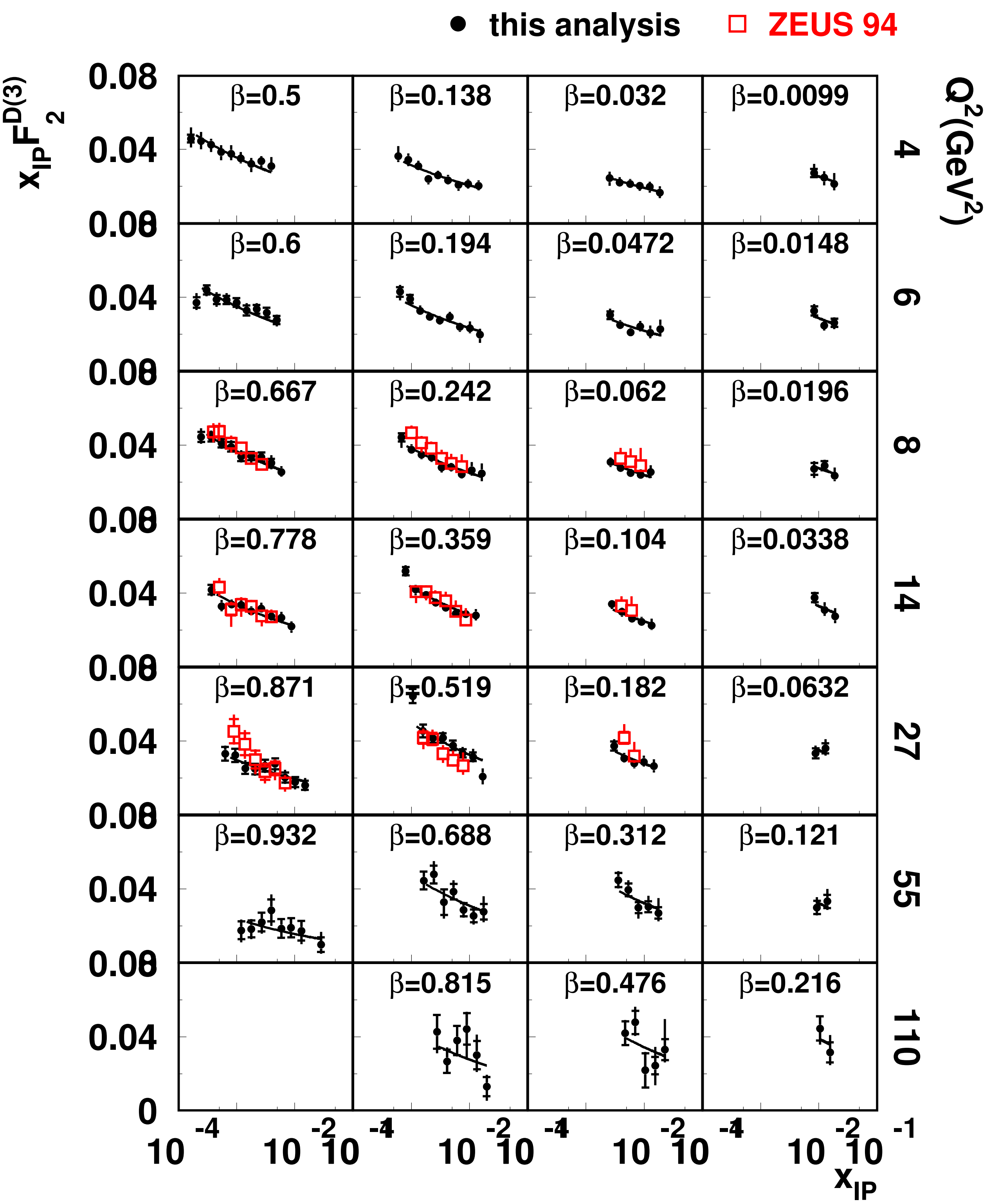

Figure 11.8: The measured values of $x_{I\!P}F_2^{D(3)}$ are shown as a function of $x_{I\!P}$ for different values of Q^2 and β. The inner error bars indicate the statistical error and the outer error bars the combined statistical and systematic error. The curves are the result of fitting the data with the form $x_{I\!P}F_2^{D(3)} = (x_0/x_{I\!P})^n F_2^{D(2)}(\beta, Q^2)$ using a common exponent n. The ZEUS 94 results published in [142] are overlaid (open points).

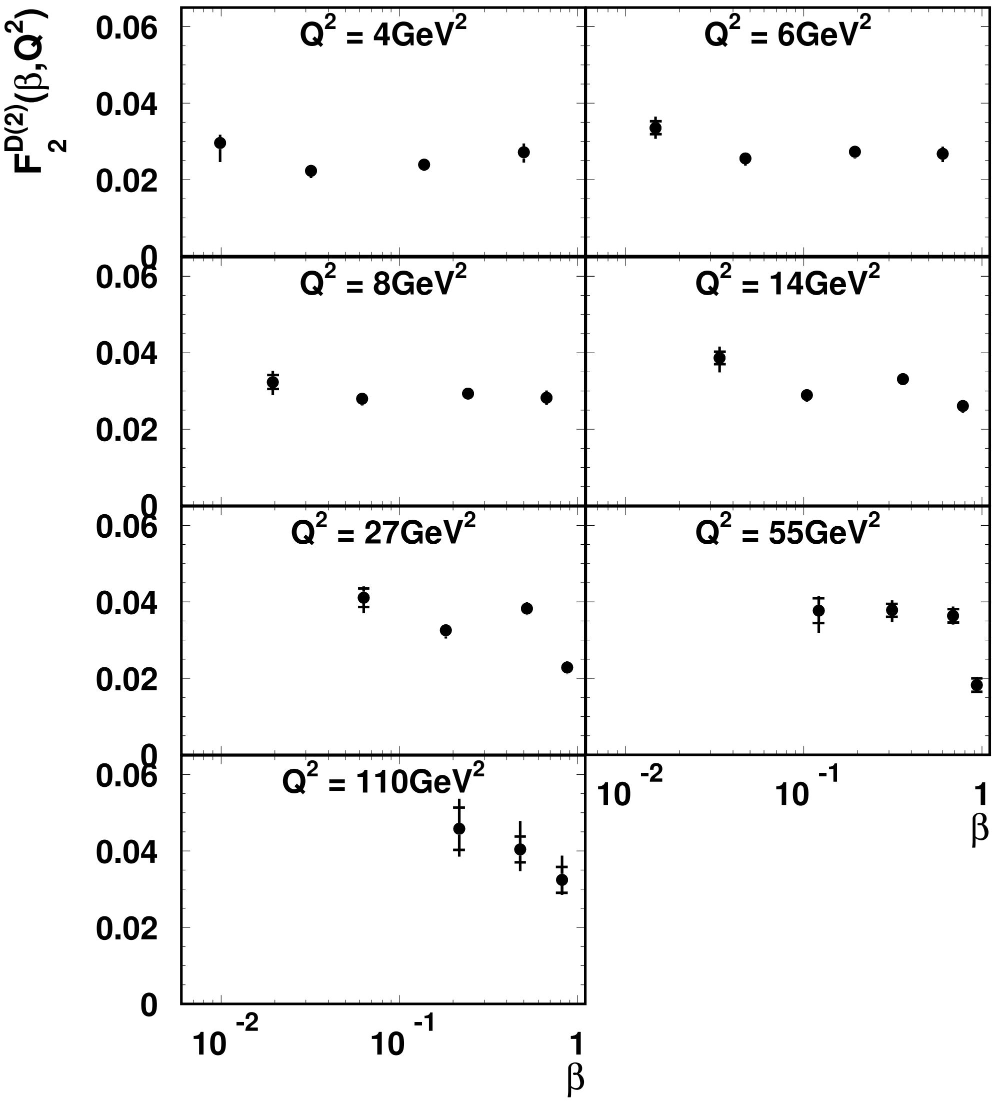

Figure 11.9: The pomeron structure function $F_x^{D(2)}(\beta, Q^2)$ is displayed as a function of β for different Q^2 values. The values were extracted from a fit to the measured $x_{I\!P} F_2^{D(3)}$ distribution. The inner error bars denote the statistical errors and the outer error bars denote the total systematic and statistical errors.

global exponent n are treated as free parameters. Using statistical errors the fit yielded $n = 0.185 \pm 0.007$, where $\chi^2/d.o.f = 202/137$. The curves in Fig. 11.8 show the results of the fit.

The values of $F_x^{D(2)}(\beta, Q^2)$ obtained in the fit are displayed in Fig. 11.9 and 11.10 as a function of β. The extraction of $F_x^{D(2)}(\beta, Q^2)$ does not depend on the assumption that $F_2^{D(3)}$ factorizes. The fit was only used to inter/extrapolate to $x_{I\!P} = x_0$ since $F_x^{D(2)}(\beta, Q^2) = x_0 F_2^{D(3)}(Q^2, \beta, x_0)$. For $\beta < 0.8$, $F_x^{D(2)}$ is observed to be approximately independent of β. For $\beta > 0.8$ the data show a decrease with β, which might be taken as an indication for evolution. The systematic errors on $F_x^{D(2)}$ were determined by extracting $F_x^{D(2)}(\beta, Q^2)$ for each of the systematic checks described in section 11.2.1 separately. The total systematic error was then evaluated as the quadratic sum of the individual deviations from the nominal value.

The Q^2 behavior of $x_{I\!P} F_2^{D(3)}$ is shown in Fig. 11.11 for fixed values of W and M_X, the variables

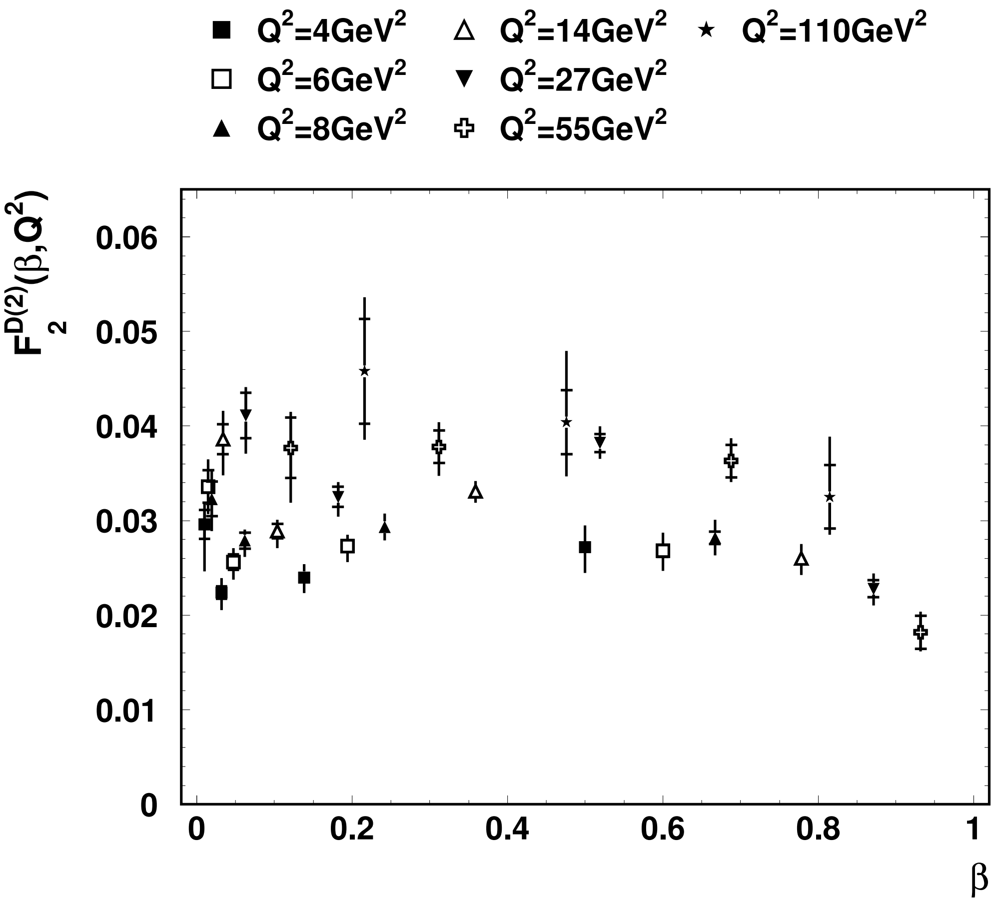

Figure 11.10: The pomeron structure function $F_x^{D(2)}(\beta, Q^2)$ is displayed as a function of β in a linear scale. The different Q^2 values are indicated by different symbols. The values were extracted from a fit to the measured $x_{I\!P}F_2^{D(3)}$ distribution.

in which the diffractive cross section is determined. In the lowest M_X bin $x_{I\!P}F_2^{D(3)}$ is observed to decrease with Q^2. For the higher M_X bins the Q^2 dependence is rather weak. The strong Q^2 variations of $Q^2 d\sigma_{\gamma^* p}^{diff}/dM_X$ and r_{tot}^{diff} (see Fig. 11.5 and 11.7) which are found for the low M_X region are mainly determined by the kinematic factor $M_X/(Q^2 + M_X^2)$ in Eq. 11.7.

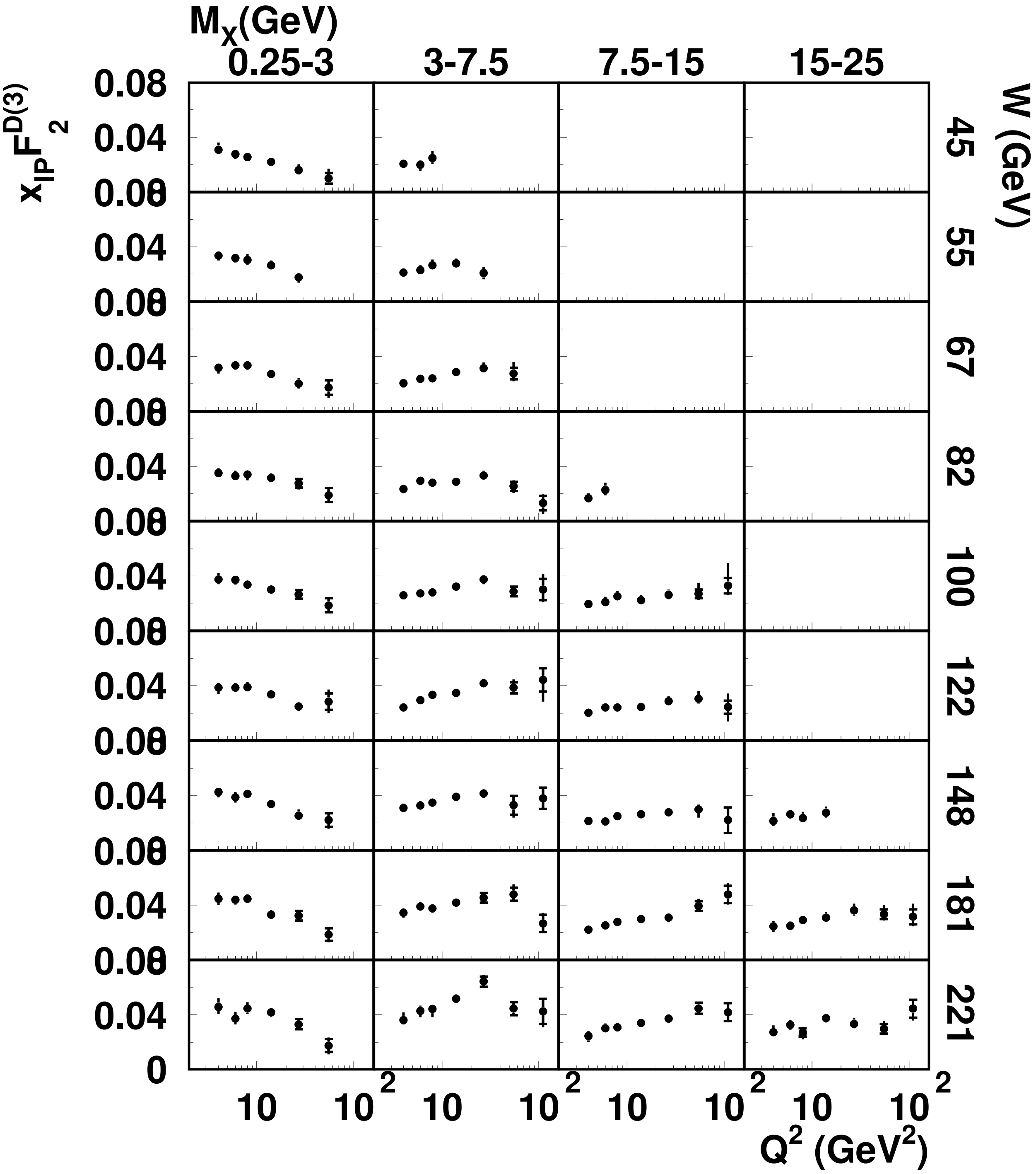

Figure 11.11: The measured values of $x_{IP} F_2^{D(3)}$ are shown as a function of Q^2 for the indicated W and M_X values.

Summary and conclusions

In this thesis a measurement of the cross section $d\sigma^{\gamma^* p \to XN}/dM_X(Q^2, W, M_X)$ of the diffractive process $\gamma^* p \to XN$ is presented. The measurement is based on a data sample corresponding to an integrated luminosity of 4.2 pb^{-1} which was collected with the ZEUS detector during the 1998/99 data taking period when HERA was running with 27.6 GeV electrons and 920 GeV protons. The analysis covers the kinematic range $3\,\mathrm{GeV}^2 < Q^2 < 160\,\mathrm{GeV}^2$, $40\,\mathrm{GeV} < W < 245\,\mathrm{GeV}$ and $M_X < 25\,\mathrm{GeV}$ which represents a significant increase of the measurement region in all three kinematic variables compared to previously published ZEUS results.

The maximum mass M_X of the photon dissociation system X up to which the separation of the systems X and N, and hence the study of diffractive events, is feasible depends on the calorimeter coverage in forward direction. In order to extend the measurement of the diffractive cross section towards higher M_X values a Forward Plug Calorimeter (FPC) has been installed into the 20 × 20 cm forward beam hole for the ZEUS calorimeter. With a 6.3 cm diameter inner hole it extends the calorimetric coverage in pseudorapidity from $\eta \leq 4.0$ to $\eta \leq 5.0$.

In the first part of this thesis the emphasis is placed on the design, construction, test, calibration and operation of the FPC. The FPC is built as a lead-scintillator sampling calorimeter with wave length shifter fiber readout. Before installation in ZEUS the FPC was tested and calibrated at the X5 test beam facility at CERN with electron, pion and muon beams in the momentum range of 10-100 GeV. The energy resolution for electrons was found to be $\sigma_E/E = 34\%/\sqrt{E} \oplus 7\%$ and for pions the energy resolution of the combined signal from the FPC and the surrounding FCAL was determined to be $\sigma_E/E = 53\%/\sqrt{E} \oplus 11\% \oplus 3\% \ln(E)$ thus outperforming the required resolution.

The FPC was calibrated using the CERN test beam data. The calibration of the entire detector response was monitored using a ^{60}Co source. After installation in ZEUS the FPC was operated only 3 cm from the beam providing stable data. The FPC was integrated into the ZEUS detector MC package and was incorporated into the energy flow algorithm which is used to reconstruct the hadronic final state of DIS events.

An extension of the measured kinematic range towards lower Q^2 values was possible since in 1995 the beam hole of the calorimeter in rear direction was reduced from 20 × 20 cm to 8 × 20 cm thus increasing the acceptance for low Q^2 events. The scattered electron is reconstructed using the combined information from the calorimeter and the position sensitive components SRTD, HES and CTD.

A measurement of the inclusive structure function $F_2(Q^2, W)$ is performed in the kinematic range covered by the measurement of the diffractive cross section. Satisfactory agreement is observed with the CTEQ4D parameterization which was obtained form fits to previously published results form H1 and ZEUS.

The diffractive contribution to the DIS cross section is extracted using the M_X method developed by the ZEUS collaboration [140]. The measured range in M_X for a fixed value of W is increased by a factor of 1.7 due to the installation of the FPC. Alternatively, for a given value of M_X the lower W limit is reduced by a factor of 0.6.

The ratio r_{tot}^{diff} of the diffractive and the total $\gamma^* p$ cross section is found to be within errors independent of the $\gamma^* p$ center of mass energy W over the entire measured region. This was observed in [142] for a smaller kinematic range and was predicted in [63]. A strong decrease of r_{tot}^{diff} with increasing Q^2 is observed for small values of M_X while the ratio is independent of Q^2 for the highest measured M_X values. The fraction of diffractive events with high masses M_X thus increases with Q^2.

The diffractive data are analyzed in terms of the diffractive structure function $x_{I\!P} F_2^{D(3)}(Q^2, \beta, x_{I\!P})$ introduced in [51]. This approach is based on the idea that diffraction is mediated by the exchange of a pomeron which is composed of partons. A rise of $x_{I\!P} F_2^{D(3)}$ is observed for $x_{I\!P} \to 0$ which reflects the rise of $d\sigma^{\gamma^* p \to XN}/dM_X$ with W. The data are consistent with the assumption that $F_2^{D(3)}$ factorizes into a pomeron flux factor $f_{I\!P/p}$ which depends only on $x_{I\!P}$ and a pomeron structure function $F_2^{D(2)}$ which only depends on Q^2 and β. The dependence of $F_2^{D(2)}$ on Q^2 and β is found to be weak in the measured range. However, a tendency of increasing $F_2^{D(2)}$ towards small β values is observed which might be taken as an indication for parton evolution.

Bibliography

[1] R.K.Ellis, W.J.Stirling, B.R.Webber, *QCD and Collider Physics*, Cambridge University Press

[2] E. Rutherford, *Phil. Mag.* **211** (1911) 669.

[3] N.F. Mott, *Proc. Roy. Soc.* **124** (1929) 425.

[4] M.N. Rosenbluth, *Phys. Rev.* **79** (1950) 615.

[5] R. Hofstadter, *Rev. Mod. Phys.* **28** (1956) 214;
R.W. McAllister and R. Hofstadter, *Phys. Rev.* **102** (1956) 851.

[6] E.D. Bloom et al, *Phys. Rev. Lett.* **23** (1969) 930;
M. Breidenback et al, *Phys. Rev. Lett.* **23** (1969) 935.

[7] J.D. Bjorken, *Phys. Rev.* **163** (1967) 1767.

[8] R.P. Feynman, *Phys. Rev. Lett.* **23** (1969) 1415.

[9] M. Gell-Mann, *Phys. Rev.* **125** (1962) 1067;
Y. Ne'eman, *Nucl. Phys.* **26** (1961) 222.

[10] M. Gell-Mann, *Phys. Lett.* **8** (1964) 214;
G. Zweig, CERN-8192/TH 401 (1964),
G. Zweig, CERN-8419/TH 402 (1964).

[11] J.D. Bjorken and E.A. Paschos *Phys. Rev.* **185** (1969) 1975.

[12] H. Fritzsch, M. Gell-Mann and H. Leutwyler, *Phys. Lett.* **B 47** (1973) 365.

[13] S. Weinberg, *Phys. Rev. Lett.* **31** (1973) 494.

[14] D.J. Gross and F. Wilczeck, *Phys. Rev.* **D 8** (1973) 3633.

[15] G. Wolf *HERA Physics* DESY report 94-022.

[16] L.N. Hand, *Phys. Lett.* **B 129** (1963) 1834.

[17] C.G. Callan and D. Gross, *Phys. Rev. Lett.* **22** (1969) 156.

[18] H. Deden et al., *Nucl. Phys.* **B 85** (1975) 269.

[19] T. Eichen et al., *Phys. Lett.* **B 46** (1973) 274.

[20] TASSO Collab., R. Bradelik et al., *Phys. Lett.* **B 86** (1979) 243.

[21] F. Halzen and A.D. Martin, *Quarks & Leptons*, J. Wiley and Sons (1984)

[22] H1 Collaboration, S. Aid et al., *Nucl. Phys.* **B 470** (1996) 3.

[23] ZEUS Collaboration, M.Derrick et al., *Z. Phys.* **C 72** (1996) 3, 399-424.

[24] Y.L. Dokshitzer, *Sov. Phys. JETP* **46** (1977) 641.

[25] V.N. Gribov and L.N. Lipatov, *Sov. J. Nucl. Phys.* **15** (1972) 438.

[26] G. Altarelli and G. Parisi, *Nucl. Phys.* **B 126** (1977) 298.

[27] L.N. Lipatov, *Sov. J. Nucl. Phys.* **23** (1976) 338.

[28] E.A. Kuraev, L.N. Lipatov and V.S. Fadin, *Sov. Phys. JETP* **45** (1977) 199.

[29] Y.Y. Balitskii and L.N. Lipatov, *Sov. J. Nucl. Phys.* **28** (1978) 822.

[30] A. Levy, *Low-x Physics at HERA*, *DESY report 97-013* (1997).

[31] K. Goulianos, *Phys. Rep.* **101** (1983) 169.

[32] G. Alberi and G. Goggi, *Phys. Rep.* **74** (1981) 1.

[33] T. Regge, *Nuovo Cimento*, **14** (1959) 951;
T. Regge, *Nuovo Cimento*, **18** (1960) 947.

[34] P.D.B. Collins, *An introduction to Regge Theory and High Energy Physics*, Cambridge University Press (1977).

[35] G.F. Chew and S.C. Frautschi, *Phys. Rev. Lett.* **8** (1962) 41.

[36] A. Donnachie and P.V. Landshoff, *Phys. Lett.* **B 296** (1992) 227.

[37] J.R. Cudell, K. Kang and S.K. Kim, *Phys. Lett.* **B395** (1997) 311.

[38] V.N. Gribov, *Sov. Phys. JETP* **14** (1962) 478.

[39] A.H. Mueller, *Phys. Rev.* **D 2** (1979) 2963.

[40] CEA-Bubble-Chamber Collab., *Phys. Rev.* **146** (1966) 994;
Aachen-Berlin-Bonn-Hamburg-Heidelberg-München Collab., *Phys. Rev.* **175** (1968) 1669 and **188** (1969) 2060;
J. Ballam et al., *Phys. Rev. Lett.* **21** (1968) 1544.

[41] J.J. Sakurai, *Ann. Phys.* **11** (1960) 1;
M. Gell-Mann and F. Zachariasen, *Phys. Rev.* **124** (1961) 124;
Y. Nambu and J.J. Sakurai, *Phys. Rev. Lett.* **8** (1962) 79;
M. Gell-Mann, D. Sharp and W.G. Wagner, *Phys. Rev. Lett.* **8** (1962) 261.

[42] J.J. Sakurai, *Phys. Rev. Lett.* **22** (1969) 981.

[43] T.H. Bauer et al., *Rev. Mod Phys.* **50** (1978) 261.

[44] ZEUS Collaboration, J. Breitweg et al., *Z. Phys.* **C 75** (1997) 421.

[45] H1 Collaboration, C. Adloff et al., *Z. Phys.* **C 74** (1997) 221.

[46] T.J. Chapin et al., *Phys. Rev.* **D 31** (1985) 17.

[47] ZEUS Collaboration, J. Breitweg et al., *Eur. Phys J.* **C 2** (1998) 237.

[48] ZEUS Collaboration, M. Derrick et al., *Phys. Lett.* **B 315** (1993) 481.

[49] H1 Collaboration, T. Ahmed et al., *Nucl. Phys.* **B 429** (1994) 477.

[50] UA8 collaboration, A. Brandt et al., *Phys. Lett.* **B 297** (1992) 417.

[51] G. Ingelman and P.E. Schlein, *Phys. Lett.* **B 152** (1985) 256.

[52] UA8 Collaboration, R. Bonino et al., *Phys. Lett.* **B 211** (1988) 239;
UA8 Collaboration, A. Brandt et al., *Phys. Lett.* **B 297** (1992) 417.

[53] J.D. Bjorken and J.B. Kogut, *Phys. Rev.* **D 8** (1973) 1341.

[54] F.E. Low, *Phys. Rev.* **D 12** (1975) 163;
S. Nussinov, *Phys. Rev. Lett.* **34** (1975) 1286.

[55] M.G. Ryskin, *Z. Phys.* **C 57** (1993) 89.

[56] S.J. Brodsky et al., *Phys. Rev.* **D 50** (1994) 471.

[57] E. Gotsman, E. Levin and U. Maor, *Nucl. Phys.* **B 493** (1997) 354.

[58] N.N. Nikolaev and B.G. Zakharov, *Z. Phys.* **C 53** (1992) 331.

[59] J. Bartels, J. Ellis, H. Kowalski and M. Wüsthoff, *Eur. Phys. J.* **C 7** (1999) 443 (hep-ph/9803497).

[60] K. Golec-Biernat and W. Wüsthoff, *Phys. Rev.* **D 59** (1999) 014017 (hep-ph/9807513);
K. Golec-Biernat and W. Wüsthoff, *Phys. Rev.* **D 60** (1999) 114023 (hep-ph/9903358).

[61] H. Kowalski, *Inclusive Diffraction at HERA*, *Talk given at Ringberg Workshop*, June 1999.

[62] W. Buchmüller and A. Hebecker, *Phys. Lett.* **B 355** (1995) 573.

[63] W. Buchmüller, M.F. McDermott and A. Hebecker, *Nucl. Phys.* **B476** (1996) 203;
A. Hebecker, hep-ph/9905226.

[64] *HERA: A Proposal for a Large Electron Proton Colliding Beam Facility at DESY*, *DESY-HERA-81/10*, Hamburg (1981).

[65] ZEUS Collaboration, *The ZEUS detector, Status Report 1993*; U. Holm ed. (1993).

[66] B. Foster et al., *Nucl. Instr. and Meth.* **A 338** (1994) 254.

[67] ZEUS Collaboration *A Microvertex Detector for ZEUS DESY-PRC 97-01* (1997).

[68] A. Andresen et al. (ZEUS Calorimeter group), *Nucl. Instr. and Meth.* **A 309** (1991) 101.

[69] M. Derrick et al., *Nucl. Instr. and Meth.* **A 309** (1991) 77.

[70] A. Bernstein et al., *Nucl. Instr. and Meth.* **A 336** (1993) 23.

[71] B. Surrow *Measurement of the Proton Structure Function F_2 at Low Q^2 and Very Low x with the ZEUS Beam Pipe Calorimeter at HERA*, Ph.D. thesis, Univ. of Hamburg (1998).

[72] R. Wichmann *Properties of the Hadronic Final State in Diffractive Deep Inelastic Scattering Tagged with the Leading Proton Spectrometer of ZEUS*, Ph.D. thesis, Univ. of California, Santa Cruz (2000).

[73] S. Bhadra et al. (ZEUS FNC group), *Design and Test of a Forward Neutron Calorimeter for the ZEUS Experiment*, *DESY Report 97-006*, hep-ex/9701015 (1997).

[74] R. Hall-Wilton et al., *internal ZEUS-Note 99-024* (1999).

[75] A. Bamberger et al., *Nucl. Instr. and Meth.* **A 401** (1997) 63-80.

[76] H. Bethe and W. Heitler, *Proc. Roy. Soc.* **A 146** (1934) 83.

[77] K. Piorzkowski and M. Zachara, *internal ZEUS-Note 94-167* (1994).

[78] CERN Application Software Group, *GEANT 3.21 Detector Description and Simulation Tool*, *CERN Program Library Long Writeup W5013* (1993).

[79] H.C. Fesefeldt, *Simulation of Hadronic Showers*, *PITHA 85-02, RWTH Aachen* (1985).

[80] G.F. Hartner, *Monte Carlo Shower Terminators for ZEUS inside GEANT311*, *ZEUS-Note 88-49*.

[81] Y. Iga, *Simulation of the ZEUS calorimeter*, *DESY 95-005* (1995).

[82] H.A. Bethe, *Ann. Physik* **5** (1930) 325.

[83] F. Bloch, *Ann. Physik* **16** (1933) 285.

[84] W. Lohmann, R. Kopp and R. Voss, *Yellow Report CERN 85-03* (1985).

[85] H. Abramowicz et al. (CDHS) *Nucl. Instr. and Meth.* **180** (1981) 429.

[86] T. Akesson et al., *Nucl. Instr. and Meth.* **A 262** (1987) 243.

[87] C. Caso et al. (Particle Data Group), Review of particle physics, *Eur. Phys. J. C3* (1998).

[88] R. Wigmans, *Nucl. Instr. and Meth.* **A 259** (1987) 389.

[89] H. Brückmann et al., *DESY Report 86-155* (1986).

[90] J.B. Birks, *Proc. Phys. Soc* **A64**, (1951) 389.

[91] U. Behrens et al. (ZEUS calorimeter group), *Nucl. Instr. and Meth.* **A 289** (1990) 115.

[92] E. Bernardi et al. (ZEUS Collaboration), *Nucl. Instr. and Meth.*, **A 262** (1987) 229.

[93] ZEUS Collaboration, *A Forward Plug Calorimeter for the ZEUS Detector*, *DESY-PRC 97-02*.

[94] H. Fessler et al., *Nucl. Instr. and Meth.*. **A 240** (1985) 284.

[95] B. Loehr et al., *Nucl. Instr. and Meth.*. **A 257** (1987) 145.

[96] L. Labarga and E. Ros, *Nucl. Instr. and Meth.*, **A 249** (1986) 228.

[97] T. Hasegawa et al., *Nucl. Instr. and Meth.*, **A 311** (1992) 498.

[98] M. Kasemann et al. (ZEUS FPC group) *Data analysis of the ZEUS Forward Plug Calorimeter beam test at CERN internal ZEUS-Note 2000-001* (2000).

[99] M. Gospic, H. Groenstege, *A remote controlled high voltage supply system for photomultiplier tubes*, *internal ZEUS-Note 96-006* (1996).

[100] L. Hervas et al., *The readout electronics for the ZEUS Calorimeter upgrade components*, *internal ZEUS-Note 96-005* (1996).

[101] A. Caldwell et al., *Nucl. Instr. and Meth.*, **A 321** (1992) 356.

[102] P. Göttlicher et al., *The Frontend Readout and Trigger Electronics for the FPC*, *internal ZEUS-Note 99-013* (1999).

[103] J.P. Fernández et al., *Test of a FPC prototype at DESY*, *internal ZEUS-Note 98-068* (1998).

[104] L. Gatignon, *The West Experimental Area at the CERN SPS*, *CERN SL-99-013 EA* (1999).

[105] B. Rossi, *High Energy Particles, Prentice-Hall*, Inc., Englewood Cliffs, NJ, 1952.

[106] A. Bamberger et al. (ZEUS FPC group), *The ZEUS Forward Plug Calorimeter with Lead-Scintillator Plates and WLS Fiber Readout*, *Nucl. Instr. and Meth.*, **A 450** (2000) 235 (hep-ex/9912045).

[107] L. Khein, *An approach to the FPC HAC calibration*, *ZEUS-Note 00-025* (2000).

[108] G.A. Akopdjanov et al., *Nucl. Instr. and Meth.*, **140** (1977) 441.

[109] T.C. Awes et al., *Nucl. Instr. and Meth.*, **A 311** (1992) 130.

[110] U. Behrens et al., *Nucl. Instr. and Meth.*, **A 323** (1992) 611.

[111] I. Bohnet, *Experimentelle Untersuchung an den optischen Komponenten des ZEUS-Kalorimeters und Modifikation des ^{60}Co Meßsystems*, Ph.D. thesis, Hamburg University, I. Institute of Exp. Physics (1996).

[112] H. Spiesberger, *HERACLES and DJANGOH: Event Generation for ep Interactions at HERA Including Radiative Processes* (1998) available on WWW:http://www.desy.de/∼hspiesb/djangoh.html,
H. Spiesberger, *DJANGO6 version 2.4 - A Monte Carlo Generator for Deep Inelastic Lepton Proton Scattering Including QED and QCD Radiative Effects* (1996) available on WWW:http://www.desy.de/∼hspiesb/django6.html.

[113] H. Spiesberger, *HERACLES. An Event Generator for ep Interactions at HERA Including Radiative Processes version 4.6* available on WWW:http://www.desy.de/∼hspiesb/heracles.html,
A. Kwiatkowski, H. Spiesberger and H.-J. Möhring, *Comp. Phys. Commun.* **69** (1992) 155.

[114] G. Ingelman, A. Edin and J. Rathsman, *Comp. Phys. Commun.* **101** (1997) 108.

[115] L. Lönnblad, *Comp. Phys. Commun.* **71** (1992) 15.

[116] T. Sjöstrand, *Comp. Phys. Commun.* **82** (1994) 74.

[117] CTEQ Collaboration, H.L. Lai et al., *Phys. Rev.* **D 55** (1997) 1280.

[118] H. Jung, *The RAPGAP Monte Carlo for Deep Inelastic Scattering version 2.08* available on WWW:http://www.quark.lu.se/∼hannes/rapgap.html

[119] H1 Collaboration, C. Adloff et al., *Z. Phys.* **C 76** (1997) 613.

[120] H. Kowalski, *Inclusive Diffraction at HERA*, New Trends in HERA Physics 1999, Ringberg Workshop, June 1999, *DESY 99-141*.

[121] ZEUS Collaboration, *A measurement of the total photon-proton cross section at a center-of-mass energy of 207 GeV at HERA*, to be published.

[122] M. Kasprzak, *EPSOFT - a Monte Carlo generator of soft photon-proton collisions ZEUS-Note 95-069* (1995).

[123] G.F. Hartner et al., *ZEUS-Note 97-064* ,
G.F. Hartner, *ZEUS-Note 98-058*.

[124] A. Savin, *Study of Calorimeter Noise in the 1996 data, internal ZEUS-Note 98-07* (1998).

[125] H. Abramowicz, A. Caldwell and R. Sinkus, *Nucl. Instr. and Meth.*, **A 365** (1995) 508.

[126] R. Sinkus and T. Voss, *Nucl. Instr. and Meth.*, **A 391** (1997) 360.

[127] T. Doeker, A. Frey and M. Nakao, *Electron Position Reconstruction - Update of the ELECPO routines*, *ZEUS-Note 94-123* (1994).

[128] Ch. Amelung, *Electron Position Reconstruction in ZEUS: Further Update on the ELECPO Package (Based on 1995 Data)*, *ZEUS-Note 96-093* (1996).

[129] J. Ng and W. Verkerke *An Overview of SRTD Analysis ZEUS-Note 95-037* (1995).

[130] R. Deffner, *Measurement of the Proton Structure Function F_2 at HERA using the 1996 and 1997 ZEUS Data*, Ph.D. thesis, Univ. of Bonn (1999).

[131] G.M. Briskin, *Diffractive Dissociation in ep Deep Inelastic Scattering*, Ph.D. thesis, Tel Aviv University (1998).

[132] A. Caldwell et al., *BCAL Electron Studies Part II: Energy Scale Calibration*, *ZEUS-Note 98-018* (1998).

[133] F. Jacquet and A. Blondel, *Proc. of the study of an ep facility for Europe*, edited by U. Amaldi, *DESY 79-48* (1979) 393.

[134] S. Bentvelsen, J. Engelen and P. Kooijman, *HERA Workshop 1991, Vol. 1*, 23.

[135] K.C. Hoeger, *HERA Workshop 1991, Vol. 1*, 43.

[136] U. Bassler and G. Bernardi, *Nucl. Instr. and Meth.*, **A 361** (1995) 197.

[137] ZEUS Collaboration, J. Breitweg et al., *Eur. Phys. J.* **C 1** (1998) 81.

[138] ZEUS Collaboration, M. Derrick et al., *Phys. Lett.* **B 332** (1994) 228.

[139] ZEUS Collaboration, *Three-Jet Production in Diffractive Deep Inelastic Scattering at HERA*, to be published.

[140] ZEUS Collaboration, M. Derrick et al., *Z. Phys.* **C 70** (1996) 3, 391.

[141] H. Kowalski, M. Rocco and G. Wolf, *Material for 1996 Paper: Cross Section Measurement of Diffractive Production in Deep Inelastic Scattering*, ZEUS-Note 96-038 (1998).

[142] ZEUS Collaboration, J. Breitweg et al., *Eur. Phys. J.* **C 6** (1999) 43.

[143] R.P. Feynman, *Photon-Hadron Interactions*, *Benjamin, N.Y.* (1972), lectures 50-54.

Acknowledgments

Many people contributed to the work presented in this thesis and supported me during my Ph.D. studies. I would like to take this opportunity to thank them all.

I am thankful to Prof. Robert Klanner and Prof Günter Wolf who gave me the opportunity to work on my Ph.D. within the ZEUS collaboration at DESY. I owe special thanks to Prof Günter Wolf for the extensive effort we shared working on the ZEUS data analysis and for his careful reading of the drafts of this thesis providing me with numerous and valuable comments.

It was a great experience to work with the FPC group. I enjoyed very much working with Matthias Kasemann, Juan Pablo Fernández, Arafat Gabareen, Gastón García, Peter Göttlicher, Ricardo Graciani, Masahide Inuzuka, Lev Khein, Heuijin Lim, José del Peso, Alexandre Savin, Sabine Wölfle, Taro Yamashita and Yuji Yamazaki. The construction of the FPC would not have been possible without the smooth collaboration of many technicians and engineers, in particular Jan Hauschild, Klaus Löffler and Holger Maser. I would also like to thank Nils Gendner, Rainer Feller and Heinz Prause for their support with the cobalt scans.

I owe special thanks to Henri Kowalski, Ludger Lindemann and Mario Martínez for teaching me much of what I know about how to analyze ZEUS data.

I am very grateful for the friendly atmosphere within the ZEUS collaboration. Many thanks to Olaf Deppe, Ulrich Fricke, Oscar Gonzalez, Kirstin Hebbel, Dorian Kcira, Amaya López-Duran, Bruce Mellado, Matthias Moritz, Nikolai Pavel, Igancio Redondo, Stefan Stonjek and Mónica Vázquez for many helpful discussions and for all the activities we shared outside physics. Special thanks to Margherita Milite for all her support and for cheering up my life.

Last but not least I would like to thank my family for their continuous support.